

Durham E-Theses

Lagrangian modelling of precipitation and speleothem proxy oxygen isotope systematics in the East Asian Summer Monsoon region

BAKER, ALEXANDER,JOHN

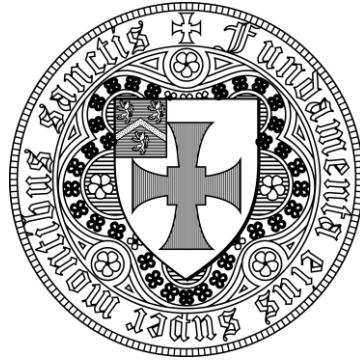
How to cite:

BAKER, ALEXANDER,JOHN (2014) *Lagrangian modelling of precipitation and speleothem proxy oxygen isotope systematics in the East Asian Summer Monsoon region*, Durham theses, Durham University. Available at Durham E-Theses Online: <http://etheses.dur.ac.uk/11460/>

Use policy



This work is licensed under a [Creative Commons Attribution Non-commercial No Derivatives 2.0 UK: England & Wales \(CC BY-NC-ND\)](https://creativecommons.org/licenses/by-nc-nd/2.0/)



**Lagrangian modelling of precipitation and speleothem
proxy oxygen isotope systematics in the East Asian
Summer Monsoon region**

Alexander John Baker

*This thesis is submitted in partial fulfilment of the
requirements for the degree of Doctor of Philosophy*

**Department of Earth Sciences
University of Durham**

2014

Abstract

The Asian Summer Monsoon generates intense seasonal precipitation across India, China and Indochina, comprising Earth's largest monsoonal climate regime, and this vital component of the global energy and water cycles directly impacts the world's most populous regions. Accurate palaeomonsoon reconstructions are required to investigate natural climate variability beyond the coverage of instrumental records and inform predictions of future monsoon trends. Stable oxygen isotope ratios ($\delta^{18}\text{O}$) are an important proxy for hydroclimate variability and stalagmite $\delta^{18}\text{O}$ is widely used to investigate East Asian palaeoclimate, typically interpreted as a semi-quantitative measure of precipitation amount. However, recent studies suggest $\delta^{18}\text{O}$ instead reflects multiple hydroclimatic processes, warranting a detailed understanding of precipitation and proxy $\delta^{18}\text{O}$ systematics. This thesis (i) presents a quantitative Lagrangian study of atmospheric moisture transport and precipitation across central and eastern China, a continental region affected by the East Asian Summer Monsoon (EASM); (ii) investigates the hydroclimatic drivers of precipitation $\delta^{18}\text{O}$ variability at Wanxiang Cave, an important site for palaeomonsoon reconstruction located near to the northerly EASM limit; (iii) evaluates the extent to which seasonal- to decadal-scale proxy $\delta^{18}\text{O}$ variability reflects terrestrial moisture fluxes by constructing a pseudoproxy record for Wanxiang.

Present-day precipitation across monsoonal China is primarily derived from the northern Indian Ocean and recycled intensely over the East Asian continent; Pacific Ocean moisture export peaks during winter. A geographically variable isotopic source effect is apparent in present-day mean monthly precipitation $\delta^{18}\text{O}$ data. Wanxiang Cave precipitation $\delta^{18}\text{O}$ variability during AD 2001-2002 is successfully reproduced by a recently-developed Lagrangian model which simulates air masses' isotopic evolution along three-dimensional atmospheric trajectories, though winter values are ~ 2 ‰ over-depleted. Contributions of Tibetan Plateau- and free troposphere-derived moisture are identified as synoptic-scale isotopic depletion processes. Overall, land-derived moisture causes isotopic enrichment during summer, thus moderating depletion due to strengthened EASM circulation or increased precipitation amount. As such, periods of elevated summer surface temperatures may attenuate the seasonal EASM signal in precipitation and proxy $\delta^{18}\text{O}$. An idealised Rayleigh-type isotope model is unable to capture these effects accurately, emphasising the importance of regional moisture fluxes. A pseudoproxy record, driven by terrestrial moisture fluxes, replicates seasonal- to decadal-scale stalagmite $\delta^{18}\text{O}$ variability at Wanxiang. The work presented in this thesis offers new insights into the influence of atmospheric moisture transport dynamics on precipitation and proxy $\delta^{18}\text{O}$ variability across central and eastern China. This constitutes an important advancement in our ability to use $\delta^{18}\text{O}$ to reconstruct past climate variability quantitatively in the EASM region.

Table of contents

List of figures	<i>vii</i>
List of tables	<i>ix</i>
Appendices	<i>x</i>
Abbreviations	<i>xi</i>
Declaration and copyright statement	<i>xii</i>
Acknowledgements	<i>xiii</i>
Chapter 1 – Introduction and background	1
1.1 Introductory remarks	2
1.2 The karst system.....	3
1.2.1 Karst hydrogeology	4
1.2.2. Calcareous speleothem deposition	6
1.2.3. Stalagmite growth rate	8
1.2.4. The cave environment	9
1.3. Stable oxygen isotope fractionation in the atmospheric branch of Earth’s hydrological cycle	10
1.3.1. Conventional ‘ δ ’ notation	11
1.3.2. Seawater evaporation	12
1.3.3. Atmospheric vapour, circulation and precipitation.....	14
1.3.3.1. Isotopic ‘effects’ in precipitation $\delta^{18}\text{O}$	15
1.3.4. The Meteoric Water Line	17
1.3.5. Modelling precipitation $\delta^{18}\text{O}$	18
1.4. $\delta^{18}\text{O}$ as a palaeoclimate proxy.....	19
1.4.1. Stalagmites as palaeoclimate archives	20
1.4.1.1. Calcite-water isotope fractionation	21
1.4.2. Modelling stalagmite $\delta^{18}\text{O}$	22
1.5. Thesis overview	24
Chapter 2 – Reconstructing modern stalagmite growth from cave monitoring, local meteorology, and experimental measurements of dripwater films	26
Chapter summary	27
2.1. Introduction and rationale	28
2.1.1. Controls on stalagmite growth rate	30
2.1.2. Rationale for selecting the Gib04a stalagmite sample	31
2.2. Site description.....	32
2.3. Methods.....	34
2.3.1. Experimental measurements of dripwater film thickness	34

2.3.1.1. Experimental setup and procedure	35
2.3.1.2. Analytical procedure	37
2.3.2. Construction of a time-series stalagmite growth model.....	39
2.4. Results and discussion	44
2.4.1. Relationships between local meteorological variables, cave microclimate, and growth rate.....	44
2.4.2. Control of stalagmite apex morphology on film thickness	45
2.4.3. Constraints on film thickness and reconstructing modern Gib04a growth (1951-2004)	48
2.4.3.1. Non-uniform Gib04a growth	51
2.4.4. Model validation: comparing growth seasonality with Gib04a petrography and Sr	52
2.4.5. Model validation: modelled Sr-partitioning in Gib04a calcite	54
2.4.6. Vertical growth rate sensitivity to film thickness	57
2.4.7. Local meteorological controls on interannual vertical growth rate variability	59
2.5. Conclusions	60
Chapter 3 – The Asian Summer Monsoon: meteorology and palaeoclimatology	63
Chapter summary	64
3.1. Asian Summer Monsoon meteorology.....	65
3.2. Holocene palaeomonsoon reconstructions	67
3.3. Selected cave sites within monsoonal China	71
3.3.1. Northern China.....	71
3.3.1.1. Wanxiang Cave	71
3.3.1.2. Wuya Cave	72
3.3.1.3. Huangye Cave	73
3.3.1.4. Dayu Cave.....	73
3.3.2. Southern and eastern China.....	74
3.3.2.1. Hulu Cave	74
3.3.2.2. Dongge Cave.....	74
3.4. Recent re-examination of Chinese stalagmite records	75
3.5. Concluding remarks	77
3.6. Thesis research objectives.....	78
Chapter 4 – East Asian Summer Monsoon precipitation sources: atmospheric trajectories, moisture budgets, and implications for interpreting precipitation oxygen isotope data	80
Chapter summary	81
4.1. Introduction and rationale	82
4.2. Methods.....	83
4.2.1. Lagrangian moisture source diagnostics	83
4.2.1.1. Setup of the Lagrangian moisture diagnostic.....	86

4.2.1.2. Source region sectorisation	86
4.2.2. Comparison with precipitation isotopes	89
4.3. Results and discussion	91
4.3.1. Sub-continental scale spatial moisture uptake patterns.....	91
4.3.1.1. Moisture uptake within the atmospheric boundary layer	91
4.3.1.2. Free troposphere moisture contributions.....	92
4.3.2. Lagrangian forward projections of moisture source location	95
4.3.3. Comparison of Lagrangian and instrumental precipitation.....	100
4.3.4. Moisture source seasonality	103
4.4. Implications for EASM precipitation $\delta^{18}\text{O}$ interpretation.....	106
4.4.1. Source effect in precipitation $\delta^{18}\text{O}$	106
4.4.2. Geographic variability in EASM precipitation signal strength.....	106
4.5. Summary and conclusions	108

Chapter 5 – Modelling the stable oxygen isotope composition of precipitation at the northerly limit of the East Asian Summer Monsoon region 111

Chapter summary	112
5.1. Introduction and rationale	113
5.1.1. Stable water isotope modelling	113
5.1.2. Rationale for selecting Wanxiang Cave.....	114
5.2. Data and methods	116
5.2.1. Stable water isotope measurements from Wanxiang Cave	116
5.2.2. The Isotra3 model	118
5.2.2.1. Overview	118
5.2.2.2. Model parameterisations	119
5.2.2.3. Lagrangian trajectory data for Isotra3 model runs	122
5.2.2.4. Constraints on initial source water $\delta^{18}\text{O}$	123
5.2.2.5. Exclusion of non-precipitating trajectories	124
5.3. Modelling Wanxiang Cave precipitation $\delta^{18}\text{O}$ with Isotra3	125
5.3.1. Results	125
5.3.1.1. Trajectories and event-scale moisture uptake	125
5.3.1.2. Precipitation amount and $\delta^{18}\text{O}$	129
5.3.2. Discussion: precipitation $\delta^{18}\text{O}$ response to moisture fluxes.....	131
5.3.2.1. Isotopic enrichment due to terrestrial moisture.....	131
5.3.2.2. Isotopic depletion due to Tibetan Plateau moisture	133
5.3.2.3. Isotopic depletion due to free troposphere moisture	134
5.4. Summary and conclusions	136

Chapter 6 – Validating stalagmite oxygen isotope proxy data interpretations: an ECHAM4-MCIM approach to constructing pseudoproxy records 139

Chapter summary	140
6.1. Introduction and rationale	141

6.2. The Mixed Cloud Isotope Model	142
6.2.1. Overview	142
6.2.2. MCIM sensitivity tests	144
6.3. Data and methods	146
6.3.1. Diagnosed isotopic fractionation conditions	146
6.3.2. MCIM precipitation event $\delta^{18}\text{O}$ model runs	148
6.3.3. ECHAM4-MCIM approach to creating pseudoproxy records	148
6.4. Wanxiang Cave precipitation $\delta^{18}\text{O}$ modelled by MCIM	152
6.5. Wanxiang proxy $\delta^{18}\text{O}$ response to terrestrial moisture fluxes	157
6.6. Summary and conclusions	161
Chapter 7 – Synthesis of results, their implications, and the outlook for future research	164
7.1. Introductory remarks	165
7.2. Synthesis of results	165
7.2.1. EASM precipitation moisture sources	165
7.2.2. Precipitation isotope modelling	167
7.2.3. Comparing proxy and pseudoproxy records at Wanxiang Cave	169
7.3. Implications and research outlook	171
7.3.1. The importance of moisture dynamics in EASM variability predictions	171
7.3.2. Future systematic multi-proxy comparisons	172
7.3.3. Future pseudoproxy modelling	173
7.4. Concluding remarks	174
Bibliography	175

List of figures

Chapter 1

Figure 1.1. Schematic illustration of karst hydrogeology and cave system processes	5
Figure 1.2. Schematic illustration of stable oxygen isotope fractionation during hydroclimatic processes	13
Figure 1.3. Modern global precipitation $\delta^{18}\text{O}$ distribution.....	17

Chapter 2

Figure 2.1. Study locations	33
Figure 2.2. Illustration of experimental procedure.....	36
Figure 2.3. Example dripwater droplet photograph	38
Figure 2.4. Synthesis of data originally presented by Dreybrodt (1999).....	42
Figure 2.5. Gib04a monitoring data (2004-2009)	43
Figure 2.6. Experimental measurements of dripwater film thickness.....	47
Figure 2.7. Cut section of the modern growth of Gib04a (AD 1951-2004).....	49
Figure 2.8. Gib04a growth reconstruction AD 1951-2004	50
Figure 2.9. Gib04a growth, Sr and petrography	55
Figure 2.10. Estimated K_d^{Sr} from R_0	57
Figure 2.11. First-order quantification of δ -sensitivity of R_0	58
Figure 2.12. Inferred relationships between Gib04a R_0 and local climate parameters	60

Chapter 3

Figure 3.1. Present-day ASM meteorology.....	66
Figure 3.2. High-resolution Holocene ISM and EASM speleothem $\delta^{18}\text{O}$ records	70
Figure 3.3. Map of selected cave sites within monsoonal China.....	71

Chapter 4

Figure 4.1. Lagrangian moisture source diagnostic technique.....	84
Figure 4.2. Precipitation target domains and source regions	89
Figure 4.3. Monthly boundary layer moisture sources for precipitation over China.....	94
Figure 4.4. Seasonal mean free troposphere moisture contribution.....	95
Figure 4.5. Seasonal moisture source longitude Lagrangian forward projections.....	97

Figure 4.6. May-August moisture source longitude Lagrangian forward projections	98
Figure 4.7. Seasonal moisture source latitude Lagrangian forward projections	99
Figure 4.8. Mean seasonal Lagrangian precipitation estimate	102
Figure 4.9. Correlation between Lagrangian precipitation estimates and station data	103
Figure 4.10. Monthly source region moisture contributions to precipitation in China.....	105
Figure 4.11. Amount effect <i>versus</i> source effect in precipitation $\delta^{18}\text{O}$	108

Chapter 5

Figure 5.1. Local meteoric water line and Wanxiang Cave water isotope data.....	117
Figure 5.2. Schematic illustration of fractionation processes simulated by Isotra3.....	119
Figure 5.3. Example summer back trajectories arriving at Wanxiang Cave.....	127
Figure 5.4. Example winter back trajectories arriving at Wanxiang Cave	128
Figure 5.5. Wanxiang Cave precipitation $\delta^{18}\text{O}$ modelled by Isotra3	130
Figure 5.6. Observed precipitation $\delta^{18}\text{O}$ versus terrestrial moisture contribution	133
Figure 5.7. Modelled precipitation $\delta^{18}\text{O}$ versus synoptic FT moisture contribution	136

Chapter 6

Figure 6.1. Schematic overview of MICM	144
Figure 6.2. MCIM sensitivity test results.....	145
Figure 6.3. Diagnosed synoptic fractionation conditions.....	147
Figure 6.4. Seasonal mean source locations for precipitation at Wanxiang Cave	150
Figure 6.5. Correlation between surface temperature and terrestrial moisture uptake	152
Figure 6.6. Wanxiang Cave precipitation $\delta^{18}\text{O}$ modelled by MCIM.....	153
Figure 6.7. Correlation between modelled precipitation $\delta^{18}\text{O}$ and temperature change	156
Figure 6.8. Comparison of Wanxiang stalagmite $\delta^{18}\text{O}$, nearby records, and pseudoproxy data	159
Figure 6.9. Comparison of normalised Wanxiang stalagmite $\delta^{18}\text{O}$, nearby records, and pseudoproxy data	160

List of tables

Chapter 4

Table 4.1. Input parameters for Lagrangian diagnostics	88
Table 4.2. Geographic definition of target domains	90
Table 4.3. ABL and FT moisture contributions	93

Chapter 5

Table 5.1. Regionally-averaged terrestrial water isotope values	122
---	-----

Appendices

Appendix 1. Full Gib04a monthly growth rate reconstruction.

Appendix 2. Geographical areas of moisture source sectors and target domains.

Appendix 3a. Sectorised monthly time series of boundary layer evaporative moisture uptake from terrestrial areas.

Appendix 3b. Sectorised monthly time series of combined boundary layer and free troposphere moisture contributions from oceanic areas.

Appendix 3c. Sectorised monthly time series of combined boundary layer and free troposphere total moisture contributions.

Appendix 3d. Sectorised monthly time series of combined boundary layer and free troposphere moisture contributions (summary dataset).

Appendix 4a. Example Isotra3 input file.

Appendix 4b. Example Isotra3 output file.

Appendix 5. Initial and arrival conditions diagnosed for sampled precipitation events.

Appendix 6. ECHAM4-MCIM pseudoproxy dataset.

Abbreviations

a.m.s.l.	above mean sea level
ABL	Atmospheric Boundary Layer
ASM	Asian Summer Monsoon
EASM	East Asian Summer Monsoon
ECHAM	ECMWF Hamburg
ECMWF	European Centre for Medium-Range Weather Forecasting
ERA	ECMWF Reanalysis
FT	Free Troposphere
GCM	Global Climate Model / General Circulation Model
GNIP	Global Network of Isotopes in Precipitation
GPCC	Global Precipitation Climatology Centre
ISM	Indian Summer Monsoon
ITCZ	Intertropical convergence zone
MCIM	Mixed Cloud Isotope Model

Declaration and copyright statement

This thesis describes my own work, except where acknowledgement is made in the text, and is not the same as any work that has been submitted to this or any other university for any degree, diploma or other qualification.



2nd December 2014

© Copyright, Alexander John Baker, 2014.

The copyright of this thesis rests with the author. No quotation from it should be published without the author's prior written consent and information derived from it should be acknowledged.

Acknowledgments

This thesis would not have been possible without the support of many people. I first very gratefully acknowledge the Sir Kingsley Dunham Trust for funding my research. My supervisors, James Baldini and Jeroen van Hunen, have offered their time and advice generously over the past few years. They've read countless chapter and manuscript drafts, sat through presentation rehearsals, and continually guided me and my work. For James' conception of this project and for giving me the opportunity to pursue a doctorate, I could not be more grateful. Members of the Palaeoclimate Group at Durham – Harriet, Iza, Bob, Lisa and Marianne – were a pleasure to work alongside and I have learned from you all. Durham colleagues – Howard Armstrong, Ed Llewellyn, Simon Mathias, and Darren Gröcke – are thanked for taking an interest in my work, and I have no doubt that their advice improved this thesis. I am grateful to Howard also for excellent fieldwork experiences on Cyprus. I also offer much gratitude to Colin Wintrip, who machined apparatus used in part of my work.

In 2012 and 2014, I visited ETH Zürich to conduct research and I appreciate enormously the enthusiastic collaboration of all those with whom I worked. Harald Sodemann became a *de facto* third supervisor, to whose atmospheric modelling expertise I am very much indebted. I owe much of my understanding of oxygen isotope systematics to Harald, Marina Dütsch and Alexander Läderach. I must thank Heini Wernli for welcoming me into the Atmospheric Dynamics group, many members of which supported me during my visits, particularly Atsumu Ohmura, Andreas Winshall, Stephan Pfahl, Hanna Joos, and Michael Sprenger. I am very grateful to Sebastian Breitenbach (ETH) for our many insightful discussions and for involving me in his work, and Kathleen Johnson (UC Irvine, USA) and Zhang Pingzhong (CAS, China), who kindly provided their Wanxiang Cave precipitation isotope data. I also extend sincere thanks to my examiners, Prof. Gideon Henderson FRS (Oxford) and Prof. Fred Worrall (Durham), whose feedback improved this thesis.

That the last few years were immensely enjoyable is down to so many people. In particular, I thank all my housemates: Beej, Clayton and Tim for our scrapes; Abi, Kristina and Alice for their friendship; Harriet for showing me just how motivating good breakfasts can be. For the very best of times – travel, antics, sport, even dancing – I also thank, among many others, Pete, Bob, Iza, Claire, Suzie, Leo, Iain, Rachel, Ahmed, Muneer, and Matt. I've enjoyed many highs and lows with Durham Earth Sciences' five-a-side team, and I am particularly grateful to three players – Ian, Chris and James – for developing a healthy staff-postgraduate rivalry and for indulging me when I got carried away.

Lastly, and perhaps most importantly, there is much I owe to Mary, who I am so very lucky to have, and my family, especially my parents, without whom I quite simply would not be where I am. I love you all.

“My magnificent octopus.”

- *Baldrick*

Chapter 1

Introduction and background

1.1. Introductory remarks

The development of accurate palaeoclimate reconstructions underpins our understanding of natural climate variability on various timescales and of the response of the climate system to forcing mechanisms (Jones *et al.*, 2009). Palaeoclimate proxy data provide insights into past climate change well beyond the earliest instrumental records and inform climate modelling studies, advancing our understanding of interactions between climate system components and providing context against which anthropogenic climate change may be assessed. Global and regional palaeoclimate data and modelling are therefore of considerable societal as well as scientific value (IPCC, 2013).

Speleothems are secondary cave precipitates, deposited by infiltrating vadose water, which provide precisely-dated, multi-proxy geochemical proxy records of past climate change (Henderson, 2006). Stalagmites in particular routinely yield records because their morphology is conducive to constructing high-resolution records using current microanalytical laboratory techniques (Spötl and Matthey, 2006). Stable oxygen isotope ratios are the most commonly applied palaeoclimate proxy and such records have significantly advanced our understanding of continental temperature and precipitation variability during the period ~500 ka-present (McDermott, 2004), providing insights into global teleconnections in Earth's climate system (e.g., Cheng *et al.*, 2009; Frisia *et al.*, 2003; Griffiths *et al.*, 2009; Wang *et al.*, 2004; Wang *et al.*, 2005).

However, isotopic climate signals are transmitted non-linearly to speleothems. Interpreting stable oxygen isotope ratios measured in rainfall or speleothems is complicated by three principal issues. Firstly, multiple fractionating hydroclimatic processes transporting moisture from source to cave site control the isotopic evolution of atmospheric vapour and

precipitation. Therefore, final oxygen isotope ratios do not necessarily provide a direct proxy for any single climatic variable, such as precipitation (Lachniet, 2009). Secondly, the net isotopic signature transmitted to a given cave site may be modified and time-averaged by site-specific karst hydrogeology (Fairchild *et al.*, 2006b). Thirdly, multiple surface and cave processes control stalagmite growth rate (Dreybrodt, 1988), variability in which may induce biases in proxy records (Baldini *et al.*, 2008). To understand these sources of climate signal modification, researchers undertake meteorological and cave monitoring campaigns (e.g., Matthey *et al.*, 2010; Miorandi *et al.*, 2010) and forward modelling studies (e.g., Jex *et al.*, 2013; Wackerbarth *et al.*, 2010), which inform palaeoclimatic interpretations of proxy data.

This chapter presents introduces central aspects of speleothem palaeoclimatology: (i) the deposition of speleothems, (ii) cave environments and karst hydrogeology, (iii) stable oxygen isotope fractionation in the atmospheric branch of the hydrological cycle, and (iv) the application of stable oxygen isotope ratios as a palaeoclimate proxy. The most recent and comprehensive review of speleothem palaeoclimatology is that of Fairchild and Baker (2012). Lastly, the organisation of this thesis is summarised and the purpose of each of the subsequent chapters given.

1.2. The karst system

Cave environments, their interactions with the exterior atmosphere, karst hydrogeology, and the magnitude of local climate variability each have consequences for preserving climate signals in speleothems. Taking a systems perspective, this was termed ‘speleophysiology’ by Fairchild *et al.* (2006a).

1.2.1. Karst hydrogeology

Karst geomorphology is characterised by cave development, deficient drainage and non-Darcian groundwater flow through aquifers (White, 1988). Groundwater run-off and subsurface fluxes through carbonate porosity (micropore), fractures and solution-enhanced conduits (macropore) transport water through the epikarst (alternatively, the subcutaneous zone), and karst hydrology therefore responds to local climate variability (Fig. 1.1). Water infiltrating the soil zone and permeable epikarst eventually reaches cave cavities, and this vadose water may participate in calcareous speleothem deposition in the unsaturated zone (Dreybrodt, 1988), as described in section 1.2.2 (Fig. 1.1).

The distribution of flow path types delivering karst water to drip sites in caves and the storage capacity and outflow rates of karst aquifers determine the response of those drip sites to rainfall events (Fig. 1.1). Hydrologically responsive drip sites are required to convey a geochemical (stable isotopes and/or trace elements) climate signal from the surface to an actively-growing stalagmite (Fairchild *et al.*, 2006b), and these factors are site-specific. Therefore, multi-annual, instrumental monitoring of surface and cave environmental parameters (e.g., temperature, humidity, $p\text{CO}_2$) and hydrology (i.e., rainfall and drip rates) is a necessary pre-requisite for determining appropriate samples and for interpreting the resultant proxy data. Monitoring data are used to characterise drip sites (e.g., Genty, 2008; Miorandi *et al.*, 2010), groundwater hydrochemistry (e.g., Matthey *et al.*, 2010), and karst aquifer storage and mixing (e.g., Fairchild *et al.*, 2006c; Tooth and Fairchild, 2003; Yonge *et al.*, 1985). Monitoring data have also been used to calibrate dripwater and speleothem geochemistry with instrumental climate data (Baker *et al.*, 2007; Jex *et al.*, 2010; Matthey *et al.*, 2008) and combined with dye-tracing experimentation to identify karst water flow paths (Matthey *et al.*, 2010). Quantitative constraints on karst

aquifer processing within complex, interconnected reservoirs are difficult to obtain (Mariethoz *et al.*, 2012). Recently, karst hydrology forward models have been developed to address this (see section 1.4.3).

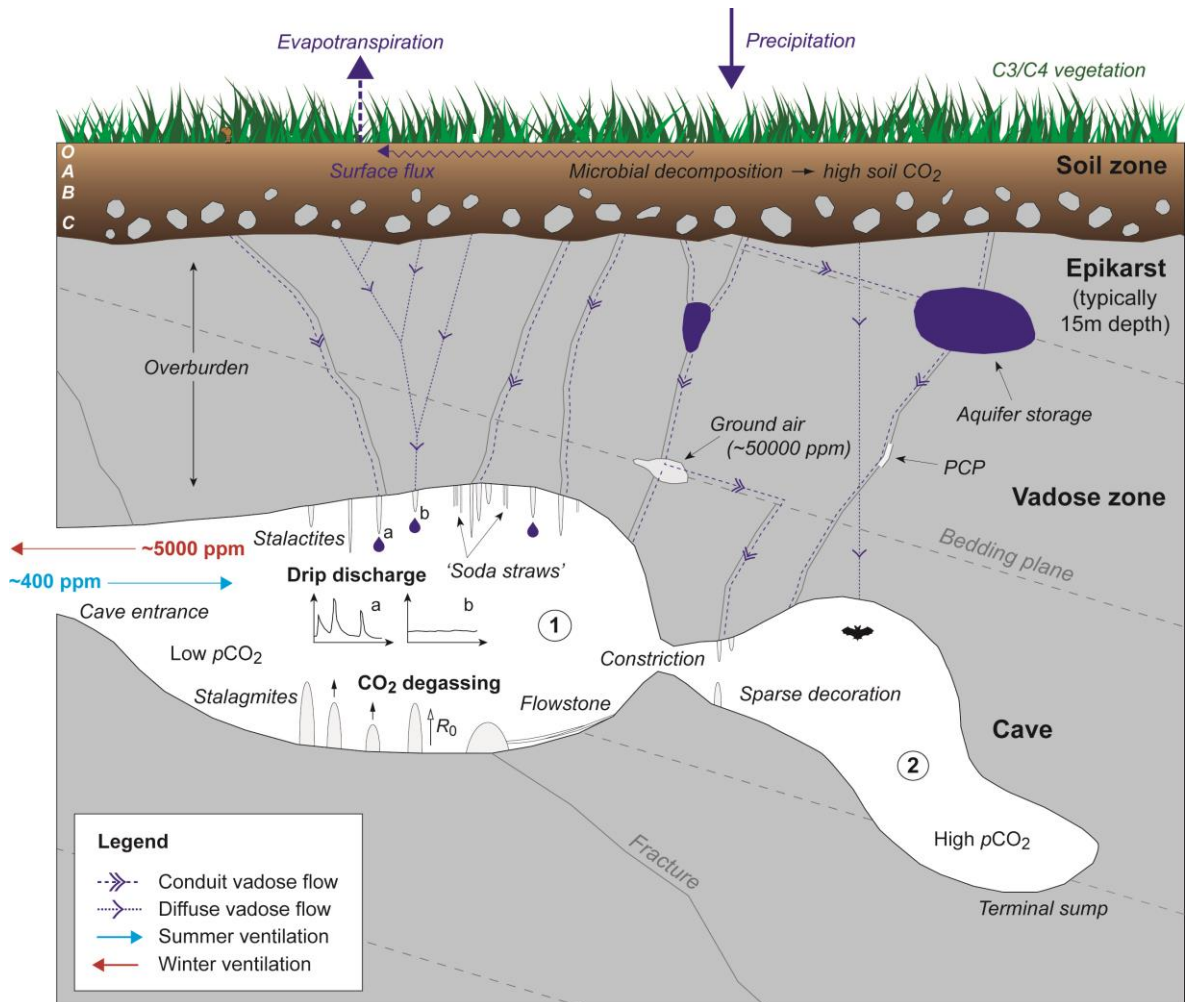


Figure 1.1. Schematic illustration of karst hydrogeology and cave system processes. Precipitation variability, surface fluxes and evapotranspiration control the net balance of water which infiltrates the epikarst, and this will vary seasonally in most environments. Hydrologically-effective precipitation is stored in karst aquifers and micropores. Note that aquifer morphology is illustrated arbitrarily. Infiltration by vadose water through the epikarst overburden and vadose zones occurs by conduit flow (through fractures, joints, bedding planes, or dissolution-enhanced pathways) and by diffusion through permeable carbonate lithologies. This hypothetical cave system has developed sub-parallel to bedding in this karstic terrain. In cave chamber 1, drip ‘a’ is fed by conduit and diffuse flow and therefore responds favourably to hydroclimatic variability. The schematic hydrograph shows rapidly increasing ascending limbs and asymptotically descending limbs, decreasing to a baseline value, in response to rainfall events. The stalagmite growing beneath this drip would be a suitable candidate for the majority of palaeoclimatological studies because the drip regime reflects surface precipitation variability but is not overly noisy. A drip fed

only by conduit flow is often unsuitably noisy. Drip 'b' is fed only by diffuse flow and its schematic hydrograph shows an approximately constant discharge because hydrological variability is greatly dampened. The primary source of CO₂ in a karst system is the soil zone, which is largely due to temperature-dependent biological processes. White letters in the soil zone indicate generic soil stratigraphy. Additionally, sporadic accumulations of ground air develop within the epikarst with very high CO₂ concentrations. Groundwater equilibrates with CO₂ from these sources, which is degassed upon intersecting the cave. The $p\text{CO}_2$ of chamber 1 is lower than that of chamber 2 because its proximity to the cave entrance allows it to ventilate more readily. Cave passage morphology also influences the degree to which cave chambers may ventilate, and the presence of a constriction also acts to reduce the inflow of externally-derived air (~400 ppm) from chamber 1 to chamber 2, particularly to the terminal sump. This hypothetical cave ventilates during summer, similar to New St Michael's Cave, Gibraltar (see Chapter 2), with higher cave air $p\text{CO}_2$ values (~5000 ppm) during winter. This ventilation regime is opposite to the majority of systems. 'Obir-type' caves ventilate with opposite seasonality. The ventilation shown can be regarded as temperature-dependent or venturi-type, but chimney effects have also been observed in caves. Prior calcite precipitation (PCP) is occurring above chamber 2, where vadose water is allowed to degas within the epikarst, deposit calcite, and is consequently less saturated with respect to calcite upon intersection with the cave. As a result of these processes and systematics, chamber 1 significantly more widespread speleothem decoration than chamber 2. Stalagmite growth rate (R_0) responds to variability in surface environment, karst hydrology and cave environmental systematics (see text and Chapter 2). After Fairchild and Baker (2012).

1.2.2. Calcareous speleothem deposition

The partial pressure of carbon dioxide ($p\text{CO}_2$) of soil air may be up to two orders of magnitude more elevated than background atmospheric values (Atkinson, 1977) – currently ~0.04 % atm – due to biological processes such as decomposition of organic matter by microbial organisms (Davidson *et al.*, 2006). Rainwater percolating through the soil zone becomes equilibrated with soil $p\text{CO}_2$ levels, and the dissolved CO₂ forms carbonic acid (H₂CO₃). Acidic vadose water dissolves carbonate epikarst lithologies; the amount of dissolution is largely dependent on the original soil $p\text{CO}_2$ and on whether dissolution occurs in open, closed or mixed conditions (Kaufmann and Dreybrodt, 2004). Hydrolysis of CO₂ and subsequent carbonic acid production is the principle mechanism by which dissolution occurs in carbonate epikarst (White, 1988) and is also largely

responsible for speleogenesis (Fairchild and Baker, 2012). Calcareous speleothem deposition occurs when infiltrating vadose water intersects a void space (i.e., cavity) within which the ambient $p\text{CO}_2$ is lower than that dissolved in the water (Fig. 1.1). Dripwater equilibrates with this ambient $p\text{CO}_2$ by degassing CO_2 (Dreybrodt *et al.*, 1992), becomes (super-)saturated with respect to calcite, and deposits calcite according to: $\text{Ca}^{2+}_{(aq)} + 2\text{HCO}_3^-_{(aq)} \leftrightarrow \text{CaCO}_{3(s)} + \text{CO}_{2(g)} + \text{H}_2\text{O}_{(l)}$ (Dreybrodt, 1988; Plummer *et al.*, 1978). CO_2 is degassed from thin films of dripwater solution draping the curved apexes of actively-growing stalagmites. Empirical constraints on film thicknesses and the consequences for vertical growth rate are presented in Chapter 2. An importance consequence of this is that the spatial distribution of cave air $p\text{CO}_2$ in any given cave system influences the distribution of speleothem deposition in the cave (Baldini *et al.*, 2006a; Whitaker *et al.*, 2009) and temporal variability may lead to non-continuous growth (Fig. 1.1).

Speleothems are usually monomineralic and the most common speleothem-forming mineral species are calcite and aragonite (Fairchild and Baker, 2012; White, 2007). Speleothems exhibit a variety of morphologies, including helictites, curtains, ribbons, ‘popcorn’ deposits, frostworks, and moonmilk (Hill and Forti, 1997), and many of these less-common forms are evaporative deposits and composed of metastable, relatively high-Mg calcite (Fairchild *et al.*, 2007). Calcareous stalagmites are best-suited to speleothem-based palaeoclimatology (Fairchild and Baker, 2012) and stalagmites were first classified by their depositional context in the early 20th Century (Baldini, 2001, and references therein). Subsequently, stalagmite architecture has been modelled mathematically (e.g., Curl, 1973) and, later, with computer models (e.g., Dreybrodt, 1999). Most recently, modelling has been attempted in relation to centennial- to millennial-scale climatic forcings (Kaufmann, 2003; Kaufmann and Dreybrodt, 2004).

1.2.3. Stalagmite growth rate

Understanding stalagmite growth rate is important for palaeoclimate research because growth rate variability may result in seasonal biases in geochemical proxy data (Baldini *et al.*, 2008) and micro-hiatuses in growth may result in loss of information. The non-biological controls on stalagmite growth are modelled and discussed in Chapter 2, which presents novel empirical constraints on the controls on film thickness, reconstructs the growth of a modern stalagmite, and tests the sufficiency of existing growth rate theory on intra- and inter-annual timescales. In principal, any process which results in a change in either the initial or equilibrated $[Ca^{2+}]$, the difference between which is termed Ca^{2+} excess concentration, is the principal control on vertical growth rate (Fairchild *et al.*, 2007; Genty *et al.*, 2001). Secondary physical controls are drip rate, dripwater film thickness (and an associated kinetic constant), droplet volume and temperature (Dreybrodt, 1999). Drop height, which is responsible for mechanical loss of water by splashing, is also important, but such an effect is effectively random and therefore difficult to quantify accurately (Genty and Deflandre, 1998).

Recently, Sherwin and Baldini (2011) measured growth-determining variables over six months and compared calcite grown *in situ* over the same period with a theoretical total growth estimate, with good agreement, providing strong evidence that our understanding of in-cave calcite accumulation is sound. However, there are three principle areas where additional research is required: (i) no time-series growth reconstruction, applying stalagmite growth theory developed largely by Wolfgang Dreybrodt (Dreybrodt, 1988), has yet been attempted; (ii) the controls on dripwater film thickness are poorly constrained and (iii) there is no accepted protocol for addressing seasonal biases in geochemical proxy data. These issues are discussed in Chapter 2.

1.2.4. The cave environment

An important feature of the cave environment for palaeoclimate research is ventilation dynamics (Ek and Gewalt, 1985; Fairchild *et al.*, 2007). Cave ventilation may be driven by barometric or temperature differences between the cave and external atmospheres (related to synoptic meteorological patterns), chimney effects, venturi effects (from wind flow), or convection, all of which reduce cave air $p\text{CO}_2$ and are therefore potentially responsible for enhancing calcite deposition rates, often seasonally (Baldini *et al.*, 2008; Banner *et al.*, 2007; Bar-Matthews *et al.*, 1996; Spötl *et al.*, 2005). Additional complications may be encountered in caves with underground bodies of water, such as streams, which may act as net sources of CO_2 , derived from the decomposition of organic matter, thereby counteracting the effects of ventilation (e.g., Baldini *et al.*, 2006a; Whitaker *et al.*, 2009). Interestingly, Baldini *et al.* (2006a) and Badino (2009) demonstrated that CO_2 accumulation in caves is focussed near to sources and is also sensitive to any prevailing thermal stratification in cave atmospheres, rather than simply accumulating near to cave floors as a result of its higher density compared to that of more common atmospheric gases (O_2 and N_2). Radon, produced from the radioactive decay of ^{238}U , has been used to trace gases, distinguish ventilation regimes, and characterise the timescales of driving advective processes (Gregorič *et al.*, 2013; Hakl *et al.*, 1997; Kowalczyk and Froelich, 2010). Several studies have modelled the effects of cave ventilation on dripwater geochemistry (e.g., Sherwin and Baldini, 2011; Spötl *et al.*, 2005).

The internal geometry of cave passages affects the ability of cave air to advect within them (Bourges *et al.*, 2001), and therefore influences ventilation. Recent spatial ‘snapshots’ of the distribution of cave air $p\text{CO}_2$ indicate that the spatial variability in stalagmite growth at any given time may be substantial (Baldini *et al.*, 2006b; Whitaker *et al.*, 2009). These

studies provide useful first order estimates for particular sites but do not consider spatial variability in dripwater chemistry due to hydrological routing or the distribution of surface vegetation and overburden. Nevertheless, one important implication of such research is that the location of a stalagmite within a cave is an important sampling consideration, supporting similar conclusions based on hydrological evidence (Asrat *et al.*, 2007).

In summary, the hydrology of individual karst systems must be characterised by multi-annual monitoring studies to isolate speleothem samples fed by dripwater discharges which reflect surface hydroclimatic variability (e.g., Fairchild and Baker, 2012; Frappier, 2008) and to enable proxy data to be interpreted within the appropriate site-specific environmental and hydrological context (e.g., Matthey *et al.*, 2010; Miorandi *et al.*, 2010). It is also important to characterise stalagmite growth in detail. In particular, the seasonality of cave ventilation has implications for the rate and timing of speleothem deposition (Spötl *et al.*, 2005) and is a potential source of bias in conservative and non-conservative proxy records (Baldini *et al.*, 2008).

1.3. Stable oxygen isotope fractionation in the atmospheric branch of Earth's hydrological cycle

Numerous hydroclimatic processes result in mass-dependent fractionation of the stable oxygen isotopes ^{16}O and ^{18}O , the ratio of which in seawater, atmospheric vapour and precipitation is thus a natural tracer for hydroclimatic variability (Fig. 1.2). During fractionation, isotopically heavier nuclei, such as ^{18}O , exhibit a preference for the least energetic state involved in the phase transition. The relevant fractionation processes discussed in this section are seawater evaporation (Lachniet, 2009; LeGrande and Schmidt, 2006), vapour condensation (Gourcy *et al.*, 2005), Rayleigh distillation during atmospheric

moisture transport (Dansgaard, 1964; Lachniet, 2009; Rozanski *et al.*, 1993), precipitation type and magnitude (Bowen, 2008; Rozanski, 2005; Rozanski *et al.*, 1992; 1993), and continental evaporation and moisture recycling (Koster *et al.*, 1993).

1.3.1. Conventional ‘ δ ’ notation

Stable oxygen isotope ratios, commonly measured using mass-spectrometric methods, are expressed in ‘ δ ’ notation and in units of ‰ relative to a material standard (Sharp, 2007), such that:

$$\delta_{\text{sample}} = \left(\frac{R_{\text{sample}}}{R_{\text{standard}}} - 1 \right) \times 1000 \quad (\text{Equation 1.1})$$

where R is the isotope ratio:

$$R = \frac{\text{rare isotope}}{\text{common isotope}} \quad e.g., = \frac{^{18}\text{O}}{^{16}\text{O}} \quad (\text{Equation 1.2})$$

Conventional material standards are Vienna Pee Dee Belemnite (VPDB) for carbonate samples and Vienna Standard Mean Ocean Water (VSMOW) for water samples. Isotope ratios are reported relative to both standards with or without the ‘Vienna’ prefix (V-), which was introduced as a result of previous scarcity of these standard materials (Sharp, 2007). Conversion between values in units of ‰ VSMOW and ‰ VPDB is performed according to the following expression:

$$\delta^{18}\text{O}_{\text{VSMOW}} = 1.03091(\delta^{18}\text{O}_{\text{VPDB}}) + 30.91 \quad (\text{Equation 1.3})$$

1.3.2. Seawater evaporation

Equatorial and low-latitude ocean regions are the predominant source of atmospheric moisture, with evaporation between 30 °S and 20 °N accounting for ~65 % of the global atmospheric moisture budget (Rozanski *et al.*, 1993). From an initial seawater $\delta^{18}\text{O}$ ($\delta^{18}\text{O}_{\text{sw}}$) composition, the degree of isotopic fractionation during seawater evaporation under equilibrium conditions (i.e., sea surface relative humidity (h) is 100 %) is controlled by sea surface temperature (SST). If sea h is <100 %, fractionation is enhanced by kinetic effects related linearly to h (Clark and Fritz, 1997) – see Fig. 1.2. The global $\delta^{18}\text{O}_{\text{sw}}$ distribution is determined by SST, proximity to and prevailing global extent of glacial ice (Duplessy *et al.*, 1992), and seawater salinity (Clark and Fritz, 1997). Currently, no complete instrumental survey of the spatial distribution of $\delta^{18}\text{O}_{\text{sw}}$ exists, so LeGrande and Schmidt (2006) generated a global, 1°-resolved gridded dataset, based on the available data and relationships between $\delta^{18}\text{O}_{\text{sw}}$ and other measurable parameters (e.g., SST) for which more extensive datasets exist.

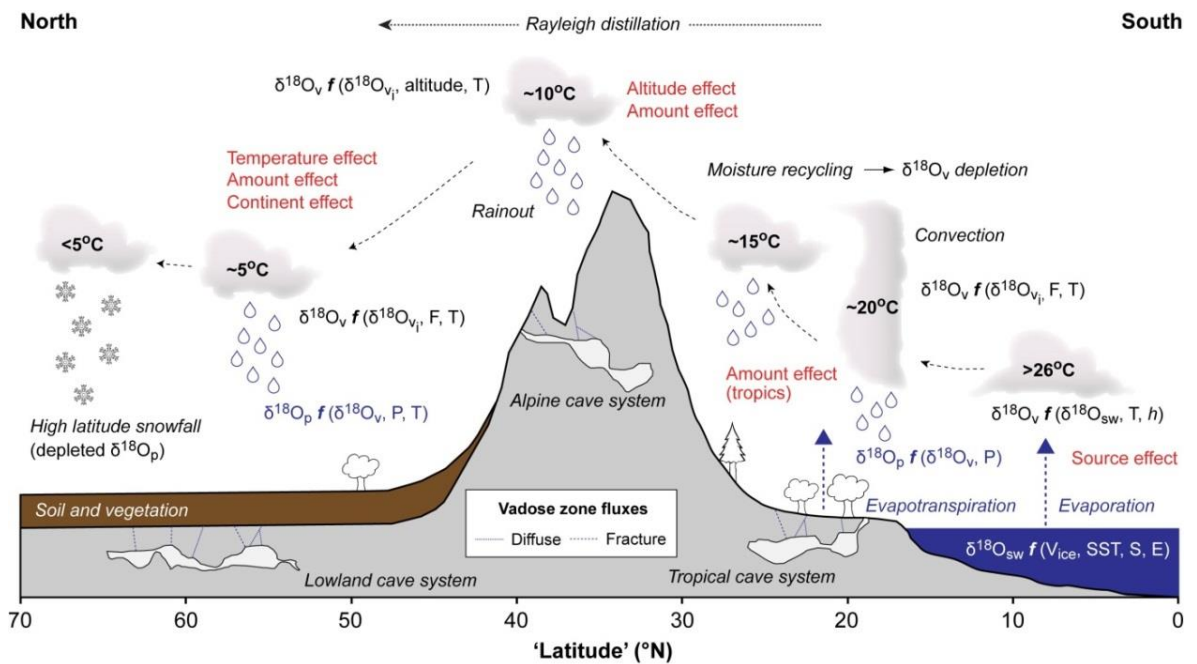


Figure 1.2. Schematic illustration of stable oxygen isotope fractionation during hydroclimatic processes. Schematic representation of the multi-determinate, physical hydroclimatic processes involved in transmitting a net climate signal from the atmosphere to an actively-growing stalagmite. Note that the latitude axis is also schematic and this figure is not to scale. f denotes ‘function of’. Seawater $\delta^{18}\text{O}$ reflects ice volume (V_{ice}), SST, salinity (S), and evaporation (E). The $\delta^{18}\text{O}$ of this evaporate is a function of the initial seawater composition, SST and relative humidity (h), which causes kinetic fractionation, and therefore reflects source conditions. The kinetic component is also reflected by d -excess. This vapour is subsequently advected through the troposphere, according to prevailing temperature and pressure gradients. The dashed black arrows represent the poleward trajectory of an atmospheric vapour mass. A linear relationship between vapour and precipitation $\delta^{18}\text{O}$ and atmospheric residence time exists globally (Aggarwal *et al.*, 2012). Vertical air parcel movements associated with convective processes lead to internal recycling of moisture within clouds and $\delta^{18}\text{O}$ depletion. Tropical precipitation $\delta^{18}\text{O}$ will reflect this ‘amount effect’ and may also reflect the contribution of evapotranspired moisture (blue dashed arrow). Altitude and amount effects are significant for precipitation $\delta^{18}\text{O}$ in high elevation regions. With increasing moisture migration and Rayleigh distillation, both vapour and precipitation $\delta^{18}\text{O}$ are controlled by the residual moisture fraction after rainout events (F) as well as temperature-dependent fractionation. Precipitation (and therefore speleothem) $\delta^{18}\text{O}$ therefore responds to multiple hydroclimatic processes; such proxy data cannot be interpreted as a direct reflection of a single climatic variable, to the exclusion of other effects. Speleothems from tropical, Alpine and lowland cave systems should reflect the dominant fractionation effects in these climatic settings. Adapted from Lachniet (2009).

1.3.3. Atmospheric vapour, circulation and precipitation

Atmospheric moisture masses migrate according to prevailing wind fields which result from gradients in ambient pressure and air temperature. Air mass temperature partially controls fractionation, which is largely a function of altitude (Bowen and Wilkinson, 2002; Darling *et al.*, 2006). The $\delta^{18}\text{O}$ of atmospheric vapour ($\delta^{18}\text{O}_v$) at any given point during the global hydrological cycle has evolved from an initial $\delta^{18}\text{O}_{sw}$, the prevailing evaporative fractionation conditions, and transport. Generally, atmospheric circulation processes advect moisture masses poleward. Along such advection pathways, decreasing ambient temperature, condensation into clouds, and progressive Rayleigh distillation result in increasingly depleted precipitation $\delta^{18}\text{O}$ ($\delta^{18}\text{O}_p$) with increasing latitude (Alley and Cuffey, 2001; Bowen and Wilkinson, 2002; Dansgaard, 1964; Gat, 1996). This is not complicated by exceptionally preferential removal of D_2^{18}O molecules, because a simple linear relationship between precipitation $\delta^{18}\text{O}$ and δD exists globally (Craig, 1961) – see section 1.3.4. Convection intensity and precipitation rate also deplete $\delta^{18}\text{O}_v$ (Fig. 1.2). However, recycled moisture sourced from continental evaporation / evapotranspiration, which is enriched in lighter isotopes, comprises a variable proportion of any given air mass (Koster *et al.*, 1993).

In addition to rainout, temperature-dependent fractionation also controls vapour and precipitation $\delta^{18}\text{O}$. A positive correlation between $\delta^{18}\text{O}_p$ and temperature (T) exists in mid- to high-latitude regions, with a mean $\Delta\delta^{18}\text{O}_p/\Delta T$ slope of $0.69 \text{ ‰ } ^\circ\text{C}^{-1}$ (Dansgaard, 1964), increasing to $\sim 0.9 \text{ ‰ } ^\circ\text{C}^{-1}$ in polar regions and reaching near-zero values in low-latitude settings (Rozanski *et al.*, 1992). Importantly, $\delta^{18}\text{O}_p$ -temperature correlations have been quantified using *surface*-measured temperature rather than air mass temperature, owing to the practical difficulties involved in measuring atmospheric temperature at altitude. This

$\delta^{18}\text{O}_p$ -T relationship is less strongly expressed in low-latitude regions (Fig. 1.2), where a negative correlation between $\delta^{18}\text{O}_p$ and precipitation amount often exists because air masses undergo convergent and deep-convective motions and experience relatively small temperature gradients (Fricke and O'Neil, 1999). The isotopic evolution of migrating atmospheric air parcels is modelled in Chapter 5.

1.3.3.1. Isotopic 'effects' in precipitation $\delta^{18}\text{O}$

The factors affecting precipitation $\delta^{18}\text{O}$ have been mapped and quantified primarily using data collected by the Global Network of Isotopes in Precipitation (GNIP), a global monitoring programme initiated by the International Atomic Energy Agency and World Meteorological Organisation in 1961 (IAEA/WMO, 2014). GNIP data (Fig. 1.3) exhibit four principal isotope fractionation effects; each related to temperature-dependent fractionation and rainout. The *continent effect* is the observed $\delta^{18}\text{O}$ depletion with increasing inland moisture transport and results from progressive rainout during air mass migration (Rozanski *et al.*, 1993). For example, this effect is observed across Eastern Europe and North America (Fig. 1.3). The *altitude effect* results from the adiabatic lifting of air masses (i.e., over topography), which decreases cloud temperature and causes condensation and rainout, resulting in $\delta^{18}\text{O}$ depletion. This is particularly notable in precipitation over the Himalayan and Andean regions (Fig. 1.3). The *amount effect* is the apparent $\delta^{18}\text{O}$ depletion with increasing amount of rainfall, which is most pronounced in tropical regions where precipitation is strongly seasonal (Dansgaard, 1964). This depletion is primarily caused by water vapour recycling in mesoscale convective weather systems (Bony *et al.*, 2008; Risi *et al.*, 2008). Amount effect-type depletion is observed in monsoonal regions during the seasonal intensification of monsoonal frontal and convective

systems (Hoffmann and Heimann, 1997) and in tropical depressions (Vuille *et al.*, 2003). An extreme case is tropical cyclone precipitation, where moisture may undergo multiple depletive convection cycles (Lawrence and Gedzelman, 1996). Deep convection associated with mountainous regions also produces intense precipitation; therefore the amount effect also plays a role in depleting precipitation in areas with a strong altitude effect (Dansgaard, 1964). On longer timescales, however, increased sensitivity to temperature variations is experienced at high altitude (Rozanski *et al.*, 1992). The *source effect* is the observed $\delta^{18}\text{O}$ depletion with increasing distance from moisture source and results from progressive Rayleigh distillation along moisture advection pathways (Dansgaard, 1964). In temperate and low-latitude regions, surface temperatures are sufficient to allow significant evaporation and evapotranspiration of moisture (Thornthwaite, 1948), generating precipitation recycling (Eltahir and Bras, 1996). Typically, this moisture is isotopically lighter than that evaporating from oceanic regions (Cole *et al.*, 1999), enhancing the continent effect. In general, this is more pronounced in summer due to higher mean seasonal temperature and greater vegetation cover, and winter isotope gradients are therefore often more pronounced (Eames, 2008), except in regions dominated by an ‘amount effect’.

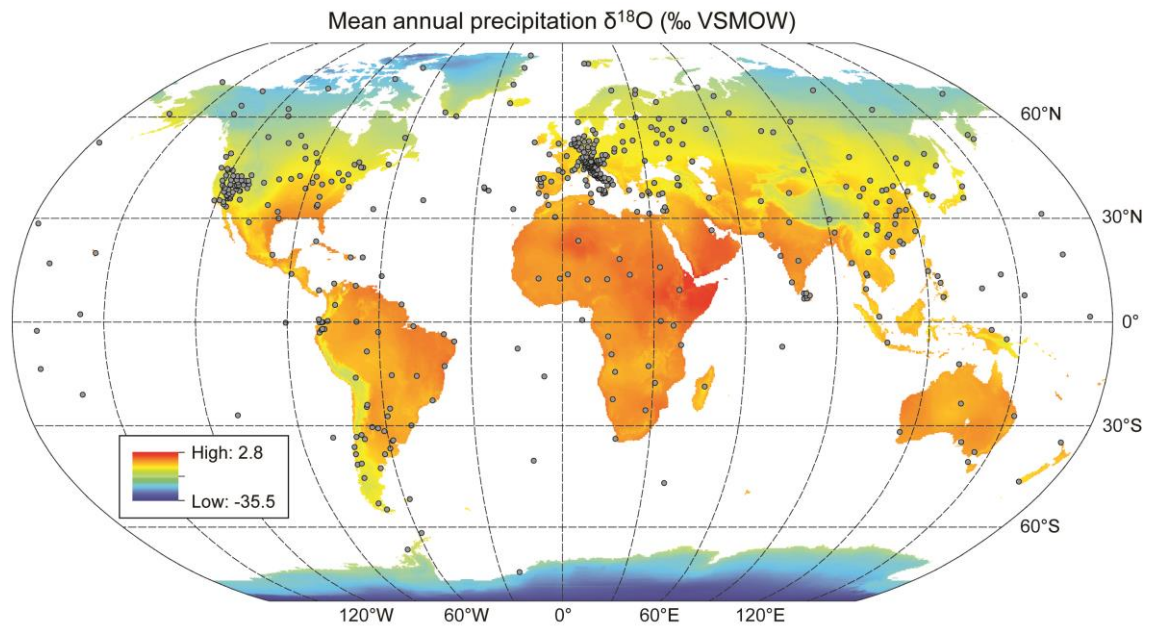


Figure 1.3. Modern global precipitation $\delta^{18}\text{O}$ distribution. Precipitation $\delta^{18}\text{O}$ map obtained by regressing the available GNIP station data (Bowen and Wilkinson, 2002) against latitude and altitude. Grey circles show locations of monthly stations. Note that the geographical distribution of stations is non-uniform, with dense coverage only in central Europe and western USA, and moderately dense coverage in Western Europe, eastern USA and eastern China. Nevertheless, the GNIP dataset has provided a basis for mapping and quantifying the relationships between precipitation $\delta^{18}\text{O}$ and latitude, altitude, temperature, and hydroclimatic regime.

1.3.4. The Meteoric Water Line

Oxygen and hydrogen isotopes are coupled throughout the global hydrological cycle and therefore $\delta^{18}\text{O}$ and δD co-vary; this is described by a Meteoric Water Line (MWL), the global expression of which is (Faure and Mensing, 2005):

$$\delta\text{D} = 8 \delta^{18}\text{O} + 10 \quad (\text{Equation 1.4})$$

The gradient of this relationship exhibits regional variability and seasonal changes (Rozanski *et al.*, 1982). The deviation of a precipitation $\delta\text{D}/\delta^{18}\text{O}$ value from a global or

regional MWL is termed *deuterium excess* (alternatively, *d-excess*), which depends upon SST and h at the moisture source region of that moisture (Pfahl and Sodemann, 2014). In this thesis, air mass history is considered from a Lagrangian perspective, but it is noted that *d-excess* provides an additional, measureable constraint on moisture source. However, any source signal in *d-excess* decreases with increasing inland migration of the moisture mass (Vimeux *et al.*, 1999) or obscured by air mass convergence and mixing (Moore *et al.*, 2014).

1.3.5. Modelling precipitation $\delta^{18}\text{O}$

The principal approaches to modelling isotopes in precipitation are (i) linear Rayleigh distillation models, (ii) isotope-enabled GCMs, and (iii) Lagrangian-based models simulating fractionation along atmospheric trajectories of moisture masses (Eames, 2008), each of which has made important contributions to understanding precipitation and proxy $\delta^{18}\text{O}$ systematics. Rayleigh models are appropriate for first-order sensitivity studies and are able to reproduce $\delta^{18}\text{O}$ variability in mid-to-high latitudes (Jouzel *et al.*, 2000), and also demonstrate that $\delta^{18}\text{O}$ integrates moisture mass history (Rozanski *et al.*, 1982). These models are sensitive may be rectified by considering atmospheric moisture residence time (Aggarwal *et al.*, 2012). Isotope-enabled GCMs are able to reproduce the latitudinal and continental patterns of $\delta^{18}\text{O}_p$, but performance on regional scale is more variable (Jouzel *et al.*, 1997). However, on a synoptic scale, these models do not yet provide conclusive results (e.g., Sturm *et al.*, 2005). GCMs have also been used to tag moisture parcels within Eulerian co-ordinates to evaluate bulk moisture source contributions to precipitation in an area of interest (e.g., Joussaume *et al.*, 1984; Koster *et al.*, 1986; Numaguti, 1999).

Lagrangian isotope fractionation models simulate the isotopic evolution of atmospheric air parcels migrating along three-dimensional trajectories, which are output by Lagrangian particle dispersion models, such as FLEXPART (Stohl *et al.*, 2005), or trajectory models, such as LAGRANTO (Wernli and Davies, 1997). By simulating realistic isotopic evolution during moisture transport, the processes to which precipitation $\delta^{18}\text{O}$ at a given site respond may be investigated quantitatively. Previous research with Lagrangian isotope models suggests that initial source temperature, pressure and humidity values are important (Ciais and Jouzel, 1994) and that tuning to local hydroclimatic conditions is required (Sodemann, 2006). In Chapters 5 and 6, Lagrangian isotope models are used to help identify the influence of moisture transport dynamics on precipitation and proxy $\delta^{18}\text{O}$ in central China, and further discussion of this methodology is presented.

1.4. $\delta^{18}\text{O}$ as a palaeoclimate proxy

As a result of the processes described in the previous section, the present-day geographical distribution of precipitation $\delta^{18}\text{O}$ (Fig. 1.3) is an order of magnitude greater than stable oxygen isotope fractionation in calcite-water systems and, although acting on different scales, therefore dominates the $\delta^{18}\text{O}$ signature preserved by stalagmites (Baker *et al.*, 2007; Bowen, 2008; Lachniet, 2009). Moreover, the fundamental physical fractionation processes that control $\delta^{18}\text{O}$ evolution through the global hydrological cycle should not be different in the past, nor should the atmospheric circulation mechanisms involved in moisture mass transportation. Therefore, stalagmite $\delta^{18}\text{O}$ is a powerful proxy for *variability* in the climate system. Recent reviews of stalagmite proxy systematics are those of Fairchild *et al.* (2006b), who examined karst hydrology, cave environment and in-cave

calcite-water isotopic fractionation, and Lachniet (2009), who considered the hydroclimatic controls on precipitation $\delta^{18}\text{O}$.

1.4.1. Stalagmites as palaeoclimate archives

Proxy $\delta^{18}\text{O}$ variability in terrestrial archives (speleothems, ice cores, tree rings and soil and sediment successions) is often interpreted as reflecting temperature or precipitation directly (Jones *et al.*, 2009). Speleothems, particularly stalagmites, provide precisely-dated (by U-series methods), multi-proxy (geochemical and petrographical) records of late Quaternary climate variability across various timescales, from glacial-interglacial shifts (e.g., Cheng *et al.*, 2009; Drysdale *et al.*, 2004; Wang *et al.*, 2004; Wang *et al.*, 2001), to millennial and centennial variability (e.g., Cai *et al.*, 2012; Lachniet *et al.*, 2012; Wang *et al.*, 2008; Zhang *et al.*, 2008), to recent trends (e.g., Matthey *et al.*, 2008) and seasonal fluctuations (e.g., Johnson *et al.*, 2006). Generally, the range in speleothem $\delta^{18}\text{O}$ variability is less than that exhibited by instrumental precipitation $\delta^{18}\text{O}$ time series datasets, due to temporal averaging by hydrogeological processes in karst systems (Fairchild *et al.*, 2006b) – see section 1.2.

Although speleothems form in various environmental settings, speleothem proxy records are particularly valuable in low- and mid-latitude regions where few alternative sources of high-resolution proxy data, such as ice cores, are available. Coincidentally, such regions are characterised by relatively high human population and greater biodiversity, so understanding past climate variability in these regions is of considerable importance. However, interpreting precipitation and stalagmite $\delta^{18}\text{O}$ at low latitudes is complicated by the range of potential hydroclimatic controls on $\delta^{18}\text{O}$ (see section 1.3); interpreting $\delta^{18}\text{O}$ as

directly reflecting a single climatic variable, such as precipitation amount, is untenable (Lachniet, 2009). Stalagmite $\delta^{18}\text{O}$ data are often interpreted in this way, assuming that modern relationships between instrumental and proxy data (i.e., observed precipitation depletion with increasing latitude, altitude, moisture transport distance, rainfall amount, convective intensity, or climate index) have remained stationary. There is growing evidence that palaeomonsoon records from cave sites in central and eastern China indeed reflect multiple hydroclimatic factors. In East Asia, $\delta^{18}\text{O}$ integrates a complex climate signal, including non-local source effects and moisture transport (Clemens *et al.*, 2010; Laskar *et al.*, 2014; Maher, 2008; Maher and Thompson, 2012; Pausata *et al.*, 2011) and atmospheric circulation patterns (Lekshmy *et al.*, 2014). The main body of research in this thesis, presented in Chapters 4, 5 and 6, contribute to this research frontier and to achieving more robust palaeomonsoon reconstructions from stalagmite $\delta^{18}\text{O}$.

1.4.1.1. Calcite-dripwater isotope fractionation

The pioneering palaeoclimate studies based on speleothem $\delta^{18}\text{O}$ (Duplessy *et al.*, 1970; Emiliani, 1971; Hendy, 1971; Hendy and Wilson, 1968) indicated that in-cave equilibrium fractionation between calcite and dripwater was essential to preserve a climatic signal. More recent developments include (i) laboratory experimental results that suggest ^{16}O incorporation into calcite is enhanced with increasing growth rate (Day and Henderson, 2011), (ii) a demonstration of the potential of clumped isotope measurements for identifying temporal variability in kinetic fractionation (Kluge and Affek, 2012), and (iii) a compilation of European stalagmite $\delta^{18}\text{O}$ records, finding pronounced geographical trends with longitude, regardless of whether or not speleothem calcite precipitated in isotopic

equilibrium from parent dripwaters (McDermott *et al.*, 2011), suggesting that disequilibrium effects do not preclude the usefulness of stalagmite proxy data completely.

1.4.2. Modelling stalagmite $\delta^{18}\text{O}$

Palaeoclimate reconstructions require stationary quantitative relationships between stalagmite $\delta^{18}\text{O}$ and regional climate parameters, such as precipitation (Bowen and Wilkinson, 2002; Fischer and Treble, 2008; Jones *et al.*, 2009). Researchers therefore calibrate high-resolution proxy data against the longest available coeval instrumental records (e.g., Asrat *et al.*, 2007; Baker *et al.*, 2007; Jex *et al.*, 2010) and base interpretations of the palaeo-record on these modern relationships. However, the stationarity of such calibrations requires validation from climate-proxy modelling studies (Jex *et al.*, 2013; LeGrande and Schmidt, 2009; Sturm *et al.*, 2010).

Synthetic, model-generated records are termed *pseudoproxy* records (Jones *et al.*, 2009). To-date, pseudoproxy stalagmite $\delta^{18}\text{O}$ records have been generated by forward-modelling karst hydrology systematics (see section 1.2.3), which is a process-based approach to generate pseudoproxy data without explicitly targeting an ‘observed’ proxy record (Sturm *et al.*, 2010). The KarstFOR model (previously KarstHydroMod) is based on lumped parameters describing karst aquifer size and outflow rates, under- and overflow aquifer connectivity, and mixing ratios between conduit and diffuse flow (Baker and Bradley, 2010; Baker *et al.*, 2012; Bradley *et al.*, 2010). The Oxygen isotope Drip water and Stalagmite Model, is driven by weighted $\delta^{18}\text{O}_p$ -temperature and -amount correlations (Wackerbarth *et al.*, 2010). This forward modelling approach has progressed to being driven by Global Climate Model (GCM) outputs, such as surface temperature,

evapotranspiration and hydrologically-effective precipitation (Baker *et al.*, 2013; Lohmann *et al.*, 2013; Wackerbarth *et al.*, 2012), providing constraints on the stationarity of climate-proxy calibrations for particular sites (Jex *et al.*, 2013).

Investigating the role of the role of groundwater processing quantitatively has demonstrated that (i) complex karst storage and mixing relationships may produce a large range of drip discharge patterns from a single hydrological input (Bradley *et al.*, 2010), and (ii) combining GCM outputs with hydrological models can reproduce first-order climate signals (Baker *et al.*, 2013; Wackerbarth *et al.*, 2012). However, because $\delta^{18}\text{O}$ may reflect multiple hydroclimatic phenomena (Baldini *et al.*, 2010; Dayem *et al.*, 2010; Lachniet, 2009), a quantitative understanding of which is also key to interpreting the net climate signal transmitted to cave sites of interest.

If stalagmite $\delta^{18}\text{O}$ records can be accurately reproduced, then $\delta^{18}\text{O}$ variability observed over various timescales may be attributed to forcing mechanisms with greater confidence. Christiansen *et al.* (2009) showed that various statistical climate reconstruction methods may underestimate the low frequency component of palaeoclimate variability, resulting from inherent methodological stochasticity (e.g., Moberg *et al.*, 2008). The magnitude and rate of past climate changes observed in statistical (Tingley *et al.*, 2012), GCM-based (e.g., Tan *et al.*, 2009), and proxy-based (e.g., Esper *et al.*, 2002; Mann and Jones, 2003; Moberg *et al.*, 2005) climate reconstructions can be ambiguous because different approaches and processing methods are employed. Therefore, robust interpretations of stalagmite proxy data based on forward modelling, ideally for multiple records, provide important validation. Potentially, these advances will allow past climate *dynamics* to be reconstructed, which has particular importance for understanding natural climate

variability on regional scales and informing model projections of future, anthropogenic climate change in the many regions where this is less well constrained at present (IPCC, 2013).

1.5. Thesis overview

Key concepts in speleothem-based palaeoclimate research and the rationale for informing proxy data interpretations with new modelling techniques to quantitatively isolate net climate signals are discussed in this introductory chapter. **Chapter 2** (i) presents a case study which quantifies the roles of dripwater film thickness and stalagmite morphology in vertical stalagmite growth rate variability; (ii) investigates links between growth rate and surface environmental parameters; (iii) discusses the importance of quantifying growth rate changes to assess their impact on net climate signals preserved in stalagmites. Owing to insufficient cave monitoring data from sites in China, this case study is based on a modern stalagmite sampled from a cave site in Gibraltar. This chapter is published in *Earth and Planetary Science Letters* by Baker *et al.* (2014). **Chapter 3** presents an overview of the Asian Monsoon system, introduces selected cave sites that are considered in this thesis and the high-profile speleothem records published from these sites, and synthesises recent research that has re-examined initial interpretations of those records. The research questions concerning monsoonal $\delta^{18}\text{O}$ systematics addressed in this thesis are stated at the end of this chapter. Motivated by the need to characterise moisture transport for accurate precipitation and proxy $\delta^{18}\text{O}$ interpretation, **Chapter 4** presents a sub-continental scale study of the annual cycle of moisture sources driving present-day precipitation across central and eastern China and discusses the implications for understanding the net climate signal transmitted to selected cave sites and for predicting monsoon rainfall variability.

Chapter 5 presents an investigation of the factors controlling precipitation $\delta^{18}\text{O}$ at Wanxiang Cave, an important proxy site proximal to the monsoon boundary in northern China, using a recently-developed Lagrangian isotope model and compares model output with an unpublished precipitation event isotope dataset (kindly provided by K. R. Johnson, University of California at Irvine, USA). In **Chapter 6**, the extent to which terrestrial moisture transport processes influence Wanxiang Cave proxy $\delta^{18}\text{O}$ is investigated by (i) modelling Wanxiang precipitation $\delta^{18}\text{O}$ under average hydroclimatic conditions and (ii) undertaking the first attempt to construct a pseudoproxy record based on moisture transport processes stalagmite growth rate equations presented in Chapter 2. Finally, **Chapter 7** is a synthesis of the work presented in this thesis, its implications, and a discussion of the future research outlook. Each chapter is presented as a stand-alone study because they are intended to be, or are, published.

Chapter 2

Reconstructing modern stalagmite growth from cave monitoring, local meteorology, and experimental measurements of dripwater films^{*}

^{*} This chapter is published as: Baker, A. J., Matthey, D. P., and Baldini, J. U. L., 2014. Reconstructing modern stalagmite growth from cave monitoring, local meteorology, and experimental measurements of dripwater films. *Earth and Planetary Science Letters* **392**, 239-249.

Chapter summary

Interpretations of high-resolution proxy datasets from stalagmites require support from long-term cave monitoring data and quantified changes in sample growth rate. One cave site for which the modern climate signal transfer systematics are relatively well characterised by cave monitoring is New St Michael's Cave, Gibraltar. This site provides a rare opportunity to reconstruct modern calcite growth, to link growth with the cave environment and local climate, and to test the sufficiency of existing growth rate theory on monthly to inter-annual timescales. Monitoring of cave sites in monsoonal China is currently less-well developed and therefore deriving statistically significant relationships between stalagmite growth rate, meteorology and cave processes, which are required to create pseudoproxy records (Chapter 6), must at present be based on data from other sites. In this chapter, a numerical time-series growth rate model, driven by cave monitoring and local meteorological data, and the results of an experimental investigation into variation in dripwater film thickness as a function of stalagmite apex morphology are used to reconstruct the modern growth (AD 1951-2004) of 'Gib04a', a stalagmite retrieved from New St Michael's Cave. Experimental measurements demonstrate that dripwater film thickness decreases linearly with increasing stalagmite curvature and that the presence of millimetre-scale surface microtopography reduces film thickness by an order of magnitude. Changes in growth laminae curvature identified from a Gib04a cut section constrain film thickness variability through time, and this is combined with estimated dripwater $[\text{Ca}^{2+}]$ and cave air $p\text{CO}_2$ seasonality to drive the model. The reconstruction exhibits strong seasonality and tracks variability in calcite $[\text{Sr}^{2+}]$, a trace metal whose incorporation into calcite is partially growth rate-controlled. Reconstructed growth also shows co-variation with seasonal changes in calcite fabric, with high growth corresponding to a greater density of calcite grain boundaries. Potential links between secular trends in karst recharge, film thickness and Gib04a growth are discussed, and the overall sensitivity of vertical growth rate to film thickness variability is assessed. This approach could be used to characterise the growth of other samples retrieved from well-monitored cave systems and may prove particularly useful in quantifying seasonal bias in geochemical proxy datasets, facilitating greater robustness of palaeoclimate reconstructions.

2.1. Introduction and rationale

Cylindrical stalagmites undergo uniform growth and are most often sampled for palaeoclimate research, and many stalagmite records benefit from robust chronologies based on petrographic or geochemical annual laminae (Baker *et al.*, 2008). The acquisition of multi-annual cave monitoring datasets not only allows these records to be interpreted within the appropriate environmental context but also provides valuable information about stalagmite growth rate, both of which are important to palaeoclimate reconstruction using speleothems (e.g., Matthey *et al.*, 2008; Spötl *et al.*, 2005).

Existing empirical relationships between cave environmental parameters, such as cave atmosphere temperature and $p\text{CO}_2$ (CO_2 partial pressure), and stalagmite growth rate appear robust (Baker *et al.*, 1998; Baldini *et al.*, 2008; Genty *et al.*, 2001) and recent studies have attempted to quantify the effects of cave processes, such as ventilation, on stalagmite growth and net geochemical proxy records (Sherwin and Baldini, 2011; Wong *et al.*, 2011). Previous speleothem growth studies include modelled spatial variability based on ‘snapshot’ cave atmosphere CO_2 concentration maps (Baldini *et al.*, 2006b; Whitaker *et al.*, 2009) and comparisons of modelled and actual growth rates. Such studies have compared average values (Baker and Smart, 1995), investigated the sensitivity of growth rate to cave dripwater hydrochemistry (Genty *et al.*, 2001), and compared modelled growth with calcite grown *in situ* (Sherwin and Baldini, 2011). Collectively, this research provides first-order tests of our theoretical understanding of both instantaneous calcite growth rate and vertical stalagmite extension rate. Attempting to link stalagmite growth and morphology to climate variability, Kaufmann (2003) combined temperature estimates from ice core (GRIP and VOSTOK) and deep marine sediment core (SPECMAP) proxy data with approximations of glacial-interglacial precipitation and soil cover changes to

drive a model of vertical stalagmite growth and equilibrium diameter, and Kaufmann and Dreybrodt (2004) adopted the inverse approach in attempting to derive climatic information from such stalagmite stratigraphies.

Understanding stalagmite growth variability is important for palaeoclimate research for various reasons. (i) Several studies (e.g., Polyak and Asmerom, 2001; Proctor *et al.*, 2000) employed stalagmite growth rate itself as a palaeoclimate proxy and others have described seasonally variable stable isotope ratios (e.g., Johnson *et al.*, 2006; Matthey *et al.*, 2008) and trace element concentrations (e.g., Huang *et al.*, 2001) in stalagmites that potentially result from cave ventilation dynamics and/or karst hydrological processes, both of which also affect stalagmite growth. (ii) High vertical extension rates are conducive to generating high-resolution geochemical proxy datasets from stalagmites, yet to-date few studies have characterised stalagmite growth on intra-annual to decadal timescales and its implications for geochemical climate signal capture. (iii) Seasonal growth rate fluctuations potentially bias net proxy signals towards the season favourable to deposition (Baldini *et al.*, 2008; Banner *et al.*, 2007; Fairchild *et al.*, 2006; Frisia *et al.*, 2000; Matthey *et al.*, 2008; Spötl *et al.*, 2005). (iv) Growth rate variability may be related to climate signal modification by other processes, such as biomass change above the cave (e.g., Baldini *et al.*, 2005) and surface and epikarst hydrology (Baker and Bradley, 2010; Bradley *et al.*, 2010; Darling, 2004). Moreover, stalagmite growth rate may provide a proxy for surface or soil temperature (Genty *et al.*, 2001), rainfall amount (Genty and Quinif, 1996), or vegetation changes (Baldini *et al.*, 2005). The work of Kaufmann (2003) and Kaufmann and Dreybrodt (2004) represents an important advance in linking stalagmite growth with climate variability, but the model resolutions used (1000 and 200 years, respectively) are

too low to be directly applicable to many high-resolution palaeoclimate studies using stalagmites.

2.1.1. Controls on stalagmite growth rate

The principal non-biological controls on calcareous speleothem deposition (temperature, drip rate, dripwater $[Ca^{2+}]$, and soil and cave air pCO_2) are relatively well understood (Dreybrodt, 1999; Genty *et al.*, 2001). Recent research has characterised their spatio-temporal variability at certain sites (Banner *et al.*, 2007; Whitaker *et al.*, 2009) and, in particular, highlighted the importance of cave atmosphere pCO_2 dynamics for speleothem palaeoclimatology (Baldini *et al.*, 2008; Fairchild *et al.*, 2006). Although interpreting climatic variability from stalagmite morphology alone is challenging (Dreybrodt, 1988), understanding the physical controls on stalagmite growth, such as drop volume and dripwater film thickness, is necessary for proper linkage of local climate variability, cave environment systematics, and stalagmite growth behaviour.

The following equation describes *vertical* stalagmite extension rate (R_0) fed by a punctiform drip source theoretically (Baker *et al.*, 1998; Baldini *et al.*, 2008; Buhmann and Dreybrodt, 1985; Dreybrodt, 1980; 1999):

$$R_0 = 1174 \left([Ca^{2+}] - [Ca^{2+}]_{app} \right) \left(\delta \text{ t}^{-1} \right) \left(1 - e^{-\alpha \text{ t} \delta^{-1}} \right) \quad (\text{Equation 2.1})$$

where the constant 1174 converts molecular accumulation rate of calcite ($\text{mmol mm}^{-1} \text{ s}^{-1}$) to vertical extension rate (mm a^{-1}); $[Ca^{2+}]$ is the initial calcium cation concentration of the dripwater (mmol L^{-1}); $[Ca^{2+}]_{app}$ is the apparent dripwater $[Ca^{2+}]$ (mmol L^{-1}) after

equilibration with a given cave atmospheric $p\text{CO}_2$; δ is the dripwater film thickness (mm) from which calcite precipitates; t is the drip interval (s); and α is a ‘kinetic constant’ (mm s^{-1}) that is sensitive to change in δ and ambient cave temperature. Note that R_0 may also be denoted ‘ W_0 ’ (e.g., by Kaufmann, 2003). This equation was tested by Sherwin and Baldini (2011), who found close agreement between measured *in situ* calcite deposition and a model estimate. However, the main source of uncertainty encountered in this study was in estimating δ , highlighting the need to constrain this parameter before any time-series reconstruction of stalagmite growth may be attempted. Of particular interest is whether δ tends to remain constant or varies significantly with time, according to relationships with other variables.

2.1.2. Rationale for selecting the Gib04a stalagmite sample

In this chapter, the 51-year growth of a modern stalagmite (‘Gib04a’) retrieved from New St Michael’s (NSM) Cave, Gibraltar (Mattey *et al.*, 2008), is reconstructed in an *a priori* forward model driven by cave monitoring (cave atmosphere $p\text{CO}_2$ and temperature and drip discharge) and local meteorological (surface temperature, rainfall, and water excess) time series datasets. Additionally, this model is refined with experimental measurements of dripwater films, which provide basic constraints on the role of film thickness on growth rate. The rationale for selecting Gib04a as a target specimen is as follows. (i) Cave monitoring data (continuous logging and spot measurements) are available since 2004 (Mattey *et al.*, 2008) and modern climate signal transfer systematics have been relatively well constrained at NSM Cave by Mattey *et al.* (2010). (ii) Continuous monthly meteorological time series datasets (surface air temperature and precipitation) are available from the nearby Royal Air Force Meteorological Office (RAFMO) station, which is also

the site of GNIP sampling since 1962 (Fig. 2.1), with a temporal coverage appropriate to drive the time series growth model. (iii) Gib04a underwent relatively fast vertical extension ($\sim 0.9 \text{ mm a}^{-1}$) and exhibits annual petrographic laminae, providing a robust age model, which is substantiated by annual carbon isotope cyclicity and correct identification of the atmospheric ^{14}C activity ‘bomb spike’ (Mattey *et al.*, 2008). Altogether, these factors provide a rare opportunity to (i) develop, to our knowledge, the first time-series growth reconstruction for a modern speleothem and (ii) test the sufficiency of existing growth rate theory (as a natural system description) in capturing seasonal and interannual variation. To conclude, the implications for linking stalagmite growth and local climate are considered.

2.2. Site description

NSM Cave developed within the dolomitised Gibraltar Limestone Formation of the Rock of Gibraltar (Gibraltar peninsula, southern Iberia; $36^{\circ} 9' \text{ N}$, $5^{\circ} 21' \text{ W}$), whose maximum elevation is 426 m above mean sea level (Fig. 2.1). Pervasive fracturing provides extensive macroporosity, and drips sites within NSM Cave are fed by down-dip and sub-vertical fracture systems. NSM Cave is at least Pleistocene in age (Rodríguez-Vidal *et al.*, 2004), phreatic in origin, has experienced uplift of $\sim 275 \text{ m}$, and preserves evidence for multiple phases of drainage and secondary speleothem decoration (Tratman, 1971). NSM Cave has no known natural entrances; however, a 1 m^2 trap door, constructed in 1942 and the only link with Old St Michael’s Cave, does not significantly disturb the natural chimney-effect ventilation (Mattey *et al.*, 2010; 2008 and references therein).

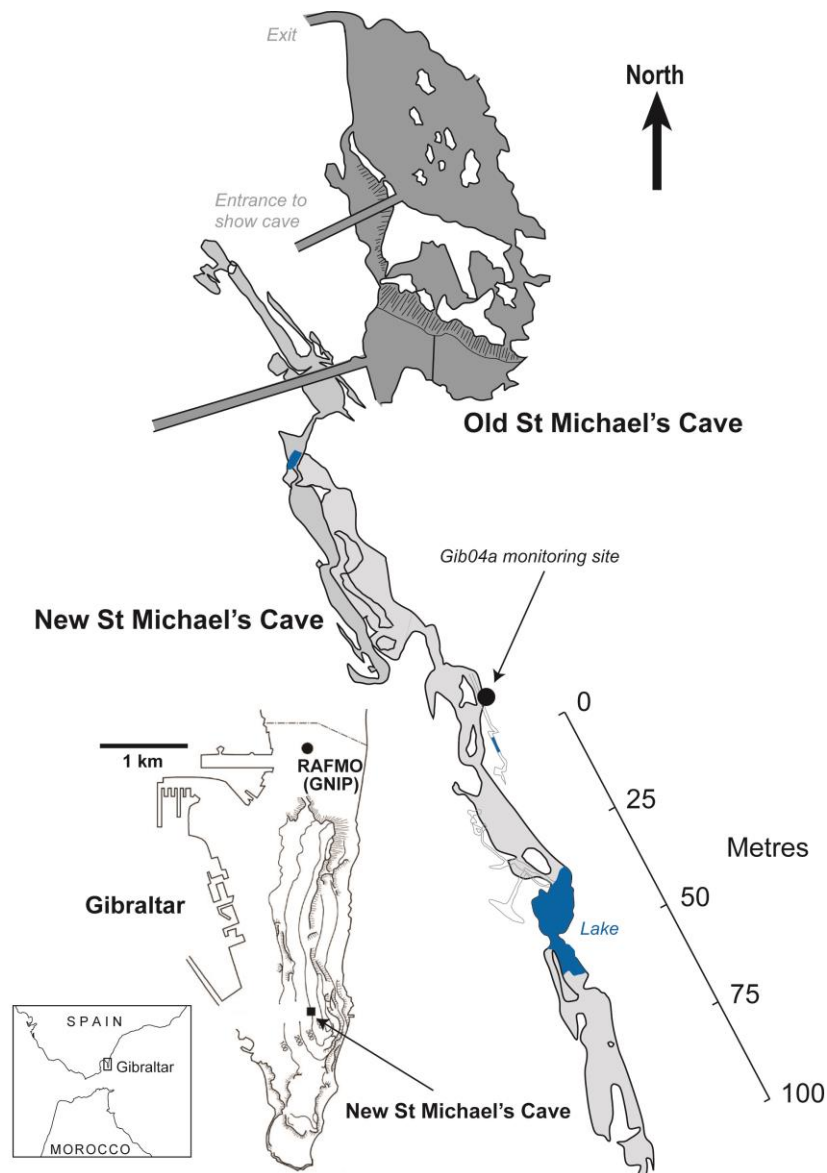


Figure 2.1. Study locations. Location and most recent survey map (undertaken in 2007) of NSM Cave and location and map of Gibraltar with locations of Gibraltar's RAFMO/GNIP station at North Front (World Meteorological Organisation station code: 8495; 36.2 °N, 5.4 °W, 5 m asl). Topographic contour lines on the Gibraltar map are in 100 metre intervals. Figure adapted from Matthey *et al.* (2010).

Matthey *et al.* (2010) identified links between ventilation dynamics, calcite fabrics, stable isotope ratio and trace element seasonality, and dripwater trace element variability. Seasonal ventilation of NSM Cave is characterised by rapid summer-to-winter increases and winter-to-summer decreases in cave atmosphere $p\text{CO}_2$, between near-atmospheric

values and ~3000-8000 ppm, occurring over several days (Fig. 2.3). Ventilation of this cave system is the focus of on-going research and therefore a full explication of ventilation processes and controls on cave air $p\text{CO}_2$ variability is beyond the scope of this chapter. Here, reasonable simplifications are made in light of this on-going work, which are explained in the following section. Matthey *et al.* (2010) also compared drip discharge and hydrologically-effective precipitation data and performed groundwater dye tracer experimentation, suggesting that coherence in dripwater hydrochemistry between separate monitoring sites results from common hydrochemical control, given the observed distinct recharge responses and inferred epikarst flow paths for each drip site.

2.3. Methods

The approach taken to reconstructing the growth of Gib04a is untargeted, *a priori* forward modelling driven by cave monitoring and local meteorological monthly time series datasets. In addition, experimental measurements of dripwater film thicknesses were performed using an analogue material under experimental conditions to provide constraints on this parameter and therefore refine the stalagmite growth rate model.

2.3.1. Experimental measurements of dripwater film thickness

Collister and Matthey (2008) determined an empirical relationship between stalactite radius and drop volume experimentally using analogue materials, constraining a previously poorly understood parameter impacting stalagmite width. Hansen *et al.* (2013) determined time constants for CO_2 degassing, new $p\text{CO}_2$ equilibration, and calcite precipitation using

experimental analogue materials, demonstrating that the geochemical evolution of cave dripwater is a function of these constants, not simply of CO₂ degassing rate. This experimental literature has implications for cave monitoring and speleothem sampling strategies. However, the role of stalagmite morphology on vertical extension is yet to be quantified empirically.

2.3.1.1. *Experimental setup and procedure*

The dependency of dripwater film thickness (δ) on stalagmite curvature and surface microtopography was investigated using 10 plano-convex Al domes (uniform spherical curvature), and employed image analysis techniques to calculate the thickness of water films formed from a known volume of water dispensed from a known height. In geometric terms, the domes utilised for these experimental measurements are chords of spheres of various known radii. The curved surface area, A , of each dome is given by:

$$A = 2\pi\rho^2 \left(1 - \sqrt{1 - \frac{x^2}{\rho^2}} \right) \quad (\text{Equation 2.2})$$

where ρ is the spherical radius and x is the projected radius of the base of the subtended cone of the chord (i.e., the radius of the circular base of the dome). As $x \rightarrow \rho$, $A \approx 2\pi\rho^2$ (i.e., the area of a hemisphere). A is expressed here in terms of *projected* radius because this parameter is known for all domes. (Alternatively, A may be expressed more simply in terms of arc length, but use of Eq. 2.2 favourably avoids the need for additional measurements of arc length and propagating their associated error to the final δ calculations.)

A camera was positioned directly above the position of the Al domes. The experimental setup (Fig. 2.2) required a fixed camera viewshed to obtain consistent images of water droplets. An example photograph (Fig. 2.3) shows a drip at rest on the surface of a curved wetted Al surface. Image analysis techniques provide a precise measurement of the projected area covered by the dispensed water droplet.

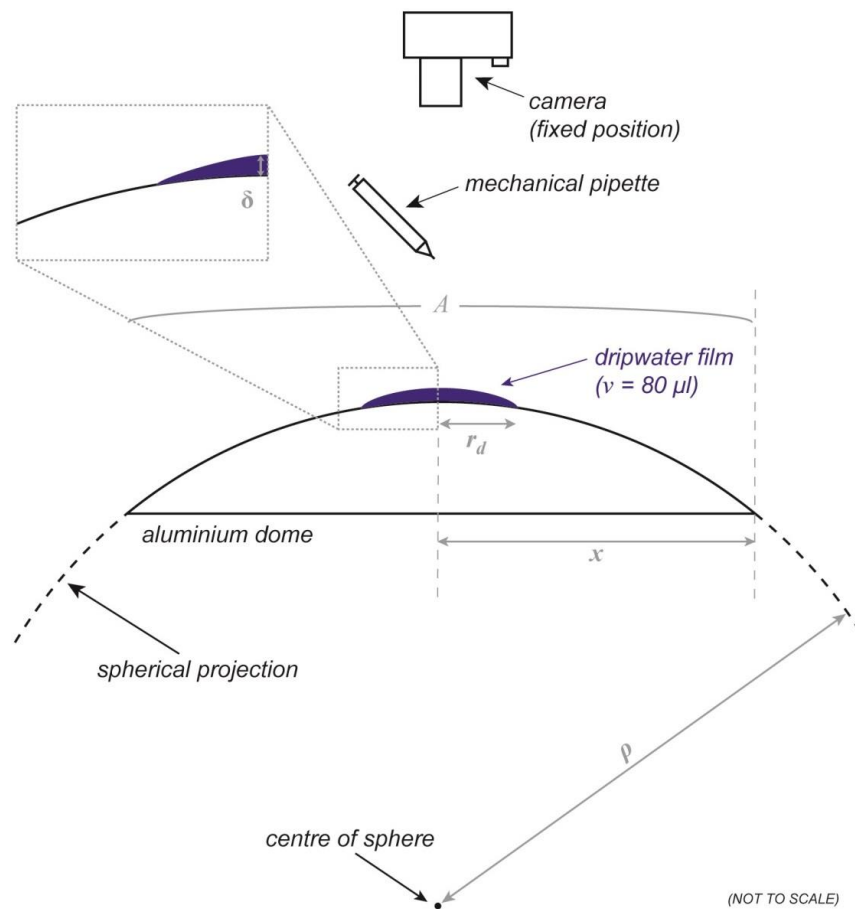


Figure 2.2. Illustration of experimental procedure. Schematic illustration of the experimental procedure for obtaining δ measurements from a fixed quantity of dyed water dispensed onto a wetted, curved Al surface. Terms are defined by Eq. 2.2 and Eq. 2.3. Note that figure is not to scale and that the morphology of the dripwater film in section view is also schematic.

Each dome was wetted and an $80 \mu\text{l}$ droplet dispensed onto its apex using a calibrated mechanical pipette, allowed to spread, and photographed. The position of domes in each image and the viewshed of the camera were fixed (Fig. 2.2). Droplets were dyed to create a

colour contrast between the droplet and the dome in the image (Fig. 2.3). For each image, the Java™-based, public domain software *ImageJ* (Schneider *et al.*, 2012) was used to threshold the colour of the dyed water film from that of the surface of the dome (Fig. 2.3) and a particle analysis tool was used to determine the projected area (2-D) of the dripwater film, which was corrected for dome curvature using Eq. 2.2. Water droplets were dispensed from a height of 10 mm to prevent splashing and conform to experimental conditions, but this is less than ‘typical’ drop heights at natural drip sites. Five replicates were performed for each dome.

2.3.1.2. Analytical procedure

Simplistically, calculating δ assumes that a droplet spreads radially from the dome’s apex, forming a uniform disc of curvature equal to ρ . However, because many photographed droplets exhibited non-circular forms (Fig. 2.3), it is necessary to avoid this simplification by calculating the (curved) surface area of each dome and the precise proportion covered by the 80 μl droplet. δ is given by:

$$\delta = \frac{v}{A_d} \quad (\text{Equation 2.3})$$

where v is droplet volume (mm^3) and A_d is the curved surface area of the dripwater film at rest on the dome (mm^2). Using a high-precision balance, the error associated with v is estimated to be of the order of 0.01 %.

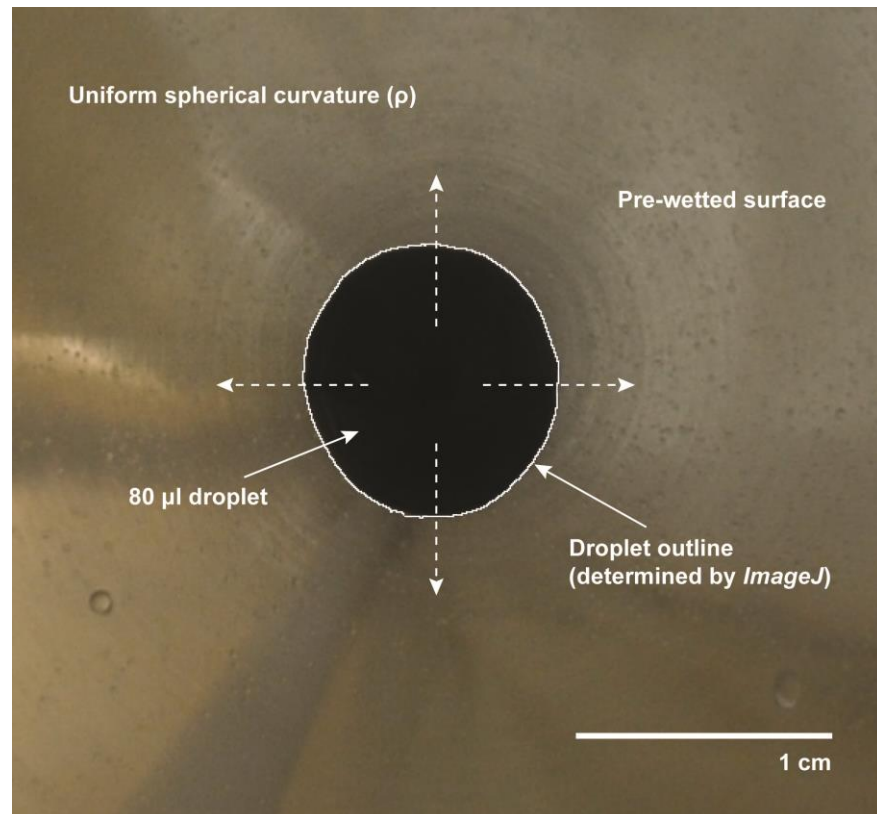


Figure 2.3. Example dripwater droplet photograph. Top-view example photograph of a curved wetted aluminium surface with 80 μ l dyed water droplet dispensed onto its apex. The droplet spreads, indicated by the dashed arrows, over the uniformly curved surface ($\rho = 37.5$ mm in this image). The outline of the water film (solid white line), as determined by *ImageJ*, is accurate. Spreading does not necessarily displace existing water from pre-wetting the surface. Note that the image shows only the central area of the dome's surface; the width of this dome, $2x$, is equal to 90 mm (see Fig. 2.2).

A second set of measurements was performed using non-smooth domes, which were created by affixing a layer of laboratory-grade quartzose sand (pre-filtered through a 0.15-0.425 mm particle mesh) to the surface each dome. The grain size is comparable to previous estimates of δ by Dreybrodt (1981) and acts as an opposite end-member to the idealised, smooth surfaces. This analogue for stalagmite surface microtopography is favoured because it preserves the original curvature of each dome, thus isolating the microtopography effect. A second set of δ calculations was performed.

This approach incurs two important uncertainties. (i) The interfacial properties and contact angles associated with water, air and dry Al are different from those associated with water, air and dry calcite, potentially giving rise to erroneous results. Dripwater films would be thickest at a dome's apex if dispensed onto a dry dome, so wetted dome surfaces were used to better approximate the interfacial properties of a natural speleothem substrate. Additionally, measurements were duplicated on Al (with $\rho = \infty$) using wetted calcite spar, a precaution undertaken by Collister and Matthey (2008). (ii) In this study, the magnitudes of drop height and microtopography are constants. Therefore, future experimental work should attempt to quantify the role of variable drop height and degree of microtopography on film thickness.

2.3.2. Construction of a time-series stalagmite growth model

Transfer functions were derived to estimate $[\text{Ca}^{2+}]_{app}$ and α , both of which are based on earlier calculations by Dreybrodt (1999), to provide inputs for Eq. 2.1. A non-linear relationship between cave atmosphere $p\text{CO}_2$ and $[\text{Ca}^{2+}]_{app}$ was determined for a constant temperature of 20 °C (Fig. 2.4a) and a linear relationship between temperature and $[\text{Ca}^{2+}]_{app}$ was determined for a constant $p\text{CO}_2$ of 2000 ppm (Fig. 2.4b). Combining these relationships gives the following transfer function:

$$[\text{Ca}^{2+}]_{app} = \frac{1}{2} \left((5.872 p\text{CO}_2^{0.2526}) + (-0.0167 T_c + 1.5146) \right) \quad (\text{Equation 2.4})$$

where $p\text{CO}_2$ is that of cave air (atm) and T_c is in-cave temperature (°C).

A non-linear relationship between α and T_c was determined for several values of δ . Selecting a single value is not necessary because our experimental measurements provide independent constraints on δ (Fig. 2.4c) and α depends only on T_c for $\delta < 0.4$ mm (Baker *et al.*, 1998; Hansen *et al.*, 2013). A non-linear relationship between α and δ was determined for a constant temperature of 20 °C (Fig. 2.4d). Combining these gives the following transfer function:

$$\alpha = \frac{1}{2} \left(\left(2.22 \times 10^{-7} T_c^2 + 6.36 \times 10^{-6} T_c + 3.88 \times 10^{-5} \right) + \left(-0.0057 \delta^2 + 0.002 \delta + 0.0001 \right) \right)$$

(Equation 2.5)

The constant values for which Eq. 2.4 and Eq. 2.5 were derived are those of Dreybrodt (1999) which best represent conditions at the Gib04a site since cave monitoring began. Mean annual cave air $p\text{CO}_2$ is 2496 ppm and T_c remains constant at 17.9 °C at the Gib04a drip site (Fig. 2.5), which is satisfactorily close to the temperature for which the relationships in Fig. 2.4a and Fig. 2.4d were derived. Therefore, Eq. 2.4 and Eq. 2.5 are used with minimal systematic error and α varies with δ , rather than assuming a constant value for the entire reconstruction.

Finally, an input time series of dripwater $[\text{Ca}^{2+}]$ is required for Eq. 2.1. Dripwater $[\text{Ca}^{2+}]$ measured at the Gib04a site likely equilibrated with soil $p\text{CO}_2$ of ~1 % (Mattey *et al.*, 2010). Unfortunately, there is no overlap between on-going monitoring at NSM Cave and the period of modern Gib04a growth (1951-2004). To compensate for this, dripwater $[\text{Ca}^{2+}]$ were correlated with surface environmental parameters. Genty *et al.* (2001) derived an empirical relationship between mean annual cave temperature and dripwater $[\text{Ca}^{2+}]$ based on data from temperate European sites. Although this is a useful relationship, it is

not appropriate to use temperature as a single predictor for dripwater $[\text{Ca}^{2+}]$ at NSM Cave, despite the similarity between mean annual surface and cave temperatures (18.3 and 17.9 °C, respectively). In a Mediterranean climate, with relatively distinct dry and rainy seasons, moisture availability as well as surface temperature control soil CO_2 productivity (Baldini *et al.*, 2008; Murthy *et al.*, 2003). Measured dripwater $[\text{Ca}^{2+}]$ at the Gib04a site is highest in winter, suggesting a potential connection to moisture availability, and other Mediterranean sites (e.g., Clamouse Cave, southern France) do not plot along the Genty *et al.* (2001) relationship. Given these observations, multivariate regression was performed between NSM Cave dripwater $[\text{Ca}^{2+}]$ (Mattey *et al.*, 2010) and surface environmental (predictor) variables (temperature, rainfall and potential evapotranspiration) for Gibraltar, obtaining the following expression:

$$[\text{Ca}^{2+}] = \frac{123 - 3.45 T_s - 0.0139 (P - E)}{40.078} \quad (\text{Equation 2.6})$$

where P is total monthly precipitation and E is potential evapotranspiration (Fig. 2.5), calculated according to the method of Thornthwaite (1948). Dividing by the molecular mass of Ca (40.078) converts $[\text{Ca}^{2+}]$ from ppm to mmol L^{-1} . Combined, T_s and epikarst recharge explain 67 % of $[\text{Ca}^{2+}]$ dripwater variability observed at the Gib04a site, with 0.23 mmol L^{-1} uncertainty.

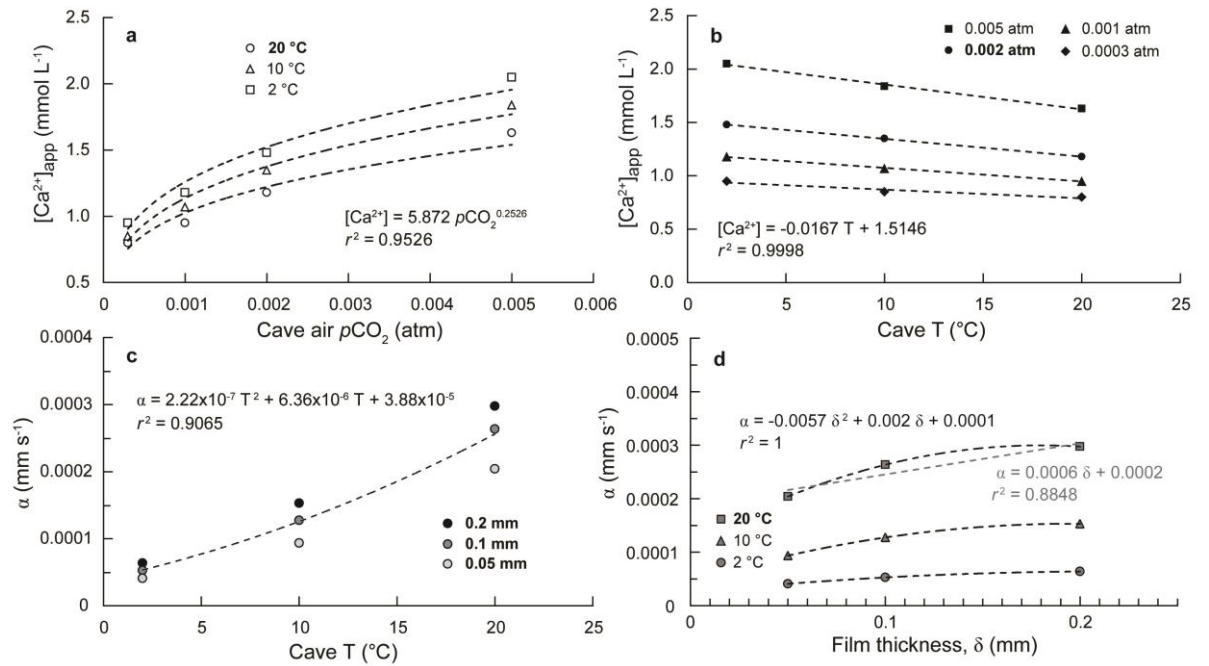


Figure 2.4. Synthesis of data originally presented by Dreybrodt (1999). Transfer functions derived from these published data by bivariate regression are used in the time series growth reconstruction for Gib04a. **(a)** A power law fit (correlation coefficient, $r^2 = 0.95$) between $[Ca^{2+}]_{app}$ and cave atmosphere pCO_2 for a constant cave temperature of 20 °C. **(b)** A linear fit ($r^2 = 0.99$) between $[Ca^{2+}]_{app}$ and temperature for a constant pCO_2 of 0.002 atm. **(c)** A 2nd-order polynomial fit ($r^2 = 0.91$) between the ‘kinetic constant’ (α) and cave temperature for all data. **(d)** A 2nd-order polynomial fit ($r^2 = 1$) between α and film thickness (δ) for a constant temperature of 20 °C. A linear fit ($r^2 = 0.89$) is also shown for comparison, but not used in the growth reconstruction (grey line). Terms are defined in the text.

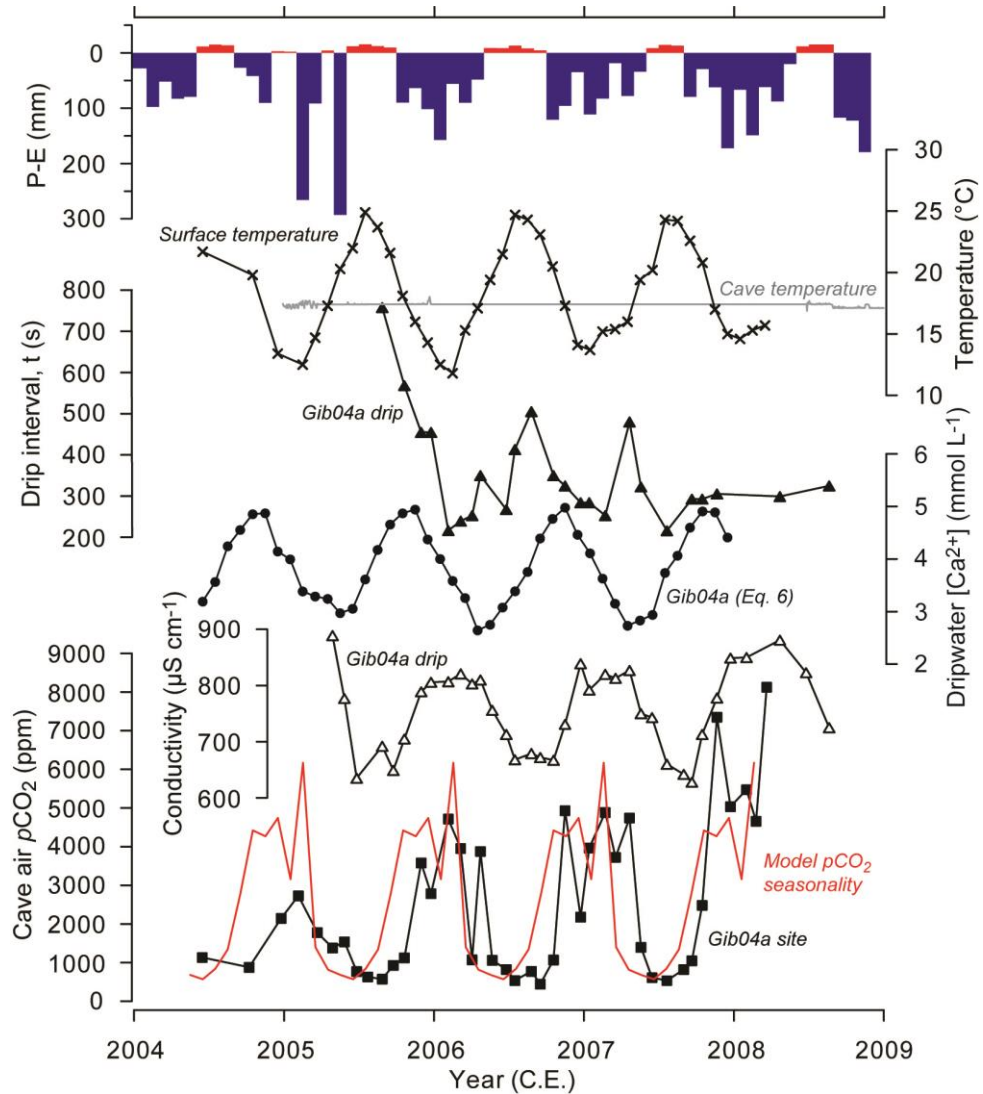


Figure 2.5. Gib04a monitoring data (2004-2009). Monitoring data from the Gib04a drip site in NSM Cave (Fig. 2.1) and calculated model parameters: cave atmosphere $p\text{CO}_2$ spot measurements (squares) and monthly mean trend (red line); dripwater electrical conductivity (triangles); modelled dripwater $[\text{Ca}^{2+}]$ using Eq. 2.6 (circles); drip discharge (filled triangles); surface temperature measured at Gibraltar's RAFMO station (crosses) and continuously logged cave air temperature (grey line); surface water excess (blue – positive, red – negative) calculated by subtracting potential evapotranspiration (E) from total monthly rainfall (GNIP data). E was calculated according to the method of Thornthwaite (1948), following Matthey *et al.* (2008), with heat index values and reduction factors taken from Patra (2001). Cave monitoring data were originally published by Matthey *et al.* (2010; 2008). RAFMO meteorological data © Crown Copyright, the Met Office.

2.4. Results and discussion

2.4.1. Relationships between local meteorological variables, cave microclimate, and growth rate

Gibraltar's Mediterranean maritime climate is characterised by mean summer (June-August) and winter (December-February) temperatures of 22.8 and 13.2 °C, respectively, with ~0.7 °C warming over the last ~30 years (Wheeler, 2011), and mean summer (April-September) and winter (October-March) total precipitation of 135 and 668 mm, respectively, with a ~20 mm decrease mean annual rainfall since 1960 (IAEA/WMO, 2014; Wheeler, 2006; 2007). Clear seasonality in NSM Cave microclimate exists. Winter months produce seasonally low temperature, high water excess, high cave atmosphere $p\text{CO}_2$, and low dripwater $[\text{Ca}^{2+}]$. The opposite is therefore true of each during summer months. Dripwater $[\text{Ca}^{2+}]$ is not exactly in-phase with surface temperature because it depends also on water excess, which is sensible given that existing monitoring data from NSM Cave and from the overlying soil cover show that cave air $p\text{CO}_2$ seasonality is not in exact phase with soil moisture availability (i.e., rainfall seasonality). Predictable $p\text{CO}_2$ seasonality at the Gib04a site co-varies with modelled dripwater $[\text{Ca}^{2+}]$ because both are primarily temperature-dependent (Fig. 2.5). Ventilation of NSM Cave is probably venturi- and/or chimney-type (Mattey *et al.*, 2010) and the subject of on-going research. These monitoring data are discussed in much greater detail by Mattey *et al.* (2010) and indicate fast growth of Gib04a, whose actual mean linear extension rate was ~0.9 mm a⁻¹ during 1951-2004 (Mattey *et al.*, 2008).

2.4.2. Control of stalagmite apex morphology on film thickness

Dreybrodt (1988) estimated δ to be in the range 0.05 – 0.4 mm, yet microtopography is not parameterised explicitly in growth models. Baldini *et al.* (2008) found that δ may tend towards the upper end of that range (0.32 mm) for a stalagmite exhibiting mm-scale surface microtopography, consistent with the measurements of Baker *et al.* (1998), but Kaufmann (2003) fixed δ at 10^{-4} mm. Therefore, few constraints on δ exist. Two empirical δ - ρ relationships for smooth and microtopographical surfaces were derived (Fig. 2.6, Table 1), providing experimental constraints. Both relationships are linear and negatively correlated. For smooth surfaces, δ decreases with increasing curvature ($r^2 = 0.74$) because droplets spread under gravity and are retarded only by surface tension effects. Over microtopography ($r^2 = 0.47$), spreading is greatly encouraged by capillary action and reduced surface tension. Importantly, microtopography (0.15-0.425 mm) reduces film thickness by an order of magnitude compared to idealised, smooth substrates, and these results are consistent with those of Baker *et al.* (1998). These results indicate that stalagmites with irregular morphologies or high surface roughness are less likely to undergo fast vertical extension conducive to generating high-resolution palaeoclimate records.

For flat surfaces ($\rho = \infty$), mean δ values for smooth and non-smooth surfaces are similar: 0.93 and 0.77 mm, respectively, indicating flat surfaces behave differently from curved surfaces. Spreading over a smooth surface under gravity or by capillary action over a microtopographical surface is reduced if that surface is flat, and the effect of microtopography to encourage spreading is significantly reduced. For comparison, additional measurements were performed on wetted calcite spar with $\rho = \infty$, providing natural interfacial properties between calcite, water and air. Mean δ for flat calcite is 0.83

mm, which is similar to values for wetted Al (Fig. 2.6). These observations are important because many actively-growing stalagmites selected for research, including Gib04a, exhibit uniform cylindrical morphology and possess low-curvature apices, particularly if initial surfaces are near-flat (Dreybrodt, 1999). It is speculated that water spreading over curved microtopographical surfaces is reduced by the development of minute menisci over the substrate (i.e., between sand grains in our analogue), but this is less significant for stalagmites exhibiting undulatory rather than granular microtopography.

For low-curvature smooth surfaces ($\rho > 75$ mm), the empirically-derived δ values overestimate those of Dreybrodt (1999) and Hansen *et al.* (2013), highlighting the role of other mechanical processes affecting the amount of dripwater at rest on a stalagmite surface and therefore δ . Under experimental conditions, water dispensation onto Al and calcite spar involves no water loss through mechanical processes, such as splashing. In natural cave settings, with greater drop heights, the net effect of splashing is a reduction of δ , and potentially results in unconventional growth features, such as splash coronae, where maximum calcite accumulation occurs away from the vertical extension axis. Potentially, a relationship between drip height and amount of water lost by mechanical processes for a given droplet volume, which depends on stalactite radius and ambient barometric pressure (Collister and Matthey, 2008), may be demonstrable. Quantifying this and the role of different types and magnitudes of microtopography will provide future modelling challenges.

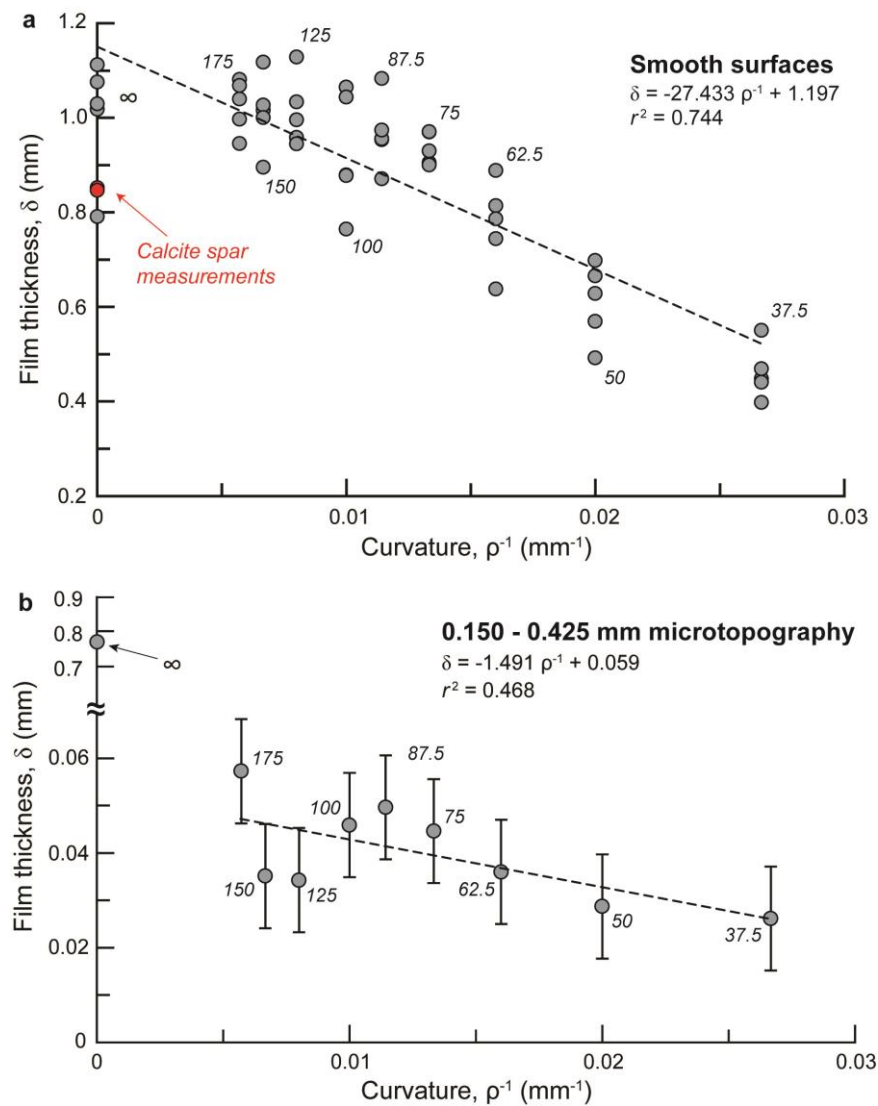


Figure 2.6. Experimental measurements of dripwater film thickness. Change in film thickness (δ) as a function of surface curvature (ρ) for wetted surfaces; δ increases with decreasing curvature. (a) Smooth surfaces ($r^2 = 0.74$; $p = 8.48 \times 10^{-16}$; $n = 50$) and (b) surfaces with 0.15 – 0.425 mm microtopography ($r^2 = 0.47$; $p = 0.09$; $n = 9$). Mean values for wetted calcite spar (red; $n = 7$; $\sigma = 0.012$) are shown in (a). Greater scatter was found for these measurements, so (b) shows mean values with 1 standard deviation. The δ values determined for smooth surfaces are an order of magnitude greater than those for microtopographical surfaces. In the case of flat (infinite curvature) surfaces, δ values are similar, indicating that wet Al provides a useful, though not perfect, analogue for calcite, supporting recent research (e.g., Collister and Matthey, 2008).

Surface	ρ (mm)	ρ^{-1} (mm ⁻¹)	Height (mm)	Mean δ (mm)
11	36.5	0.027	45.59	0.232
10	29.0	0.034	42.35	0.129
9	40.0	0.025	36.03	0.267
8	58.0	0.017	29.56	0.379
7	77.0	0.013	25.15	0.440
6	72.0	0.014	19.85	0.427
5	88.0	0.011	17.21	0.464
4	155	0.006	12.21	0.535
3	25.5	0.039	8.09	0.061 [†]
2	39.0	0.026	7.06	0.257 [†]
1	157.0	0.006	0.00	0.536 [‡]
				0.365 [§]

Table 2.1. Film thickness data for Gib04a growth laminae based on experimental measurements. Estimated curvature and associated mean film thickness (given as the mean of values calculated using both transfer functions in Fig. 2.4 for 11 growth surfaces identified in Gib04a (Fig. 2.7)). For each surface, height denotes the start point of the interval of vertical calcite accumulation for the estimated δ is used in the growth model.

In summary, these data show a linear decrease in film thickness with increasing surface curvature and that the presence of sub-millimetre scale microtopography reduces δ by an order of magnitude, providing constraints on temporal δ variation in Gib04a, which is discussed in the following section.

2.4.3. Constraints on film thickness and reconstructing modern Gib04a growth (1951-2004)

The mean curvature of 11 visible growth laminae in Gib04a (Fig. 2.7) were estimated and the associated δ values for each (Table 1) were calculated using the new empirical relationships (Fig. 2.6). Excepting laminae 2 and 3, a decreasing trend in δ is found with decreasing equilibrium diameter of Gib04a during the period 1951-2004, showing broadly

[†] Non-classical stalagmite growth (see text for discussion).

[‡] Initial surface from which modern growth initiated.

[§] Growth-weighted mean value.

uniform stalagmite growth (Fig. 2.7). Broadly, these δ estimates for Gib04a are within the range described by previous research (Dreybrodt, 1999; Kaufmann, 2003), though they tend towards higher values of that range during the early phase of Gib04a growth. Note that δ was not estimated for every macroscopic growth lamina in Gib04a. Instead, locations were identified at an approximately regular interval where curvature changes notably. In the Gib04a R_0 reconstruction, each value of δ is ‘active’ until the subsequent identified surface (Table 1).

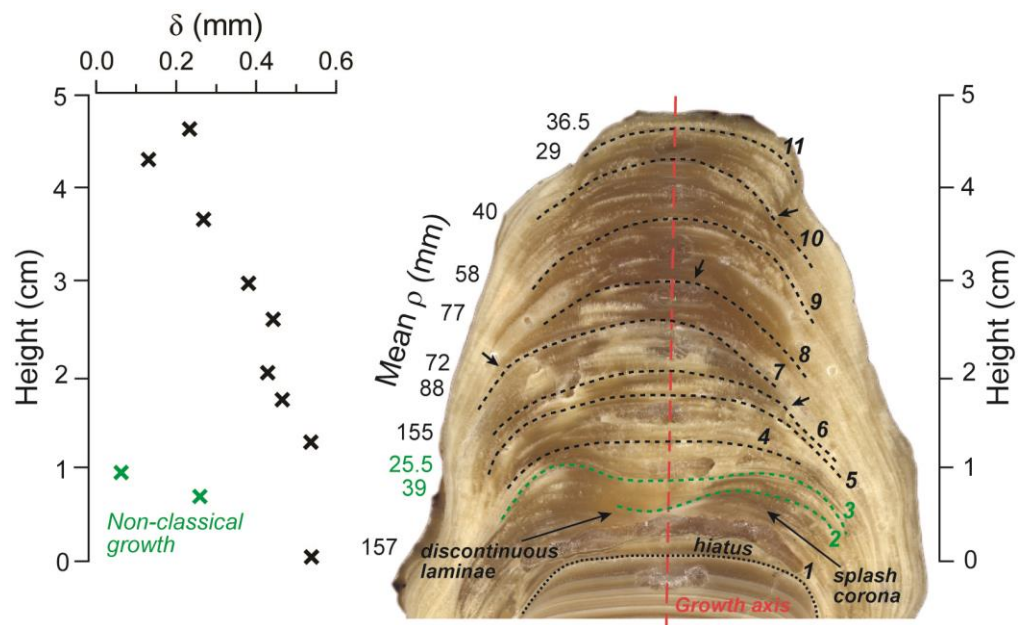


Figure 2.7. Cut section of the modern growth of Gib04a (AD 1951-2004). The dotted line indicates the hiatus separating ancient (pre-Holocene) and modern growth, termed growth surface 1. The dashed lines indicate laminae 2 to 11. For each lamina, estimated curvature (mm) is given on the left, with corresponding mean δ values plotted against height (see Table 2.1). Laminae 2 and 3 (highlighted green) represent non-uniform stalagmite growth. The dashed red line indicates the vertical growth axis and the black arrows indicate clear inflections in laminae curvature that are visible in this 2-D cut section. See text for discussion.

The full Gib04a R_0 reconstruction shows clear seasonality (Fig. 2.8; Appendix 2) that is related to dependence on surface temperature, water excess, and cave atmosphere $p\text{CO}_2$. Total modelled vertical extension is 55.99 mm, which overestimates Gib04a’s actual

growth by 8.16 mm. Overall, model performance demonstrates that existing growth rate theory sufficiently describes Gib04a growth on seasonal to interannual timescales. However, an overestimation of calcite growth was also observed by Day and Henderson (2013). These intriguing deviations from existing theory warrant the application of this modelling approach to other well-monitored cave sites, given that local meteorological data (surface temperature and water excess) provide constraints on dripwater $[Ca^{2+}]$ using Eq. 2.6 or previous work by Genty *et al.* (2001) for semi-arid or temperate environmental settings, respectively.

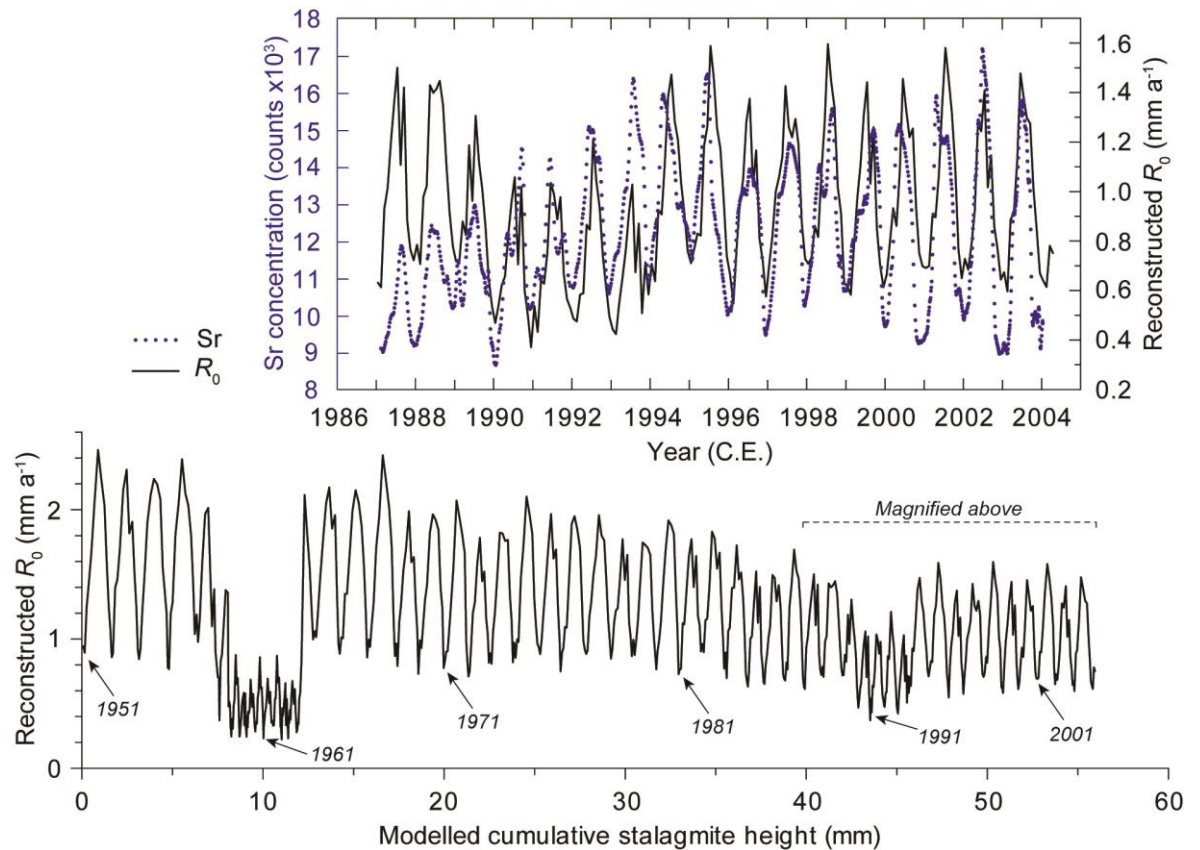


Figure 2.8. Gib04a growth reconstruction AD 1951-2004. The full R_0 reconstruction (black), with a magnification of the period January 1987 to April 2004 that is compared with Gib04a Sr concentration (blue). Sr data originally published by Matthey *et al.* (2008).

2.4.3.1. *Non-uniform Gib04a growth*

Growth laminae 2 and 3 in Gib04a (Fig. 2.7) represent the development of a splash corona; during this interval, calcite precipitation has occurred away from the central growth axis. Pre-Holocene Gib04a growth provided a low-curvature lower edifice above which modern growth initiated (Fig. 2.7). Therefore, the development of this feature is unexpected, given the results of Dreybrodt (1999). Nevertheless, if non-uniform growth and the development of the splash corona began close to lamina 1, the estimated δ value for this initial surface may be an overestimate. Additionally, this suggests that shifts in the position of the vertical extension axis occurred, potentially explaining the ~8 mm model overestimation. At their intersection with the vertical growth axis, lamina 2 is inclined and lamina 3 is near-flat, and several laminae immediately below and above lamina 3 exhibit convex (i.e., negative) curvature. Additionally, several laminae exhibit relatively sharp inflections in ρ (Fig. 2.7), though these do not affect the curvature uniformity of calcite deposited immediately above them, and only one such inflection is proximal to the vertical growth axis. Such observations may be difficult to make in 2-D sections of slower-growing stalagmites. Our empirical relationships give realistic δ estimates for negative ρ values, but their physical plausibility is uncertain. The δ values for laminae 2 and 3 plot away from the linearly decreasing δ trend and several indistinct or discontinuous laminae are apparent (Fig. 2.7), both of which produce a period of low vertical extension and reduced seasonal variability (Fig. 2.8). This non-uniform growth, totalling ~6 mm, persisted for ~10 years.

Alternatively, a decrease in calcite saturation index, related to surface temperature changes, or to changes in drip rate or dry season deposition, may have caused this temporary change in calcite distribution. However, the growth reconstruction and temperature data do not support this explanation (see section 6.4.5) and there is no evidence for decreased

dripwater $[\text{Ca}^{2+}]$ saturation in the past (e.g., reduce soil/vegetation cover). Additionally, calcite precipitation may still occur at the point where water droplets impact a stalagmite (Hansen *et al.*, 2013), but the distribution of calcite precipitation over pre-existing laminae is affected by splashing. Vertical calcite accumulation at the central growth axis is reduced by the development of splash coronae, partly as a result of a reduction in δ .

2.4.4. Model validation: comparing growth seasonality with Gib04a petrography and Sr

Stalagmite R_0 , calcite microfabric and Sr concentrations may be linked because Sr incorporation into calcite is partially dependent on R_0 (Fairchild and Baker, 2012). At low instantaneous growth rates, Sr may substitute for Ca in the calcite lattice, but is susceptible to competition with other species such as Mg and Na (Boch, 2008; Fairchild *et al.*, 2001) and incorporation of organic macromolecules (McGarry and Baker, 2000). At higher rates, Sr occupies interstitial and defect lattice sites, the abundance of which increases with R_0 (Boch, 2008), because the lattice is less able to distinguish between Ca^{2+} (ionic radius = 1.08 Å) and larger divalent trace metals, such as Sr^{2+} (1.44 Å) (Gabitov and Watson, 2006; Huang and Fairchild, 2001; Lorens, 1981). Therefore, R_0 and the effective partition coefficient for Sr in calcite (K_d^{Sr}) may co-vary (Fairchild and Treble, 2009; Gabitov *et al.*, 2014; Gabitov and Watson, 2006). Boch (2008) reported higher Sr and vertical extension rate associated with porous laminae (summer deposition) in stalagmites sampled from Katerloch Cave, southeast Austria. However, Borsato *et al.* (2007) found no ostensible seasonal co-variation between trace element concentrations and calcite fabric in a stalagmite from Grotta di Ernesto, northeast Italy, but Sr maxima increased linearly with growth. Experimental evidence indicates R_0 and Sr incorporation are strongly related above $R_0 \approx 0.5 \text{ mm a}^{-1}$ (Gabitov and Watson, 2006), but there is also evidence that R_0 increases

well above the natural range are required to produce such co-variation (Day and Henderson, 2013). These results suggest that links between growth mechanics and Sr variability may vary temporally or from site to site. For NSM cave, several observations indicate that K_d^{Sr} should respond to Gib04a R_0 : (i) modelled Gib04a R_0 falls only occasionally below 0.5 mm a^{-1} , most notably between 1956 and 1965 (Fig. 2.8), (ii) Gib04a site temperature remained constant over the monitored period (Fig. 2.5), and (iii) soil cover above NSM Cave is minimal, so competition between Sr incorporation and molecular organic matter deposition in speleothem calcite is less a factor compared with other sites. Therefore, comparing our R_0 reconstruction with high-resolution synchrotron μXRF Sr data, available for the upper $\sim 13 \text{ mm}$ (corresponding to 1987-2004) of Gib04a (Mattey *et al.*, 2010) provides a critical test of the reconstruction's fidelity.

The R_0 reconstruction tracks Gib04a Sr concentrations closely, capturing the seasonal and, occasionally, the sub-seasonal variability (Fig. 2.8). Therefore, R_0 , Sr and calcite fabrics can be compared with confidence, and across the most recent $\sim 4 \text{ mm}$ the discrepancy between actual and modelled vertical extension is 0.18 mm (Fig. 2.9). Gib04a exhibits annual couplets of pale columnar calcite and darker compact calcite (Fig. 2.9a), which represent winter and summer deposition, respectively (Mattey *et al.*, 2010). Dark compact calcite is characterised by a greater density of calcite grain boundaries (Fig. 2.9b), and this associated with high summer Sr and R_0 , although this is less clear for 2000-1 (Fig. 2.9c, d). This suggests that Gib04a calcite lattice changes with increased linear extension rate appear to favour Sr incorporation, consistent with experimental data (e.g., Gabitov *et al.*, 2014). The amplitudes of seasonal R_0 and Sr variations match well, though higher frequency variability indicates non- R_0 effects inhibit Sr incorporation. A potential microhiatus in Gib04a growth was identified by Mattey *et al.* (2010) at 2001-2, which is

characterised by an abrupt change in the density of calcite grain boundaries (Fig. 2.9b), indicating that the year-to-year deposition of calcite couplets is not regular. These abrupt changes in calcite fabric are likely due to ventilation dynamics at NSM Cave. Rapid summer-to-winter increases in cave atmosphere $p\text{CO}_2$ from near atmospheric values occur (Fig. 2.5), potentially leading to weekly-to-monthly scale cessation of calcite deposition. However, this is not apparent in reconstructed R_0 , Sr or other previously-published trace element data from Gib04a. Dripwater $[\text{Ca}^{2+}]$ is sufficient to maintain vertical extension at lower than average rates $\sim 0.5 \text{ mm a}^{-1}$, through winters when cave air $p\text{CO}_2$ is high.

2.4.5. Model validation: modelled Sr-partitioning in Gib04a calcite

To further test the validity of the R_0 reconstruction, how well its output captures the partitioning of Sr between calcite and dripwater solution is examined. Ionic competition affects Sr incorporation, implying that the $K_d^{\text{Sr}}-R_0$ relationship may vary temporally, responding to changes in ionic supply. Despite R_0 -Sr co-variation apparent in Gib04a, it is necessary to estimate Sr incorporation. Unfortunately, the available dripwater hydrochemistry and Gib04a trace element time series datasets do not overlap, but this is compensated for by calculating K_d^{Sr} based on an extrapolation of the R_0 reconstruction.

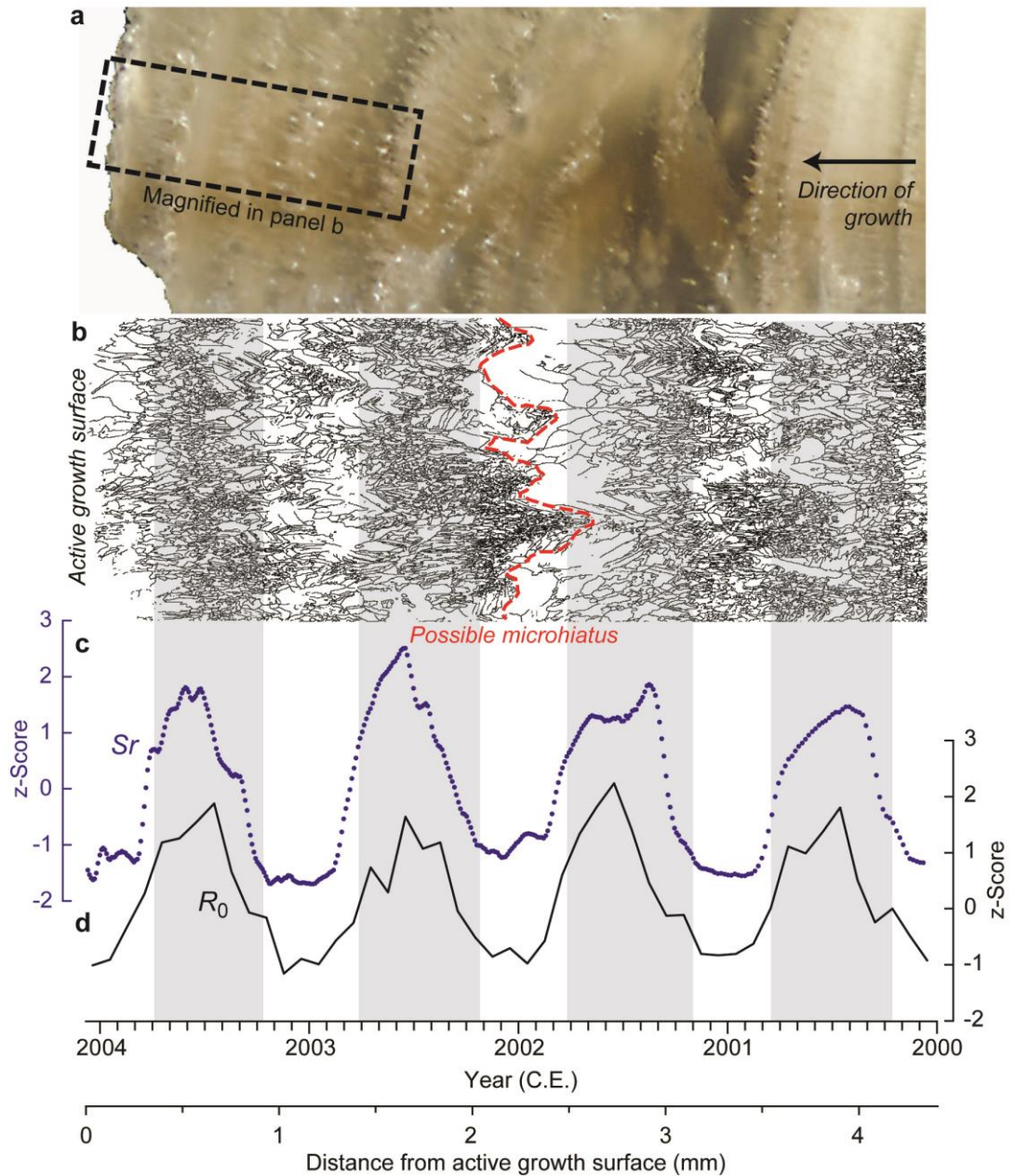


Figure 2.9. Gib04a growth, Sr and petrography. Comparison of modelled growth during the period 2000 to April 2004 (corresponding to the upper ~4 mm of Gib04a) with (a) Gib04a petrography, (b) an electron backscatter grain boundary map of the area outlined in (a), and (c) high-resolution Sr concentration transect across the upper ~4 mm of Gib04a (blue), each of which were originally published by Matthey *et al.* (2010). (d) Reconstructed growth seasonality over this period, totalling 4.18 mm (black). Both Sr and R_0 are plotted as normalised z-Scores, calculated by subtracting the mean and dividing by 1 standard deviation, so that the amplitude of seasonal changes in each dataset may be compared fairly. Vertical grey shading illustrates the association of R_0 , Sr, and grain-scale calcite fabric. See text for discussion.

The R_0 reconstruction was extended beyond the sampling date of Gib04a, through the cave monitoring period, and derived K_d^{Sr} variability from these hypothetical vertical growth rate values using the relationship of Gabitov and Watson (2006). (It is important to note that the aim is not to provide modelling constraints on K_d^{Sr} in speleothem calcite that may be used directly in future studies, but only to undertake an assessment of the R_0 -Sr comparison for this study.) Mean calculated K_d^{Sr} between 2005 and 2007 is 0.39 (Fig. 2.10), which is higher than but close to experimentally-determined values (Day and Henderson, 2013; Gabitov *et al.*, 2014; Gabitov and Watson, 2006; Huang and Fairchild, 2001; Lorens, 1981; Tang *et al.*, 2008; Tesoriero and Pankow, 1996) and natural speleothem calcite values deposited at cave temperatures comparable to those of NSM Cave (Bourdin *et al.*, 2011; Gascoyne, 1983). This overestimation is expected, given the higher vertical extension rate of Gib04a relative to the rates considered in those studies. This comparison is made cautiously because higher K_d^{Sr} values in some experimental studies were derived at instantaneous growth rates which are higher than those applicable to speleothem deposition (Day and Henderson, 2013). Nevertheless, this result is broadly consistent with association between vertical calcite growth, calcite fabrics, and Sr concentration variability identified in Gib04a (Fig. 2.9), but other factors (e.g., karst hydrology, crystallographic growth kinetics) influence Sr incorporation into speleothem calcite (Fairchild and Baker, 2012).

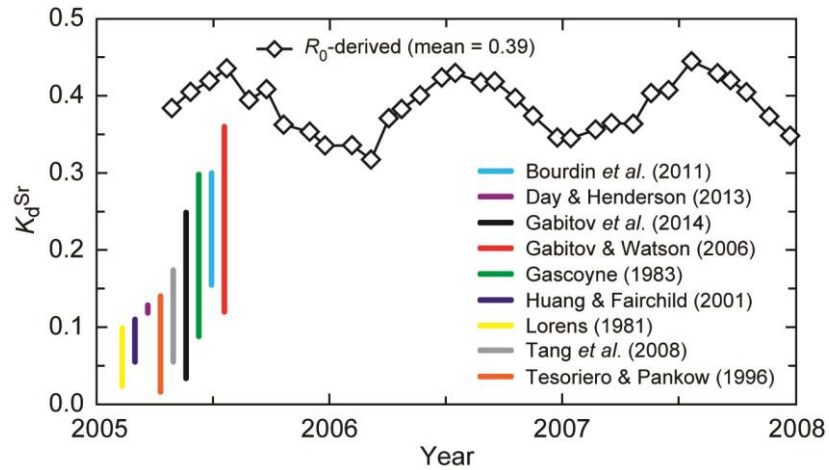


Figure 2.10. Estimated K_d^{Sr} from R_0 . K_d^{Sr} time series derived from an extrapolation of the Gib04a R_0 reconstruction beyond the sampling date and into the cave monitoring period (diamonds). The mean K_d^{Sr} value of 0.39 is higher than but close to the range described by published data (coloured bars; not plotted against x-axis) (Bourdin *et al.*, 2011; Day and Henderson, 2013; Gabitov *et al.*, 2014; Gabitov and Watson, 2006; Gascoyne, 1983; Huang and Fairchild, 2001; Lorens, 1981; Tang *et al.*, 2008; Tesoriero and Pankow, 1996).

2.4.6. Vertical growth rate sensitivity to film thickness

The full R_0 reconstruction, including surface environmental variables and dripwater $[Ca^{2+}]$, calculated using Eq. 2.6, are provided in Appendix 2. Quantifications of the sensitivity of R_0 to various parameters are largely absent from the literature. A first-order, quantitative assessment of the δ -sensitivity of R_0 was undertaken by re-calculating Gib04a R_0 during the period 1951-2004 using constant values of δ and α and comparing this to the original Gib04a growth reconstruction. Theoretically, assessing R_0 's sensitivity to δ alone is not possible because α partially depends on δ (Eq. 2.5 and Fig. 2.4c, d). Therefore, this sensitivity test takes α into account, but because T_c is approximately constant (Fig. 2.5), primarily reflects δ . Gib04a R_0 was recalculated using a weighted mean values of δ (0.365 mm; Table 1) and α (5.12×10^{-4} mm s $^{-1}$). All other growth conditions remained as per the original R_0 reconstruction (Fig. 2.8). Recalculated in this way, the total vertical Gib04a

growth during 1951-2004 is 6.3 mm, which underestimates actual vertical growth by an order of magnitude. The recalculated data are poorly, negatively correlated with the original reconstruction ($r^2 = 0.23$) and exhibit much scatter. Many recalculated R_0 values are negative (Fig. 2.11), which suggest potential re-dissolution of previously-deposited calcite (Baldini *et al.*, 2006a; Whitaker *et al.*, 2009), causing microhiatuses in growth, but the original R_0 reconstruction and Sr data indicate that this is not the case. Moreover, the largest R_0 values in the original monthly reconstruction, though potential overestimates, in fact correspond to negative values in the recalculation with constant δ . The seasonal timing of these negative values therefore indicates they are implausible. Overall, this strongly suggests that using a single value for δ is not appropriate for modelling R_0 on interannual timescales and classical stalagmite growth can be significantly sensitive to δ , with important implications for quantifying the cave and meteorological controls on Gib04a morphology and vertical growth.

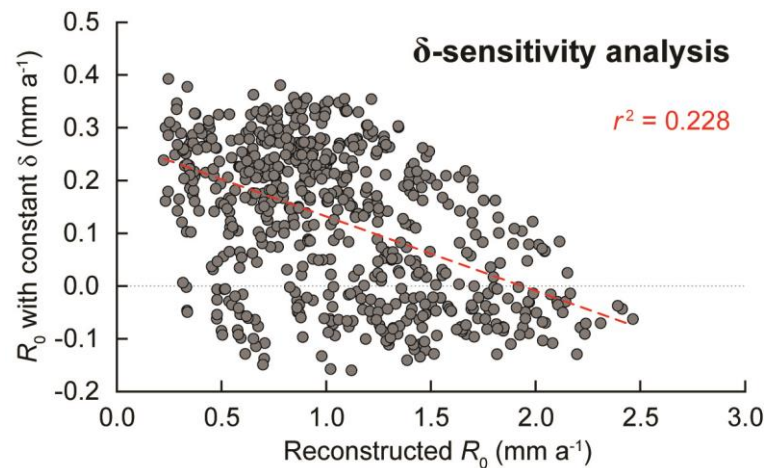


Figure 2.11. First-order quantification of δ -sensitivity of R_0 . R_0 values recalculated with constant δ and α (y-axis) versus original R_0 reconstruction for Gib04a as per Fig. 2.8 (x-axis). Linear regression between these two datasets gives $r^2 = 0.23$ ($p = 1.04 \times 10^{-43}$; $n = 684$).

2.4.7. Local meteorological controls on interannual vertical growth rate variability

A first order sensitivity analysis suggests that R_0 is sensitive to δ variability (Fig. 2.11). Inter-annual morphological change in modern Gib04a growth is characterised by decreasing equilibrium diameter and increasing ρ , resulting in a decreasing δ trend (Fig. 2.7). Consequently, α also decreases during the period 1951-2004 according to Eq. 2.5. The secular decrease in R_0 (Fig. 2.12), most obviously after the non-uniform growth period, potentially reflects drying in Gibraltar. Stalagmite equilibrium diameter can reflect long term trends in karst aquifer recharge (and therefore rainfall). An overall ~30 mm decline in mean annual rainfall and increasing T_s since 1973 result in a linear decrease in total annual water excess feeding Gib04a (Fig. 2.12). (Note that 1996/1997 winter rainfall is anomalous.) Qualitatively, the tapered shape of Gib04a may be explained in this way. Decreasing Gib04a equilibrium diameter and increasing ρ (Fig. 2.7) cause decreases in other growth-determining parameters (δ and α) and result in a secular decline in R_0 since 1965, providing a first-order link between Gibraltar climate and Gib04a's growth history. Interestingly, step-like decreases in R_0 during the non-uniform growth period and during 1990-1994 coincide with large temperature fluctuations, but secular temperature changes do not correlate with R_0 (Fig. 2.12). Cave air $p\text{CO}_2$ seasonality, which is effectively invariant, also cannot explain this, indicating that the dominant control on long-term changes in vertical extension and morphology of Gib04a is karst recharge.

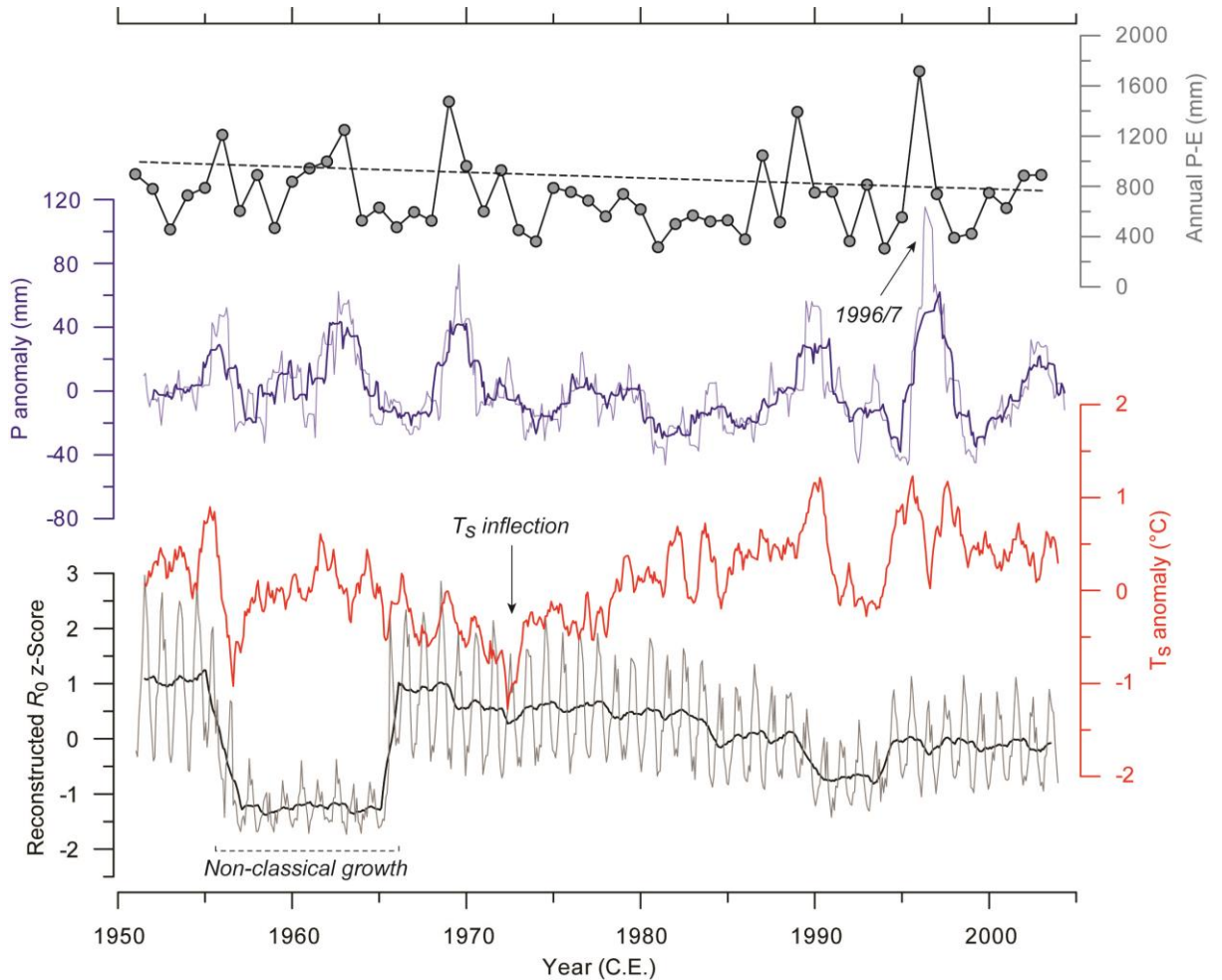


Figure 2.12. Inferred relationships between Gib04a R_0 and local climate parameters. Comparison of R_0 (grey; black curve is a 12-month running mean) with T_s anomalies (red), P anomalies (pale blue; dark blue curve is a 24-month running mean), and total annual water excess during the period 1951-2004 (grey). The non-uniform period of Gib04a growth, an inflection in secular T_s variability, and the anomalously wet 1996/1997 winter are indicated.

2.5. Conclusions

This chapter presents (i) experimental measurements of dripwater film thickness performed on analogue materials, which are used to model δ variation during modern Gib04a growth (1951-2004), and (ii) the first attempt to reconstruct temporal vertical growth rate variability in a modern stalagmite. Experimental measurements demonstrate that δ decreases linearly with increasing surface curvature and that the presence of sub-millimetre

scale microtopography reduces δ by an order of magnitude compared to idealised, smooth surfaces (Fig. 2.6). These observations are attributed to spreading under gravity and by capillary action versus surface tension effects. By examining changes in growth laminae curvature, a linearly decreasing δ trend in the Gib04a stalagmite was identified (Fig. 2.7), consistent with its uniform tapered morphology (decreasing equilibrium diameter and increasing curvature). A period of non-uniform growth, with two δ outliers resulting from the development of a splash corona, occurs during 1956-1965 (comprising ~6 mm vertical extension). Furthermore, a first-order δ -sensitivity analysis of R_0 (using only weighted mean δ and α values) demonstrates that Gib04a's total vertical growth is underestimated by an order of magnitude and non-sensible negative R_0 values arise if δ variability is not taken into account.

The Gib04a growth reconstruction, based on cave monitoring, meteorological data, captures growth seasonality but overestimates total vertical accumulation by ~8 mm. Seasonality in surface temperature, hydrologically effective precipitation (both of which control dripwater [Ca^{2+}]), cave atmosphere $p\text{CO}_2$, and moderate seasonality in drip interval, at NSM Cave (Fig. 2.5) forces strongly seasonal growth of Gib04a (Fig. 2.8 and Fig. 2.9). Seasonality in R_0 co-varies with high-resolution Sr concentration data (Fig. 2.8) and Sr partitioning between dripwater and calcite is captured reasonably by the reconstruction (Fig. 2.10). A high-resolution comparison of R_0 with Sr and changes in grain-scale calcite fabric across the upper ~4 mm shows that the amplitude of seasonal R_0 and Sr variation is comparable, and both are associated with sub-annual layers of dense calcite grain boundaries (Fig. 2.9). An inter-annual decrease in reconstructed Gib04a R_0 is likely linked to a similar decrease in rainfall in Gibraltar since 1960 and this is explained by secular decreases in δ and equilibrium diameter of Gib04a. Therefore, these results

demonstrate that growth rate theory is sufficient on inter- and intra-annual timescales, but represent not the first example of overestimating vertical extension rate. Future work should therefore apply this approach to other well-monitored cave systems to determine whether modifications of growth rate theory are necessary in particular environmental settings.

Recent research has indicated that (i) seasonal dripwater trace element hydrochemistry, if recorded by stalagmites, may provide geochemical markers of seasonal growth laminae (Fairchild and Treble, 2009; Wong *et al.*, 2011), and (ii) δ controls the time constant for CO₂ degassing (Hansen *et al.*, 2013). In light of these results, the empirical constraints on the relationship between δ and stalagmite morphology and R_0 modelling results presented in this chapter provide a timely test of stalagmite growth rate theory. Immediate experimental and modelling studies should quantify the roles of drop height and microtopography magnitude (involving various stalagmite morphologies) on vertical growth. Future possibilities include constraining past variability in multiple environmental parameters from stalagmite data; such an approach is tenable because only a limited proportion of parameter space will produce good model fits to data (e.g., Sr concentrations), and there are now studies confirming the sufficiency of existing growth rate theory on various time scales. Finally, for well-monitored cave systems, modelling growth provides a way to *quantify* biases in geochemical proxy data, aiding the interpretation of records irrespective of resolution.

Chapter 3

The Asian Summer Monsoon: meteorology
and palaeoclimatology

Chapter summary

The Asian Summer Monsoon generates intense seasonal precipitation in India, China and Indochina, therefore impacting the world's most populous regions. This chapter *(i)* summarises the basic meteorological processes responsible for the Asian Summer Monsoon, *(ii)* presents an overview of late Quaternary palaeomonsoon evolution from absolute-dated speleothem proxy records, and *(iii)* discusses recent re-examination of previous proxy record interpretations. Stable oxygen isotope proxy data are commonly used to reconstruct palaeomonsoon variability from speleothems. Existing records track Northern Hemisphere insolation from centennial to orbital timescales, provide evidence for teleconnections with remote, high-latitude climate change, and offer insights into rapid millennial-scale palaeoclimate variability, such as Heinrich events or Dansgaard-Oeschger events, to seasonality changes. However, recent climate modelling, re-analysis of meteorological data, and comparisons of speleothem records with other terrestrial proxy datasets firmly suggest that the conventional interpretation of speleothem $\delta^{18}\text{O}$ as an exclusively palaeo-precipitation or monsoon intensity proxy requires reconsideration. In monsoonal China, rather than preserving a direct EASM precipitation amount signal, speleothem $\delta^{18}\text{O}$ variability instead reflects multiple hydroclimatic processes, the most important of which on annual and longer timescales are precipitation moisture source and atmospheric moisture transport history.

3.1. Asian Summer Monsoon meteorology

The East Asian Summer Monsoon (EASM) and Indian Summer Monsoon (ISM) are two sub-systems which comprise the Asian Summer Monsoon (ASM), the largest monsoonal climate region on Earth and a vital component of the global energy and water cycles (Webster *et al.*, 1998). The EASM and ISM are driven by seasonal reversals in sensible continent-ocean temperature gradients, which drive seasonal changes in mean wind vectors, generating low pressure anomalies over land (Ding and Sikka, 2006). These seasonal changes in atmospheric circulation cause warm, moisture-bearing air masses to migrate inland, engendering extreme summer wet seasons (Fig. 3.1). Approximately 80% of the total annual continental precipitation across China is received between May and August (Webster *et al.*, 1998). Additionally, the mean northerly extent of the intertropical convergence zone (ITCZ), which is affected by land mass distribution and effectively the thermal equator, modulates ASM intensity (Sinha *et al.*, 2011b). Precipitation outside the summer ASM season, particularly that north of the EASM boundary (Fig. 3.1), is influenced by the strength of the mid-latitude Westerlies (Ding *et al.*, 2004).

ISM precipitation is derived from southerly moisture transport from equatorial latitudes and subsequent westerly transport across the northern Indian Ocean, a strong gyre-like circulation into the Indian subcontinent. EASM precipitation is generated by the convergence of south-westerly transport, northward ITCZ shift during boreal summer, and easterly Pacific Ocean trade winds (Liu *et al.*, 2014) (Fig. 3.1). Thus, the geographical distribution of present-day precipitation in Asia (Fig. 3.1) reflects the entire low-latitude monsoonal circulation system (Wang and Lin, 2002). Moreover, satellite observations indicate that monsoonal precipitation rates over oceanic areas are more intense than those over adjacent continental areas (Wang and Lin, 2002). However, the relative seasonal

contributions of these transport mechanisms to precipitation across monsoonal China remain un-quantified.

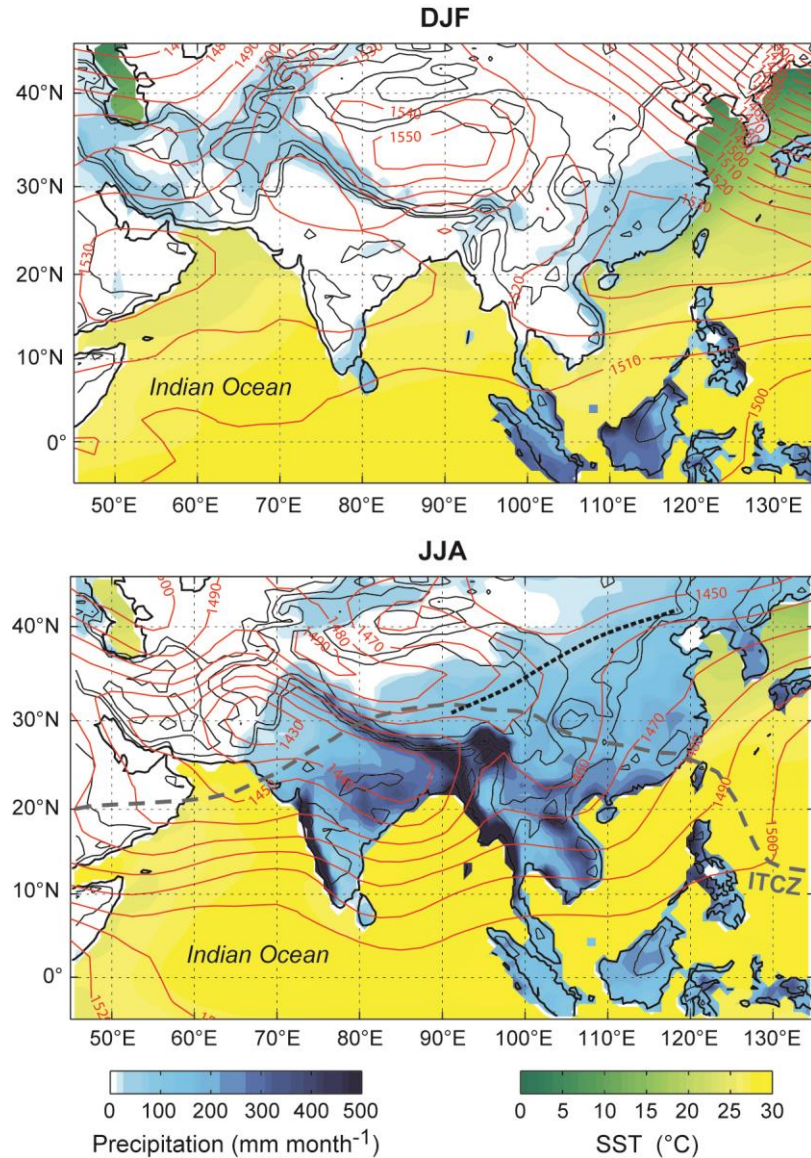


Figure 3.1. Present-day ASM meteorology. During boreal summer (June-August; JJA), the rate of sensible land heating exceeds that over the oceans, due to differential mean specific heat capacities. This warms atmospheric boundary layer air over the land surface, which rises, generating a low pressure zone. Seasonal ocean surface warming at tropical latitudes induces evaporation and these moisture masses migrate poleward. This poleward transport is coupled with seasonal northward ITCZ migration, the mean July position of which is indicated (grey dashed line) according to Lutgens and Tarbuck (2000). These seasonal changes in atmospheric circulation are responsible for intense precipitation across monsoonal Asia between May and August. Onset months of the ISM and EASM are May and June, respectively, with pre-onset to onset dates

between 1st May and 11th June (Wang and Lin, 2002; Xie and Arkin, 1997). Mean boreal winter (December-February; DJF) and summer (peak monsoon; June-August; JJA) precipitation data are taken from the Global Precipitation Climatology Centre gridded precipitation monitoring dataset. Mean sea surface temperature (SST) data are the Extended Reconstruction SST version 3b (Reynolds *et al.*, 2002; Smith *et al.*, 2008), obtained from the National Climatic Data Center. Both precipitation and SST are interpolated to a 1° spatial resolution. Overlain are seasonal mean height of the 850 hPa geopotential surface data (solid red lines), obtained from the Climatic Data Center Derived National Centers for Environmental Prediction Reanalysis Products (available at a 2.5° grid resolution). Precipitation and pressure data are average over the period 1981-2010 and SST data are averaged over 1971-2000. Topographic contours (solid black lines) are shown at 0, 500, 1000, 2000 and 4000 m a.m.s.l. The mean northerly limit of the EASM (dotted black line) is shown, following Liu *et al.* (2014).

3.2. Holocene palaeomonsoon reconstructions

Precipitation is a key meteorological parameter in describing monsoon climate (An, 2000; Wang and Lin, 2002). Therefore, quantifying rainfall variability provides important information about monsoonal fluctuations. A relatively high density of meteorological observatories and monitoring stations exists in China (van Oldenborgh and Burgers, 2005) and the earliest instrumental data for the monsoonal region are from the late 19th Century. However, many such instrumental datasets are too short or temporally discontinuous to allow statistically significant climate calibrations. Documentary indices extend the temporal coverage of observations to AD 960 (Tan *et al.*, 2008). However, documentary evidence for monsoon variability is often too low-resolution, recorded discontinuously, often provides only qualitative observations of climate variability, and is potentially biased towards extreme conditions (Jones *et al.*, 1998). It is therefore necessary to reconstruct past variability in meteorological parameters, such as precipitation and surface temperature, in this region from proxy data.

Stalagmites, terrestrial sediment successions (e.g., loess and palaeosol), lacustrine sediments, and tree-rings are the principal proxy data archives used to reconstruct palaeomonsoon variability (Wang *et al.*, 2010). Li *et al.* (2014) assert that speleothems' amenability to precise, absolute U-series dating is crucial for constraining the timing and rate of monsoon intensity fluctuations and for linking such variability to remote regions. To-date, the majority of published interpretations of proxy $\delta^{18}\text{O}$ datasets are based heavily on the 'amount effect' and therefore assume that stalagmite $\delta^{18}\text{O}$ primarily reflects precipitation amount or ASM intensity (i.e., summer-to-winter precipitation ratio).

Within the ISM region, Holocene stalagmite $\delta^{18}\text{O}$ records from the western Arabian peninsula (e.g., Fleitmann *et al.*, 2003; Neff *et al.*, 2001), the southern Tibetan Plateau (e.g., Cai *et al.*, 2012), and north-eastern India (e.g., Berkelhammer *et al.*, 2012) track mean Northern Hemisphere insolation (at 30 °N), providing evidence for gradual southward shift in the mean boreal summer ITCZ position and ISM rain belt, as well as gradual ISM weakening from the mid to late Holocene (Fig. 3.2). Stalagmite records from the so-called "transition zone" (Li *et al.*, 2014) between the ISM and EASM (within approximately 95 and 105 °E and encompassing Indochina) and from the EASM region of eastern and southern China (Cai *et al.*, 2010b; Cosford *et al.*, 2008; Dong *et al.*, 2010; Dykoski *et al.*, 2005; Hu *et al.*, 2008) also indicate a decline in monsoon intensity during the Holocene, indicating synchronous Holocene ISM and EASM evolution in response to insolation forcing and ITCZ position shift. In addition to solar forcing, other modes of annual- and decadal-scale $\delta^{18}\text{O}$ variance implicate internal climate dynamics, such as the El Niño-Southern Oscillation (ENSO) and the Indian Ocean Dipole (IOD), in EASM variability (e.g., Muangsong *et al.*, 2014). Secular trends in lacustrine sediment records from the Qinghai-Tibetan Plateau are generally consistent with the absolute-dated

speleothem records and therefore support these interpretations (Li *et al.*, 2014; Zhang *et al.*, 2011).

Despite this apparent ISM-EASM phase relationship, the overall ASM response to extra-regional forcing exhibits regional differences. For example, the prominent 8.2 ka event recorded in the North Atlantic region (Alley *et al.*, 1997) is expressed as a monsoon failure between approximately 8.6 and 8.1 ka in speleothem records across the ASM region (Cheng *et al.*, 2009b; Liu *et al.*, 2013). However, ISM records (e.g., Cai *et al.*, 2012; Cheng *et al.*, 2009b; Fleitmann *et al.*, 2003) show a more pronounced $\delta^{18}\text{O}$ increase than EASM records (e.g., Cai *et al.*, 2010a; Dong *et al.*, 2010; Dykoski *et al.*, 2005), suggesting that precipitation $\delta^{18}\text{O}$ in the tropical ISM region is more sensitive to this North Atlantic forcing than precipitation $\delta^{18}\text{O}$ in the sub-tropical EASM region. This inference is supported by recent GCM modelling results (Pausata *et al.*, 2011), discussed in section 3.4.

High-resolution, instrumentally-calibrated palaeomonsoon records spanning the last two millennia suggest regional-scale coherence in ISM and EASM precipitation variability. However, within the ISM region, stalagmite $\delta^{18}\text{O}$ data from central and western India show differing precipitation trends on multi-decadal to centennial timescales (Sinha *et al.*, 2011a), if precipitation amount is directly inferred from stalagmite $\delta^{18}\text{O}$. Similarly, within the EASM region, differing $\delta^{18}\text{O}$ trends during the period 2 ka-present have also been reported from southern China (Cosford *et al.*, 2008; Hu *et al.*, 2008) and near to the northerly EASM limit (Tan *et al.*, 2009; Zhang *et al.*, 2008). Potentially, such spatial heterogeneity in precipitation patterns during this period as well as over the entire Holocene (Fig. 3.2) is evidence for complex ASM behaviour in response to relatively

moderate climate forcing (e.g., insolation), and highlights the need for a full understanding of local and regional controls on $\delta^{18}\text{O}$ variability across monsoonal Asia.

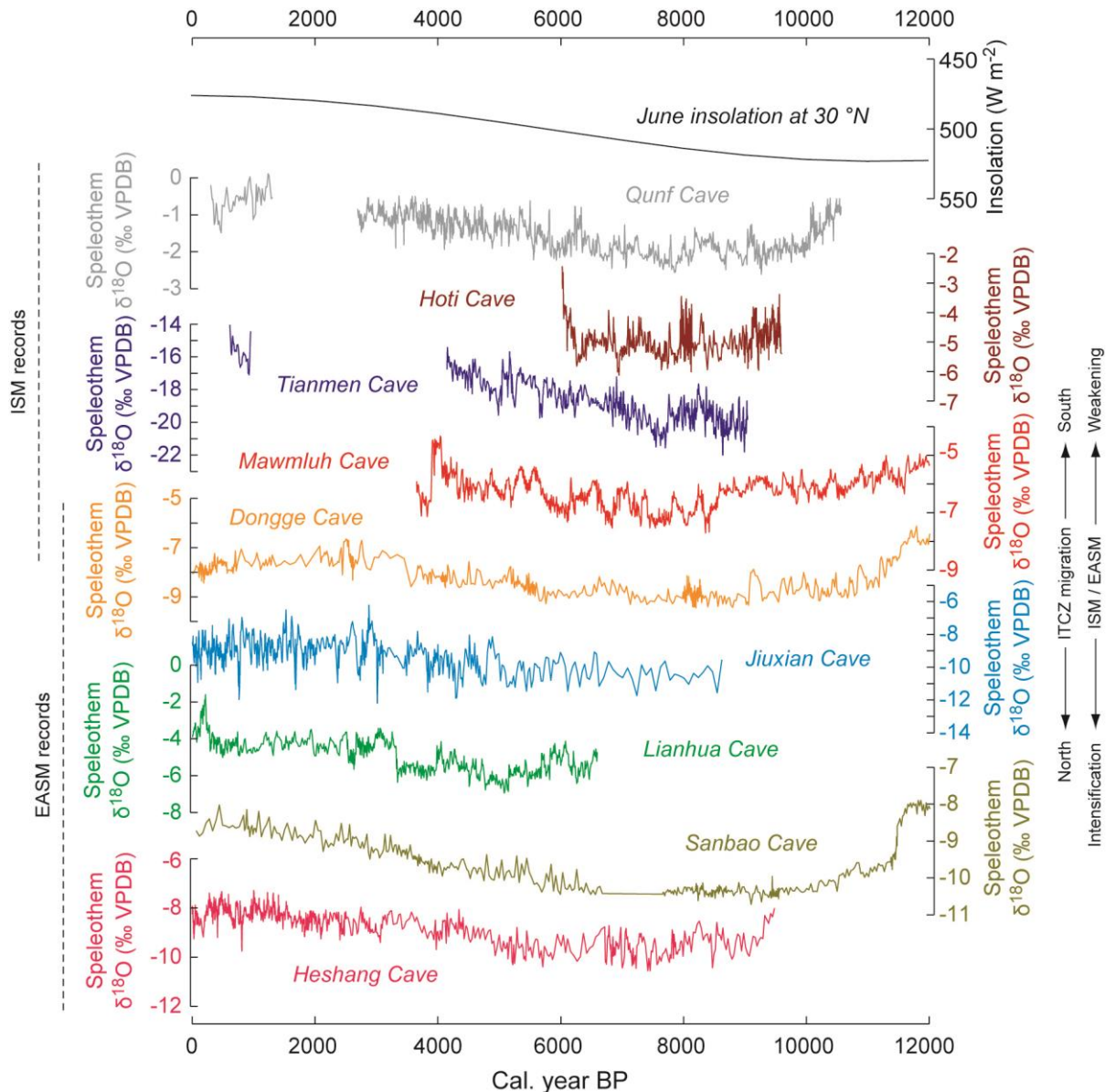


Figure 3.2. High-resolution Holocene ISM and EASM speleothem $\delta^{18}\text{O}$ records. A comparison of absolute-dated, high-resolution $\delta^{18}\text{O}$ records from the ISM and EASM domains and June insolation at 30°N (Berger and Loutre, 1991). Note that the insolation y-axis is inverted. Top-to-bottom, proxy records are arranged west-to-east. ISM records are from Qunf Cave (Fleitmann *et al.*, 2003), Hoti Cave (Neff *et al.*, 2001), Tianmen Cave (Cai *et al.*, 2012), and Mawmluh Cave (Berkelhammer *et al.*, 2012). EASM records are from Dongge Cave (Dykoski *et al.*, 2005), Jiuxian Cave (Cai *et al.*, 2010b), Lianhua Cave (Cosford *et al.*, 2008), Sanbao Cave (Dong *et al.*, 2010), and Heshang Cave (Hu *et al.*, 2008). Northward ITCZ migration and decreasing ISM or EASM precipitation during the Holocene was inferred from secular trends towards increasingly depleted speleothem $\delta^{18}\text{O}$ values, broadly tracking decreasing Northern Hemisphere summer insolation.

3.3. Selected cave sites within monsoonal China

Chapters 4, 5 and 6 refer to six particular cave sites (Fig. 3.3), which are located in southern China (Dongge Cave), eastern China (Hulu Cave) and proximal to the northerly EASM limit (Wanxiang, Dayu, Wuya and Huangye Caves). In this thesis, these areas are demonstrated to show differential isotopic sensitivity to EASM precipitation variability (Chapter 4), and precipitation isotope modelling (Chapter 5) and proxy-pseudoproxy comparisons (Chapter 6) focus on the northerly EASM limit region.

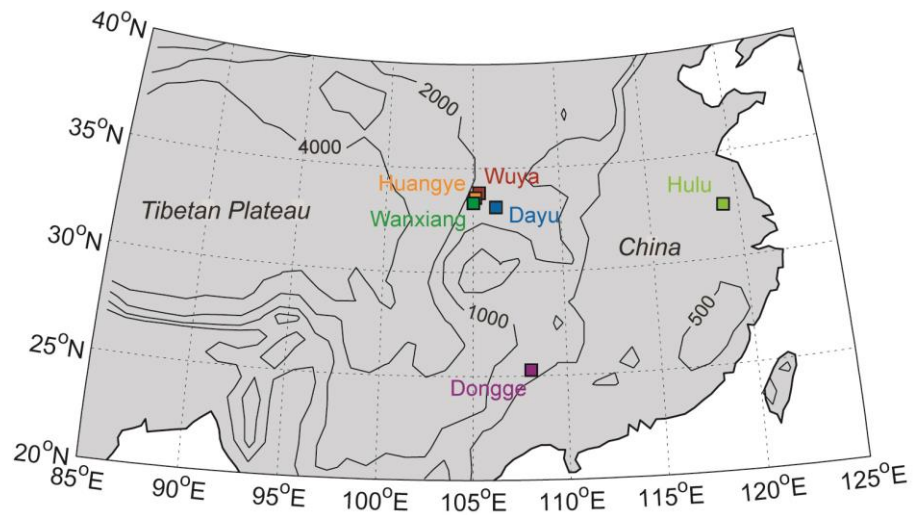


Figure 3.3. Map of selected cave sites within monsoonal China. Map showing the locations of Wanxiang, Wuya, Huangye, Dayu, Hulu, and Dongge Caves, each described in section 3.3.

3.3.1. Northern China

3.3.1.1. Wanxiang Cave

Zhang *et al.* (2008) published an 1810-year $\delta^{18}\text{O}$ record from the WX42B stalagmite retrieved from Wanxiang Cave (Gansu Province; 33° 19' N, 105° 0' E; 1200 m a.m.s.l.),

which has received attention. Qualitatively, secular WX42B trends are consistent with the Northern Hemisphere temperature reconstructions of Esper *et al.* (2002), Mann and Jones (2003) and Moberg *et al.* (2005), which both substantiates these reconstructions and provides a long-term context against which current, anthropogenic temperature trends in this region may be assessed. Moreover, the Zhang *et al.* (2008) record matches a North Atlantic Oscillation reconstruction from speleothem proxy data (Proctor *et al.*, 2000), solar irradiance proxy data, Alpine glacial retreat records, and patterns of dynastic societal change in China. The most recent WX42B data also mimic instrumental EASM (Jiang and Wang, 2005), ISM (Li and Zheng, 2003) and Global Monsoon indices (Wang and Ding, 2006), and are anti-correlated with precipitation amount and correlated with temperature, both recorded at a nearby meteorological station in Wudu (AD 1960-2000).

3.3.1.2. Wuya Cave

Tan *et al.* (2014) identified 52-year cyclic precipitation variability during the last 370 years from two stalagmites retrieved from Wuya Cave (Gansu Province; 33° 49' N, 105° 26' E, 1370 m a.m.s.l.), located in the south-western Loess Plateau region. Inferring rainfall amount from Wuya stalagmite $\delta^{18}\text{O}$, these records are evidence for co-variation of northern China and ISM precipitation, which exhibits 55- to 60-year periodic variability. Tan *et al.* (2014) argue this cyclic precipitation variability is driven by the Pacific Decadal Oscillation (PDO), which exhibits a 50 to 70-year periodicity (Mantua and Hare, 2002), and show that warm-phase, positive PDO index values correspond to drought periods in the semi-humid Loess Plateau region inferred from Wuya Cave $\delta^{18}\text{O}$. However, this is not found consistently through the records.

3.3.1.3. Huangye Cave

Three stalagmites retrieved from Huangye Cave (Gansu Province; 33° 35' N, 105° 7' E, 1650 m a.m.s.l.) by Tan *et al.* (2011) corroborate the WX42B record (Zhang *et al.*, 2008), a Yellow River Basin palaeo-precipitation record spanning the past ~300 years (Zheng *et al.*, 2005), and a documentary drought and flood occurrence record from Longxi, north-eastern Tibetan Plateau margin, since AD 960 (Tan *et al.*, 2008). These records indicate synchronous decadal- to centennial-scale late Holocene precipitation variability across semi-humid northern China. Together, the Huangye and Wanxiang Cave stalagmite $\delta^{18}\text{O}$ records also provide insights into the impact of climate change on Chinese societal changes.

3.3.1.4. Dayu Cave

Tan *et al.* (2009) published a 570-year long $\delta^{18}\text{O}$ record from the DY-1 stalagmite retrieved from Dayu Cave (Shaanxi Province, China; 33° 08' N; 106° 18' E; 870 m a.m.s.l.). Palaeo-precipitation was inferred directly from this record and spectral analysis provides evidence for the influence of decadal-scale solar variability (Gleissburg and Brückner cycles) and sub-decadal-scale ENSO activity on EASM precipitation. Although these inferences are in agreement with other records from monsoonal China, the secular variability is in antiphase with the Wanxiang record (Zhang *et al.*, 2008), particularly during the Little Ice Age, despite the relative proximity of the two cave sites (~120 km apart).

3.3.2. Southern and eastern China

3.3.2.1. Hulu Cave

Proxy datasets from Hulu Cave (Jiangsu Province; 32° 30' N, 119° 10' E, 90 m a.m.s.l.) speleothems underpin contemporary understanding of millennial-scale palaeomonsoon variability and its linkage with high-latitude North Atlantic climate. Wang *et al.* (2001) interpreted a composite $\delta^{18}\text{O}$ record from five Hulu stalagmites as EASM intensity, which matches Northern Hemisphere temperature records from Greenland ice cores (Greenland Ice Sheet Project 2 and Greenland Ice Core Project) remarkably between 75 and 11 ka, where warmer Greenland temperature corresponds to intensified EASM. These proxy datasets thus appear to link North Atlantic climate with the meridional transport of heat and moisture from the tropical Pacific Ocean. Extending the record of Wang *et al.* (2001) back to the penultimate glacial period with three additional stalagmite samples, Cheng *et al.* (2006) observed that Hulu $\delta^{18}\text{O}$ and SH temperature vary antipathetically, with weak EASM intensity during this period of elevated atmospheric greenhouse gas concentrations and Antarctic temperature. Rohling *et al.* (2009) reinterpreted these observations, arguing that the EASM is instead strengthened during boreal warming and austral cooling.

3.3.2.2. Dongge Cave

Numerous existing palaeomonsoon reconstructions are based on speleothems retrieved Dongge Cave (Guizhou Province; 25° 17' N, 108° 5' E; 680 m a.m.s.l.) because it is located centrally in south-eastern monsoonal China and should therefore be sensitive to precipitation changes resulting from EASM variability, and present-day meteorological data show that such changes are comparable to those at Hulu Cave (Yuan *et al.*, 2004). The

Dongge and Hulu stalagmite $\delta^{18}\text{O}$ records co-vary during the last interglacial, tracking Northern Hemisphere summer insolation, and provide evidence for EASM weakening in response to North Atlantic forcing (Duan *et al.*, 2014; Dykoski *et al.*, 2005; He *et al.*, 2005; Wang *et al.*, 2005; Yuan *et al.*, 2004) and Antarctic warming, including glacial terminations (Kelly *et al.*, 2006).

3.4. Recent re-examination of Chinese stalagmite records

Late Quaternary southeast Asian speleothem $\delta^{18}\text{O}$ variability tracks centennial- to orbital-scale change in Northern Hemisphere insolation (e.g., Cheng *et al.*, 2009a; Wang *et al.*, 2001; Wang *et al.*, 2005; Wang *et al.*, 2008; Yuan *et al.*, 2004; Zhang *et al.*, 2008), relatively rapid millennial-scale climate variability, such as Heinrich events or Dansgaard-Oeschger events, and also seasonal changes (e.g., Johnson *et al.*, 2006). Over these timescales, the conventional interpretation for precipitation (and therefore speleothem) $\delta^{18}\text{O}$ in sub-tropical regions is in terms of precipitation amount. However, a growing body of literature, particularly from modelling efforts, firmly suggests a need to re-evaluate interpretations of speleothem $\delta^{18}\text{O}$ records from this region.

Based on instrumental (GNIP) precipitation amount, precipitation $\delta^{18}\text{O}$ and temperature data, Johnson and Ingram (2004) and Dayem *et al.* (2010) demonstrate that the polarity and strength of $\delta^{18}\text{O}$ -amount and -temperature correlations potentially vary with EASM intensity, which itself varies on annual to glacial-interglacial timescales, and that the strength of these correlations varies spatially across monsoonal China. Dayem *et al.* (2010) also show that, if speleothem $\delta^{18}\text{O}$ reflects only precipitation amount, early Holocene rainfall would be ~1.5 times greater than present-day values, yet atmospheric GCMs and

the quantitative rainfall reconstruction of Hu *et al.* (2008) suggest the difference is only ~10 %. In China, the range exhibited by modern precipitation $\delta^{18}\text{O}$ is comparable to that of proxy records, and that the physical isotopic fractionation mechanisms affecting atmospheric moisture (e.g., evaporation, moisture transport, rainout processes) in the past should not be different from the present (see section 1.3). Consequently, several studies (Burns, 2011; Cheng *et al.*, 2006; Dayem *et al.*, 2010; Wang *et al.*, 2008) suggest speleothem $\delta^{18}\text{O}$ variability on orbital timescales at East Asian sites (as well as other mid-latitude regions) reflects hydroclimatic multiple processes, such changes in atmospheric circulation, moisture recycling and rainout (Lachniet, 2009).

Maher and Thompson (2012) highlight an important discrepancy between speleothem $\delta^{18}\text{O}$ records, which show declining ASM strength during the Holocene, and other proxies (e.g., loess magnetic susceptibility records), which show variable monsoon activity over the same period. If $\delta^{18}\text{O}$ responds to remote processes rather than local rainfall amount, this may be reconciled. For example, the EASM stalagmite records of Dykoski *et al.* (2005) and Dong *et al.* (2010) from Dongge Cave and Sanbao Cave, respectively, are correlated with the Qunf Cave ISM record (Fleitmann *et al.*, 2003) but matches other Holocene speleothem records from ISM and EASM sites less well (Fig. 3.2). Such spatially heterogeneous coeval precipitation signals (note also section 3.2) can be accounted for if $\delta^{18}\text{O}$ variability reflects not precipitation changes but precipitation moisture source and transport (Maher and Thompson, 2012). Clemens *et al.* (2010) compiled a composite stalagmite $\delta^{18}\text{O}$ record spanning the last 390 ka that exhibits a response to both summer and winter monsoon signals, consistent with modern precipitation seasonality (in amount and $\delta^{18}\text{O}$) and circulation regimes (Ding and Chan, 2005).

Pausata *et al.* (2011) used an isotope-enabled GCM to investigate the apparent teleconnection between EASM strength and North Atlantic climate (Wang *et al.*, 2005) by simulating the climate of the Last Glacial Maximum (LGM) and a Heinrich event, which causes a relatively long-lived cold climate state. According to these modelling experiments, a North Atlantic Heinrich event reduces northern Indian Ocean SST, weakening the ISM and exporting enriched- $\delta^{18}\text{O}$ moisture to China. This study provides evidence that Chinese speleothem $\delta^{18}\text{O}$ may respond preferentially to non-local Indian Ocean effects, particularly SST variability, over EASM intensity fluctuations. Other terrestrial proxies potentially provide more accurate records of local precipitation signals than speleothem $\delta^{18}\text{O}$ within China, but speleothems within the ISM region may preserve a precipitation signal more faithfully (Clemens *et al.*, 2010; Maher, 2008; Maher and Thompson, 2012; Pausata *et al.*, 2011; Porter and Zhou, 2006). Nevertheless, Chinese speleothems potentially offer opportunities to reconstruct large-scale climate features, such as ASM dynamics, circulation strength, and constraining EASM precipitation sensitivity to greenhouse gas forcing (Pausata *et al.*, 2011).

3.5. Concluding remarks

The ISM and EASM are driven by seasonal changes in atmospheric circulation, which cause warm, moisture-bearing air masses to migrate inland, engendering extreme boreal summer wet seasons (Fig. 3.1) in the world's most populous regions. In China, summer monsoonal precipitation accounts for ~80 % of the annual total and winter precipitation is influenced by the strength of the Westerlies.

Palaeo-precipitation reconstructions from well-dated proxy datasets, particularly speleothem $\delta^{18}\text{O}$, provide insights into past ASM intensity fluctuations and a long-term context against which to assess contemporary ASM trends, and constrain boundary conditions for monsoon prediction based on GCM experiments. Existing high-resolution late Holocene palaeomonsoon records from the ISM and EASM regions provide evidence of geographical heterogeneous precipitation variability. Potentially, such spatial heterogeneities reveal complex monsoon behaviour in response to moderate climate forcing, and a full understanding of the controls on precipitation $\delta^{18}\text{O}$ variability across monsoonal Asia is therefore required. Recent climate modelling, re-analysis of meteorological data, and comparisons of recent speleothem records with other terrestrial proxy datasets indicate precipitation (and therefore speleothem) $\delta^{18}\text{O}$ variability in this region reflects moisture source variability and atmospheric moisture transport history, and these processes are investigated in subsequent chapters in this thesis.

3.6. Thesis research objectives

To fully exploit high-resolution, absolute-dated speleothem $\delta^{18}\text{O}$ records such that *quantitative* palaeomonsoon reconstructions are tenable, numerical modelling studies are required to isolate net precipitation amount signals in precipitation and proxy $\delta^{18}\text{O}$. To this end, the primary research questions addressed in this Ph.D. are:

- i.* What is the present-day annual cycle of moisture sources precipitation across monsoonal China, and what is the importance of moisture source variability for EASM precipitation and how does it affect precipitation $\delta^{18}\text{O}$?

- ii.* As Wanxiang Cave is “sensitive to and integrates broad changes in the [EASM]” (Zhang *et al.*, 2008), how important are moisture transport processes for interpreting proxy $\delta^{18}\text{O}$ data at this site? To what synoptic processes do precipitation $\delta^{18}\text{O}$ at Wanxiang Cave, a monsoon-sensitive site located near to the northerly EASM margin, respond, and how do these processes impact the inference of palaeomonsoon variability?
- iii.* What is the potential for Lagrangian methodologies, combined with other model data, to construct pseudoproxy records, which may be used to validate stalagmite $\delta^{18}\text{O}$ record interpretations? What is the potential for forward modelling of stalagmite records for reconstructing climate *dynamics* through time?

Chapter 4

East Asian Summer Monsoon precipitation sources: atmospheric trajectories, moisture budgets, and implications for interpreting precipitation oxygen isotope data^{*}

^{*} The work presented in this chapter comprises a manuscript entitled ‘Seasonality of westerly moisture transport in the East Asian Summer Monsoon and its implications for interpreting precipitation $\delta^{18}\text{O}$ ’ currently under review at *Journal of Geophysical Research: Atmospheres*.

Chapter summary

Projections of future monsoon rainfall variability necessitate reliable palaeoclimate reconstructions from proxy data (IPCC, 2013). As discussed in Chapter 3, absolute-dated speleothem $\delta^{18}\text{O}$ records from Chinese cave sites have been interpreted as direct records of palaeomonsoon intensity fluctuations, but recent research (Clemens *et al.*, 2010; Dayem *et al.*, 2010; Maher, 2008; Pausata *et al.*, 2011) suggests that this proxy integrates multiple hydroclimatic processes. In this chapter, a Lagrangian precipitation source diagnostic (Sodemann *et al.*, 2008) is used to detect the sources of modern precipitation received across central and eastern China. The results demonstrate that modern monsoonal precipitation (May-August) in this region is primarily derived from the northern and western Indian Ocean, consistent with recent isotope-enabled global climate model results (Lewis *et al.*, 2010; Pausata *et al.*, 2011) and satellite-based bulk moisture observations (Liu and Tang, 2004), and a rapid transition between dry winter and intense EASM phases occurs. Conversely, Pacific Ocean moisture export peaks during winter and the moisture uptake area does not differ significantly between summer and winter, presenting a significant challenge to the traditional model of predominantly Pacific sources. These results accurately reproduce spatial summer and winter rainfall distributions across China. The seasonality of recycled precipitation over China sourced from evapotranspired moisture is also quantified and found to be an important contributor to overall west-to-east moisture transport during the monsoon season. These data also show that the strength of the Asian Monsoon precipitation signal in precipitation oxygen isotope ratios differs between northern, southern and eastern China. Not only will these results improve researchers' ability to isolate the precipitation amount or monsoon intensity signal in palaeomonsoon reconstructions, but also firmly indicate that future monsoonal precipitation variability will respond to changes in Indian Ocean, not Pacific Ocean, sea surface temperature and the associated evaporation budget.

4.1. Introduction and rationale

Reliable prediction of future EASM precipitation variability is a matter of considerable scientific and societal concern, which necessitates robust palaeoclimate reconstructions from high-resolution proxy archives to place present day monsoon trends in a longer-term context (IPCC, 2013). Reliable prediction of future EASM rainfall variability is a matter of considerable scientific and societal concern, and depends upon the availability of robust palaeoclimate reconstructions from high-resolution proxy archives (IPCC, 2013). In many palaeomonsoon reconstruction studies, precipitation amount (Wang *et al.*, 2001; Zhang *et al.*, 2008) or monsoon intensity (i.e., summer-winter precipitation ratio) is inferred directly from absolute-dated stalagmite $\delta^{18}\text{O}$ records (Cheng *et al.*, 2009) primarily because a negative correlation between precipitation $\delta^{18}\text{O}$ and precipitation amount or rate (the ‘amount effect’) is apparent in modern instrumental data from low-latitude regions (Rozanski *et al.*, 1992), albeit with considerable spatial variability (Johnson and Ingram, 2004). As discussed in Chapter 3, these records exhibit systematic co-variation and track NH summer insolation on millennial and glacial-interglacial timescales (Cheng *et al.*, 2009), and provide evidence monsoonal fluctuations in response to high-latitude climate change, particularly to North Atlantic temperature (Li *et al.*, 2014). However, within the EASM region, disparate $\delta^{18}\text{O}$ trends have been reported from southern China (e.g., Cosford *et al.*, 2008; Hu *et al.*, 2008) and near to the northerly EASM limit (e.g., Tan *et al.*, 2009; Zhang *et al.*, 2008). Potentially, such spatial heterogeneity in apparent precipitation patterns is evidence for complex monsoon behaviour in response to moderate climate forcing. Therefore, using proxy $\delta^{18}\text{O}$ data to explicate past EASM dynamics requires a full understanding of the controls on $\delta^{18}\text{O}$ variability across monsoonal Asia.

As discussed in Chapter 2, instrumental data (Dayem *et al.*, 2010; Johnson and Ingram, 2004) and recent climate modelling (Clemens *et al.*, 2010; Liu *et al.*, 2014; Pausata *et al.*, 2011) demonstrate that local and mesoscale processes cause spatio-temporal variability in $\delta^{18}\text{O}$ -climate correlations. Specifically, these studies present evidence for a strong response of precipitation $\delta^{18}\text{O}$ in monsoonal China to upstream depletion during atmospheric moisture transport from tropical oceanic sources, rather than to local rainfall variability (Liu *et al.*, 2014). This highlights a critical challenge for palaeomonsoon reconstructions: the need to isolate the precipitation signal from other processes which affect precipitation (and therefore stalagmite) $\delta^{18}\text{O}$. Moreover, reconciling mismatches between stalagmite $\delta^{18}\text{O}$ and other terrestrial palaeo-precipitation proxy records from China (e.g., magnetic susceptibility records from loess-palaeosol successions) requires an understanding of the complex hydroclimatic signals integrated by stalagmite $\delta^{18}\text{O}$ (Maher and Thompson, 2012). In this chapter, two critical yet poorly understood controls on Chinese precipitation $\delta^{18}\text{O}$ are quantified: (i) moisture source region variability and (ii) moisture transport, both of which are necessary for developing accurate palaeomonsoon reconstructions.

4.2. Methods

4.2.1. Lagrangian moisture source diagnostics

The moisture origin of continental precipitation over central and eastern China between November 1999 and March 2005 was investigated using a Lagrangian moisture source diagnostic of Sodemann *et al.* (2008), which detects specific humidity changes along three-dimensional, kinematic backward trajectories of atmospheric air parcels delivering precipitation to a target region (Fig. 4.1). The examined period is similar in length to

previous studies using this Lagrangian technique, which successfully provided quantitative constraints on the modern moisture source climatology in disparate climate regions, such as Greenland (Sodemann *et al.*, 2008), Belize (Kennett *et al.*, 2012), the European Alps (Sodemann and Zubler, 2010) and Antarctica (Sodemann and Stohl, 2009).

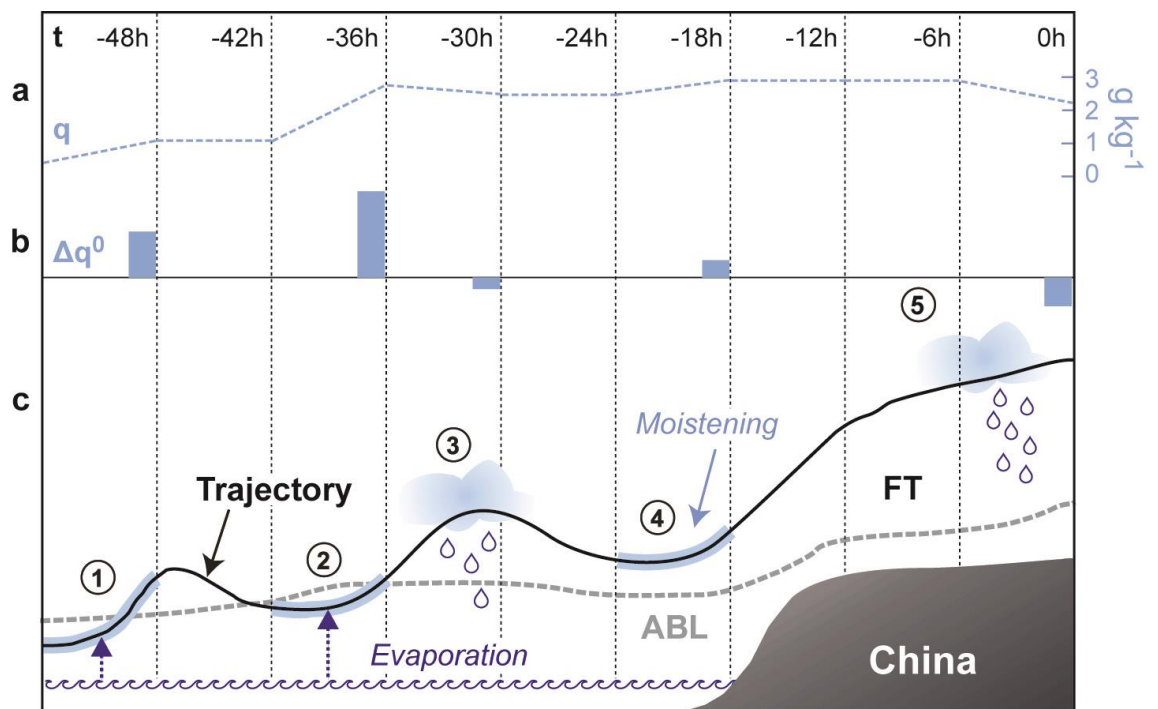


Figure 4.1. Lagrangian moisture source diagnostic technique. (a) Specific humidity (q) time series (dashed blue line) for a hypothetical air mass back trajectory (-48 hours; 6-hour timestep). (b) Schematic change in specific humidity (Δq^0) at particular points along trajectory (blue bars). (c) Schematic representation of air mass trajectory, the temporal sequence of moisture uptake and rainout, and its interaction with the atmospheric boundary layer. Air mass within ABL at points of Δq^0 increase (#1 and #2), indicating moisture uptake, and above ABL (#4), indicating convective moistening of air parcel. Rainout locations diagnosed by Δq^0 decreases (#3 and #5). After Sodemann *et al.* (2008).

Trajectories were computed with the widely-used particle dispersion model FLEXPART (version 8.2) (Stohl *et al.*, 2005) and in the simulation used for this study (Stohl, 2006), the global atmosphere was divided homogeneously into 1.4 million particles, representing

infinitesimal air parcels, each traced for 20 days using three-dimensional wind field data from data from the European Centre for Medium-Range Weather Forecasting operational analyses, available every six hours at a $1^\circ \times 1^\circ$ horizontal resolution and at 60 vertical levels. Only trajectories delivering precipitation to a target area defined over China, the minimum (maximum) longitude and latitude of which are 95 (121) $^\circ\text{E}$ and 20 (40) $^\circ\text{N}$, respectively (Fig. 4.2), were considered. This target area is based on the known spatial EASM precipitation distribution and encompasses the area influenced by the Meiyu Front, a stationary sub-tropical frontal system, which demarcates the mean northerly extent of the EASM (Fig. 4.2). Additionally, areas >2 km a.m.s.l., such as the eastern Tibetan Plateau, were excluded to properly isolate lowland, monsoonal eastern China. Based on air parcel latitude, longitude, altitude, pressure and specific humidity output at each 6-hour time step, the temporal sequence of evaporation and precipitation was determined along the trajectory of each air mass precipitating within the target area using a relatively conservative threshold specific humidity criterion of $0.2 \text{ g kg}^{-1} \text{ 6h}^{-1}$ to define moisture uptake and rainout. A first-order model sensitivity estimate to this parameter was also performed using $0.1 \text{ g kg}^{-1} \text{ 6h}^{-1}$, but this did not significantly alter the distribution of diagnosed moisture uptake areas.

There are important advantages to this approach. Firstly, precipitation source regions are diagnosed quantitatively because the degree of local evaporation contribution to the total moisture in the air parcels is calculated. Previous studies have relied on trajectory end points (Helsen *et al.*, 2007) or the superposition of evaporation minus precipitation along trajectories (James *et al.*, 2004). Secondly, direct evaporative moisture uptake is only diagnosed for a given air parcel if it is below the atmospheric boundary layer (ABL) at a point of specific humidity increase. Thereby, this method distinguishes evaporative

moisture uptake originating within the ABL from moistening of air parcels in the free troposphere (FT) due to convective processes.

The total amount of precipitation to which the Lagrangian diagnostic attributes moisture sources is termed *accounted precipitation*. Considering longer trajectories (~20 days) increases the fraction of precipitation for which source regions may be attributed, but in general, increasing trajectory length also increases the uncertainty associated with their three-dimensional positions in space. However, previous research (Sodemann and Stohl, 2009) employing the Sodemann *et al.* (2008) diagnostic has shown that this uncertainty is minimised by considering a large number of air parcels.

4.2.1.1. Setup of the Lagrangian moisture diagnostic

Table 4.1 summarises the input and set-up parameters for running the Lagrangian moisture source diagnostic. These parameters define the start date and length of the model run, the target domain, specific humidity (Δq^0) thresholds for uptake / precipitation, model constants (e.g., timeStep, partMass) and atmospheric boundary layer envelope (blhScale). The original input (.txt) files conform to the format of Table 4.1.

4.2.1.2. Source region sectorisation

The Lagrangian diagnostic employed in this study allows quantitative moisture uptake to be identified along trajectories, which has successfully provided constraints on modern moisture source climatology in disparate climate regions, such as Belize (Kennett *et al.*, 2012), Greenland (Sodemann *et al.*, 2008), the European Alps (Sodemann and Zubler,

2010), and Antarctica (Sodemann and Stohl, 2009). These previous studies have demonstrated that geographically sub-dividing the area over which FT moisture uptakes were detected provides information on moisture source region seasonality and land-ocean moisture contribution differences. Critically, the importance of particular source regions for moisture delivered to and precipitation $\delta^{18}\text{O}$ characteristic of proxy record sites may be quantified.

Continental Asia, the Philippine Sea, northern and low-latitude Indian Ocean and surrounding terrestrial and oceanic areas were divided into 11 discrete sectors (see Appendix 2) and the moisture contribution from each to precipitation within the regional and site-specific target regions was determined. Data for individual sectors were further segregated into land and oceanic areas and the sectorised data were then area-weighted and combined to form meaningful source regions (e.g., the South China Sea) for these geographic regions of interest. ABL and FT moisture uptake data for individual sectors were further segregated into their constituent land and oceanic areas and used to compute the mean and total area-weighted contributions from various oceanic and terrestrial source regions (Fig. 4.2) to precipitation in monsoonal China. These data establish the seasonality of eastward versus westward moisture advection and characterising the importance of particular moisture source regions for proxy record sites provides a way to quantify the source effect in precipitation $\delta^{18}\text{O}$. Therefore, this information can be used to better isolate the precipitation amount signal in $\delta^{18}\text{O}$ -based palaeomonsoon reconstructions. These raw sectorised data are provided in Appendix 3.

Variable name	Value(s)	Notes
startDate	20050401	01/04/2005
endDate	19991001	01/10/1999
minLon	80; 95; 104; 118.1; 107; 105.3	degrees East
maxLon	125; 121; 106; 120.1; 109; 107.3	degrees East
minLat	20; 20; 32; 31.5; 24.3; 32.1	degrees North
maxLat	40; 40; 34; 33.5; 26.3; 34.1	degrees North
grid_minLon	77; 101; 115.1; 104; 102.3	+3 degrees East
grid_maxLon	128; 109; 123.1; 112; 110.3	+3 degrees East
grid_minLat	17; 29; 28.5; 21.3; 29.1	+3 degrees North
grid_maxLat	43; 37; 36.5; 29.3; 37.1	+3 degrees North
grid_dx	0.5	Grid interval (°)
grid_dy	0.5	Grid interval (°)
grid_radius	60	Gridding radius for air parcels in arrival domain
timeStep	6	6 hours
partMass	3.64054E+12	Particle mass
blhScale	1.5	Atmospheric boundary layer envelope
rhMin	80	Relative humidity minimum (%)
rhMax	110	Relative humidity maximum (%)
uptakeThreshold	0.2	Specific humidity threshold ($\text{g kg}^{-1} \text{6h}^{-1}$)
precipTreshold	-0.2	Specific humidity threshold ($\text{g kg}^{-1} \text{6h}^{-1}$)
arrPrecipMin	-0.2	Precipitation estimate minimum ($\text{g kg}^{-1} \text{6h}^{-1}$)
arrPrecipMax	-40	Precipitation estimate maximum ($\text{g kg}^{-1} \text{6h}^{-1}$)
arrOroMin	10	Elevation minimum (m)
arrOroMax	9000; 2000	Elevation maximum (m)
arrAltMin	0	Surface (m)
arrAltMax	50000	Altitude limit (m)
anaVapour	0	Diagnose moisture origin for estimated precipitation

Table 4.1. Input parameters for Lagrangian diagnostics. Summary table of input parameters for the Lagrangian moisture source diagnostic of Sodemann *et al.* (2008), with coordinates given (minLon; minLat) for the extended target domain, Wanxiang Cave, Hulu Cave, Dongge Cave and Dayu Cave, respectively. All other parameters, including the specific humidity threshold (Δq^0) for detecting evaporation and precipitation, remained unchanged for individual cave site diagnostics. The gridding radius is described by +3 degrees in each horizontal direction. Orographic thresholds refer to European Centre for Medium-Range Weather Forecasting ERA-Interim reanalysis model topography.

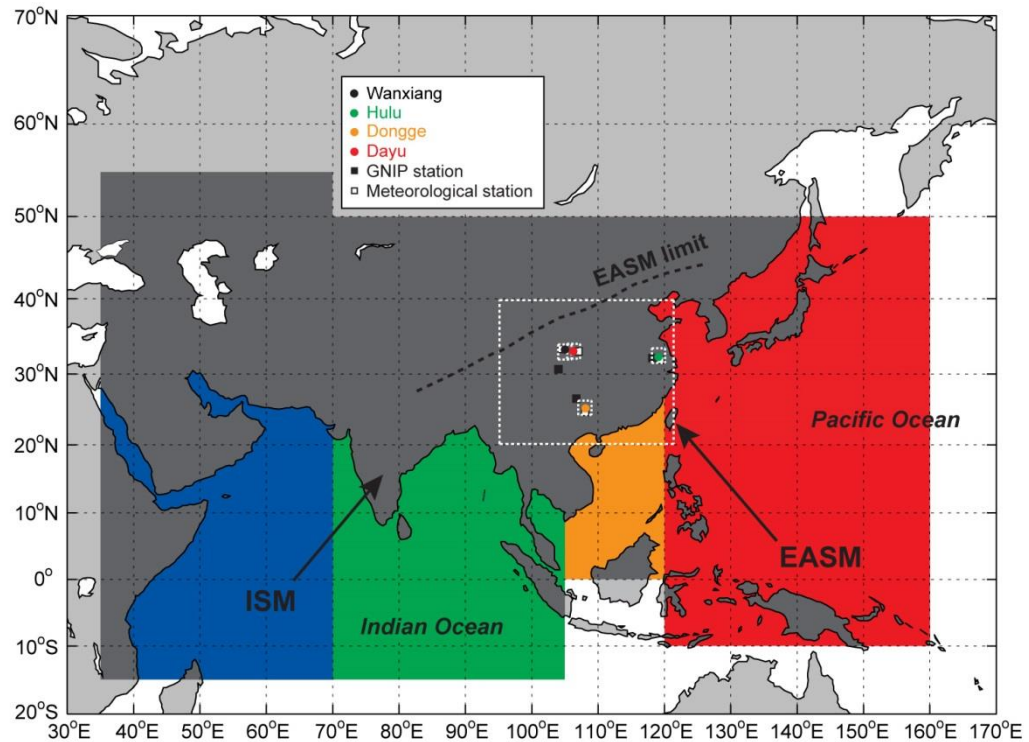


Figure 4.2. Precipitation target domains and source regions. Target domains for precipitation source diagnostic study (white dotted lines) and moisture source sectors defined over the northwest Indian Ocean (blue), northeast Indian Ocean (green), South China Sea (orange), Philippine Sea (red), and terrestrial regions (dark grey). Sector colour-coding corresponds to Fig. 4.10. Sectors were first demarcated by meridians and parallels; oceanic and land areas within each were subsequently separated, giving the source sectors shown (see Appendices 1 and 2). Black arrows indicate the traditionally-assumed bulk transport direction of moisture masses in the tropical ISM and extra-tropical EASM sub-systems based on mean boreal summer atmospheric pressure patterns (see Fig. 3.1). The GNIP (black markers) and meteorological stations (white markers) from which data were obtained for multivariate correlation analyses and the locations of each cave site discussed in the text are shown (colour markers). Cave site marker colours correspond to those on Fig. 4.11. For clarity, remaining land areas are shaded pale grey.

4.2.2. Comparison with precipitation isotopes

To quantify the source effect on precipitation $\delta^{18}\text{O}$ at key cave sites in China, the Lagrangian diagnostic was run with additional $2^\circ \times 2^\circ$ target domains centred on four selected cave sites in key locations in monsoonal, continental China (see section 3.3; Fig. 4.2; Table 4.2): Hulu Cave, Dongge Cave, Wanxiang Cave and Dayu Cave. From the

output for each target domain, mean monthly source longitude and latitude were composited, as per the regional diagnostics. These data and precipitation amount data, obtained from nearby meteorological stations, were used as predictor variables in multivariate correlations with instrumental precipitation $\delta^{18}\text{O}$ data, obtained from GNIP (IAEA/WMO, 2014). Long-term instrumental precipitation and precipitation $\delta^{18}\text{O}$ records are not available from the selected cave sites themselves. To reduce the uncertainty associated with this, for each cave site, GNIP stations (Nanjing, Guiyang and Chengdu, respectively) and meteorological stations (Hulu, Hechi, Wudu and Hanzhong, respectively) that are both within or near to the respective target domains and within the area of significant spatial precipitation correlation found by Dayem *et al.* (2010) were selected.

Target domain	Run name	Longitude (°E)		Latitude (°N)	
		Min.	Max.	Min.	Max.
China (extended)	'China_analysis'	80.0	125.0	20.0	40.0
China (EASM domain)	'EASM_analysis'	95.0	121.0	20.0	40.0
Wanxiang Cave	'Wanxiang'	104.0	106.0	32.0	34.0
Hulu Cave	'Hulu'	118.1	120.1	31.5	33.5
Dongge Cave	'Dongge'	107.0	109.0	24.3	26.3
Dayu Cave	'Dayu'	105.3	107.3	32.1	34.1

Table 4.2. Geographic definition of target domains. Longitude and latitude defined in the input files for Lagrangian moisture source diagnostics.

4.3. Results and discussion

4.3.1. Sub-continental scale spatial moisture uptake patterns

4.3.1.1. Moisture uptake within the atmospheric boundary layer

The seasonal cycle of moisture sources for precipitation in monsoonal China shows a marked transition between a dry winter period, with easterly moisture contributions, and an intense summer monsoon phase, with extensive contributions from the northern Indian Ocean and moisture recycling over continental areas (Fig. 4.3). During December-February, evaporative contributions of $\leq 15 \text{ mm month}^{-1}$ occur principally over the western Philippine Sea and relatively low evapotranspiration ($\leq 35 \text{ mm month}^{-1}$) is detected over southern China. The geographic extent of moisture uptake is relatively fixed over central China during these winter months, consistent with global oceanic evaporation simulations (Gimeno *et al.*, 2010; van der Ent and Savenije, 2013). During March-April, prior to ISM onset, the moisture uptake region expands westward towards India, with ongoing uptake over the westernmost Philippine Sea. Greater evapotranspiration is detected over Bangladesh and northeast India, with additional contributions from the eastern Tibetan Plateau. Increased evaporation during ISM onset (May) occurs over the Bay of Bengal, consistent with recent back trajectory results over comparably small target domains (Breitenbach *et al.*, 2010; Chen *et al.*, 2013; Liu *et al.*, 2011), and the Arabian Sea, synchronous with the seasonal timing of increased latent heat supply to the Asian Summer Monsoon (ASM) from the equatorial and southern Indian Ocean and the associated lower troposphere moisture budget distributions (Ding *et al.*, 2004; Martius *et al.*, 2013). A major limb of Indian Ocean evaporation extends westward and southward during EASM onset (June), consistent with NCEP/NCAR reanalysis 1000 hPa mean wind vectors (Clemens *et al.*, 2010). This limb develops during peak EASM (July-August) and recedes during the

cessation of EASM precipitation over China (September). However, evaporation over the Philippine and South China Seas during the EASM is not markedly different from that during winter. Evapotranspired moisture is primarily sourced from southern and eastern China and the Indian sub-continent during summer months. During the ASM, evapotranspiration contributes the greatest mean monthly uptake values ($\leq 70 \text{ mm month}^{-1}$) and recycled moisture does not fully recede to its 'winter state' until November.

4.3.1.2. Free troposphere moisture contributions

The Lagrangian diagnostic used (Sodemann *et al.*, 2008) allows evaporative moisture uptake within the ABL to be distinguished from convective moistening of air parcels in the FT. Seasonally composited FT moisture contributions do not represent moisture sources directly because such moistening occurs above the ABL. Rather, these contributions represent convective moistening of air parcels, with shallow- and deep-convective detrainment of upper ABL moisture into the FT. The geographic distribution of the FT moisture contribution to precipitation in monsoonal China is similar to that of ABL uptake, but exhibits a broader spatial pattern (Fig. 4.4), particularly over the northern Indian Ocean, where contributions are $\leq 40 \text{ mm month}^{-1}$. The limb of moisture uptake over the northwest Pacific Ocean is present throughout the AM season, but represents a lower contribution ($\leq 10 \text{ mm month}^{-1}$) that is likely associated with the mean boreal summer ITCZ position. Zonal moisture advection from the Indian Ocean increases rapidly at the point of ASM onset, with maxima in June-July. Pacific Ocean contribution exhibits comparatively limited seasonality (see also section 4.3.4), with two anomalously high values of Pacific moisture export in December 1999 and December 2001. Interestingly, these values correspond with increased monthly recycling ratios, suggesting that rainout

associated with this anomalous winter advection is recycled rapidly. By combining ABL and FT moisture contributions, moisture sources were attributed to 93.5 % mean annual precipitation (Table 4.3) during 1999-2005.

Month	ABL fraction (%)	FT fraction (%)	Accounted fraction (%)
Jan	46.03	47.06	93.09
Feb	48.62	43.46	92.08
Mar	50.99	40.95	91.93
Apr	52.22	39.79	92.01
May	50.74	43.53	94.27
Jun	49.03	45.52	94.55
Jul	47.67	46.53	94.20
Aug	47.26	46.85	94.12
Sep	47.85	46.60	94.45
Oct	46.05	47.62	93.67
Nov	45.97	47.76	93.73
Dec	45.34	48.68	94.01
DJF mean	46.66	46.40	93.06
JJA mean	47.99	46.30	94.29
Annual mean	48.15	45.36	93.51

Table 4.3. ABL and FT moisture contributions. Mean monthly fraction of ABL and FT moisture contributions, and the mean December-February, June-August and annual values. The accounted fraction represents the total fraction of mean monthly precipitation to which the Lagrangian diagnostic attributed moisture sources.

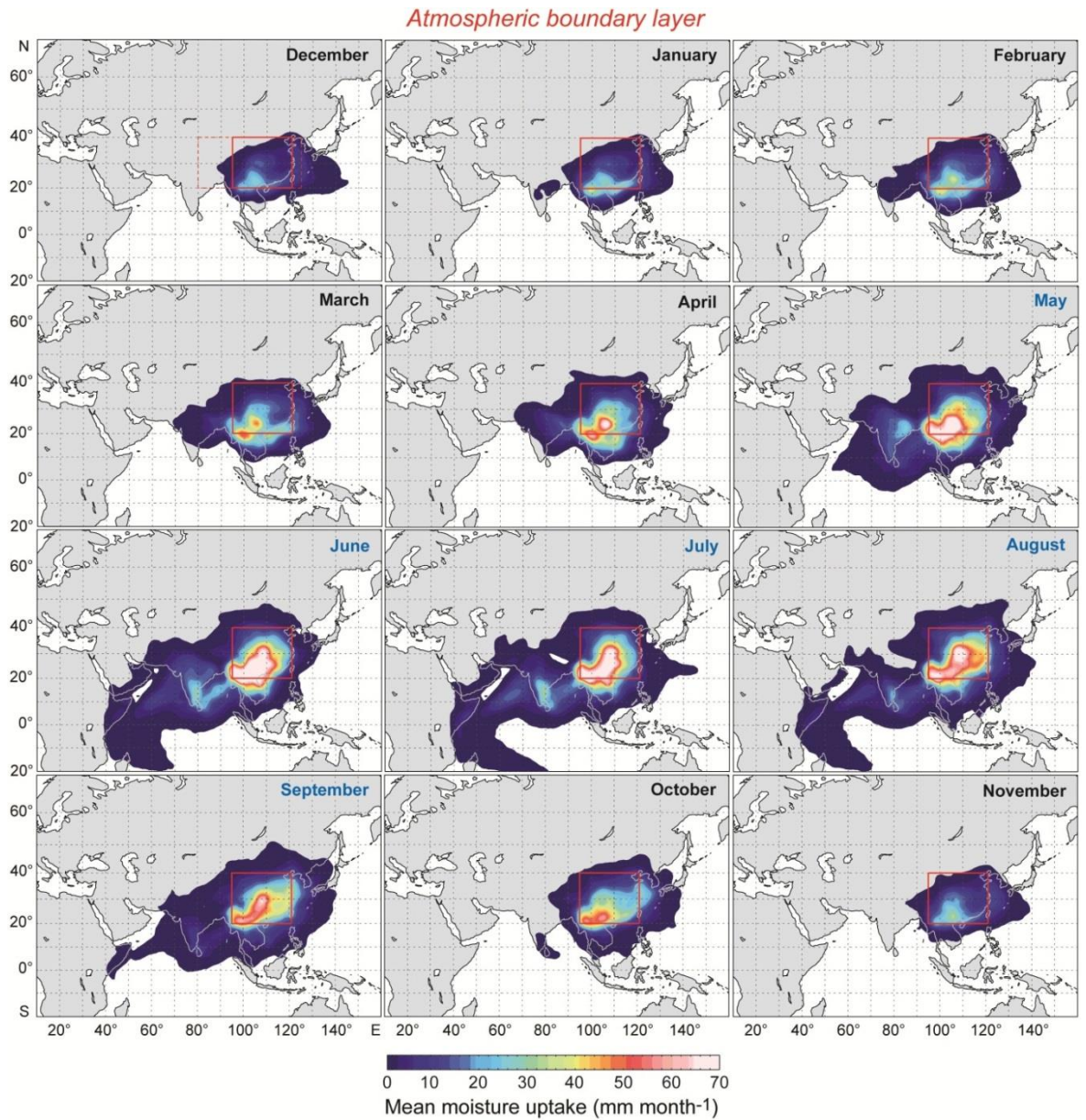


Figure 4.3. Monthly boundary layer moisture sources for precipitation over China. Mean monthly evaporative moisture uptake (within the ABL) contributing to precipitation in central and eastern China for the period November 1999 – March 2005, showing mean precipitation within the target domain (red box) projected back over its respective source locations. The EASM season is June-September; ASM months are in blue text. The area covered in Fig. 4.5 – 3.8 is outlined in the December panel (red dashed box). Note that areas >2 km elevation were excluded from the Lagrangian model runs and numerical analyses.

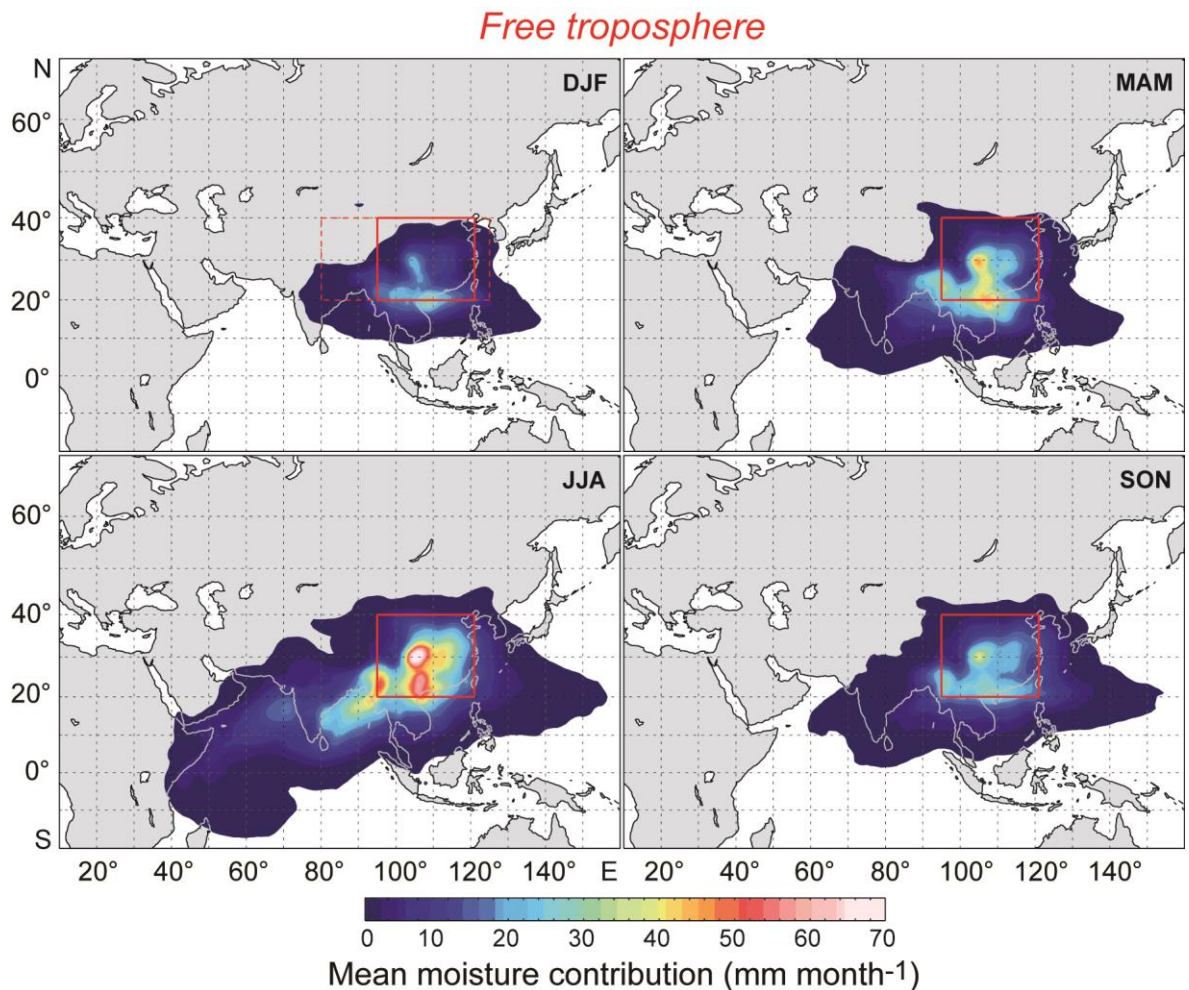


Figure 4.4. Seasonal mean free troposphere moisture contribution. Mean seasonal free troposphere (above the ABL) moisture uptake contributing to precipitation within the extended target domain (red box) from Lagrangian diagnostics for AD 1999-2005. The region covered in Fig. 4.5 – 3.8 is outlined in the DJF panel (red dashed box). Change in FT moisture patterns was found to occur on a seasonal timescale; for clarity, mean seasonal rather than mean monthly data are therefore plotted here.

4.3.2. Lagrangian forward projections of moisture source location

To characterise moisture source spatial distribution over monsoonal China, Lagrangian forward projections of seasonal mean source longitude (Fig. 4.5 and Fig. 4.6) and latitude (Fig. 4.7) were mapped. Fig. 4.5 summarises the seasonal progression of moisture source longitude diagnosed for precipitation over central and eastern China, Fig. 4.6 shows mean

April-August maps composited from the same dataset to highlight the winter-to-summer transition. During December-February, source longitude exhibits a southeast-northwest gradient, with a degree of topographic influence apparent along the eastern margin of the Tibetan Plateau and strong influence of the Westerlies in northwest China. Data for winter months show little variation; a northeast-southwest gradient in source longitude persists during winter and early spring months (Fig. 4.5). During April, this gradient remains apparent but is less well defined, representing an incipient shift in moisture source distribution across monsoonal China (Fig. 4.6). During March-May, this axis shifts to a meridional orientation, which is most marked between April and May (Fig. 4.6), representing ISM pre-onset. During May-August, monsoonal precipitation over eastern and southern China is sourced from relatively westerly locations ($90 - 105^{\circ}\text{E}$), derived from the significant Indian Ocean evaporation detected (Fig. 4.3). The winter southeast-northwest gradient is resumed from October. The onset of the ISM is responsible for precipitation in southeast China which is derived from a relatively westerly mean longitudinal range of $95 - 105^{\circ}\text{E}$. This west-to-east advection into southeast China intensifies during the onset of the EASM in June and persists through July. During August, this zonal ingress of moisture recedes westward and data for September-November exhibit the 'winter mode', suggesting that winter precipitation, which is modulated by the strength of the Westerlies, is relatively fixed over central and eastern China (Fig. 4.5).

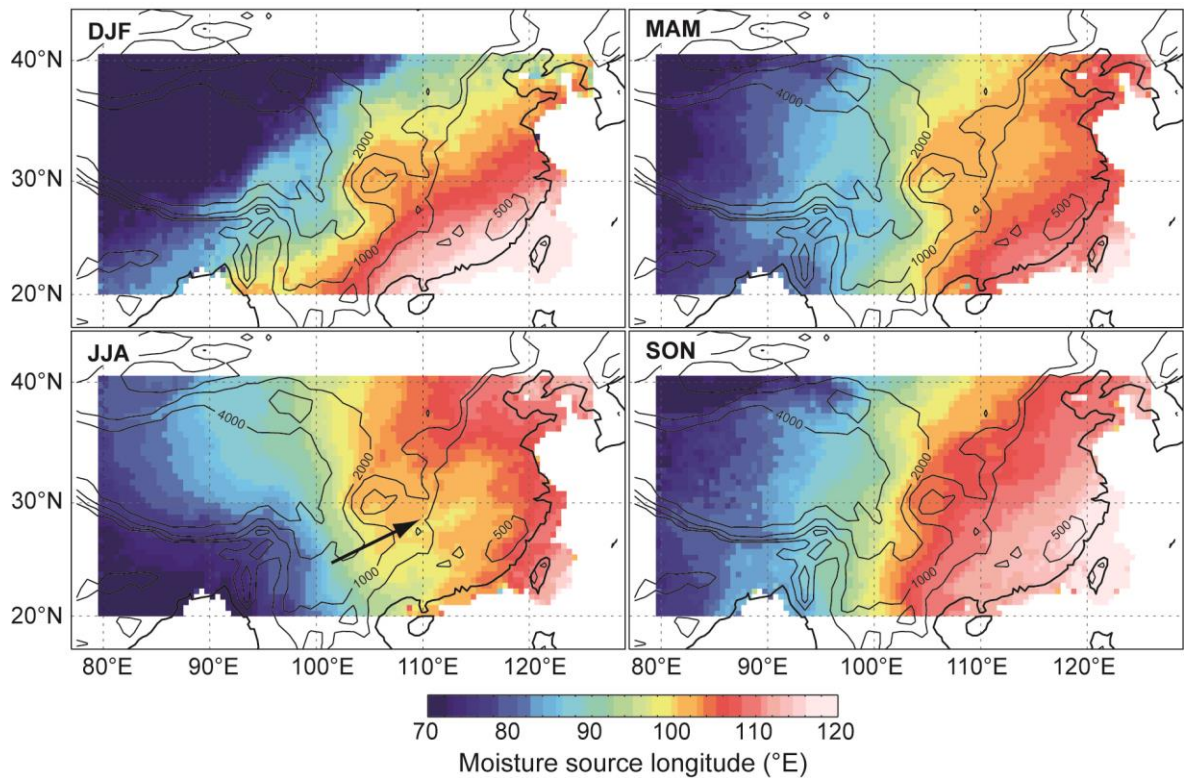


Figure 4.5. Seasonal moisture source longitude Lagrangian forward projections. Mean seasonal source longitude of moisture advected to monsoonal China, averaged over December-February (DJF), March-May (MAM), June-August (JJA), and September-November (SON). Topographic contours (solid lines) are in metres a.m.s.l. Summer precipitation within the target domain is sourced from westerly longitudes (black arrow in the JJA panel) and this zonal moisture advection into eastern China is most intense during June (see Fig. 4.6). Note that although areas $> 2\text{km}$ elevation were excluded from the Lagrangian model runs and numerical analyses consistently, these forward projections show a larger dataset which includes these areas for clarity.

Seasonal Lagrangian forward projections of moisture source latitude (Fig. 4.7) exhibit a zonal gradient throughout the year, with precipitation sourced between 20 and 35°N during winter (December-February) and expanding to 10 and 40°N during peak EASM. Within the target domain, particularly in southern China, summer monsoonal precipitation is derived from a greater amount of moisture from relatively southerly latitudes than winter precipitation, consistent with ABL uptake maps (Fig. 4.3). Moreover, summer moisture

uptake occurs up to $\sim 40^\circ\text{N}$, which represents increased evapotranspiration feeding recycled moisture to EASM precipitation.

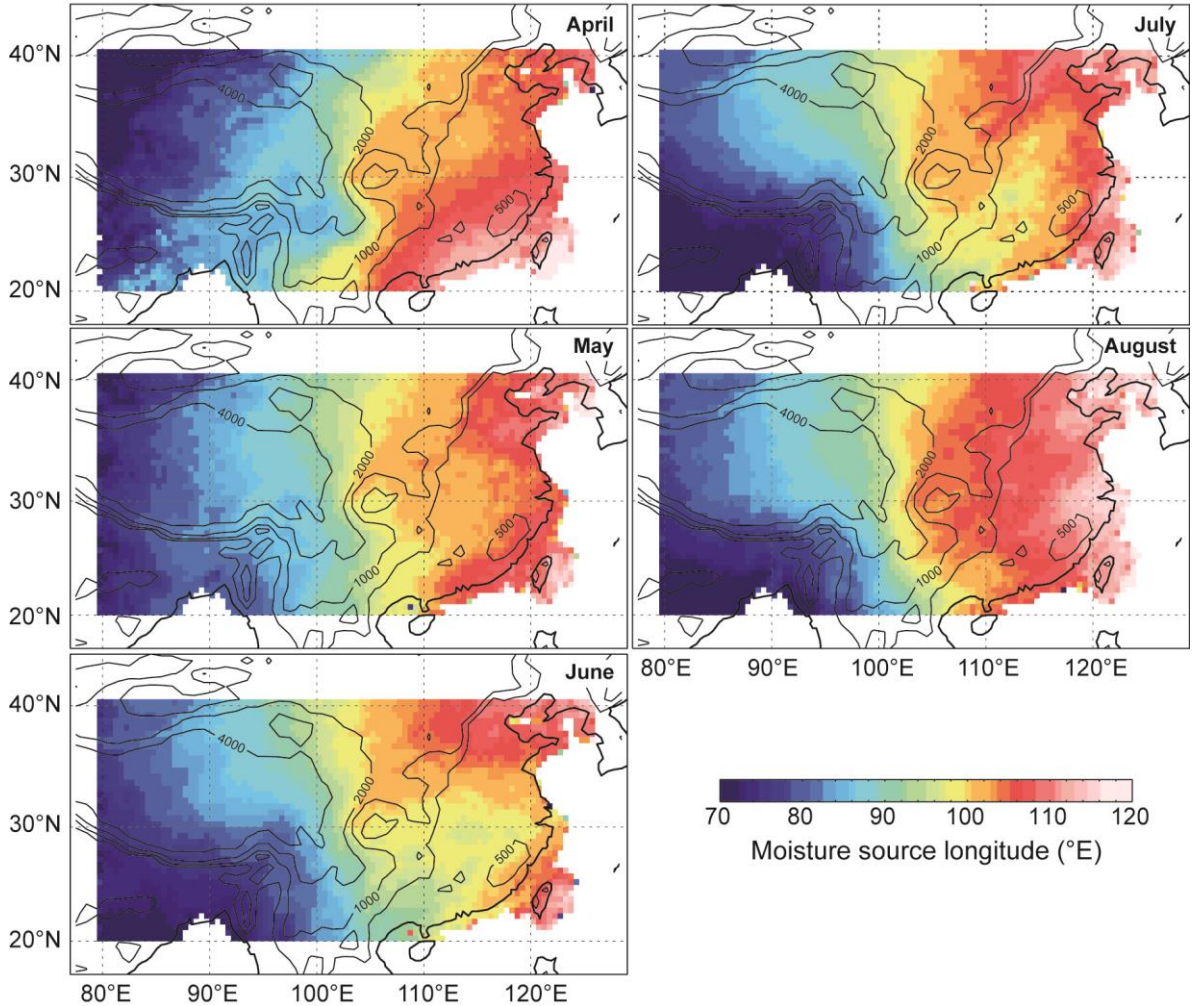


Figure 4.6. May-August moisture source longitude Lagrangian forward projections. Composited mean monthly source longitude of moisture masses responsible for precipitation within monsoonal China forward-projected onto China for April-August. Data for pre-ISM onset show incipient zonal moisture advection into southern and eastern China from relatively westerly longitudes, which intensifies during June (EASM onset) and July. Data for August show an incipient return to a winter state with easterly transport. Topographic contours (solid lines) are in metres a.m.s.l.

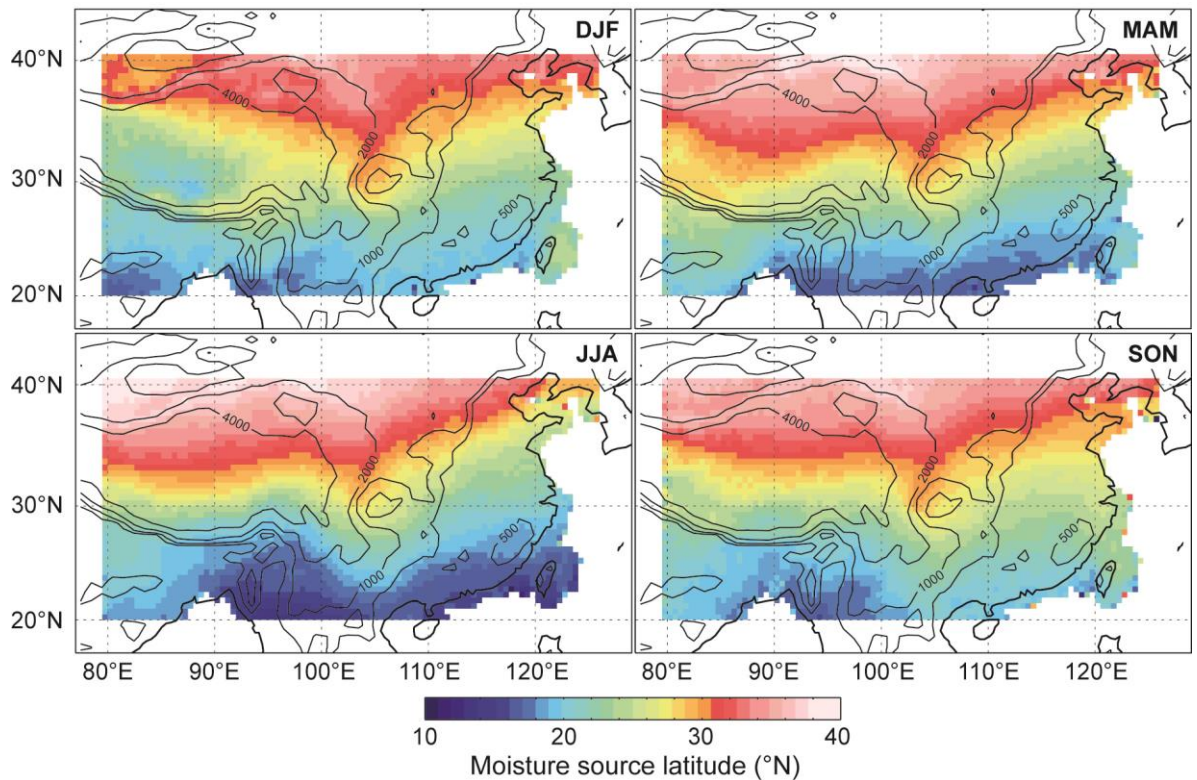


Figure 4.7. Seasonal moisture source latitude Lagrangian forward projections. Composited mean seasonal source latitude of moisture masses responsible for precipitation within monsoonal China forward-projected onto China. These source latitude data are averaged over December-February (DJF), March-May (MAM), June-August (JJA), and September-November (SON). Topographic contours (solid lines) are in metres a.m.s.l.

The identified moisture source patterns quantify the seasonal progression of evaporative moisture contribution to precipitation in central and eastern China. The transport of rain-bearing moisture from the north-western and low-latitude Pacific Ocean during the EASM season is minimal and largely indistinguishable from that during winter (*cf* Ran and Feng, 2013) and no significant contribution to EASM rainfall from the Westerlies was detected (*cf* Liu *et al.*, 2014). The spatial extent of Pacific Ocean moisture contributions is comparatively limited and seasonally invariant (Fig. 4.3); free tropospheric convective moistening is also more restricted than that over Indian Ocean regions (Fig. 4.4). These results quantify a significant Indian Ocean contribution across the EASM region,

predominately originating from the northern Indian Ocean, and demonstrate that zonal westerly advection reaches China's eastern continental margin and the wettest southern region during peak EASM (Fig. 4.5, Fig. 4.6 and Fig. 4.7). They also provide a plausible mechanism for observed precipitation multiproxy co-variability across east Asia (Rehfeld *et al.*, 2013).

4.3.3. Comparison of Lagrangian and instrumental precipitation

Fig. 4.8 illustrates seasonally composited precipitation estimated by the Lagrangian diagnostic compared with the Global Precipitation Climatology Centre version 6 (GPCC6) dataset (Schneider *et al.*, 2011), comprised of rain gauge and historical data averaged between 1981-2010. Precipitation amount within the target area is calculated from any specific humidity decrease during the final 6h timestep, following Sodemann *et al.* (2008). Lagrangian precipitation estimates are generally biased high, which is a commonly observed characteristic due to neglecting the influence of cloud microphysics in generating model-derived precipitation (Sodemann and Zubler, 2010). However, in this study the Lagrangian estimate compares favourably with the GPCC6 data. Mean seasonal Lagrangian precipitation captures the seasonal spatio-temporal distribution of rainfall across China well. Mean data for December-February show relatively high precipitation in southeast China and immediately northeast of the Himalaya. A similar spatial rainfall distribution is characteristic of March-May, although the Lagrangian data do not capture the relatively low levels of precipitation in east India and the Indochina peninsula during spring. Data for June-August exhibit a well-defined gradient orientated WSW-ENE, sub-parallel to the Meiyu Front (Sampe and Xie, 2010), and reproduce high precipitation in northeast India. Precipitation distribution and magnitude during September-November is

also reproduced well. The Lagrangian spatio-temporal precipitation distribution is also in agreement with the globally gridded interpolation of precipitation monitoring observations of Legates and Willmott (1990).

In addition to comparing Lagrangian precipitation estimates to GPCC6 data (Fig. 4.8), individual correlations between mean monthly Lagrangian precipitation for each cave site run target domain and instrumental data from nearby meteorological stations were performed. At each elected cave site, mean monthly Lagrangian precipitation is significantly and positively correlated with the available instrumental data, but the instrumental data are underestimated by a factor of ~ 4 (Fig. 4.9). It is important to note that instrumental precipitation data are not taken from the exact cave site locations, rather only the nearest meteorological stations. Distances separating these stations from Wanxiang, Hulu, Dongge, and Dayu Caves are 15, 31, 65, and 68 km, respectively. The known magnitude of local precipitation variability across such spatial scales can be significant in mountainous regions (Buytaert *et al.*, 2006; Tokay *et al.*, 2013) and is sufficient to explain the difference between modelled and instrumental data. Note that Wanxiang Cave is closest to its respective meteorological station and exhibits the closest to a 1:1 linear relationship. In contrast, Dayu Cave is furthest from its respective meteorological station and exhibits the least favourable comparison. While this reliance on *nearby* station data is an important source of uncertainty in site-based analyses, the confidence in the Lagrangian diagnostic established by capturing the seasonal precipitation distribution across monsoonal China accurately (Fig. 4.8), and by previous research, nonetheless remains.

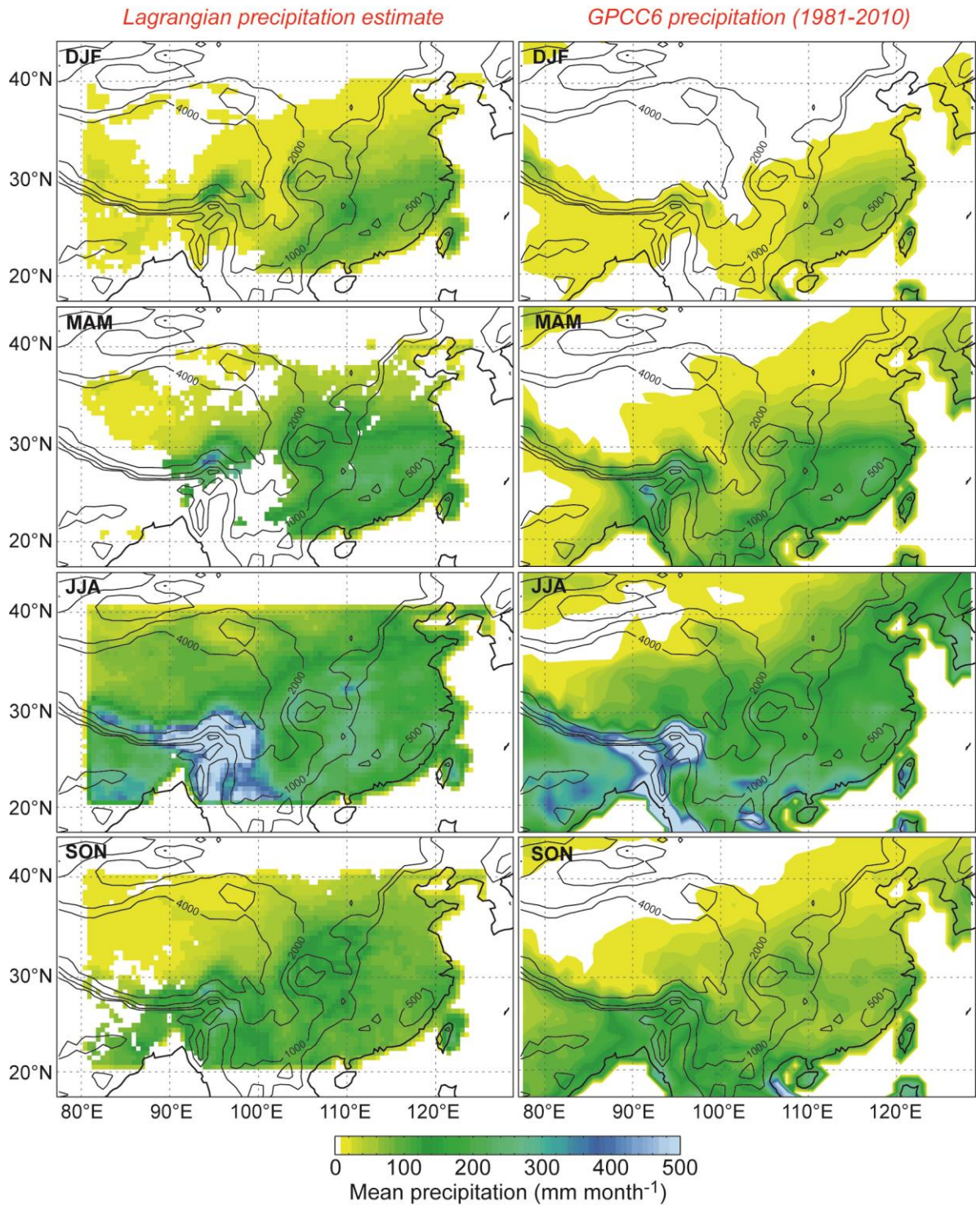


Figure 4.8. Mean seasonal Lagrangian precipitation estimate. Composited mean seasonal estimated precipitation within China to which moisture source was attributed (left-hand panels) exhibit a good spatial and seasonal agreement with GPCP6 data (right-hand panels) (Schneider *et al.*, 2011). These data were obtained from Deutscher Wetterdienst (available at www.dwd.de) and data are averaged over December-February (DJF), March-May (MAM), June-August (JJA), and September-November (SON). Topographic contours (solid lines) are in metres.

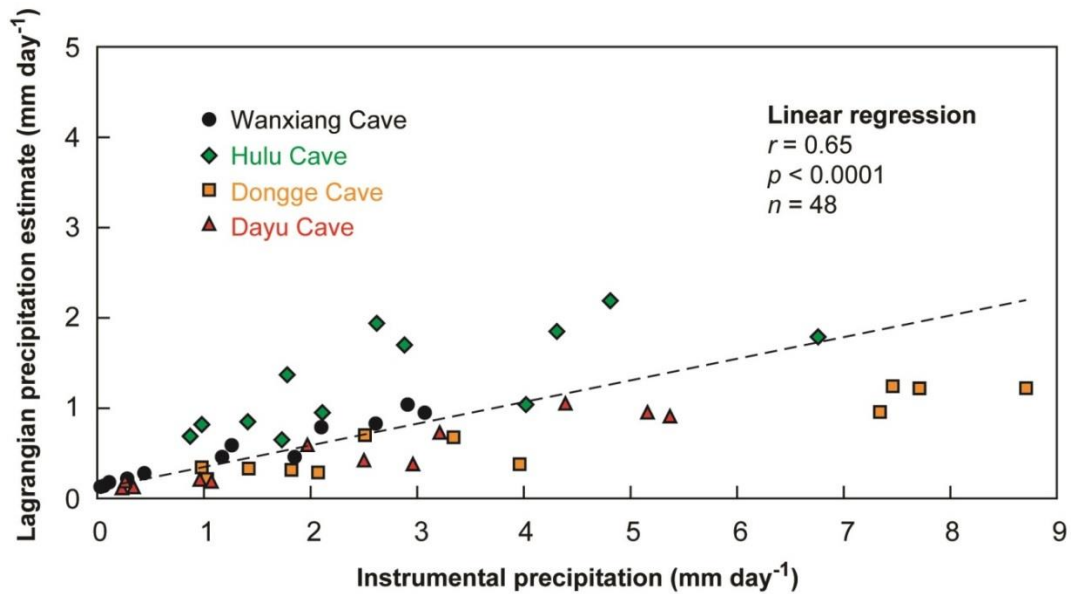


Figure 4.9. Correlation between Lagrangian precipitation estimates and station data. Mean monthly Lagrangian precipitation is significantly ($p = 7.53 \times 10^{-7}$), positively correlated with instrumental data from the nearest meteorological stations to the selected cave sites (see Fig. 4.2) of Wanxiang (black circles), Hulu (green squares), Dongge (orange squares) and Dayu (red circles). This correlation analysis was undertaken prior to performing multivariate regressions of precipitation amount, mean source longitude and mean source latitude with precipitation $\delta^{18}\text{O}$ from nearby GNIP stations. Modelled precipitation underestimates observed precipitation (see text for discussion). Colours correspond to Fig. 4.2.

4.3.4. Moisture source seasonality

The moisture contribution from different oceanic regions varies both seasonally and interannually, and a clear contrast in the seasonality of Indian versus Pacific Ocean contributions to EASM rainfall is apparent (Fig. 4.10). Non-monsoon season uptake from the northern Indian Ocean is low ($<5 \text{ mm day}^{-1}$) and increases rapidly after ISM onset ($\leq 10 \text{ mm day}^{-1}$) then decreases following peak EASM activity. Northwest and northeast Indian Ocean contributions are in-phase, consistent with the available satellite-based scatterometry data (Liu and Tang, 2004). Northwest Indian Ocean uptake is higher, resulting from the limb of evaporation that develops over the western Indian Ocean (Fig.

4.3). South China Sea uptake minima, unlike those of the other oceanic source regions, never reach near-zero values; a small moisture contribution ($\sim 7 \text{ mm day}^{-1}$) to the furthest south-eastern (coastal) areas of China and to Taiwan is therefore entrained during northward ASM advancement (Fig. 4.5). Moisture uptake from the Philippine Sea exhibits limited seasonality and that from the South China Sea exhibits peak contributions during winter months. Pacific contributions therefore dominate winter moisture supply, whereas westerly advection dominates EASM precipitation (Fig. 4.10).

Moisture recycling over China contributes significantly to total precipitation, particularly during the EASM, and the spatial distribution of continental recycling determined in this study (Fig. 4.3) is consistent with the results of Lee *et al.* (2012). Precipitation recycling exhibits strong seasonality, approaching 0 % in winter and with a June-August mean value of 57 % (Fig. 4.10b). However, no clear phase relationship with the area-weighted total moisture contribution from land surfaces exists (Fig. 4.10a, b). This is potentially linked to increasing intensive agricultural irrigation in central China, one potential influence on sub-regional scale water cycling (Niyogi *et al.*, 2010), implying that recycling is coupled to evapotranspiration, although other factors may modulate this relationship, and it is important to note that this is speculative. Nevertheless, these data show that annual mean moisture uptake from land (62 mm day^{-1}) represents a substantial contribution to EASM precipitation, and recycling is in-phase with the seasonal timing of Indian Ocean, not Pacific Ocean, moisture export (Fig. 4.3).

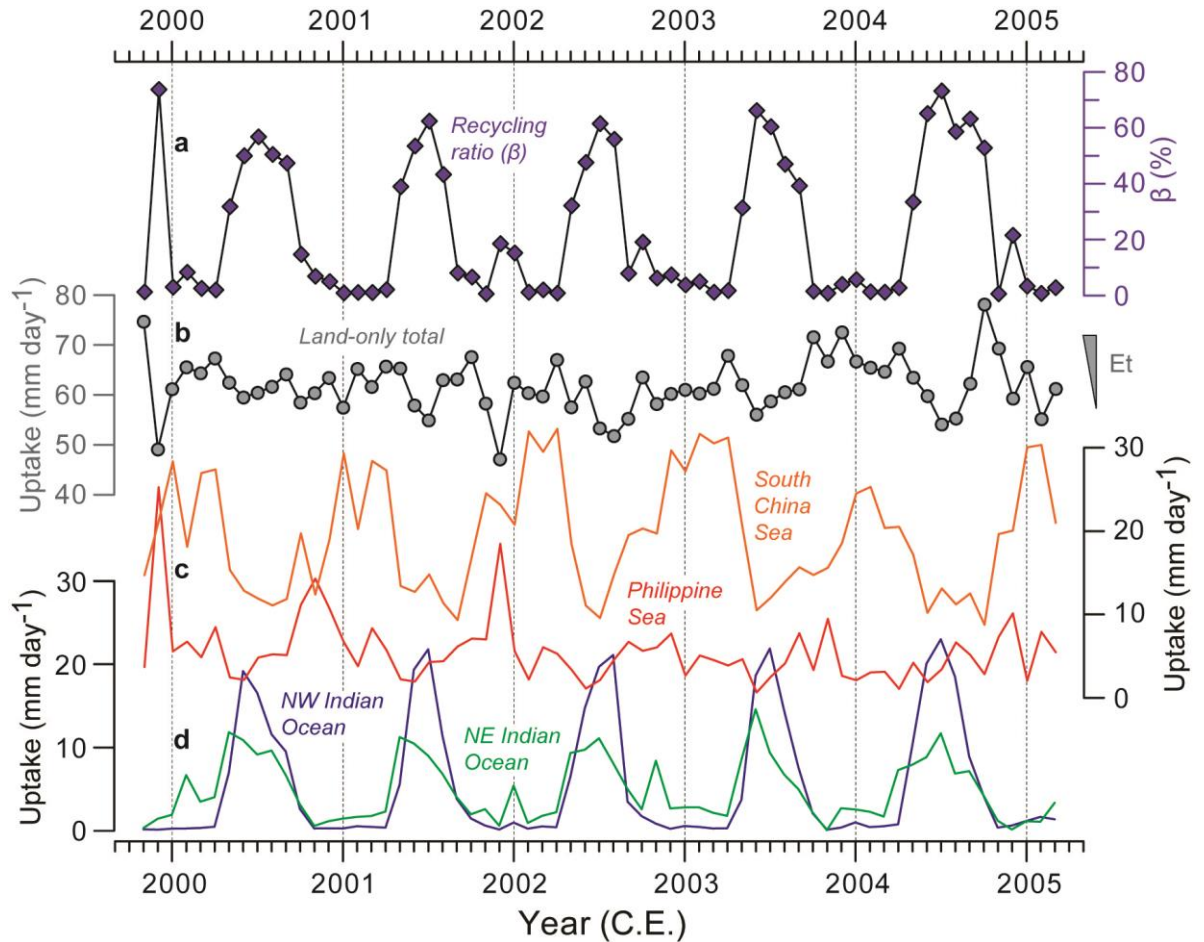


Figure 4.10. Monthly source region moisture contributions to precipitation in China. Time series of monthly (a) precipitation recycling ratio, (b) land-derived moisture, and moisture contributions from (c) Pacific and (d) Indian Ocean source regions (see Fig. 4.2) to precipitation in monsoonal China. Indian Ocean and Pacific Ocean contributions exhibit opposite seasonality. The precipitation recycling ratio (β) is defined as the ratio of precipitation source from local evaporation to total precipitation within a domain sourced (Schär *et al.*, 1999). Summer recycling maxima increased by $\sim 10\%$ during 2000–2005. Data in (b) show evaporative uptake only, representing the evapotranspiration (‘Et’) signal. Data in (c) and (d) are area-weighted and combine ABL and FT moisture, giving a total contribution. These combined data attribute moisture sources to 94 % of mean monthly precipitation (see Table 4.3). Colours correspond to Fig. 4.2.

4.4. Implications for EASM precipitation $\delta^{18}\text{O}$ interpretation

4.4.1. Source effect in precipitation $\delta^{18}\text{O}$

Reliable palaeomonsoon reconstructions from speleothem $\delta^{18}\text{O}$ require a detailed understanding of ‘amount effect’ variability (Dayem *et al.*, 2010), extra-regional forcings (e.g., oceanic source conditions) (Lewis *et al.*, 2010; Pausata *et al.*, 2011) and moisture source variability. The Lagrangian data were used to assess source signal variability in precipitation $\delta^{18}\text{O}$ at selected cave sites (Fig. 4.2) in key locations: eastern China (Hulu Cave), southern China (Dongge Cave) and near to the northerly EASM limit (Wanxiang Cave and Dayu Cave). For each site, multivariate correlations are higher between mean monthly precipitation $\delta^{18}\text{O}$ and a combination of precipitation amount, source longitude and source latitude than those quantifying individual site-specific amount or source effects (Fig. 4.11). This is particularly true for Hulu, where amount and source effects are similar (34 % and 29 %, respectively), and Dongge, where individual amount and source effects explain only a limited proportion of the precipitation $\delta^{18}\text{O}$ variability (18 % and 26 %, respectively). Precipitation $\delta^{18}\text{O}$ variance not explained by amount and source effects for the selected sites is likely due to the influence other hydroclimatic parameters, such as cloud temperature or convective intensity (Risi *et al.*, 2008). Nevertheless, precipitation $\delta^{18}\text{O}$ integrates a significant source signal, which differs between the selected sites within monsoonal China.

4.4.2. Geographic variability in EASM precipitation signal strength

Mean source regions for EASM precipitation at Hulu and Dongge are located ~1,700 and ~1000 km southwest, respectively, and for Dayu and Wanxiang, are ~500 and ~400 km

south, respectively. Each site predominantly receives moisture advected west-to-east, and the relative proximity of the northern Dayu and Wanxiang sites to their mean source regions indicates that they receive a greater proportion of recycled moisture, where mean June-August moisture transport distance is relatively short (Fig. 4.11). The apparent intensity of summer moisture recycling within monsoonal China is greater than that over northeast India, where mean moisture transport distance is lower. (Note that the lowest transport distance values are found over the Tibetan Plateau.) However, these results show no obvious transitional zone between the ISM and EASM regions (Wang and Lin, 2002), instead demonstrating predominant west-to-east moisture transport across continental eastern Asia.

Precipitation $\delta^{18}\text{O}$ at these key proxy sites is therefore indicative of not only of monsoonal intensity but also of moisture transport. Of these sites, based on these results and the available isotope data, Dongge potentially records precipitation amount the most directly. Conversely, Wanxiang and Dayu may record monsoon intensity in terms of variability in the maximum north-western extent of EASM precipitation. In agreement with the data in this chapter, recent isotope-enabled GCM results (Pausata *et al.*, 2011) indicate that Chinese precipitation $\delta^{18}\text{O}$ reflects extra-regional forcings, such as ISM strength or Indian Ocean source conditions (e.g., sea surface temperature or relative humidity).

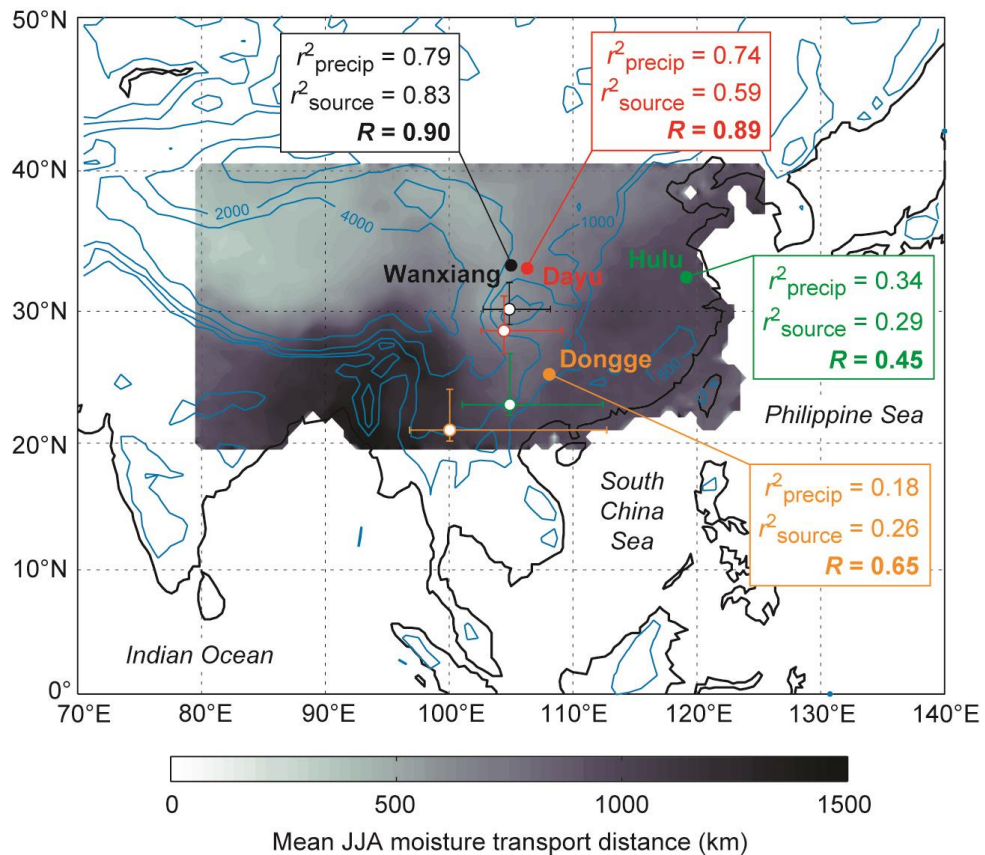


Figure 4.11. Amount effect *versus* source effect in precipitation $\delta^{18}\text{O}$. Map of selected cave sites (filled circles), their respective mean June-August moisture source locations (open circles), and moisture source weighted mean annual range (bars). Contoured data (greyscale) show the modelled mean June-August moisture transport distance (km) from uptake location to precipitation location. Northeast India and the Ganges-Brahmaputra deltaic region receive moisture transported over the greatest mean distance from the Indian Ocean (Fig. 4.3 and Fig. 4.4). In the EASM region, a southeast-northwest gradient in moisture transport distance exists. Correlation coefficients (r^2) for mean monthly precipitation $\delta^{18}\text{O}$ versus mean moisture source longitude and latitude (r^2_{source}) for the four selected cave sites are given. Also shown is the multivariate r^2 for precipitation $\delta^{18}\text{O}$ against amount, source longitude and source latitude (R), which is geographically variable and higher than individual amount and source correlations at each site. Topographic contours (pale blue) are at 500, 1000, 2000 and 4000 m a.m.s.l.

4.5. Summary and conclusions

In summary, this chapter presents quantification of moisture export from the Indian and Pacific Oceans that drives EASM precipitation in central and eastern China. The seasonal cycle of moisture sources shows a rapid transition from a dry winter period, with

predominately easterly moisture contributions, to an intense summer monsoon phase, with extensive contributions from the northern Indian Ocean and moisture recycling over continental areas. The Lagrangian modelling accurately reproduces the observed EASM precipitation distribution across southern and eastern China. Despite distinct differences in the onset and characteristics of the monsoon season over India, eastern China and the western North Pacific (Wang and Lin, 2002), the ISM contribution to EASM precipitation is significant.

These results present a significant challenge to the widely assumed Pacific Ocean origin for EASM precipitation in China (Ran and Feng, 2013; Xu *et al.*, 2004) and provide a highly plausible mechanistic explanation for overall precipitation proxy co-variation between China and India during late Holocene warm phases (Rehfeld *et al.*, 2013) and synchronous Holocene ISM and EASM decline (Li *et al.*, 2014) – see Fig. 3.2.

The expression of the source effect in modern precipitation $\delta^{18}\text{O}$ in monsoonal China is significant, yet varies in strength between the Hulu, Dongge, Dayu and Wanxiang Cave sites, which is most likely due to differences in mean moisture transport distance during summer. Precipitation $\delta^{18}\text{O}$ at each site may be more accurately interpreted as reflecting both rainfall amount and moisture transport. Given existing GCM evidence for a strong response of precipitation $\delta^{18}\text{O}$ in China to upstream rainout (Liu *et al.*, 2014; Pausata *et al.*, 2011), it is now increasingly clear that while $\delta^{18}\text{O}$ does not directly record only local precipitation variability at sites within monsoonal China, it provides a direct proxy for changes in moisture dynamics and EASM circulation strength and therefore remains a crucial tool for palaeomonsoon reconstruction.

Finally, it is important to consider that GCM studies project significant anthropogenic CO₂-induced warming over the tropical oceans (IPCC, 2013), resulting in considerable increases in lower atmosphere moisture content (Ueda *et al.*, 2006). The results presented in this chapter firmly suggest that changes in Indian Ocean, rather than Pacific Ocean, sea surface temperature and evaporation will drive future EASM rainfall variability in central and eastern China. This is discussed further in Chapter 7.

Chapter 5

Modelling the stable oxygen isotope composition of precipitation at the northerly limit of the East Asian Summer Monsoon region^{*}

^{*} A manuscript based on the work presented in this chapter is currently in preparation for *Journal of Geophysical Research: Atmospheres*.

Chapter summary

Palaeoclimate reconstructions based on stalagmite $\delta^{18}\text{O}$ from cave sites in monsoonal China likely respond to multiple hydroclimatic processes. A strong precipitation amount signal in precipitation (and thus stalagmite) $\delta^{18}\text{O}$ is preferable for reconstructing palaeomonsoon fluctuations, but the results presented in Chapter 4 demonstrate that the strength of this signal and that of source effects is geographically variable. In this chapter, the moisture source constraints presented in Chapter 4 and additional Lagrangian and reanalysis data are used to model the stable oxygen isotope composition of precipitation events at Wanxiang Cave, China. To achieve this, the isotope evolution of atmospheric vapour during moisture transport is modelled using the recently-developed Lagrangian model, Isotra3 (Dütsch, 2013), which simulates all of the phase changes and fractionation processes affecting air masses along actual three-dimensional atmospheric trajectories. Isotra3 reproduces observed precipitation $\delta^{18}\text{O}$ comparably well, though winter values are ~ 2 ‰ over-depleted. Tibetan Plateau-derived moisture and free troposphere contributions cause synoptic scale isotopic depletion. Overall, however, land-derived moisture causes isotopic enrichment during summer and is positively correlated with observed $\delta^{18}\text{O}$, thus moderating isotopic depletion due to strengthened EASM circulation or increased precipitation amount. This terrestrial moisture effect is important because intense moisture recycling occurs within monsoonal China during summer. This attenuation of a seasonal EASM signal in $\delta^{18}\text{O}$ may therefore increase during periods of elevated summer surface temperatures, which enhance terrestrial moisture flux.

5.1. Introduction and rationale

5.1.1. Stable water isotope modelling

As discussed in Chapter 1, measurements of oxygen isotope ratios in atmospheric vapour and water are a proven natural tracer of hydroclimatic variability, therefore providing a palaeoclimate proxy archived in speleothems and other terrestrial deposits. However, owing to the complexity of dynamical and microphysical atmospheric processes (Fig. 1.2) and the scarcity of temporally high-resolution observational isotope datasets (e.g., Moerman *et al.*, 2013; Wu *et al.*, 2014), particularly vapour measurements, numerical modelling studies are required to improve and validate our understanding of the causes of isotopic variability through the atmospheric water cycle. Isotopic fractionation processes have been incorporated into GCMs (e.g., Hoffmann and Heimann, 1997; Hoffmann *et al.*, 1998; Noone and Simmonds, 2002; Risi *et al.*, 2010), including all known fractionation effects during phase changes, to simulate isotopic values on a global scale. These studies successfully reproduced mean surface precipitation $\delta^{18}\text{O}$ and δD values, supporting the interpretation of long-term isotopic trends in ice cores and speleothems, but not smaller-scale spatial and temporal variability nor isotopic seasonality (Pfahl and Wernli, 2008; Sodemann *et al.*, 2008a). Regional isotope-enabled models, however, perform better. Sturm *et al.* (2005) successfully reproduced the known isotopic effects (see section 1.3.3.1) observed in GNIP data and Pfahl *et al.* (2012) show the potential of high resolution, event-based simulations for understanding synoptic-scale isotopic variability by reproducing spatial precipitation $\delta^{18}\text{O}$ in a winter storm over the eastern USA using a mesoscale forecast model.

The results of such GCM-based studies cannot be compared to present-day observations directly because GCMs do not properly replicate hydrological cycle variability at regional scales (Sodemann *et al.*, 2008a). A multi-annual present-day isotopic simulation by Yoshimura *et al.* (2008) demonstrated that temporal isotopic variability may be more accurately replicated by constraining atmospheric circulation processes using three-dimensional reanalysis data. Lagrangian studies (Ciais and Jouzel, 1994; Sodemann *et al.*, 2008a) have used kinetic Rayleigh models which calculate isotopic fractionation along idealised pressure-temperature pathways. Developing this approach, Helsen *et al.* (2007; 2006) modelled Antarctic precipitation $\delta^{18}\text{O}$ based on fractionation calculated along realistic five-day back trajectories (i.e., source to sink), initialised by three-dimensional GCM isotope data. Pfahl and Wernli (2009) simulated vapour $\delta^{18}\text{O}$ in evaporation events based on precipitation moisture sources diagnosed explicitly by a Lagrangian analysis similar to that described in Chapter 4, but focused only on parameters describing ocean water evaporation in their $\delta^{18}\text{O}$ model. More recently, this model has been expanded to incorporate all of the phase changes which occur during moisture transport (Dütsch, 2013). In this chapter, the most comprehensive Lagrangian isotope model available to-date, that of Pfahl and Wernli (2009) and Dütsch (2013), is used to simulate the along-trajectory isotopic evolution of atmospheric vapour and precipitation for 37 precipitation events sampled at Wanxiang Cave.

5.1.2. Rationale for selecting Wanxiang Cave

Wanxiang Cave is located in the semi-arid region between the Qinghai-Tibetan Plateau and the Chinese Loess Plateau and close to the northerly EASM limit, “and is thus sensitive to and integrates broad changes in the [EASM]” (Zhang *et al.*, 2008). This site therefore

provides an interesting opportunity to explicate the controls on precipitation $\delta^{18}\text{O}$ in a locality that is predominately influenced by the EASM and the Westerlies, primarily during boreal winter, and that experiences a relatively minor ISM contribution compared to southern and eastern China (see Chapter 4). Mean annual surface and cave temperatures are $\sim 11^\circ\text{C}$ and mean annual precipitation is 480 mm, $\sim 80\%$ of which is received between May and September. During winter, the Siberian-Mongolian High and westerly winds maintain cold and dry conditions (Zhang *et al.*, 2008).

Zhang *et al.* (2008) inferred declining East Asian summer monsoon intensity during the modern period from a trend towards depleted proxy $\delta^{18}\text{O}$ values, consistent with similar trends observed in EASM, ISM and global monsoon indices. However, the interannual correspondence between the Wanxiang proxy data and monsoon indices is unsatisfactory, suggesting that monsoon intensity is not a major control on sub-decadal timescales. Moreover, the observed disparities between the Wanxiang record, the nearby Dayu Cave stalagmite record of Tan *et al.* (2009), and Chinese Loess Plateau records (Maher and Thompson, 2012) indicate that precipitation $\delta^{18}\text{O}$ reflects multiple hydroclimatic parameters, particularly upstream depletion during moisture transport. The average temporal resolution of the Wanxiang Cave record is ~ 2.5 years and ~ 1 year over the instrumental period, both of which are too coarse to allow direct comparison to parameters describing synoptic scale hydroclimatic processes that control precipitation $\delta^{18}\text{O}$. Therefore, to quantify the net climate signal for a particular site (i.e., the strength of temperature or amount signals in precipitation $\delta^{18}\text{O}$), high-resolution isotopic and meteorological monitoring data representing the hydrological or isotopic year cycle (e.g., Moerman *et al.*, 2013; Wu *et al.*, 2014; Yang *et al.*, 2011), and process-based modelling on event timescales are required.

In Chapter 4, modelled precipitation over monsoonal China matches GPCC6 data well (Fig. 4.8) and modelled precipitation at Wanxiang Cave is positively correlated with instrumental data from the nearby Wudu meteorological station (Fig. 4.9). Therefore, quantitatively diagnosed precipitation moisture sources and the satisfactory reproduction of hydrological variability during the study period provide a robust basis for modelling precipitation $\delta^{18}\text{O}$ using the Lagrangian approach. The following section details the available observational data from Wanxiang Cave and the Lagrangian isotope model used in this study.

5.2. Data and methods

5.2.1. Stable water isotope measurements from Wanxiang Cave

Wanxiang Cave monitoring data are unpublished (Johnson, 2004) and were kindly provided by Kathleen Johnson (Department of Earth System Science, University of California at Irvine, USA). The available precipitation isotope dataset is comprised of 42 event samples collected outside the Wanxiang Cave entrance at irregular intervals between October 1999 and December 2002, and 6 vapour samples (re-evaporated precipitation). Wanxiang precipitation data plot within the GNIP data spread (Fig. 5.1), except for two depleted rainfall events sampled on 21/10/1999, and this is expected because GNIP data are monthly means. The available dripwater dataset is comprised of 64 samples throughout the Wanxiang system, which plot in a single dense cluster towards the depleted end of the overall data spread. Also available are isotopic data for 14 cave pool water samples. However, in-cave sampling was undertaken only in October 1999, September 2001 and

May 2002, and does not therefore constitute long-term monitoring. As such, this chapter focusses on precipitation isotope data.

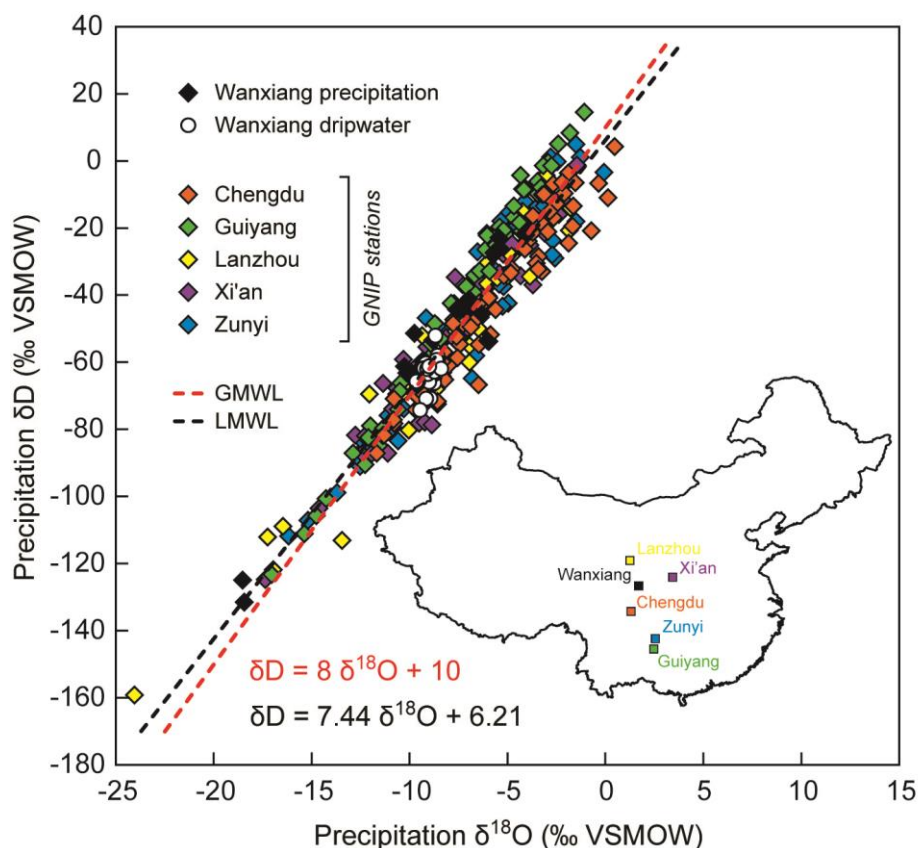


Figure 5.1. Local meteoric water line and Wanxiang Cave water isotope data. Monthly mean precipitation $\delta^{18}\text{O}$ and δD data (coloured diamonds) from five GNIP stations closest to Wanxiang Cave, encompassing central and southern China, describing a local meteoric water line (LMWL). Temporal coverage of these data is 1985-2002. Locations are indicated on inset map: Chengdu (orange), Guiyang (green), and Zunyi (blue) are located south of Wanxiang Cave (black); Lanzhou (yellow) is located north; Xi'an (purple) is located east. The local meteoric water line describing these data (LMWL; black dashed line) is similar to the Global Meteoric Water Line (GMWL; red dashed line). Precipitation (black diamonds) and dripwater (white circles) isotope data from Wanxiang Cave are also plotted (note that of the 64 dripwater samples, 37 lack a δD measurement).

5.2.2. The Isotra3 model

5.2.2.1. Overview

Air parcels migrate through the atmosphere experiencing variable temperature, pressure and relative humidity conditions. The recently-developed Isotra3 model (Dütsch, 2013; Pfahl and Wernli, 2009) simulates isotopic evolution along three-dimensional Lagrangian trajectories, accounting for all phase changes that occur during moisture uptake, transport and precipitation (Fig. 5.2), and therefore takes the quantitatively diagnosed moisture source regions into account. As such, Isotra3 potentially calculates more realistic isotopic values for the resulting precipitation than those simulated by an idealised Rayleigh-type model (Pfahl and Wernli, 2009), especially on a synoptic timescale. Previous along-trajectory modelling used an adapted version of the Mixed Cloud Isotope (MCIM) model (Helsen *et al.*, 2007; Helsen *et al.*, 2006), but source regions were not explicitly specified. Isotra3 therefore constitutes an important development.

Dütsch (2013) described the implementation of the current version of the Isotra3 model and conducted systematic sensitivity and performance testing. The model was found to perform better after additional hydroclimatic fractionation processes (rain formation, terrestrial evaporation, air parcel ascent through the ABL, equilibration with surrounding moisture, and snow formation) were incorporated. By implementing these processes in Isotra3, Dütsch (2013) achieved significant reductions in the root mean square errors associated with comparisons between modelled and observed $\delta^{18}\text{O}$ at sites in Rehovot, Israel, and Tustervatn, Norway. Crucially, the processes to which to this improvement were attributed are rain formation and mixing with surrounding moisture, each concerning liquid precipitation, and therefore Isotra3 appears to be ideally suited to this study.

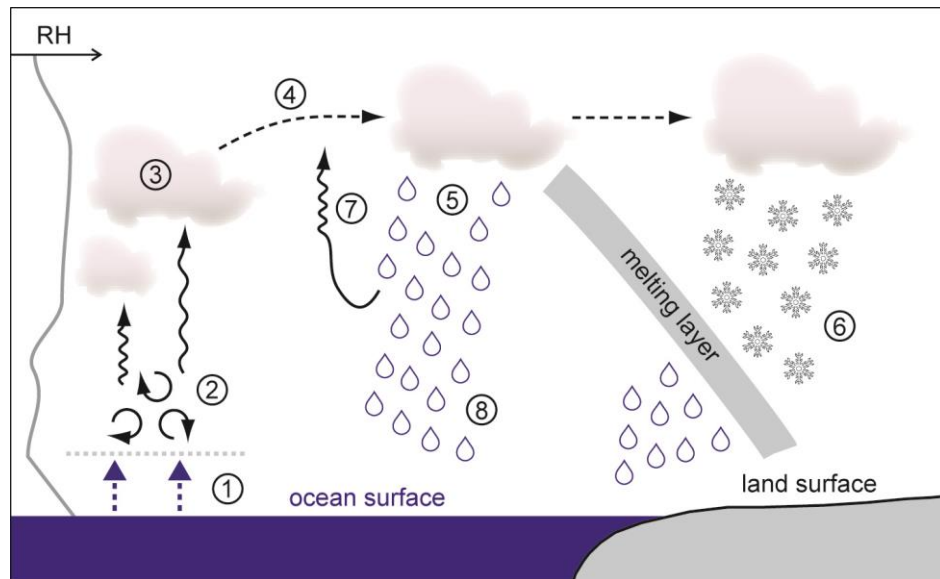


Figure 5.2. Schematic illustration of fractionation processes simulated by Isotra3. Evaporation from the ocean surface (1) causes equilibrium and kinetic fractionation (Craig, 1965). Evaporation and evapotranspiration from land surfaces is assumed to occur without fractionation. Moisture transport in the turbulent marine boundary layer (2) also occurs without isotopic fractionation. Atmospheric vapour masses rise and cool adiabatically, condensing to form clouds (3), and equilibrium fractionation occurs (Rozanski and Sonntag, 1982). During rainout, light isotopes remain in the vapour phase (4) and heavy isotopes are preferentially incorporated into condensed liquid precipitation (5) or snow (6), each with differing fractionation factors. Liquid precipitation that falls through the atmospheric column below cloud base is subject to additional fractionation processes (Lawrence *et al.*, 1998). Processes not parameterised by Isotra3 are re-evaporation below the cloud base, which may be fed back into cloud condensation (7) and precipitation re-equilibrating with surrounding moisture during rainfall (8), the rate of which depends on relative humidity (RH; grey line). Lagrangian isotope models are not able to take post-condensation processes (Lee and Fung, 2008) into account. After Sodemann (2006).

5.2.2.2. Model parameterisations

The isotopic ratio R (Eq. 1.2) is the prognostic variable of Isotra3, which is output at each 6-hour timestep along each 20-day backward trajectory, from -480 to 0 hours. For each timestep, the specific humidity difference between timestep t and $t+1$ (Δq) is given by:

$$\Delta q = q_{t+1} - q_t \quad (\text{Equation 5.1})$$

As discussed in Chapter 4, Δq is diagnostic of moisture flux into and out of air parcels. Positive Δq indicates moisture addition from surface evaporation or mixing, and the resultant isotope ratio at time $t+1$ is given by:

$$R_{t+1} = \frac{R_t \times q_t^{\text{exp}} + R_{\text{in}} \times \Delta q}{q_{t+1}^{\text{exp}}} \quad (\text{Equation 5.2})$$

where q_t^{exp} and q_{t+1}^{exp} are the amounts of moisture for which sources have been attributed by the Lagrangian diagnostic at times t and $t+1$ ($q^{\text{exp}} \geq q$), respectively, R_t is the previous isotope ratio, and R_{in} is the isotope ratio of the moisture added to the air parcel. Evaporative moisture uptake is distinguished from free troposphere mixing if the trajectory height is less than 1.5 times ABL height, following Dütsch (2013). If Δq is negative, moisture is lost from the air parcel by precipitation if relative humidity is greater than 80 %, causing Rayleigh fractionation, or by convective processes if relative humidity is less than 80 %, which occurs without fractionation. This humidity threshold for precipitation generation is consistent with that in the published MCIM.

For $\delta^{18}\text{O}$, the equilibrium vapour-liquid fractionation factor ($\alpha_{v/l}$) is temperature-dependent, following Majoube (1971), and the constant kinetic fractionation factor (k) used to parameterise isotopic fractionation during seawater evaporation is independent of wind speed, according to Cappa *et al.* (2003). Following Pfahl and Wernli (2009) and Dütsch (2013), $k = 0.9925$. Fractionation during seawater evaporation is calculated according to the widely-used linear resistance model of Craig and Gordon (1965), and is thus a function of k , $\alpha_{v/l}$, ambient relative humidity, and the isotopic compositions of seawater and evaporate. During terrestrial evaporation, it is assumed that no isotopic fractionation occurs, principally because intercept storage water evaporates completely (Pfahl *et al.*,

2012; Risi *et al.*, 2010; Rozanski and Sonntag, 1982). Therefore, terrestrial surface water $\delta^{18}\text{O}$ is represented by precipitation $\delta^{18}\text{O}$ measurements from nearby GNIP stations, following Dütsch (2013). Despite the existence of a relatively dense network of GNIP stations in monsoonal China (Fig. 1.3), many station datasets contain significant temporal gaps or provide only a short instrumental record. Therefore, a simple precipitation $\delta^{18}\text{O}$ climatology was computed to represent the mean annual terrestrial water $\delta^{18}\text{O}$ cycle in the Wanxiang Cave region (Table 5.1), which is required by Isotra3. During air parcel ascent, saturation may result from adiabatic cooling. In Isotra3, air parcels initially ascend vertically in 10 m intervals, following the dry adiabat until the lifting condensation level and then following the moist adiabat until the trajectory height is reached. Isotopic fractionation along the moist adiabat is given by Eq. 5.3. Fractionation during rain formation is represented by the Rayleigh process, whereby increasing condensation depletes the residual vapour in ^{18}O and hence the condensed precipitation itself, which is given by:

$$\frac{R_t}{R_0} = f^{(\alpha_l/\nu-1)} \quad (\text{Equation 5.3})$$

where f is the residual vapour fraction. Fractionation increases at lower temperatures. Moisture addition above the ABL is assumed to result from mixing with surrounding vapour and therefore occurs without fractionation (Dütsch, 2013). The isotopic composition and other properties of surrounding air are unknown quantities in Lagrangian models. Therefore, monthly mean $\delta^{18}\text{O}$ values are obtained from the Isotope Global Spectral Model (IsoGSM) (Yoshimura *et al.*, 2008), which are linearly interpolated to the location of the trajectory and assigned to the quantity of moisture entering the air parcel above the ABL. Isotra3 thus follows a similar approach taken by Helsen *et al.* (2006).

Lagrangian models are not, however, able to account for re-evaporation of precipitating moisture below the cloud base (Fig. 5.2).

Month	Mean $\delta^{18}\text{O}$ (‰ VSMOW)	Mean δD (‰ VSMOW)
January	-4.14	-24.58
February	-3.33	-18.55
March	-3.59	-20.48
April	-3.3	-18.36
May	-3.77	-21.83
June	-6.36	-41.11
July	-9.57	-65.02
August	-8.89	-59.92
September	-9.45	-64.1
October	-7.13	-46.81
November	-5.3	-33.2
December	-4.09	-24.24

Table 5.1. Regionally-averaged terrestrial water isotope values. Amount-weighted mean monthly precipitation $\delta^{18}\text{O}$ and δD were calculated for the GNIP stations at Chengdu, Guiyang, Xi'an and Zunyi, and then averaged to create a single climatology. Lanzhou was excluded due to data discontinuity at this station.

5.2.2.3. Lagrangian trajectory data for Isotra3 model runs

In Chapter 4, moisture sources for modern precipitation over central and eastern China were investigated quantitatively using the Lagrangian diagnostic of Sodemann *et al.* (2008b), which determines the temporal sequence of uptake and rainout along kinematic backward trajectories of air parcels based on specific humidity data. Used in this chapter are 20-day backward trajectories, computed at a 6-hour temporal resolution using FLEXPART (version 8; Stohl *et al.*, 2005), for every sampled precipitation event. For consistency with Chapter 4, trajectories follow the same ECMWF operational analysis wind fields, providing realistic three-dimensional pathways. Unfortunately, the

precipitation sampling times and event durations are unknown. To compensate for this, trajectories begun at 00:00, 06:00, 12:00 and 18:00 UTC on each precipitation sampling date were used, and subsequently combined.

The Isotra3 model reads the parameters required for isotopic fractionation calculations (sea surface temperature, pressure, specific and relative humidity, and ABL height) trajectory files for each atmospheric trajectory precipitating in a $2^\circ \times 2^\circ$ target region centred on Wanxiang Cave (Fig. 4.2) for each sampled precipitation event. Example input and output trajectory text files are given in Appendix 4. Additional parameters required by Isotra3 are surface pressure, 2-metre temperature and 2-meter dew-point temperature, and 10-metre horizontal windspeed, which were retrieved from ECMWF ERA-Interim reanalysis data (Dee *et al.*, 2011)[†] exactly along the three-dimensional trajectories[‡].

5.2.2.4. Constraints on initial source water $\delta^{18}\text{O}$

During the EASM, direct moisture uptake from land is significant (Fig. 4. 10 and Fig. 4.3) and the weighted mean source region for Wanxiang Cave is located over land (Fig. 4.11). Therefore, a potential bias associated with the isotopic composition of terrestrial moisture uptake exists because Isotra3 requires isotope ratios to be assigned to terrestrial uptakes and the 4th generation European Centre Hamburg (ECHAM4) GCM tends to overestimate precipitation $\delta^{18}\text{O}$ depletion. To mitigate this, the Isotra3 model was run using mean monthly terrestrial water isotope ratios derived from observational GNIP station data

[†] ERA-Interim data are available every 6 hours from 1971-present at a T255 horizontal resolution (~80 km) and on 60 vertical levels, the highest of which is at 0.1 hPa. These data are available at http://apps.ecmwf.int/datasets/data/interim_full_daily/.

[‡] This was achieved using a computational tool (named ‘trace’) developed at the Institute of Atmospheric and Climate Science, Swiss Federal Institute of Technology (ETH), Zurich.

(Table 5.1). Oceanic moisture uptake is assigned a $\delta^{18}\text{O}$ from the dataset of LeGrande and Schmidt (2006), a linear interpolation of existing seawater $\delta^{18}\text{O}$ observations. This is possible because Lagrangian models allow exact (oceanic or terrestrial) moisture sources to be prescribed. Therefore, the $\delta^{18}\text{O}$ values assigned to terrestrial and oceanic moisture uptakes are grounded in the available observational data.

5.2.2.5. Exclusion of non-precipitating trajectories

After running Isotra3 for each sampled precipitation event, trajectories which precipitate less than 1 g kg^{-1} at the arrival timestep at Wanxiang Cave are excluded. By applying this precipitation criterion, one summer (09/06/2002) and three winter (20/01/2002, 28/02/2002 and 20/11/2002) events were excluded from further analysis because no trajectories therein generated sufficient precipitation. Each final precipitation event $\delta^{18}\text{O}$ is an average of individual $\delta^{18}\text{O}$ compositions modelled for the precipitating trajectories. Eames (2008) observed $\sim -6.5 \text{ ‰}$ variation across 100 individual trajectories for a single precipitation date, resulting from small variations in trajectory locations. It is therefore critical to consider numerous trajectories and define well-constrained source regions. Only 1 sampled precipitation event (30/03/2002) could not be modelled due to the absence of trajectories arriving in the Wanxiang Cave target region on this date.

5.3. Modelling Wanxiang Cave precipitation $\delta^{18}\text{O}$ with Isotra3

5.3.1. Results

5.3.1.1. Trajectories and event-scale moisture uptake

In this section, kinematic back trajectories for select precipitation events are discussed. For each sampled precipitation event, all trajectories begun at 00:00, 06:00, 12:00 and 18:00 UTC at Wanxiang Cave are combined. The specific humidity and $\delta^{18}\text{O}$ evolution along trajectories for three select summer precipitation events, representing earliest AM onset (May), peak (August) and late (September) EASM season are shown in Fig. 5.3. Precipitation $\delta^{18}\text{O}$ values simulated for these events are -7.48, -12.57 and -12.13 ‰, respectively. Each event comprises transport from the northern Indian Ocean and from relatively high-latitude ($\sim 50^\circ\text{N}$) westerly sources. However, the number of high-latitude trajectories migrating over central Eurasia during the 20/08/2002 event is minimal, as expected during peak EASM circulation. The 20/08/2002 event also shows a significant number of trajectories tracking eastward from the northern Pacific Ocean. For each select event, high-latitude and Pacific trajectories transport less moisture ($\leq 4 \text{ g kg}^{-1}$) than those migrating over the Indian Ocean ($\leq 18 \text{ g kg}^{-1}$). As distinct are the modelled isotopic differences associated with these transport pathways. High-latitude trajectories are dry and experience cooler cloud temperatures, depleting $\delta^{18}\text{O}$, and Pacific Ocean trajectories experience significant prior rainout, also resulting in depleted $\delta^{18}\text{O}$ of ~ -15 ‰. Conversely, Indian Ocean trajectories show $\delta^{18}\text{O}$ evolution which is close to the observed range in both Wanxiang and regional $\delta^{18}\text{O}$ values (Fig. 5.1), allowing for the fact that vapour is more depleted than condensed liquid precipitation. Modelled air mass $\delta^{18}\text{O}$ for the 20/08/2002 peak EASM event exemplifies this and the selected events illustrate that summer vapour $\delta^{18}\text{O}$ variance due to air mass ‘history’ may be up to ~ 10 ‰, which approximates the total

measured precipitation $\delta^{18}\text{O}$ variability at Wanxiang ($\sim 7\%$), given that vapour is depleted relative to precipitation, and $\sim 50\%$ of total precipitation $\delta^{18}\text{O}$ variability observed across central and southern China in GNIP data (Fig. 5.1).

Specific humidity and precipitation $\delta^{18}\text{O}$ evolution along trajectories for two select winter precipitation events, representing pre- (April) and post-EASM season (October) are shown in Fig. 5.4. Precipitation $\delta^{18}\text{O}$ values simulated for these events are -12.08 and -5.65% , respectively. These events show negligible transport over the northern Indian Ocean and organised Westerly transport north and south of the Tibetan Plateau. For these events, air parcel moisture increase up to $\sim 12\text{ g kg}^{-1}$ occurs proximal to Wanxiang Cave and this is coincident with isotopic enrichment prior to rainout.

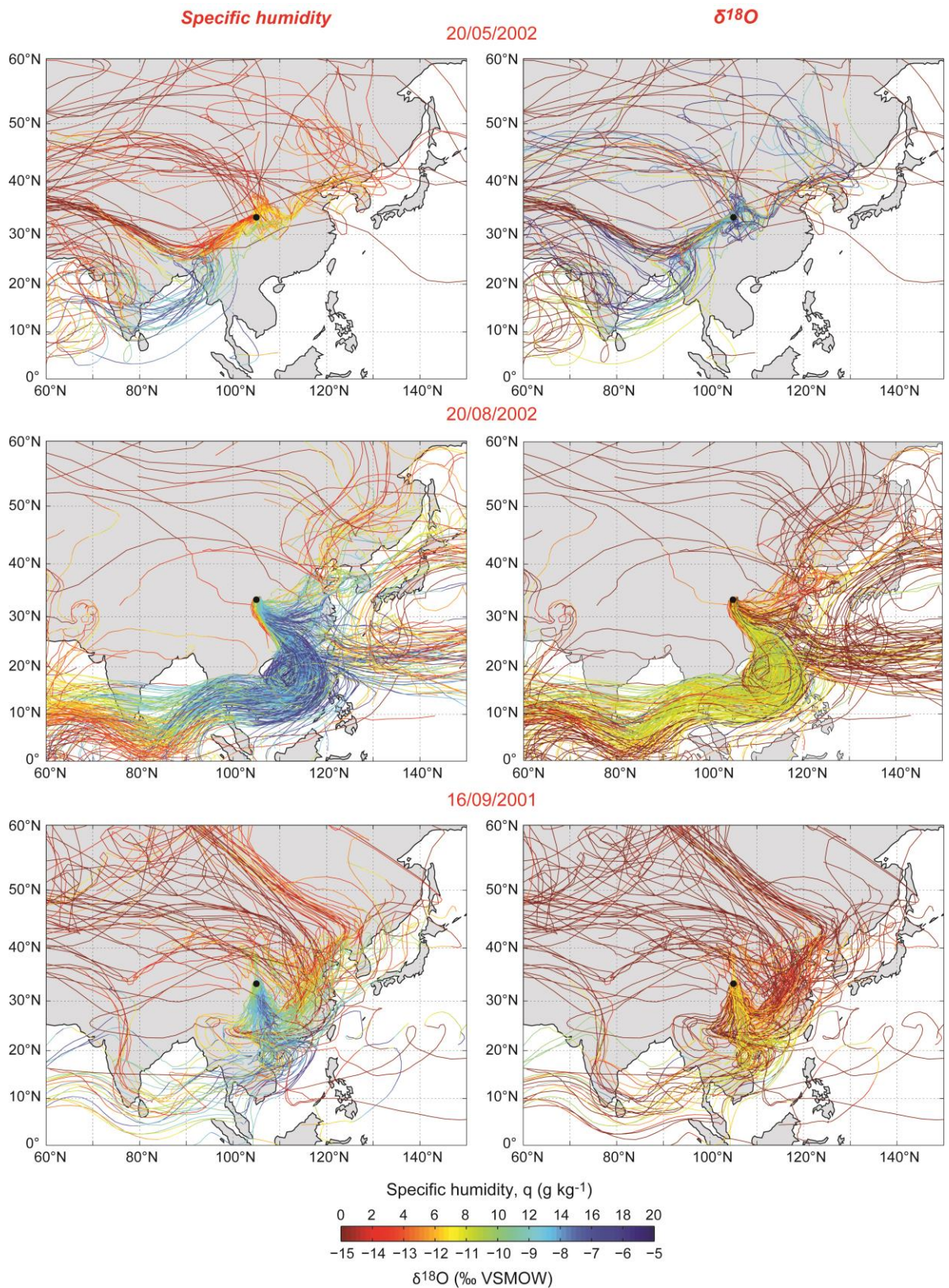


Figure 5.3. Example summer back trajectories arriving at Wanxiang Cave. Selected EASM season plots showing along-trajectory specific humidity (left) and vapour $\delta^{18}\text{O}$ (right) evolution for three precipitation events received at Wanxiang Cave on 20/05/2002, 20/08/2002 and 16/09/2001. Precipitation $\delta^{18}\text{O}$ values simulated for these events are -7.48, -12.57 and -12.13 ‰ VSMOW, respectively.

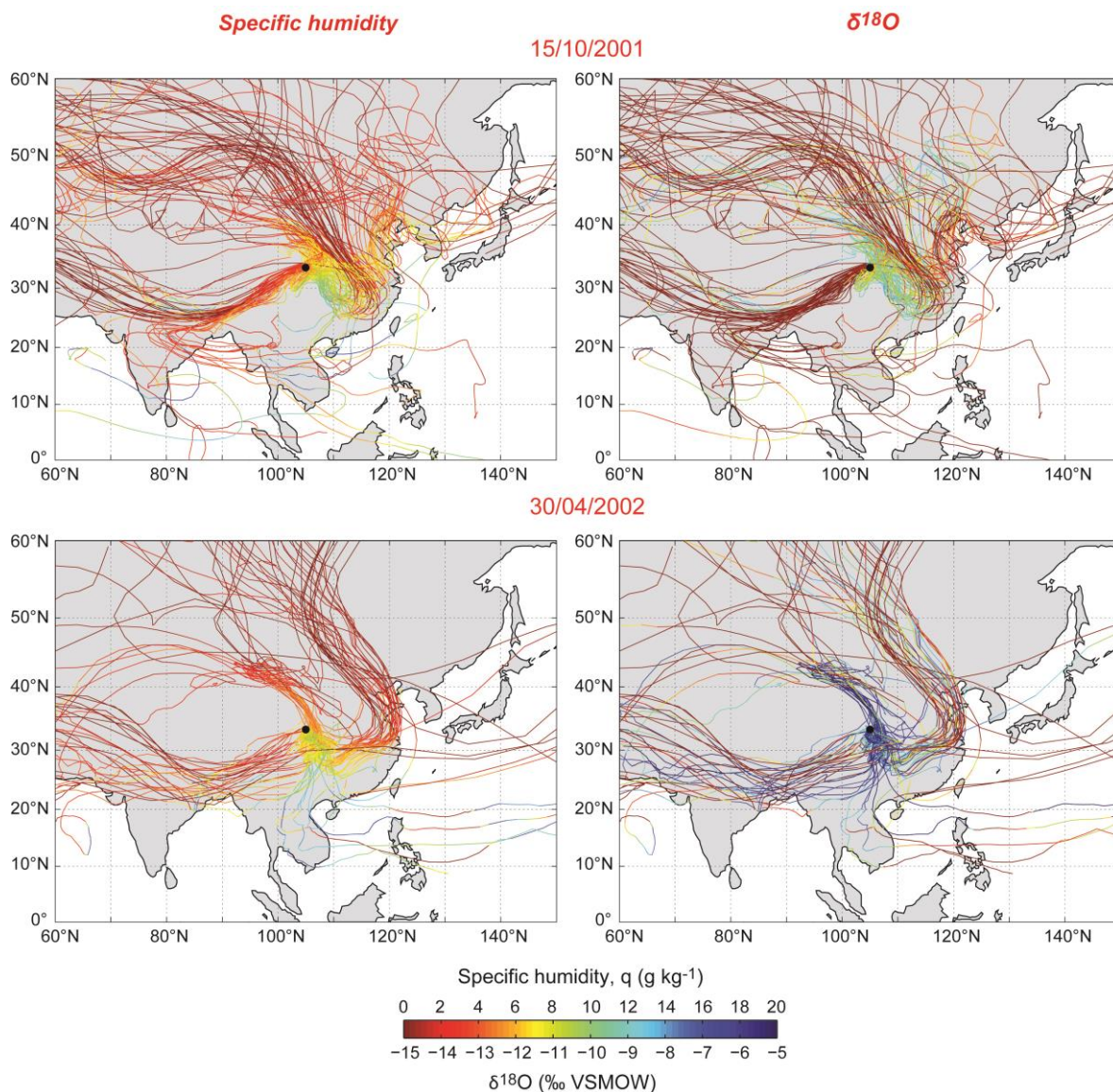


Figure 5.4. Example winter back trajectories arriving at Wanxiang Cave. Selected winter back plots showing along-trajectory specific humidity (left) and vapour $\delta^{18}\text{O}$ (right) evolution for three precipitation events received at Wanxiang Cave on 15/10/2001 and 30/04/2002. Precipitation $\delta^{18}\text{O}$ values simulated for these events are -12.08 and -5 – 65 ‰ VSMOW, respectively. Note that few trajectories migrate directly over the Tibetan Plateau, indicating that this Lagrangian modelling simulates realistic transport (and thus isotopic fractionation evolution).

5.3.1.2. Precipitation amount and $\delta^{18}\text{O}$

Modelled synoptic precipitation amount shows similarities with instrumental measurements from the nearby Wudu meteorological station (Fig. 5.5). However, only a general comparison may be made because direct daily rainfall amount measurements corresponding to the precipitation $\delta^{18}\text{O}$ samples are not available. Although only ~15 km from Wanxiang Cave, Wudu may not necessarily provide an accurate ‘substitute’ dataset because differences in the timing and duration of precipitation events may vary across such spatial scales, particularly in mountainous regions (e.g., Buytaert *et al.*, 2006; Tokay *et al.*, 2013). Indeed, Wudu data do not agree perfectly with ERA-Interim data extracted at the location of Wanxiang Cave (Fig. 5.5). A moderate amount effect is apparent in the modelled data: precipitation $\delta^{18}\text{O}$ and amount are positively correlated ($r = -0.45$; $n = 33$, $p < 0.01$). However, this is not apparent in the observed dataset, which is most likely related to uncertainties in the duration of sampled precipitation events. Mean modelled and observed precipitation $\delta^{18}\text{O}$ values for Wanxiang are -8.91 and -7.10 ‰VSMOW; modelled and observed $\delta^{18}\text{O}$ ranges are 8.62 and 6.33 ‰; and standard deviations are 2.58 and 1.86 ‰, respectively. Isotra3 therefore acceptably reproduces the basic observed Wanxiang $\delta^{18}\text{O}$ characteristics. Isotra3 reproduces the many aspects of the temporal trend described by the observational data, and also indicates that terrestrial moisture fluxes influence modelled values (Fig. 5.5). September 2001 and August 2002 values are not reproduced by Isotra3, but winter 2001/2002 and May-August 2002 values are particularly well captured, except for one clear outlier (20/03/2002). The pattern of September-November 2002 values is also well-captured, though modelled values are ~3 ‰ more depleted than observed values, suggesting that the absolute moisture contribution of high-latitude westerly sources (and thus more depleted vapour $\delta^{18}\text{O}$) contributing to these events is somewhat overestimated.

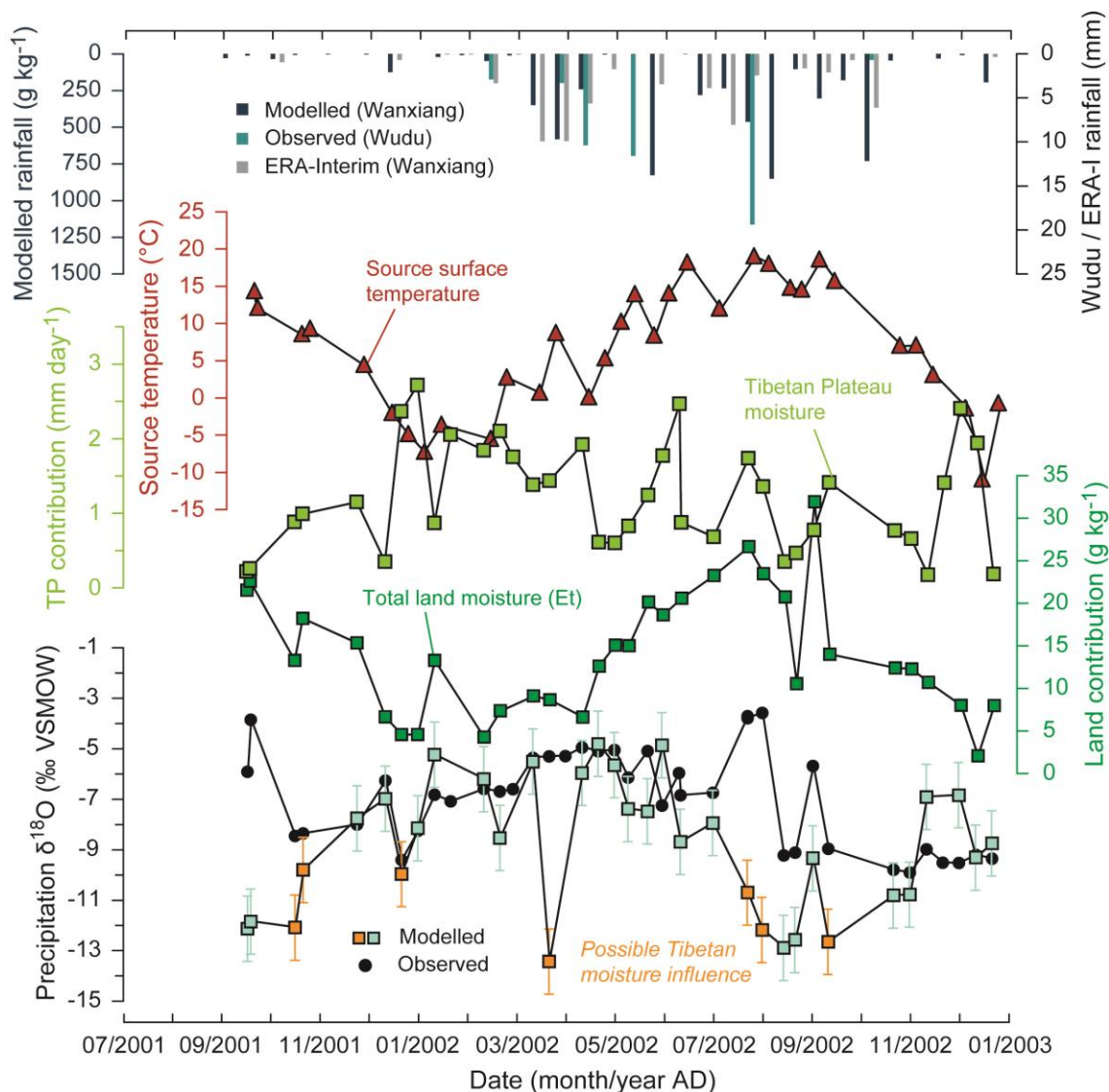


Figure 5.5. Wanxiang Cave precipitation $\delta^{18}\text{O}$ modelled by Isotra3. Daily modelled Wanxiang precipitation (dark blue bars) given as the specific humidity lost by all air parcels upon arrival over the Wanxiang target region where relative humidity is greater than 80 %. These data are compared with daily rainfall totals (turquoise bars) obtained from the nearby Wudu meteorological station (33.40 °N, 104.92 °E, 1079 m a.m.s.l.; World Meteorological Organisation station code: 56096) and ERA-Interim reanalysis data (grey bars). The Wudu station is located ~15 km southwest of Wanxiang Cave. ERA-Interim data are gridded to a 1.5 degree resolution and were extracted from the Wanxiang Cave location. Uptake-weighted mean source surface temperature (red triangles). Daily moisture uptake (combined FT and ABL uptake) from the Tibetan Plateau (TP; pale green squares) and mean moisture uptake from all terrestrial regions (dark green squares), representing evapotranspiration ('Et'). Observed (black circles) and modelled (coloured squares) Wanxiang precipitation $\delta^{18}\text{O}$. Orange data points represent depleted precipitation events which correspond to peaks in the Tibetan moisture contribution. Error bars show 1 standard deviation ($\sigma = 2.58$). Missing values in the modelled $\delta^{18}\text{O}$ series are the four excluded events for which trajectory arrival heights were greater than 1.5 times ABL height and the single event which could not be modelled.

5.3.2. Discussion: precipitation $\delta^{18}\text{O}$ response to moisture fluxes

5.3.2.1. Isotopic enrichment due to terrestrial moisture

In Chapter 4, intense EASM season precipitation recycling was observed across monsoonal China. Interestingly, selected trajectory maps (Fig. 5.3 and Fig. 5.4) demonstrate that Eq. 5.2 is realistic because each trajectory is surrounded by others which have undergone similar transport and fractionation pathways, thereby gaining similar isotopic compositions. In other words, neighbouring air parcels gain and lose moisture simultaneously during organised moisture transport and therefore experience similar isotopic evolution. For both summer and winter precipitation events, air parcels far upstream from Wanxiang are both dry and depleted (Fig. 5.3 and Fig. 5.4) and subsequently evolve more enriched $\delta^{18}\text{O}$ as a result of moisture uptake, apparently overprinting previous depleted compositions. This is consistent with the upstream depletion interpretation of precipitation (and proxy) $\delta^{18}\text{O}$ in monsoonal China (Maher and Thompson, 2012), but an additional complication pertinent to Wanxiang is that terrestrial moisture uptake may moderate $\delta^{18}\text{O}$ depletion occurring upstream.

Comparison of Isotra3 model output and the Wanxiang observations reveal two potentially important effects to which precipitation $\delta^{18}\text{O}$ may respond. Firstly, the overall terrestrial moisture contribution, which tracks moisture source surface temperature seasonality (Fig. 5.5), influences precipitation $\delta^{18}\text{O}$ observed at Wanxiang (Fig. 5.6). This evapotranspiration contribution is positively correlated with observed precipitation $\delta^{18}\text{O}$ ($r = 0.44$), with increased terrestrial uptake (no fractionation) enriching precipitation $\delta^{18}\text{O}$. Striking examples of this are the seven events between 30/07/2002 and 30/10/2002, which correspond closely to terrestrial uptake variability (Fig. 5.5). Seasonal segregation of the existing observational data demonstrates that summer $\delta^{18}\text{O}$ is influenced by this effect ($r =$

0.61) and that winter values show no such trend ($r = 0.04$). This contradicts Lee *et al.* (2012), who found minimal evaporative enrichment of vapour $\delta^{18}\text{O}$ using the isotope-enabled Laboratoire de Météorologie Dynamique Zoom GCM (version 4; Hourdin *et al.*, 2006). Potentially, this isotopic enrichment mechanism reflects only the initial-arrival temperature difference because (i) evapotranspiration is primarily driven by surface temperature seasonality (Fig. 5.5) and (ii) temperature changes may overprint the effects of other microphysical processes and along-trajectory phase changes (Fig. 5.6). However, this appears not to be the case as no trend with respect to the initial-arrival temperature difference ($T_{\text{in}} - T_{\text{arr}}$) is observed (Fig. 5.6) and terrestrial moisture is therefore an important consideration in interpreting precipitation $\delta^{18}\text{O}$ in this region.

This process is important because intense moisture recycling occurs close to the northerly EASM limit during summer (Fig. 4.11). At Wanxiang, isotopic depletion of monsoonal precipitation due to high precipitation rates or moisture transport distance may be moderated by increased terrestrial moisture uptake, thereby attenuating any seasonal EASM signal in $\delta^{18}\text{O}$, such as precipitation amount seasonality. Potentially, this explains the lack of a conventional amount effect and unclear seasonality in the available precipitation $\delta^{18}\text{O}$ observations from Wanxiang (Fig. 5.5). Given that land-derived moisture tracks source temperature seasonality (Fig. 5.5), increased summer surface temperatures, which will enhance terrestrial moisture flux, may further reduce the extent to which precipitation $\delta^{18}\text{O}$ reflects EASM precipitation.

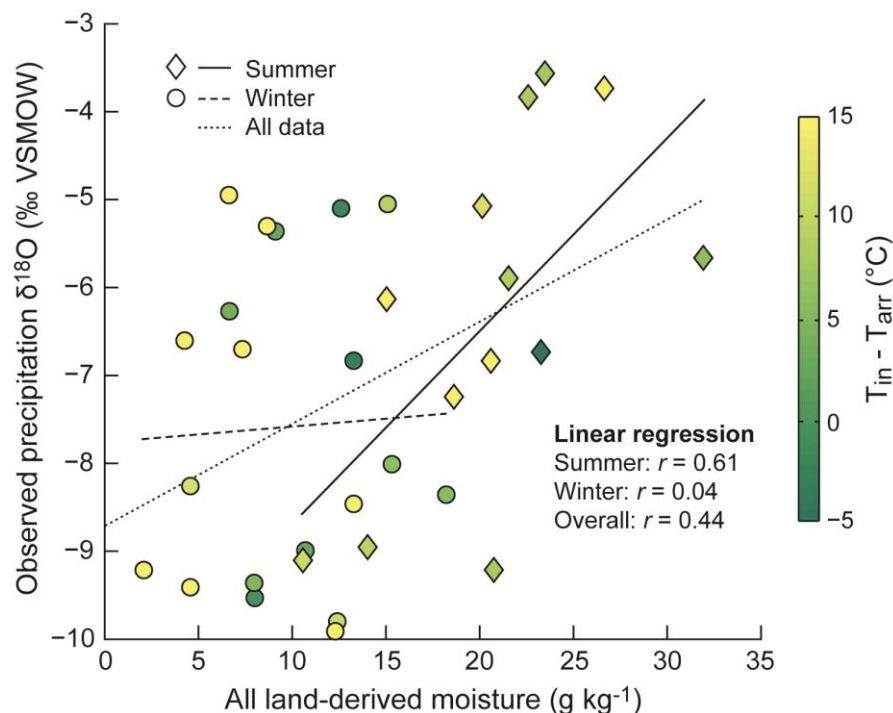


Figure 5.6. Observed precipitation $\delta^{18}\text{O}$ versus terrestrial moisture contribution. Scatter plot of and the linear regression ($n = 33$; $p = 0.01$) between observed summer (diamonds) and winter (circles) precipitation $\delta^{18}\text{O}$ and mean land-derived moisture (evapotranspiration). Summer values ($n = 13$) exhibit a strong trend, where $\sim 4.5 \text{ g kg}^{-1}$ terrestrial input causes 1 ‰ enrichment, but no trend is apparent in winter ($n = 20$). Colours indicate the initial-arrival temperature difference (fractionation potential).

5.3.2.2. Isotopic depletion due to Tibetan Plateau moisture

Wanxiang Cave is located relatively close to the Tibetan Plateau. Few trajectories migrate directly over the Tibetan Plateau (Fig. 5.3 and Fig. 5.4), but moisture is nevertheless derived from relatively high-topographic surrounding areas (see also Fig. 4.3). Given the relative proximity of these high-topographic areas, particularly to the west of Wanxiang Cave, it is hypothesised the contribution of Tibetan Plateau-derived moisture is an important isotopic depletion mechanism for this site. Such moisture is depleted by the altitude effect (see section 1.3.3.1) and by prior rainout under lower cloud temperatures. Several notably depleted modelled values (more negative than the arithmetic mean value)

coincide with peaks in the Tibetan moisture contribution (combined FT and ABL uptake) to precipitation within the Wanxiang target region (Fig. 5.5). Moreover, relatively enriched observed and modelled values during early 2002 correspond with reduced winter Tibetan Plateau moisture contributions. In the case of the 20/03/2002 and 21/07/2002 events, however, this effect was probably overestimated because modelled values (-13.43 and -10.70 ‰, respectively) do not agree with observations (-5.30 and -3.75 ‰, respectively). Modelled $\delta^{18}\text{O}$ for the 16/09/2001 and 18/09/2001 events also overestimates depletion relative to measured values. However, these events, occurring at a time of low Tibetan moisture contribution, cannot be explained by the identified Tibetan Plateau effect. The importance of this effect for sites proximal to the Tibetan Plateau is therefore an interesting focus for future research.

5.3.2.3. *Isotopic depletion due to free troposphere moisture*

Modelled precipitation $\delta^{18}\text{O}$ is significantly, negatively correlated ($r = -0.60$) with the mean amount of moisture derived from the FT by convective processes, such as mixing, averaged over all trajectories for each precipitation event (Fig. 5.7). For the precipitation sampling period, this trend is stronger in for the summer precipitation events than winter events. As the constituent FT moisture component of a given air parcel increases, so too does the degree to which its vapour $\delta^{18}\text{O}$ reflects that of the ambient moisture. This results in depleted $\delta^{18}\text{O}$ because FT moisture often resides at lower tropospheric temperatures than that within the ABL. As with the terrestrial moisture enrichment effect, it is possible that this depletion mechanism is actually temperature-driven. However, this appears not to be the case as no trend with respect to $T_{\text{in}}-T_{\text{arr}}$ is observed (Fig. 5.7). This is consistent with recent modelling linking reduced atmospheric moisture residence time and with increased

ABL-FT moisture exchange and isotopic depletion across various climatic regimes (Aggarwal *et al.*, 2012).

This process may be particularly important for Wanxiang Cave, located at $\sim 33^\circ\text{E}$ and 1200 metres elevation, because both summer and winter precipitation can be supplied by air masses migrating at altitude over central Eurasian regions. The slopes described by the summer (-0.93) and winter (-1.00) data are similar (Fig. 5.7), but mean trajectory arrival heights are lower in summer (~ 3.3 km) than winter (~ 3.9 km). Consequently, trajectory arrival temperatures are higher in summer (6.48°C) than winter (-7.36°C), a difference of $\sim 14^\circ\text{C}$. Greater isotopic depletion should therefore be expected during winter precipitation events. However, less FT moisture uptake occurs in winter than summer, resulting in a more significant summer trend. This is compounded by the intense moisture recycling during the EASM, which extends over the eastern Tibetan Plateau and surrounding high-elevation regions. In summer, therefore, additional depleted moisture derived from these areas is more likely to be mixed into air parcels.

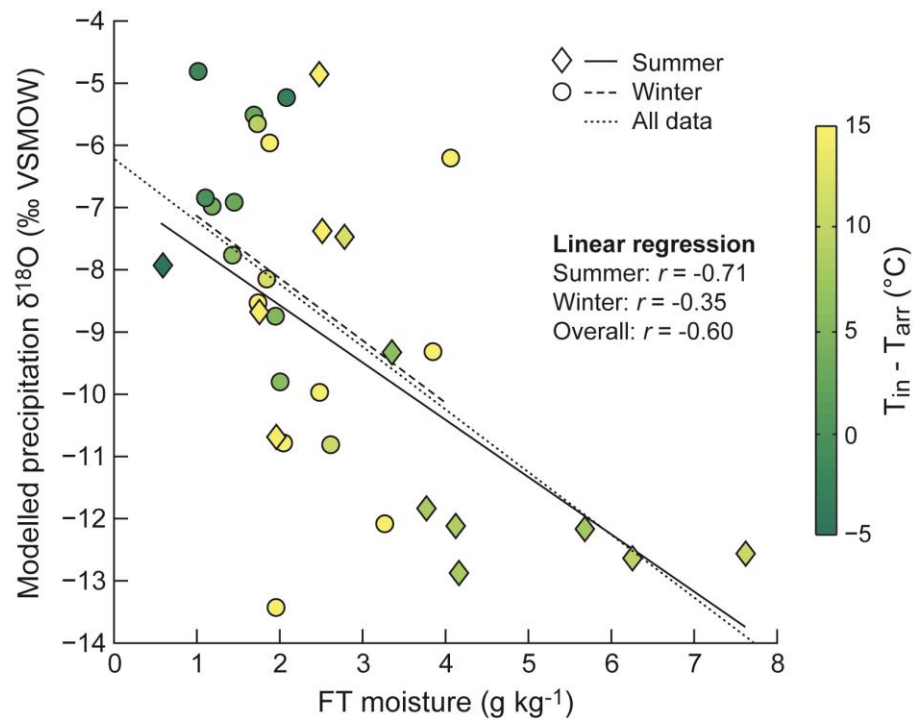


Figure 5.7. Modelled precipitation $\delta^{18}\text{O}$ versus synoptic FT moisture contribution. Scatter plot of and the linear regression ($n = 33$; $p < 0.001$) between modelled summer (diamonds) and winter (circles) precipitation $\delta^{18}\text{O}$ and the mean amount of constituent moisture derived from mixing in the free troposphere. This effect is present year-round, where $\sim 1 \text{ g kg}^{-1}$ FT moisture contribution causes 1 ‰ depletion, though the summer trend is considerably stronger. Colours indicate the initial-arrival temperature difference (fractionation potential).

5.4. Summary and conclusions

Instrumental monitoring datasets and numerical modelling studies are required to improve and validate our understanding of the controls on precipitation variability at key proxy sites. In this chapter, the recently-developed Lagrangian isotope model, Isotra3 (Dütsch, 2013), was used to investigate the hydroclimatic parameters and processes to which synoptic precipitation $\delta^{18}\text{O}$ at Wanxiang Cave, an important site for palaeomonsoon reconstruction located near to the northerly EASM limit, responds. For comparison with

modelling results, an observational dataset of 37 precipitation events sampled at Wanxiang Cave during 2001-2002 was used.

Isotra3 simulates isotopic evolution along three-dimensional Lagrangian trajectories, accounting for phase changes during moisture uptake, transport and precipitation (Fig. 5.2) and taking advantage of quantitatively diagnosed moisture source regions. Only post-condensation exchange processes cannot be represented in Lagrangian models. Mapped trajectories for select precipitation events (Fig. 5.3 and Fig. 5.4), which underwent disparate moisture transport pathways, exhibit distinct isotopic evolution, and neighbouring trajectories experience similar moisture uptake and isotopic fractionation. Modelled precipitation $\delta^{18}\text{O}$ variance of $\sim 10\text{‰}$ attributed air mass ‘history’ is similar to observed variability at Wanxiang ($\sim 7\text{‰}$) and approximately half that observed across central and southern China. Isotra3 reproduces the temporal trend described by observed Wanxiang $\delta^{18}\text{O}$ data reasonably well and provides evidence for the influence of terrestrial moisture (Fig. 5.5).

Land-derived moisture, primarily from evapotranspiration, causes isotopic enrichment, and is positively correlated with observed precipitation $\delta^{18}\text{O}$ (Fig. 5.6). Terrestrial moisture flux is temperature-driven and this effect is thus active in summer, potentially counteracting any isotopic depletion due to strengthened EASM circulation or increased precipitation rate. Conversely, Tibetan Plateau-derived moisture is weakly, negatively correlated with modelled precipitation $\delta^{18}\text{O}$ (Fig. 5.5), potentially responsible for synoptic scale isotopic depletion in particular sampled precipitation events. Moreover, the contribution of FT-derived moisture may also deplete atmospheric vapour (Fig. 5.7). Therefore, terrestrial moisture is an important consideration in using proxy $\delta^{18}\text{O}$ to

reconstructing EASM variability in northern monsoonal China, and this issue may also pertain to more southerly and easterly sites, where summer terrestrial moisture flux is also high (Fig. 4.3). An important implication is that proxy $\delta^{18}\text{O}$ may record EASM variability inaccurately during periods of elevated summer surface temperatures when terrestrial moisture influences may obfuscate any direct EASM signal.

Isotra3 calculates fractionation upon cloud arrival at altitude, yet precipitation $\delta^{18}\text{O}$ is of course measured at the surface. Therefore, accurate representation of post-condensation exchange processes in future isotope modelling studies is crucial. Future long-term precipitation isotope monitoring would benefit from accurate metadata collection, such as precipitation sampling times and event duration data, which will help refine future comparisons between observational precipitation isotope data and model results.

Chapter 6

Validating stalagmite oxygen isotope proxy data interpretations: an ECHAM4-MCIM approach to constructing pseudoproxy records^{*}

^{*} A manuscript based on the work presented in this chapter is currently in preparation for *Climate of the Past*.

Chapter summary

Moisture transport is an important consideration in precipitation and proxy $\delta^{18}\text{O}$ interpretation. Present-day precipitation $\delta^{18}\text{O}$ at Wanxiang Cave responds strongly to terrestrial moisture fluxes on synoptic timescales, as established in Chapter 5. However, the extent to which such processes impact seasonal- to decadal-scale proxy $\delta^{18}\text{O}$ variability requires investigation. In this chapter, the idealised, Rayleigh-type Mixed Cloud Isotope Model (MCIM; Ciais and Jouzel, 1994) is used to model Wanxiang Cave precipitation $\delta^{18}\text{O}$ and to construct a pseudoproxy $\delta^{18}\text{O}$ record for the period AD 1870-2003, which is compared with an annually-resolved Wanxiang stalagmite $\delta^{18}\text{O}$ record (WX42B) from and records from nearby sites. Isotopic fractionation conditions (initial and arrival temperature and pressure, relative humidity, and adiabatic lapse rate) are diagnosed from trajectory data and ECHAM4 data. MCIM does not reproduce observed synoptic precipitation $\delta^{18}\text{O}$ at Wanxiang due to an overestimation of the initial-arrival temperature difference for several events and the exclusion of vapour mixing and exchange processes. However, MCIM does capture the observed range in precipitation $\delta^{18}\text{O}$ for averaged hydroclimatic conditions. Although model optimisation for low- to mid-latitude hydroclimatic conditions is required to reproduce synoptic $\delta^{18}\text{O}$ successfully, the strong temperature-dependence of MCIM is nevertheless well-suited to modelling interannual isotopic variability at Wanxiang Cave at which temperature is a predominant control (Zhang *et al.*, 2008). ECHAM4 temperature and pressure data are input to MCIM to construct a pseudoproxy record driven by terrestrial moisture flux variability, which is weighted by estimated terrestrial moisture flux and stalagmite growth rate, applying published stalagmite growth rate relationships (Baker *et al.*, 1998; Baker *et al.*, 2014). The ECHAM4-MCIM pseudoproxy data reproduce decadal-scale variability exhibited by the WX42B record and records from three sites proximal to Wanxiang Cave, which all exhibit a late 20th Century trend to relatively enriched $\delta^{18}\text{O}$ values. Many interannual $\delta^{18}\text{O}$ fluctuations are also captured. Although the pseudoproxy and WX42B records begin to diverge at approximately 1970, the overall correspondence indicates that the isotopic signature of terrestrial transport is an important driver of multi-annual to decadal proxy $\delta^{18}\text{O}$ variability at Wanxiang Cave and surrounding region.

6.1. Introduction and rationale

Palaeoclimate reconstructions from stalagmite $\delta^{18}\text{O}$ apply a statistically significant relationship between $\delta^{18}\text{O}$ and the reconstructed climate parameter (e.g., precipitation amount, temperature, circulation indices) beyond the calibration period and therefore assume that this relationship remains stationary during the reconstructed period (Baker *et al.*, 2013; Jex *et al.*, 2013; Sturm *et al.*, 2010). Given the results presented in Chapters 4 and 5, it is necessary to (i) isolate the precipitation amount signal in precipitation $\delta^{18}\text{O}$ to develop quantitative palaeo-precipitation records for the EASM region from speleothems and (ii) understand the importance of terrestrial moisture fluxes for interpreting proxy $\delta^{18}\text{O}$ close to the northerly EASM limit. As discussed in Chapter 1, numerical modelling studies are required to quantify the hydroclimatic processes to which precipitation and proxy $\delta^{18}\text{O}$ respond, complimenting monitoring studies and improving our understanding of past climate variability and climate system sensitivity by validating proxy data interpretations. Creating synthetic, pseudoproxy records and comparing these data with ‘observed’ proxy records addresses this assumption. One *a priori* approach to this is forward modelling of speleothem $\delta^{18}\text{O}$ data to understand the causes of relatively high-frequency variability (e.g., sub-annual to annual) in proxy datasets and reducing uncertainty in palaeoclimate interpretations. Previous forward modelling studies (see section 1.4.2) have focussed on parameterising groundwater $\delta^{18}\text{O}$ evolution due to karst hydrology processes (Baker and Bradley, 2010; Baker *et al.*, 2013; Bradley *et al.*, 2010; Jex *et al.*, 2013; Truebe *et al.*, 2010) and surface environmental conditions (Managave, 2014; Wackerbarth *et al.*, 2010), and combined speleothem $\delta^{18}\text{O}$ models with GCM precipitation $\delta^{18}\text{O}$ outputs (Lohmann *et al.*, 2013; Wackerbarth *et al.*, 2012).

In this chapter, the Mixed Cloud Isotope Model (MCIM) of Ciais and Jouzel (1994), an idealised, Rayleigh-type isotope model, is used to investigate the degree to which Wanxiang proxy $\delta^{18}\text{O}$ responds to terrestrial moisture fluxes on seasonal to decadal timescales. To achieve this, (i) the sensitivity of $\delta^{18}\text{O}$ modelled by MCIM to typical subtropical fractionation conditions and the overall temperature-dependence of MCIM are assessed; (ii) MCIM is used to model precipitation event $\delta^{18}\text{O}$ at Wanxiang Cave (and compared with the available observational dataset previously discussed in Chapter 5) to test MCIM's ability to reproduce the observed range in precipitation $\delta^{18}\text{O}$ variability at Wanxiang; (iii) pseudoproxy records are constructed for the period AD 1870-2003 based on ECHAM4 temperature and pressure data (as inputs to MCIM) and estimated moisture flux data. These pseudoproxy records are compared with the approximately annually-resolved portion of the high-profile WX42B stalagmite $\delta^{18}\text{O}$ record from Wanxiang Cave to test the degree to which these proxy data respond to moisture source seasonality, as hypothesised in Chapter 5.

6.2. The Mixed Cloud Isotope Model

6.2.1. Overview

MCIM is a zero-dimensional Rayleigh distillation model in which kinetic fractionation at the moisture source and mixed-phase cloud (coexisting water vapour, liquid droplets and ice) microphysical processes are parameterised (Ciais and Jouzel, 1994). MCIM calculates fractionation along an idealised condensation pathway (Fig. 6.1) specified by evaporation and arrival temperatures and pressures, the cooling associated with which leads to rain formation. MCIM calculates the condensation temperature for a hypothetical air parcel by

elevating it from the sea surface to its lifting condensation level (i.e., 100 % relative humidity) adiabatically. Condensation and cloud formation occurs at a cloud-scale relative humidity of 100 %. To simulate this, MCIM uses a humidity threshold, which is set to 80 % to account for the discrepancy between cloud size and model resolution, following Helsen *et al.* (2006). A fixed temperature threshold of -5.15 °C is used to initiate ice formation above 80 % relative humidity; above this temperature threshold, air parcels contain no constituent ice (Ciais and Jouzel, 1994). MCIM then calculates Rayleigh fractionation along a moist adiabat until the specified arrival pressure and temperature condition is reached. However, MCIM does not take into account evaporation below the cloud base and exchange with ambient atmospheric vapour during rainout (Eames, 2008).

Following Sodemann *et al.* (2008), initial isotopic compositions of evaporated vapour are taken from an ECHAM4 simulation (Hoffmann *et al.*, 1998)[†]. ECHAM4 has been demonstrated to reproduce a realistic spatial distribution of isotopic variability (Vuille *et al.*, 2003) and previously used to simulate the sensitivity of water $\delta^{18}\text{O}$ to Asian Monsoon circulation (Vuille *et al.*, 2005). The use of GCM data avoids reliance on the global closure assumption (where the isotopic composition of global evaporation and precipitation are equal), which is inconsistent with isotope observations on local scales (Helsen *et al.*, 2006; Jouzel and Koster, 1996; Pfahl and Sodemann, 2014).

[†] These publically-available data are the result of the Stable Water Isotope Intercomparison Group (SWING) S1B experiment, a simulation driven by HadISST data (version 1.1) over the period 1870-2003, and were obtained from <http://atoc.colorado.edu/~dcn/SWING/index.php> on 16/10/2013.

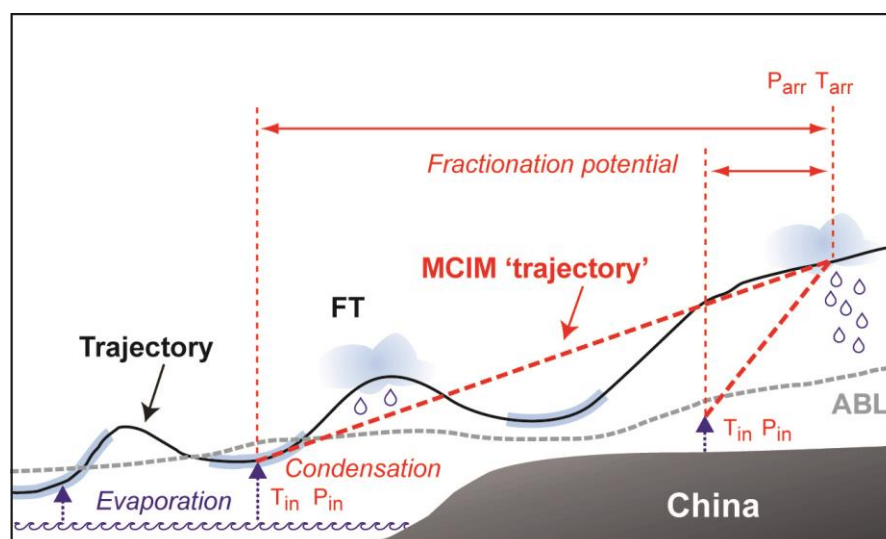


Figure 6.1. Schematic overview of MICM. MCIM calculates isotopic fractionation along an idealised fractionation pathway (red dashed line) between initial and arrival temperatures and pressures (defining fractionation potential) at given relative humidity and adiabatic lapse rate conditions. Adapted from Sodemann *et al.* (2008).

6.2.2. MCIM sensitivity tests

Recent sensitivity testing using MCIM (Eames, 2008) focussed on optimising model performance for reproducing precipitation $\delta^{18}\text{O}$ measured at stations around the British Isles. Sensitivity testing with MCIM for low latitude, tropical climatic conditions is absent from the literature. Therefore, simple tests were conducted to establish the output precipitation $\delta^{18}\text{O}$ ranges resulting from initial and arrival temperatures and pressures and relative humidity conditions representative of the region in question (Fig. 6.2). In all tests, initial (surface) pressure (P_{in}) and temperature (T_{in}) were kept constant at typical low-latitude values of 1000 hPa and 20 °C, respectively, and a constant initial relative humidity of 80 % was used. Additionally, a standard adiabatic lapse rate of -6.5 °C km^{-1} was used.

Depleted precipitation $\delta^{18}\text{O}$ values result from decreased cloud arrival temperatures (Fig. 6.2). For constant P_{in} , T_{in} , initial relative humidity, and a standard lapse rate, the mean rate of isotopic change with P_{arr} across the tested range of arrival temperatures is -0.014‰ hPa^{-1} (Fig. 6.2a). The rate of change with T_{arr} across the tested range of arrival pressures is 0.57‰ °C^{-1} (Fig. 6.2b). Precipitation $\delta^{18}\text{O}$ variation as a function of P_{arr} becomes increasingly non-linear with decreasing cloud arrival temperature. Below 0 °C , the rate of ^{18}O depletion as a function of T_{arr} increases slightly under all of the tested pressure conditions (Fig. 6.2b).

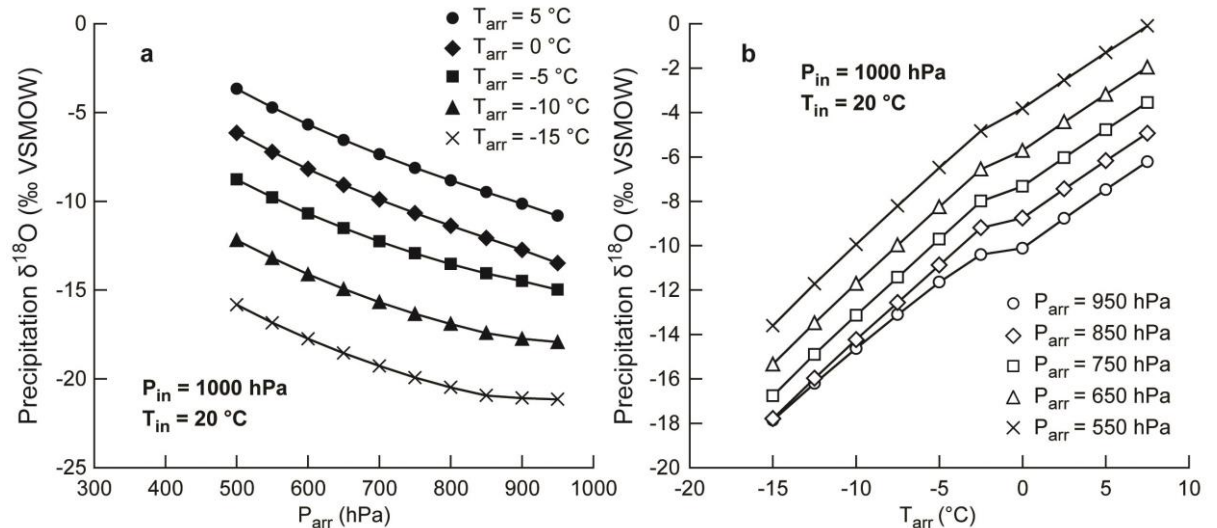


Figure 6.2. MCIM sensitivity test results. Initial (surface) pressure (P_{in}) and temperature (T_{in}) were kept constant at 1000 hPa and 20 °C, respectively. (a) Precipitation $\delta^{18}\text{O}$ output by MCIM versus P_{arr} across a range of temperature decreases from constant T_{in} (20 °C). T_{arr} is varied between 5 and -15 °C. (b) Precipitation $\delta^{18}\text{O}$ versus T_{arr} across a range of pressure decreases from $P_{\text{in}} = 1000 \text{ hPa}$ for constant T_{in} (20 °C). P_{arr} is varied between 950 and 550 hPa.

6.3. Data and methods

6.3.1. Diagnosed isotopic fractionation conditions

Atmospheric trajectories precipitating over Wanxiang Cave were used to determine representative values for each input parameter required by MCIM. For each sampled precipitation event, trajectories whose arrival height over the Wanxiang Cave target region exceeded 1.5 times ABL height were excluded. From the remaining trajectories, mean initial source conditions were computed for each sampled precipitation event by weighting each input parameter (temperature, pressure and relative humidity) by specific humidity (moisture uptake) at each timestep along every precipitating trajectory, giving a single uptake-weighted mean value for each input parameter. For each sampled precipitation event, mean arrival conditions are weighted mean values calculated from every trajectory at the arrival timestep. In addition, adjusted lapse rates for each event were calculated, following Sodemann *et al.* (2008). These initial and arrival input data as well as the initial $\delta^{18}\text{O}$, taken from monthly ECHAM4 data (Hoffmann *et al.*, 1998), are provided in Appendix 5. Therefore, although MCIM calculates fractionation along an idealised condensation pathway, the results presented in this chapter are nevertheless based on realistic initial and arrival conditions, according to the trajectory data. Fig. 6.3 gives the ranges in each input parameter across all sampled precipitation events, each of which describes an approximately normal distribution.

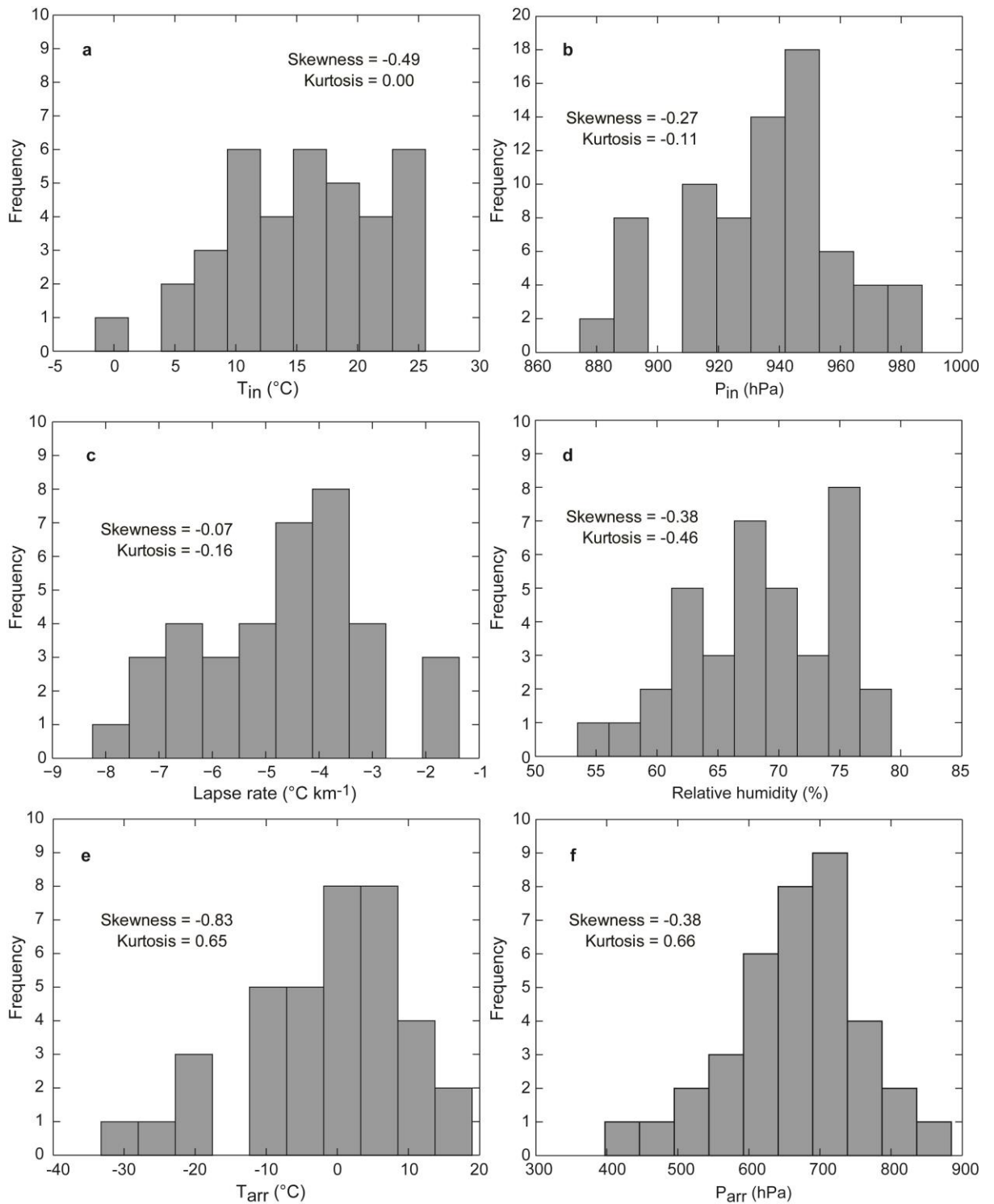


Figure 6.3. Diagnosed synoptic fractionation conditions. Histograms displaying the range in initial (a) temperature and (b) pressure, (c) adjusted lapse rates, (d) surface relative humidity, and arrival (e) temperature and (f) pressure. Kurtosis values are bias-corrected. These input data are provided in Appendix 5.

6.3.2. MCIM precipitation event $\delta^{18}\text{O}$ model runs

Prior to constructing pseudoproxy $\delta^{18}\text{O}$ records for Wanxiang Cave utilising MCIM, the extent to which MCIM (i) simulates the observed range in Wanxiang precipitation $\delta^{18}\text{O}$ based on average hydroclimatic conditions and (ii) simulates individual precipitation event $\delta^{18}\text{O}$ are investigated. It is anticipated that the strong temperature-dependence of MCIM makes this model better suited to simulating isotopic variability on interannual- to decadal-scale than synoptic timescales. As discussed in Chapter 5, simulating precipitation $\delta^{18}\text{O}$ for individual events requires detailed, event- and site-specific moisture transport information. However, it is important to first assess the overall temperature-dependence of MCIM and to establish its ability to reproduce the observed present-day range in Wanxiang precipitation $\delta^{18}\text{O}$.

For comparison with observed event-scale precipitation $\delta^{18}\text{O}$ variability at Wanxiang Cave during 2001-2002, two MCIM runs were performed using fractionation conditions diagnosed for each individual precipitation event (Fig. 6.3) with initial vapour $\delta^{18}\text{O}$ given by ECHAM4 and from the global closure assumption (i.e., without GCM initialisation of $\delta^{18}\text{O}$). A simplified MCIM run was also performed by averaging the computed input data (Fig. 6.3) across all sampled precipitation events, constituting a simulation of mean hydroclimatic conditions. In this run, each MCIM calculation in this run was performed with identical initial and arrival conditions and only initial vapour $\delta^{18}\text{O}$ value varies.

6.3.3. ECHAM4-MCIM approach to creating pseudoproxy records

Chapter 5 presents synoptic-scale evidence for control of precipitation $\delta^{18}\text{O}$ at Wanxiang Cave by surface temperature-driven terrestrial moisture fluxes, indicating that proxy $\delta^{18}\text{O}$

data will predominantly inherit the isotopic signature of precipitation recycling processes. To test the extent to which terrestrial moisture transport processes control $\delta^{18}\text{O}$ variability on seasonal to decadal timescales, monthly ECHAM4 temperature and pressure data for the period 1870-2003 are input to MCIM to simulate the average hydroclimatic fractionation conditions experienced by moistures mass responsible for precipitation over Wanxiang Cave during this period. Based on these MCIM runs, pseudoproxy stalagmite $\delta^{18}\text{O}$ records are constructed and compared with the uppermost, approximately annually-resolved portion of the record of Zhang *et al.* (2008) over the same period, obtained from the WX42B stalagmite (sampled in 2003). Additionally, pseudoproxy data are compared with published stalagmite $\delta^{18}\text{O}$ records from Huangye Cave (Tan *et al.*, 2011), Wuya Cave (Tan *et al.*, 2014), and Dayu Cave (Tan *et al.*, 2009), which are the nearest sites to Wanxiang Cave yet exploited for speleothem sampling (Fig. 6.4; see section 3.3.1). The mean temporal resolutions of the Wanxiang, Huangye, Wuya and Dayu records are 1.3, 4.7, 1.4 and 1.3 years, respectively.

ECHAM4 precipitation $\delta^{18}\text{O}$ data are primarily forced by SST variability (Hoffmann *et al.*, 1998). Wanxiang Cave's relatively northerly location results in predominantly terrestrial moisture sources and therefore these $\delta^{18}\text{O}$ data are not used to represent the isotopic variability at Wanxiang during 1870-2003. Instead, weighted mean source locations were calculated for December-February and June-August (Fig. 6.4). The mean DJF location is located east of Tibetan Plateau and the mean JJA location is located further south and closer to the Loess Plateau region. These source locations are separated by 274 km. For each, monthly surface temperature, pressure, horizontal wind speed, and initial surface water $\delta^{18}\text{O}$ were extracted from the ECHAM4 S1B dataset for the period 1870-2003.

Relative humidity was fixed at 90 % and arrival pressure was fixed at 500 hPa, at which corresponding arrival temperatures were extracted.

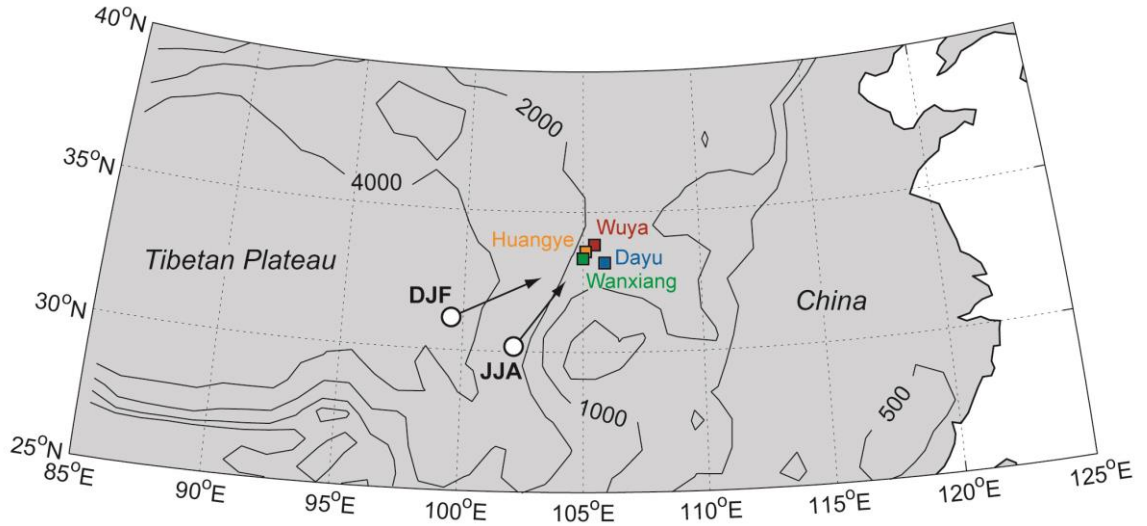


Figure 6.4. Seasonal mean source locations for precipitation at Wanxiang Cave. Specific humidity-weighted DJF and JJA source locations are 97.5 °E, 31.2 °N and 102.1 °E, 30.2 °N, respectively. Cave sites discussed in section 6.3.2 are shown. Huangye and Wuya are located ~30 and ~63 km northeast of Wanxiang Cave, respectively. Topographic contours (solid lines) are in metres a.m.s.l.

These input data were used to perform two MCIM runs, generating monthly modelled precipitation $\delta^{18}\text{O}$ time series for 1870-2003 for each source seasonal mean source location, which potentially more accurately reflect Wanxiang isotopic variability than ECHAM4 data. Moisture uptake (Q_{land}) at both source locations was then calculated based on surface temperature (Fig. 6.5) using the following transfer function:

$$Q_{\text{land}} = 0.7376 T_{\text{in}} + 7.579 \quad (\text{Equation 6.1})$$

These uptake data were used to weight modelled precipitation $\delta^{18}\text{O}$, creating a single composite monthly mean precipitation $\delta^{18}\text{O}$ time series. ECHAM4 precipitation and surface temperature data were extracted for Wanxiang and used to calculate hydrologically effective precipitation (water excess) using the equation of Thornthwaite (1948), by which composite precipitation $\delta^{18}\text{O}$ data were weighted to represent dripwater $\delta^{18}\text{O}$. These values were then converted to calcite $\delta^{18}\text{O}$ using the temperature-dependent equilibrium fractionation equation of Kim and O'Neil (1997), which was chosen assuming equilibrium fractionation based on the results of Hendy tests performed by Zhang *et al.* (2008). The Q_{land} - and water excess-weighted pseudoproxy records therefore account for precipitation seasonality in the Wanxiang region. All data described in this section are provided in Appendix 6.

Furthermore, a 'control' run was performed without explicit moisture uptake constraints and instead weighted by predicted stalagmite growth rate. This run uses the same input data from ECHAM4, but without segregating precipitation $\delta^{18}\text{O}$ inputs from two seasonal mean source locations. Monthly modelled precipitation $\delta^{18}\text{O}$ were instead weighted by predicted stalagmite growth rate, calculated assuming an ideal drip response to accurately transfer a clear net climate signal (denoted 'a' in Fig. 1.1). The ^{230}Th dates reported by Zhang *et al.* (2008) indicate that WX42B accumulated linearly at an average rate of $\sim 100 \mu\text{m yr}^{-1}$. Based on the equation for vertical stalagmite growth rate (Baker *et al.*, 1998; Baldini *et al.*, 2008; Buhmann and Dreybrodt, 1985; Dreybrodt, 1999) and relationships in Baldini (2010) and Baker *et al.* (2014), this requires a mean cave air $p\text{CO}_2$ of ~ 4000 ppm and a corresponding $[\text{Ca}^{2+}]_{\text{app}}$ of 1.67 mmol L^{-1} . The mean interval between drips for the WX42B site in Wanxiang Cave is ~ 2 s (Johnson, 2004). Monthly dripwater Ca^{2+} was calculated using a linear equation relating Ca^{2+} concentrations to surface temperature and

hydrologically-effective precipitation (Baker *et al.*, 2014). Dripwater film thickness was assumed to be ~0.2 mm because the uppermost ~15 mm of WX42B exhibits relatively sharp curvature. For further discussion on the relationships between, vertical stalagmite accumulation, cave environment, stalagmite morphology, and surface meteorological parameters, see Chapter 1 and Chapter 2 (Baker *et al.*, 2014).

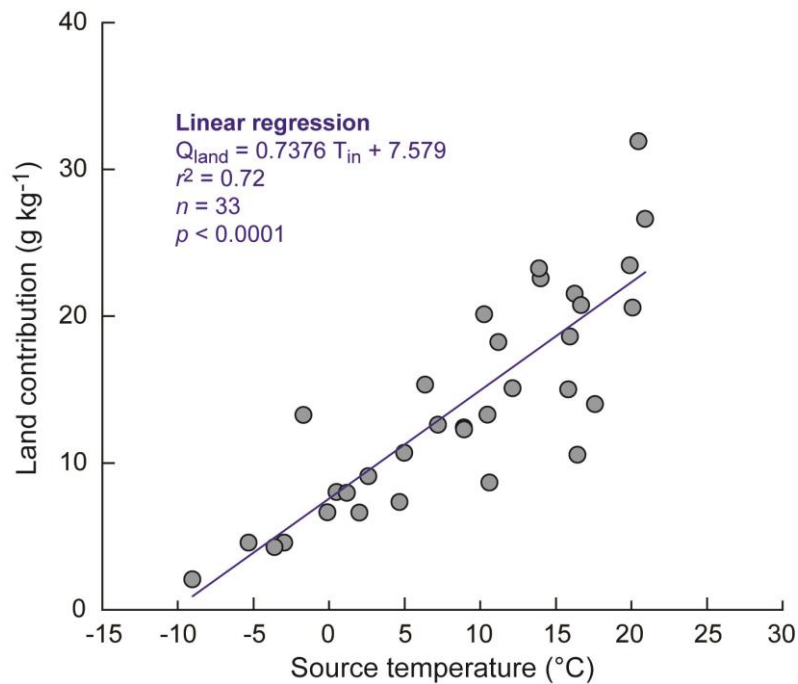


Figure 6.5. Correlation between surface temperature and terrestrial moisture uptake. Linear regression between the terrestrial moisture contribution (Q_{land}) to sampled Wanxiang precipitation events (see Chapter 5) and T_{in} , which are significantly ($p = 5.15 \times 10^{-10}$), positively correlated.

6.4. Wanxiang Cave precipitation $\delta^{18}\text{O}$ modelled by MCIM

MCIM fails to reproduce synoptic precipitation $\delta^{18}\text{O}$ observed at Wanxiang Cave, except events sampled during July-August 2002 (Fig. 6.6a). In particular, certain winter values are unrealistically depleted for this low- to mid-latitude region when compared with the global

precipitation $\delta^{18}\text{O}$ interpolation of Bowen and Wilkinson (2002), which is based on GNIP data. As discussed in section 6.3, it is anticipated that MCIM is best-suited to simulating longer-terms isotopic variability, and the idealised nature of MCIM highlights the necessity of accounting for site- and event-specific isotopic evolution, as demonstrated in Chapter 5.

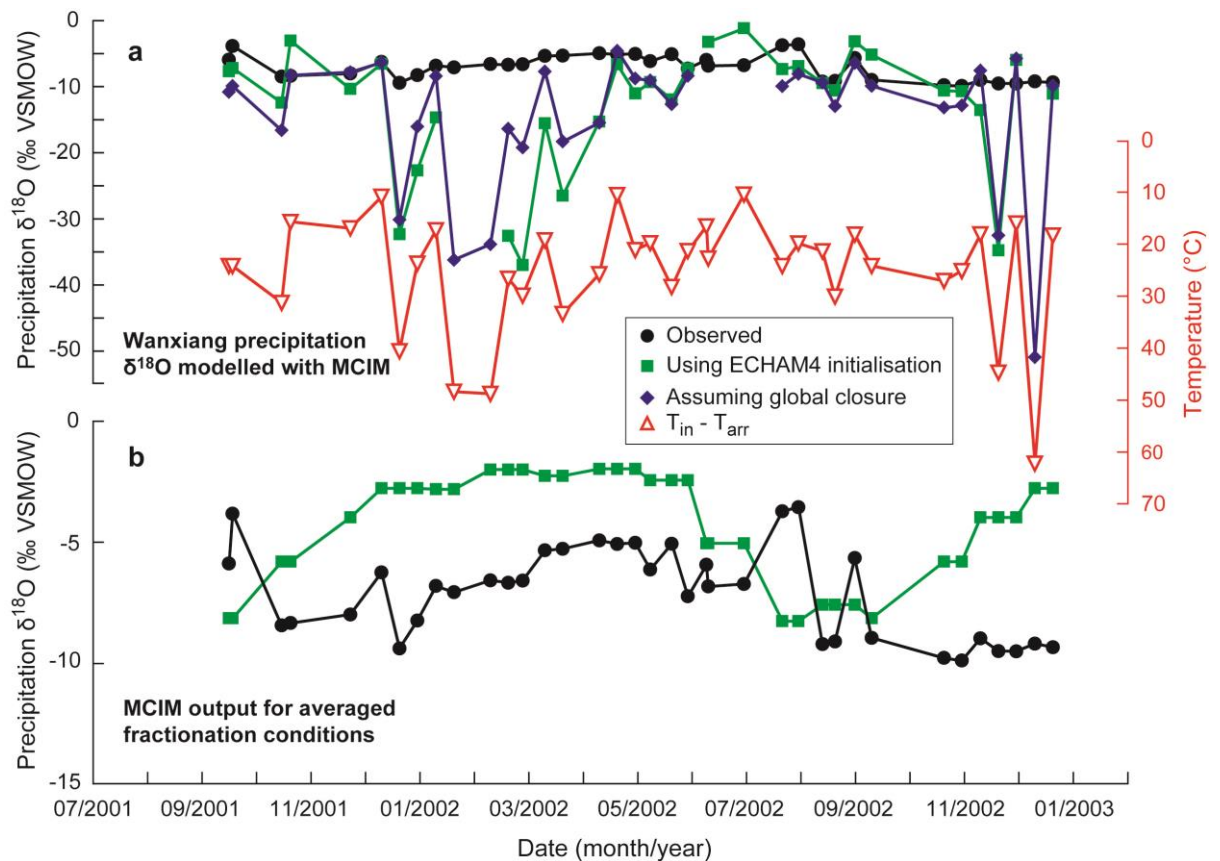


Figure 6.6. Wanxiang Cave precipitation $\delta^{18}\text{O}$ modelled by MCIM. (a) Precipitation $\delta^{18}\text{O}$ measured at Wanxiang Cave (black circles) compared with $\delta^{18}\text{O}$ modelled by MCIM (green squares) using diagnosed initial and arrival conditions (Fig. 6.3). $T_{in} = 15.6$ °C, $P_{in} = 934.8$ hPa, surface relative humidity = 68.6 %, $T_{arr} = -1.7$ °C, and $P_{arr} = 666.9$ hPa. Also shown is the MCIM run assuming global closure (i.e., without ECHAM4 $\delta^{18}\text{O}$ initialisation; blue diamonds) and the difference between initial and arrival temperature diagnosed from adjusted lapse rates (red open triangles). Note that the temperature y-axis is inverted. (b) Measured precipitation $\delta^{18}\text{O}$ (black circles) compared with MCIM run using initial and arrival conditions averaged over every sampled precipitation event. For each ECHAM4-initialised MCIM run, initial vapour $\delta^{18}\text{O}$ values were taken from ECHAM4 at the specific humidity-weighted mean uptake location. Missing values in the modelled $\delta^{18}\text{O}$ series represent the excluded events for which trajectory arrival heights (calculated from P_{arr}) exceeded 1.5 times ABL height.

During winter, Wanxiang is influenced by the Westerlies and depleted moisture is therefore sourced from mid- to high-latitude central Eurasia. For example, the extent of isotopic depletion observed in precipitation sampled during December 2001 is much overestimated by MCIM (Fig. 6.6a). One probable explanation for this is that input ECHAM4 $\delta^{18}\text{O}$ values taken from mean moisture source locations (see Appendix 5) are appreciably more depleted than the available GNIP data (Fig. 5.1), suggesting ECHAM4 overestimates depletion in low-to-mid-latitude continental Asia. However, the results of the ECHAM4-initialised and global closure runs are similar, implicating additional factors. The $T_{\text{in}}-T_{\text{arr}}$ difference, or fractionation potential, is also high at this time (Fig. 6.6a). To reiterate, MCIM calculates fractionation at altitude, yet precipitation $\delta^{18}\text{O}$ is measured at the surface, and therefore mixing and exchange processes, to which local precipitation $\delta^{18}\text{O}$ signals may be sensitive, according to recent results (Dütsch, 2013), are ignored. A combination of these factors is likely responsible for the inaccurate MCIM results and optimisation of MCIM for relatively low-latitude regions is required to accurately simulate synoptic $\delta^{18}\text{O}$.

By running MCIIM under averaged diagnosed fractionation conditions reproduces the pattern of spring and early summer values, across the onset and establishment of the EASM season, reasonably, but late EASM season and winter values are not well reproduced (Fig. 6.6b). For example, depleted values during December 2001 and August-September 2002 are not reproduced by varying initial $\delta^{18}\text{O}$ alone. Variability in modelled and observed precipitation $\delta^{18}\text{O}$ ($\sim 6\text{‰}$) agree closely (Fig. 6.6b). In regions which experience high summer precipitation recycling rates (see Fig. 4.10), local precipitation $\delta^{18}\text{O}$ signals may be conserved (i.e., reflect initial source compositions) if, as with Wanxiang, a significant proportion of moisture is derived from terrestrial regions. If

sourced directly from ocean regions, less precipitation $\delta^{18}\text{O}$ variability would be expected because seawater $\delta^{18}\text{O}$ variability (*sensu* LeGrande and Schmidt, 2006) across the northern Indian Ocean is much less than that of terrestrial water (see Table 5.1) and would therefore not reproduce the $\sim 6\text{‰}$ range in variability observed at Wanxiang.

Modelled $\delta^{18}\text{O}$ is inversely related to the $T_{\text{in}}-T_{\text{arr}}$ difference (Fig. 6.7). Therefore, resulting from the absence of explicit moisture and precipitation constraints in MCIM, a temperature effect predominates. In section 5.4, the role of isotopic evolution during different stages of moisture transport is investigated using the much less idealised Isotra3 and, though better reproducing the observed precipitation $\delta^{18}\text{O}$ variability in this case, such hydroclimatic variability is ‘smoothed’ by averaging realistic diagnosed isotopic fractionation conditions. For example, depleted values observed at Wanxiang during November-December 2002 contrast with relatively enriched values observed at proximal GNIP stations. MCIM values from this simplified run are similarly enriched, and therefore capture ‘average’ isotopic behaviour in the Wanxiang region but not event- and site-specific effects (Fig. 6.6b).

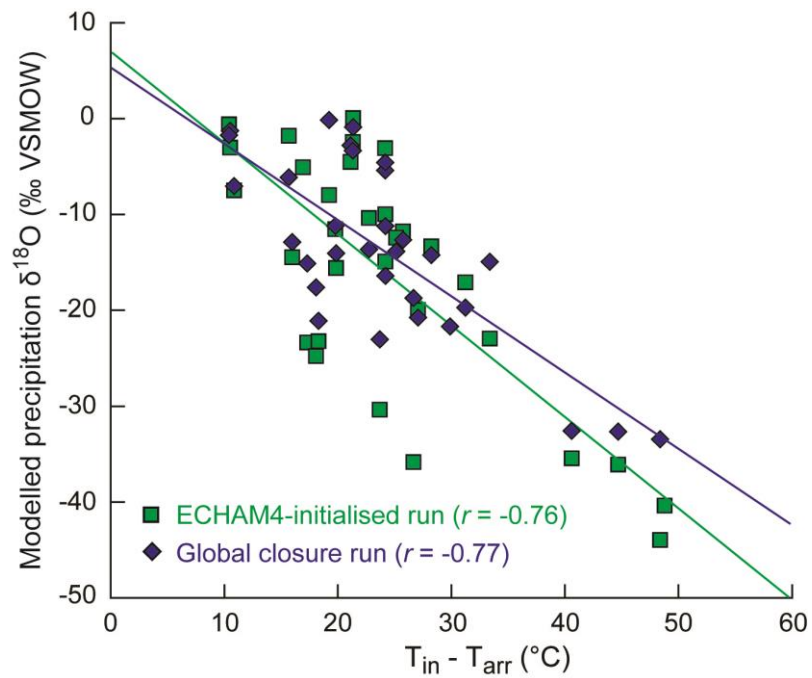


Figure 6.7. Correlation between modelled precipitation $\delta^{18}O$ and temperature change. Scatter plot of precipitation $\delta^{18}O$ output by the final ECHAM4-initialised (green squares) and global closure (blue diamonds) MCIM runs (as shown in Fig. 6.6a) versus initial-arrival temperature difference (or fractionation potential). Corresponding lines represent the linear regressions. For both the ECHAM4-initialised and global closure runs, $n = 31$ and $p < 0.0001$.

6.5. Wanxiang proxy $\delta^{18}\text{O}$ response to terrestrial moisture fluxes

The resolution of the ECHAM4-MCIM pseudoproxy records is annual, which approximates the mean resolution of the WX42B record of 1.3 years during 1870-2003. Mean pseudoproxy and WX42B stalagmite $\delta^{18}\text{O}$ are ~ 8 ‰. The modelled record exhibits greater variability than the WX42B record (Fig. 6.8), which is likely due to the exclusion of karst hydrological processes (such as groundwater storage and mixing), which may dampen surface hydrologically variability. Unfortunately, little quantitative constraints for hydrological processes exist for the Wanxiang system, and it is therefore difficult to quantify the attenuation of precipitation isotope fluctuations due to karst water processing. To mitigate the absence of such constraints, the proxy and pseudoproxy datasets were converted to normalised z-Scores (Fig. 6.9). Secular variability in the normalised WX42B and modelled records matches well between 1870 and 1970, for the majority of the period in question, except only for relatively enriched values during 1925-1931. The pseudoproxy data reproduce the WX42B interannual variability, but the records begin to diverge after approximately 1960. The modelled record also closely tracks decadal variability in the nearby Huangye Cave (Tan *et al.*, 2011), Wuya Cave (Tan *et al.*, 2014) and Dayu Cave (Tan *et al.*, 2009) records. Note that the Huangye record exhibits more depleted $\delta^{18}\text{O}$ values due to the higher elevation of this cave site (altitude effect). The pseudoproxy record mimics many interannual fluctuations exhibited by the two highest-resolution records (Wanxiang and Wuya). (Note that the lower-resolution WY27 record described by Tan *et al.* (2014) is not included here, but this co-varies closely with the WY33 record shown.) A trend towards increasingly isotopically-enriched compositions during the late 20th Century is apparent in both the proxy and pseudoproxy records, which is likely driven by increasing mean surface temperature and terrestrial moisture flux. WX42B stalagmite $\delta^{18}\text{O}$ trends towards relatively enriched $\delta^{18}\text{O}$ from approximately 1985, which is more

apparent in the normalised data, and this tracks the instrumental mean annual temperature trend recorded at the Wudu meteorological station (Fig. 6.8). The Huangye and Wuya records exhibit similar trends towards relatively enriched ratios beginning in approximately 1955 and 1980, respectively.

Both pseudoproxy records exhibit similar decadal-scale trends, though the range in variability in is ~ 0.5 ‰ lower in the growth rate-weighted record, indicating that karst storage and mixing must be invoked to further reduce the pseudoproxy data to the absolute range exhibited by the WX42B data of ~ 0.8 ‰ during this time period. Interannual correspondence between the two pseudoproxy records is reasonable, which indicates that growth rate fluctuations are unlikely to cause significant modification of net isotopic signatures in WX42B, as suggested by Baldini *et al.* (2008), at this site.

Perfect correlation between the WX42B and pseudoproxy records is not expected because net climate signatures are not transmitted linearly through a karst system (Bradley *et al.*, 2010; Fairchild *et al.*, 2006) and may also suffer from chronological uncertainties associated with the proxy records. Although the interannual correspondence between modelled and measured stalagmite $\delta^{18}\text{O}$ is variable, secular WX42B trends are relatively well reproduced. The modelled records are primarily dependent on changing temperature trends (both surface and at altitude) and moisture fluxes, and the most recent portion of the WX42B record is more strongly correlated with instrumental temperature than precipitation data (Zhang *et al.*, 2008). Therefore, precipitation amount and temperature signals may be difficult to distinguish at Wanxiang Cave. Although rainfall and stalagmite $\delta^{18}\text{O}$ may be depleted by increased rainfall; such an increase is associated with increased temperature-driven moisture fluxes in this region. In Chapter 5, this was shown to be

apparent in synoptic-scale isotopic data, but the WX42B and pseudoproxy records show common secular variability, indicating that this mechanism may also be significant on multi-annual to decadal scales.

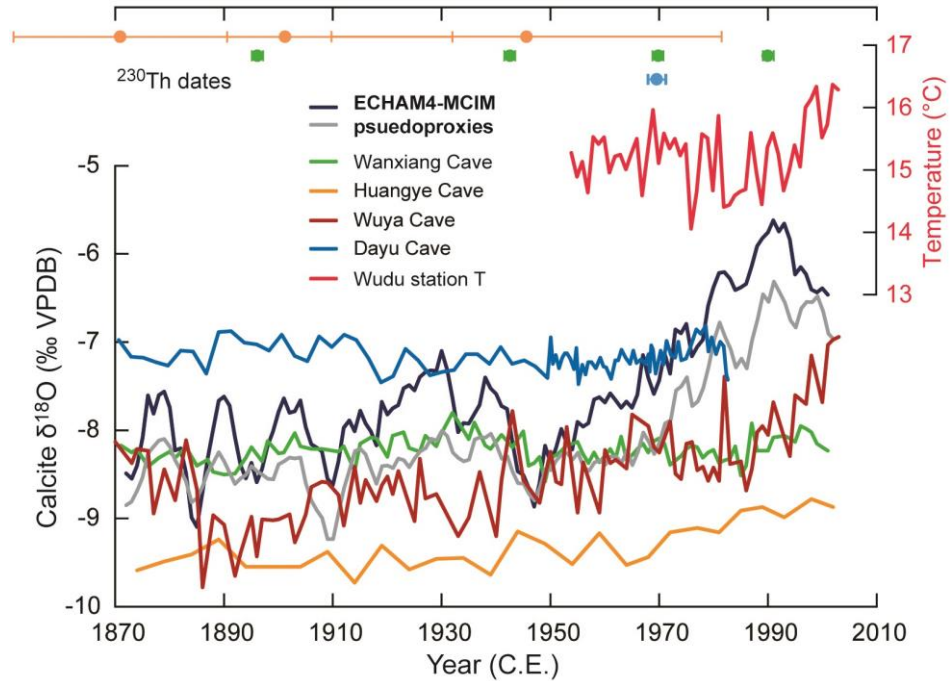


Figure 6.8. Comparison of Wanxiang stalagmite $\delta^{18}\text{O}$, nearby records, and pseudoproxy data. WX42B stalagmite $\delta^{18}\text{O}$ (green) compared with ECHAM4-MCIM pseudoproxy $\delta^{18}\text{O}$ during the period 1870–2003. The composite result from mean DJF and JJA moisture sources (dark blue) and a stalagmite growth rate-weighted ‘control’ run (grey) are shown. Shown for comparison are the nearby records of Tan *et al.* (2011), obtained from the HS3 stalagmite from Huangye Cave (orange); Tan *et al.* (2014), obtained from the WY33 stalagmite from Wuya Cave (red); and Tan *et al.* (2009), obtained from the DY-1 stalagmite from Dayu Cave (pale blue). Colours correspond to cave sites indicated on Fig. 6.4. Published ^{230}Th dates between 1870–2003 for the Wanxiang, Huangye and Dayu records are given with reported uncertainties. The WY33 record chronology is based on petrographic laminae counting. The WX42B record is shown shifted back by two years within in dating uncertainty and as a five-year running average (equal to the averaging performed prior to correlation with instrumental surface precipitation and temperature data by Zhang *et al.* (2008)). Instrumental mean annual surface temperature data (pink) recorded at the Wudu meteorological station proximal to Wanxiang Cave show an increasing trend from 1985. ECHAM4 data also exhibit this temperature increase from approximately 1960, which reflects broad regional changes in China reproduced by ECHAM4.

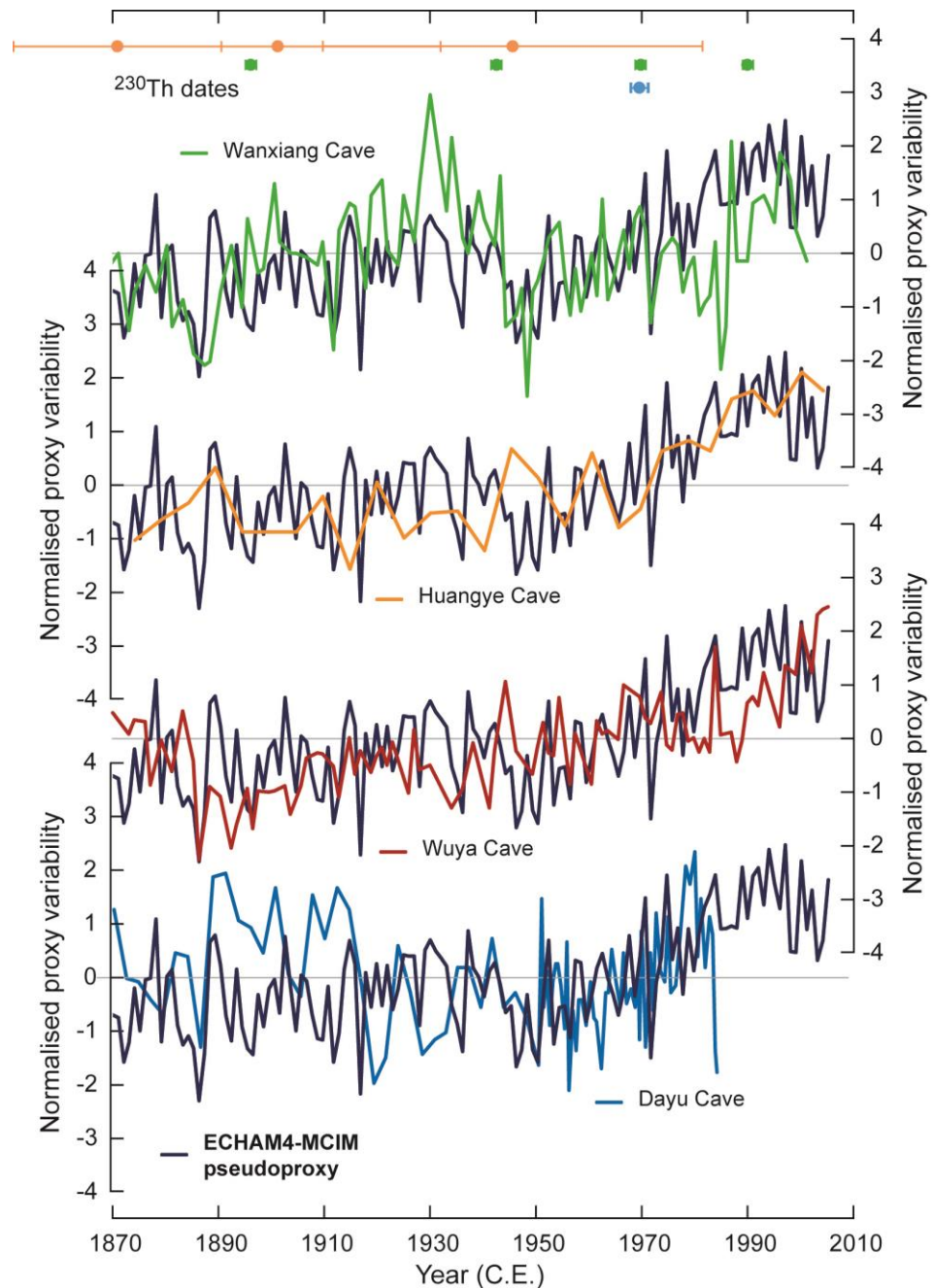


Figure 6.9. Comparison of normalised Wanxiang stalagmite $\delta^{18}\text{O}$, nearby records, and pseudoproxy data. Normalised (z-Scores) pseudoproxy $\delta^{18}\text{O}$ (dark blue) compared with normalised stalagmite proxy $\delta^{18}\text{O}$ from WX42B (green), HS3 (orange), WY33 (red), and DY-1 (pale blue). Note colours correspond to cave sites indicated on Fig. 6.4. Normalised pseudoproxy data are un-smoothed. Published ^{230}Th dates between 1870–2003 for the Wanxiang, Huangye and Dayu records are given with reported uncertainties. The WY33 record chronology is based on petrographic laminae counting. The WX42B record is shown shifted back by two years within dating uncertainty.

6.6. Summary and conclusions

In this chapter, ECHAM4 data and MCIM, an idealised Lagrangian isotope model, are used to model Wanxiang Cave precipitation event $\delta^{18}\text{O}$, assessing the temperature-dependence of MCIM in a subtropical environmental setting, and to construct 134-year pseudoproxy stalagmite $\delta^{18}\text{O}$ records, which are compared with the annually-resolved Wanxiang record of Zhang *et al.* (2008) and additional records from nearby cave sites.

To model precipitation $\delta^{18}\text{O}$, the idealised Rayleigh-type isotope fractionation model, MCIM (Ciais and Jouzel, 1994), was run under averaged initial and arrival conditions, with only initial vapour $\delta^{18}\text{O}$ allowed to vary. The resulting precipitation $\delta^{18}\text{O}$ reproduces the observed range in variability at Wanxiang reasonably well, therefore capturing isotopic fractionation under ‘simplified’ conditions. However, a finalised MCIM run, where initial and arrival temperature and pressure conditions, adjusted lapse rates and surface relative humidity also vary, each diagnosed from Lagrangian back trajectory data, does not reproduce the observed precipitation $\delta^{18}\text{O}$ at Wanxiang (Fig. 6.6). MCIM results illustrate that, without explicit moisture and precipitation constraints, and without considering isotopic evolution along trajectories, a temperature effect predominates, overprinting initial source conditions (Fig. 6.7). Thus, optimisation of MCIM for low-latitude climate regimes (e.g., parameterising convective processes) may be required.

Two pseudoproxy records were constructed using monthly ECHAM4 data and MCIM. Weighted mean December-February and June-August moisture source locations were computed, both located east of Tibetan Plateau region (Fig. 6.4), from which monthly ECHAM4 data for the period 1870-2003 were extracted to input into MCIM. The first pseudoproxy record is based on a composite of precipitation $\delta^{18}\text{O}$ at Wanxiang exported

from each source location, weighted by estimated terrestrial moisture fluxes (Fig. 6.5 and Eq. 6.1). Dripwater $\delta^{18}\text{O}$ was calculated by weighting the composite precipitation $\delta^{18}\text{O}$ by estimated hydrologically-effective precipitation (infiltration) at Wanxiang Cave and stalagmite $\delta^{18}\text{O}$ was calculated using the equation of Kim and O'Neil (1997). The second modelled record represents a 'control' run, based on no explicit moisture uptake constraints and weighted only by estimated stalagmite growth rate, which partially depends on surface meteorology. Monthly mean growth rate during 1870-2003 was estimated using published relationships discussed in the Chapter 2.

Secular variability in the WX42B and pseudoproxy records matches well between 1870 and 1970, for the majority of the period in question (Fig. 6.9). Additionally, numerous interannual stalagmite $\delta^{18}\text{O}$ excursions are reproduced by the pseudoproxy record. The modelled records also track stalagmite $\delta^{18}\text{O}$ records from Huangye Cave (Tan *et al.*, 2011), Wuya Cave (Tan *et al.*, 2014) and Dayu Cave, (Tan *et al.*, 2009), the three nearest sites to Wanxiang Cave (Fig. 6.4). The late 20th Century trend towards more relatively enriched $\delta^{18}\text{O}$ values exhibited by many stalagmite records from central China (Nan *et al.*, 2014) is also captured, though somewhat exaggerated, by the pseudoproxy records, which is most likely due to uncertainties in estimation of water excess or stalagmite accumulation rates at Wanxiang Cave, or to signal attenuation by karst processes. The modelled and actual records begin to diverge at approximately 1960. Nevertheless, the degree of correspondence between the WX42B and a pseudoproxy record driven by mean surface temperature and terrestrial moisture flux variability suggests that a terrestrial isotopic signal is a significant driver of multi-annual to decadal proxy $\delta^{18}\text{O}$ variability at Wanxiang Cave, and potentially over a larger region (Fig. 6.9). This is supported by pervasive summer precipitation recycling occurring across monsoonal China (see Chapter 4). Thus,

terrestrial moisture fluxes may also partially control proxy variability over a larger region. To test this, precipitation isotope data from both nearby and more distal sites are needed, and integrating detailed moisture source information obtained for such sites with higher-resolution isotope-enabled GCM studies may better quantify the importance of terrestrial moisture fluxes on late Holocene $\delta^{18}\text{O}$ systematics.

Chapter 7

Synthesis of results, their implications, and the outlook for future research

7.1. Introductory remarks

The overall aims of the research presented in this thesis were to (i) quantitatively establish the present-day annual cycle of moisture sources precipitation across monsoonal China; (ii) investigate the synoptic processes to which precipitation $\delta^{18}\text{O}$ at Wanxiang Cave, a monsoon-sensitive site located near to the northerly EASM margin, respond; (iii) test the potential for construct pseudoproxy records using a Lagrangian approach to validate inferred palaeomonsoon fluctuations from speleothem $\delta^{18}\text{O}$. In this final chapter, the results of the work presented in this thesis are synthesised and their implications for understanding past and future EASM dynamics are discussed.

7.2. Synthesis of results

7.2.1. EASM precipitation moisture sources

EASM precipitation is generated by the convergence of south-westerly transport, northward ITCZ shift during boreal summer, and easterly Pacific Ocean trade winds (Liu *et al.*, 2014) (Fig. 4.1). However, the relative seasonal contributions of these transport mechanisms to precipitation across monsoonal China remains un-quantified. Addressing this issue, Chapter 4 quantified moisture transport from the Indian and Pacific Oceans, driving EASM precipitation in central and eastern (monsoonal) China. The seasonal cycle of moisture sources exhibits a rapid transition from a dry winter period, with predominately easterly moisture contributions, to an intense summer monsoon phase, dominated by contributions from the northern Indian Ocean and extensive moisture recycling over terrestrial areas (Fig. 4.3 and Fig 3.7). During EASM onset in June, Indian Ocean moisture export is transported to easternmost China. These diagnosed moisture

transport patterns are strongly substantiated by close agreement between modelled and observed geographical precipitation distribution across monsoonal China (Fig. 4.8). Despite distinct differences in the onset and characteristics of the AM season over India, eastern China and the western North Pacific (Wang and Lin, 2002), the ISM contribution to EASM precipitation is significant (Fig. 4.10). In summary, these results challenge the previously-assumed Pacific Ocean origin for EASM precipitation across China (Ran and Feng, 2013; Xu *et al.*, 2004) and provide a highly plausible mechanistic explanation for precipitation proxy co-variation across the entire continental AM domain evident in existing Holocene speleothem records (Li *et al.*, 2014), and in particular, during late Holocene warm phases (Rehfeld *et al.*, 2013).

Chapter 4 also presents an effort to quantify the significance of the isotopic source effect expressed in modern Chinese precipitation $\delta^{18}\text{O}$, which varies in strength between the Hulu, Dongge, Dayu and Wanxiang Cave sites due to differences in mean moisture transport distance during summer (Fig. 4.11). The results presented in Chapter 4, combined with existing GCM evidence for a strong response of precipitation $\delta^{18}\text{O}$ in China to upstream rainout (Liu *et al.*, 2014; Pausata *et al.*, 2011), indicate precipitation $\delta^{18}\text{O}$ at these sites responds preferentially to moisture transport and monsoonal circulation, and precipitation amount is a secondary control. Although $\delta^{18}\text{O}$ at sites within monsoonal China does not exclusively record local precipitation variability at sites within monsoonal China, it nevertheless provides a direct proxy for changes in moisture dynamics and EASM circulation strength and therefore remains a crucial tool for palaeomonsoon reconstruction.

7.2.2. Precipitation isotope modelling

In Chapter 5, a recently-developed Lagrangian isotope model was used to investigate the hydroclimatic parameters and processes to which meteoric precipitation $\delta^{18}\text{O}$ at Wanxiang Cave, located near to the northerly EASM limit, responds. Modelling results were compared with an observational dataset comprised of 37 precipitation events at Wanxiang Cave, sampled during the period 2001-2002 (Fig. 5.1). The Isotra3 model (Dütsch, 2013; Pfahl and Wernli, 2009) simulates isotopic evolution along three-dimensional Lagrangian trajectories (Fig. 5.2), accounting for quantitatively diagnosed moisture source regions, and, being a Lagrangian model, excludes only post-condensation exchange processes. Mapped trajectories for select precipitation events (Fig. 5.3 and Fig. 5.4) illustrate disparate transport pathways and fractionation conditions, each event therefore exhibiting a distinct isotopic signature. Neighbouring trajectories experience similar moisture uptake and isotopic fractionation evolution. At Wanxiang, precipitation $\delta^{18}\text{O}$ variance of up to ~ 10 ‰ was attributed air mass ‘history’, almost two thirds of the measured variability at Wanxiang and approximately one quarter of observed $\delta^{18}\text{O}$ variability observed at GNIP stations across the northerly EASM region. The Isotra3 model reproduces the temporal trend described by observed Wanxiang $\delta^{18}\text{O}$ data reasonably well and provides strong evidence for isotopic enrichment due to terrestrial moisture contributions (Fig. 5.5 and Fig. 5.6), such as evapotranspiration fluxes. Crucially, this occurs during summer and may moderate isotope depletion due to increased precipitation intensity, thus affecting EASM isotopic signals. One potential complication is Tibetan Plateau moisture contributions, originating at relatively high elevations, which potentially isotopically depleted up to seven sampled precipitation events (Fig 4.5). Furthermore, the amount of free troposphere-derived moisture is negatively correlated with modelled precipitation $\delta^{18}\text{O}$, which is a probable cause of synoptic scale isotopic depletion (Fig. 5.7), consistent with recent

global-scale modelling (Aggarwal *et al.*, 2012). Moreover, FT-derived moisture contributions may also deplete atmospheric vapour (Fig. 5.7).

Temperature-driven terrestrial moisture flux is seasonal and thus enhanced during the EASM, particularly within inland monsoonal China where high terrestrial moisture uptake occurs (Fig. 5.6). Therefore, terrestrial moisture is an important consideration in interpreting precipitation and proxy $\delta^{18}\text{O}$, potentially counteracting any isotope depletion due to strengthened EASM circulation or increased precipitation amount. This effect may also pertain to more southerly and easterly sites, where summer terrestrial moisture flux is also relatively high (Fig. 4.3). On longer timescales, proxy $\delta^{18}\text{O}$ may record EASM variability inaccurately during periods of elevated summer surface temperatures when terrestrial moisture influences may increasingly obfuscate a local EASM precipitation signal.

In Chapter 6, Prior to constructing pseudoproxy $\delta^{18}\text{O}$ records for Wanxiang Cave, trajectory data and the idealised, Rayleigh-type model, MCIM (Ciais and Jouzel, 1994), are used to model the precipitation event isotope dataset from Wanxiang Cave. MCIM was first run under simplified initial and arrival conditions (averaged over all trajectories), with only initial vapour $\delta^{18}\text{O}$ allowed to vary. The resulting precipitation $\delta^{18}\text{O}$ reproduces the observed range in variability at Wanxiang reasonably well, therefore capturing isotope fractionation under ‘averaged’ conditions (Fig. 6.6a). However, without averaging, where initial and arrival temperature and pressure conditions, adjusted lapse rates and surface relative humidity diagnosed from Lagrangian back trajectory data (Fig. 6.3) for each sampled precipitation event, MCIM is unable to reproduce the observed precipitation $\delta^{18}\text{O}$ at Wanxiang well (Fig. 6.6b). These results illustrate that, without explicit moisture and

precipitation constraints, and without considering isotopic evolution along trajectories, a temperature effect predominates, overprinting initial source conditions and transport effects (Fig. 6.6). These results indicate that optimisation of MCIM for low-latitude climate regimes (e.g., parameterising isotopic changes due to convective processes) may achieve better model performance in this case. Nevertheless, the strong temperature-dependence of MCIM makes this model well-suited to simulating isotopic variability on interannual- to decadal-scale rather than synoptic timescales, raising the possibility that pseudoproxy records could be constructed using MCIM.

Lagrangian isotope models MCIM and Isotra3 calculate fractionation processes at altitude, but precipitation $\delta^{18}\text{O}$ is surface-measured hydroclimatic tracer. In future isotope modelling studies, accurate representation of post-condensation exchange processes, which cannot be parameterised in a Lagrangian framework, is crucial. Moreover, complimentary precipitation isotope modelling and monitoring studies should include accurate collection of metadata, such as precipitation sampling times and event duration information, which will refine future comparisons between observations and model results.

7.2.3. Comparing proxy and pseudoproxy records at Wanxiang Cave

Chapter 6 also presents an attempt to construct 134-year synthetic pseudoproxy stalagmite $\delta^{18}\text{O}$ records using monthly ECHAM4 data and MCIM. These records are compared with the annually-resolved record of Zhang *et al.* (2008) and to records from nearby cave sites (Fig. 6.8). Weighted mean December-February and June-August moisture source locations for Wanxiang precipitation were computed, both located east of Tibetan Plateau region (Fig. 6.4), from which monthly ECHAM4 data for the period 1870-2003 were extracted to

input into MCIM. A pseudoproxy record was constructed by combining precipitation $\delta^{18}\text{O}$ at Wanxiang exported from each source location, weighted by estimated terrestrial moisture fluxes (Fig. 6.5 and Eq. 6.1). Dripwater $\delta^{18}\text{O}$ was calculated by weighting the composite precipitation $\delta^{18}\text{O}$ series by estimated infiltration at Wanxiang Cave and stalagmite $\delta^{18}\text{O}$ was calculated assuming equilibrium calcite-water fractionation. A further, 'control' pseudoproxy record was constructed based on no explicit moisture uptake constraints and weighted only by estimated stalagmite growth rate, which partially depends on surface meteorology. Growth rate weighting was estimated using published relationships discussed in Chapter 2.

Secular pseudoproxy record variability matches the WX42B stalagmite $\delta^{18}\text{O}$ record from Wanxiang Cave well between 1870 and 1970, for the majority of the examined period (Fig. 6.9), and numerous interannual stalagmite $\delta^{18}\text{O}$ excursions are also reproduced. The pseudoproxy record also tracks stalagmite $\delta^{18}\text{O}$ records from Huangye Cave (Tan *et al.*, 2011), Wuya Cave (Tan *et al.*, 2014) and Dayu Cave (Tan *et al.*, 2009), the three most proximal sites to Wanxiang. The modelled and WX42B $\delta^{18}\text{O}$ records begin to diverge at approximately 1960 and the late 20th Century trend to relatively enriched $\delta^{18}\text{O}$ values exhibited by many stalagmite records from central China (Nan *et al.*, 2014) is somewhat exaggerated by the pseudoproxy records, probably due to uncertainties in estimation of water excess or stalagmite accumulation rates at Wanxiang Cave. Nevertheless, the degree of overall correspondence (Fig. 6.9) firmly implicates surface temperature and terrestrial moisture flux variability (and the resultant terrestrial isotopic signature) in controlling annual- to decadal-scale proxy $\delta^{18}\text{O}$ variability at Wanxiang Cave, and potentially over the immediate surrounding region.

7.3. Implications and research outlook

7.3.1. The importance of moisture dynamics in EASM variability predictions

To-date, predictions of the 21st Century Asian Monsoon response to anthropogenic climate change based on GCM simulations have presented conflicting results, with many of the discrepancies relating to moisture dynamics (Ueda *et al.*, 2006). GCMs predict either (i) reduced meridional moisture flux and ASM weakening due to a reduced land-ocean temperature contrast, or (ii) AM intensification due to increased tropical SST and the associated summer evaporative moisture budget increase. However, almost all GCM studies predict significant anthropogenic CO₂-induced warming over the tropical oceans (IPCC, 2013), making considerable increases in lower tropospheric moisture content more likely (Ueda *et al.*, 2006). The moisture source data presented in this thesis not only improve our ability to isolate the rainfall amount signal in oxygen isotope-based palaeomonsoon reconstructions, but also establish the potential importance of northern Indian Ocean evaporation budget changes in driving future monsoonal precipitation trends across central and eastern China. These results will therefore interest many involved in climate and environmental science research communities. Complicating factors which cannot be overlooked in future predictions include the role of increasing anthropogenic aerosol emissions, which potentially induce opposing precipitation responses across the ISM and EASM regions (Bollasina *et al.*, 2011; Lau and Kim, 2006), and the influence of complex Tibetan topography (Qiu, 2013).

Currently, regional predictions of future precipitation response to increased SST are hampered by insufficient moisture source information and suppressed SST variability exhibited by many CMIP5 GCMs, particularly at low-latitude marine temperatures

(Laepple and Huybers, 2014). In addition, water vapour measurements and $\delta^{18}\text{O}$ simulations have indicated that monsoonal precipitation variability may be driven by upstream moisture processes (Lee *et al.*, 2012). The results presented in Chapter 3 strongly suggest that future EASM precipitation variability across central and eastern China will respond to changes in northern Indian Ocean and South China Sea SST and evaporation. Importantly, Indian Ocean SST is currently rising more rapidly than the global average (IPCC, 2013). Conversely, winter precipitation may be primarily driven by moisture budget change in the north-western Pacific Ocean.

7.3.2. Future systematic multi-proxy comparisons

Investigating SST-precipitation relationships over longer timescales will require a targeted, systematic comparison of marine SST proxy records and well-dated stalagmite $\delta^{18}\text{O}$ palaeomonsoon records. Existing Holocene speleothem $\delta^{18}\text{O}$ data provide evidence for ISM-EASM co-variability (Li *et al.*, 2014), which is enhanced during warm periods (Rehfeld *et al.*, 2013). Clear moisture source seasonality exists across the EASM region. One recent study (Kuhnert *et al.*, 2014) compared western Indian Ocean SST proxy data with palaeo-precipitation variability inferred from a stalagmite $\delta^{18}\text{O}$ record from Liang Luar Cave, Indonesia (Griffiths *et al.*, 2009), finding strong evidence for co-variation of Australasian-Indonesian monsoonal precipitation at this cave site and western Indian Ocean SST. Similar systematic comparisons of northern Indian Ocean SST proxy data with multiple stalagmite-based palaeomonsoon reconstructions from central and eastern China could be undertaken, informed by a robust understanding of present-day moisture transport mechanisms. In this way, the relatively dense network of proxy datasets available from China could be used to reconstruct the changing *dynamics* of EASM climate though the

Holocene, providing proxy data-based constraints on likely future changes in rainfall seasonality and the geographical rainfall distribution in this populous region. Moreover, such systematic proxy comparisons could provide reliable estimates of rainfall sensitivity to SST trends and anomalies, which are crucial boundary conditions for the next generation of GCM-based climate predictions.

7.3.3. Future pseudoproxy modelling

Several recent studies (Baker and Bradley, 2010; Baker *et al.*, 2013; Baker *et al.*, 2012; Bradley *et al.*, 2010; Jex *et al.*, 2013) have advanced our collective understanding of the hydrological uncertainties involved in interpreting speleothem $\delta^{18}\text{O}$, by modelling the range of dripwater $\delta^{18}\text{O}$ signatures potentially resulting from a single precipitation $\delta^{18}\text{O}$ input. Given little quantitative constraint of karst hydrology processes at Wanxiang Cave, pseudoproxy modelling in Chapter 6 sought instead to investigate the net climate signal represented by precipitation and proxy $\delta^{18}\text{O}$ in a Lagrangian framework. Collectively, these approaches address the net climatic signal conveyed by precipitation $\delta^{18}\text{O}$ and its transmission from surface to speleothem. Jex *et al.* (2013) suggested that pseudoproxy models should be embedded within isotope-enabled GCMs. Future studies could also seek to integrate Lagrangian data with these methodologies. For example, input precipitation $\delta^{18}\text{O}$ required by a karst hydrology model may be provided a synthetic dataset constructed using more region- or site-specific relationships between observed $\delta^{18}\text{O}$, meteorology, and moisture transport. On greater-than-interannual timescales, MCIM may provide synthetic precipitation $\delta^{18}\text{O}$ time series in regions where high-resolution GCMs perform sub-optimally and is readily usable with Lagrangian moisture source information. Combining

published approaches to constructing pseudoproxy records with that taken in this thesis will broaden their use in validating palaeoclimate reconstructions.

7.4. Concluding remarks

This thesis contributes to a growing body of literature suggesting that precipitation and speleothem $\delta^{18}\text{O}$ reflect not just precipitation amount, but various hydroclimatic processes. Despite this source of uncertainty, well-dated speleothem records remain important archives of palaeoclimatic information, which are increasingly being supported by instrumental monitoring and numerical modelling studies. In particular, this thesis highlights the importance of Indian Ocean and terrestrial moisture transport in understanding the causes of $\delta^{18}\text{O}$ systematics across the EASM region. The existing network of cave sites across monsoonal China from which speleothem $\delta^{18}\text{O}$ records have been obtained is a robust basis from which to reconstruct Holocene EASM dynamics. Future multi-disciplinary studies will exploit ongoing improvements to isotope-enabled GCMs at regional scales, Lagrangian data, constraints on post-condensation processes, and karst hydrology modelling to provide quantitative tests of the fidelity of $\delta^{18}\text{O}$ -based palaeomonsoon reconstructions. Not least because this highly populous region depends greatly upon seasonal rainfall, establishing an accurate understanding of past EASM variability is an important scientific goal.

Bibliography

- Aggarwal, P. K., Alduchov, O. A., Froehlich, K. O., Araguas-Araguas, L. J., Sturchio, N. C., and Kurita, N., 2012. Stable isotopes in global precipitation: A unified interpretation based on atmospheric moisture residence time. *Geophysical Research Letters* **39**, L11705.
- Alley, R. B. and Cuffey, K. M., 2001. Oxygen- and hydrogen-isotopic ratios of water in precipitation: beyond paleothermometry. *Reviews in Mineralogy and Geochemistry* **43**, 527-553.
- Alley, R. B., Mayewski, P. A., Sowers, T., Stuiver, M., Taylor, K. C., and Clark, P. U., 1997. Holocene climatic instability: A prominent, widespread event 8200 yr ago. *Geology* **25**, 483-486.
- An, Z. S., 2000. The history and variability of the East Asian paleomonsoon climate. *Quaternary Science Reviews* **19**, 171-187.
- Asrat, A., Baker, A., Mohammed, M. U., Leng, M. J., Van Calsteren, P., and Smith, C., 2007. A high-resolution multi-proxy stalagmite record from Mechara, Southeastern Ethiopia: palaeohydrological implications for speleothem palaeoclimate reconstruction. *Journal of Quaternary Science* **22**, 53-63.
- Atkinson, T. C., 1977. Carbon dioxide in the atmosphere of the unsaturated zone: an important control of groundwater hardness in limestones. *Journal of Hydrology* **35**, 111-123.
- Badino, G., 2009. The Legend of Carbon Dioxide Heaviness. *Journal of Cave and Karst Studies* **71**, 100-107.
- Baker, A., Asrat, A., Fairchild, I. J., Leng, M. J., Wynn, P. M., Bryant, C., Genty, D., and Umer, M., 2007. Analysis of the climate signal contained within $\delta^{18}\text{O}$ and growth rate parameters in two Ethiopian stalagmites. *Geochimica et Cosmochimica Acta* **71**, 2975-2988.
- Baker, A. and Bradley, C., 2010. Modern stalagmite $\delta^{18}\text{O}$: Instrumental calibration and forward modelling. *Global and Planetary Change* **71**, 201-206.
- Baker, A., Bradley, C., and Phipps, S. J., 2013. Hydrological modeling of stalagmite $\delta^{18}\text{O}$ response to glacial-interglacial transitions. *Geophysical Research Letters* **40**, 3207-3212.
- Baker, A., Bradley, C., Phipps, S. J., Fischer, M., Fairchild, I. J., Fuller, L., Spötl, C., and Azcurra, C., 2012. Millennial-length forward models and pseudoproxies of stalagmite $\delta^{18}\text{O}$: an example from NW Scotland. *Climate of the Past* **8**, 1153-1167.
- Baker, A., Genty, D., Dreybrodt, W., Barnes, W. L., Mockler, N. J., and Grapes, J., 1998. Testing theoretically predicted stalagmite growth rate with Recent annually laminated samples: Implications for past stalagmite deposition. *Geochimica et Cosmochimica Acta* **62**, 393-404.
- Baker, A. and Smart, P. L., 1995. Recent flowstone growth rates: Field measurements in comparison to theoretical predictions. *Chemical Geology* **122**, 121-128.
- Baker, A., Smith, C. L., Jex, C., Fairchild, I. J., Genty, D., and Fuller, L., 2008. Annually Laminated Speleothems: a Review. *International Journal of Speleology* **37**, 193-206.
- Baker, A. J., Matthey, D. P., and Baldini, J. U. L., 2014. Reconstructing modern stalagmite growth from cave monitoring, local meteorology, and experimental measurements of dripwater films. *Earth and Planetary Science Letters* **392**, 239-249.
- Baldini, J. U. L., 2001. Morphologic and dimensional linkage between recently deposited speleothems and drip water from Browns Folly Mine, Wiltshire, England. *Journal of Cave and Karst Studies* **63**, 83-90.
- Baldini, J. U. L., 2010. Cave atmosphere controls on stalagmite growth rates and palaeoclimate records. In Pedley, H. M. and Rogerson, M. (Ed.) *Tufas and*

- Speleothems: Unravelling the Microbial and Physical Controls*. Geological Society of London Special Publication **336**. pp. 283-294.
- Baldini, J. U. L., Baldini, L. M., McDermott, F., and Clipson, N., 2006a. Carbon dioxide sources, sinks, and spatial variability in shallow temperate zone caves: Evidence from Ballynamintra Cave, Ireland. *Journal of Cave and Karst Studies* **68**, 4-11.
- Baldini, J. U. L., McDermott, F., Baker, A., Baldini, L. M., Matthey, D. P., and Railsback, L. B., 2005. Biomass effects on stalagmite growth and isotope ratios: A 20th century analogue from Wiltshire, England. *Earth and Planetary Science Letters* **240**, 486-494.
- Baldini, J. U. L., McDermott, F., and Fairchild, I. J., 2006b. Spatial variability in cave drip water hydrochemistry: Implications for stalagmite paleoclimate records. *Chemical Geology* **235**, 390-404.
- Baldini, J. U. L., McDermott, F., Hoffmann, D. L., Richards, D. A., and Clipson, N., 2008. Very high-frequency and seasonal cave atmosphere P_{CO2} variability: Implications for stalagmite growth and oxygen isotope-based paleoclimate records. *Earth and Planetary Science Letters* **272**, 118-129.
- Baldini, L. M., McDermott, F., Baldini, J. U. L., Fischer, M. J., and Möllhoff, M., 2010. An investigation of the controls on Irish precipitation $\delta^{18}\text{O}$ values on monthly and event timescales. *Climate Dynamics* **35**, 977-993.
- Banner, J. L., Guilfoyle, A., James, E. W., Stern, L. A., and Musgrove, M., 2007. Seasonal variations in modern speleothem calcite growth in Central Texas, USA. *Journal of Sedimentary Research* **77**, 615-622.
- Bar-Matthews, M., Ayalon, A., Matthews, A., Sass, E., and Halicz, L., 1996. Carbon and oxygen isotope study of the active water-carbonate system in a karstic Mediterranean cave: Implications for paleoclimate research in semiarid regions. *Geochimica et Cosmochimica Acta* **60**, 337-347.
- Berger, A. and Loutre, M. F., 1991. Insolation values for the climate of the last 10 million years. *Quaternary Science Reviews* **10**, 297-317.
- Berkelhammer, M., Sinha, A., Stott, L., Cheng, H., Pausata, F. S. R., and Yoshimura, K., 2012. An Abrupt Shift in the Indian Monsoon 4000 Years Ago. In Giosan, L., Fuller, D. Q., Nicoll, K., Flad, R. K., and Clift, P. D. (Ed.) *Climates, Landscapes, and Civilizations*. Geophysical Monograph Series **198**. American Geophysical Union, pp. 75-88.
- Boch, R., 2008. *Stalagmites from Katerloch Cave, Austria: Growth dynamics and high-resolution records of climate change*. PhD thesis, Leopold-Franzens-Universität Innsbruck.
- Bollasina, M. A., Ming, Y., and Ramaswamy, V., 2011. Anthropogenic Aerosols and the Weakening of the South Asian Summer Monsoon. *Science* **334**, 502-505.
- Bony, S., Risi, C., and Vimeux, F., 2008. Influence of convective processes on the isotopic composition ($\delta^{18}\text{O}$ and δD) of precipitation and water vapor in the tropics: 1. Radiative-convective equilibrium and Tropical Ocean-Global Atmosphere-Coupled Ocean-Atmosphere Response Experiment (TOGA-COARE) simulations. *Journal of Geophysical Research: Atmospheres* **113**, D19305.
- Borsato, A., Frisia, S., Fairchild, I. J., Somogyi, A., and Susini, J., 2007. Trace element distribution in annual stalagmite laminae mapped by micrometer-resolution X-ray fluorescence: Implications for incorporation of environmentally significant species. *Geochimica et Cosmochimica Acta* **71**, 1494-1512.
- Bourdin, C., Douville, E., and Genty, D., 2011. Alkaline-earth metal and rare-earth element incorporation control by ionic radius and growth rate on a stalagmite from the Chauvet Cave, Southeastern France. *Chemical Geology* **290**, 1-11.

- Bourges, F., Mangin, A., and d'Hulst, D., 2001. Le gaz carbonique dans la dynamique de l'atmosphère des cavités karstiques : l'exemple de l'Aven d'Orgnac (Ardèche). *Earth and Planetary Sciences* **333**, 685-692.
- Bowen, G. J., 2008. Spatial analysis of the intra-annual variation of precipitation isotope ratios and its climatological corollaries. *Journal of Geophysical Research: Atmospheres* **113**, D05113.
- Bowen, G. J. and Wilkinson, B., 2002. Spatial distribution of $\delta^{18}\text{O}$ in meteoric precipitation. *Geology* **30**, 315-318.
- Bradley, C., Baker, A., Jex, C. N., and Leng, M. J., 2010. Hydrological uncertainties in the modelling of cave drip-water $\delta^{18}\text{O}$ and the implications for stalagmite palaeoclimate reconstructions. *Quaternary Science Reviews* **29**, 2201-2214.
- Breitenbach, S. F. M., Adkins, J. F., Meyer, H., Marwan, N., Kumar, K. K., and Haug, G. H., 2010. Strong influence of water vapor source dynamics on stable isotopes in precipitation observed in Southern Meghalaya, NE India. *Earth and Planetary Science Letters* **292**, 212-220.
- Buhmann, D. and Dreybrodt, W., 1985. The Kinetics of Calcite Dissolution and Precipitation in Geologically Relevant Situations of Karst Areas 1. Open System. *Chemical Geology* **48**, 189-211.
- Burns, S. J., 2011. Speleothem records of changes in tropical hydrology over the Holocene and possible implications for atmospheric methane. *The Holocene* **21**, 735-741.
- Buytaert, W., Celleri, R., Willems, P., Bièvre, B. D., and Wyseure, G., 2006. Spatial and temporal rainfall variability in mountainous areas: A case study from the south Ecuadorian Andes. *Journal of Hydrology* **329**, 413-421.
- Cai, B. G., Pumijumong, N., Tan, M., Muangsong, C., Kong, X. G., Jiang, X. Y., and Nan, S. L., 2010a. Effects of intraseasonal variation of summer monsoon rainfall on stable isotope and growth rate of a stalagmite from northwestern Thailand. *Journal of Geophysical Research: Atmospheres* **115**, D21104.
- Cai, Y. J., Tan, L. C., Cheng, H., An, Z. S., Edwards, R. L., Kelly, M. J., Kong, X. G., and Wang, X. F., 2010b. The variation of summer monsoon precipitation in central China since the last deglaciation. *Earth and Planetary Science Letters* **291**, 21-31.
- Cai, Y. J., Zhang, H. W., Cheng, H., An, Z. S., Edwards, R. L., Wang, X. F., Tan, L. C., Liang, F. Y., Wang, J., and Kelly, M., 2012. The Holocene Indian monsoon variability over the southern Tibetan Plateau and its teleconnections. *Earth and Planetary Science Letters* **335**, 135-144.
- Cappa, C. D., Hendricks, M. B., DePaolo, D. J., and Cohen, R. C., 2003. Isotopic fractionation of water during evaporation. *Journal of Geophysical Research: Atmospheres* **108**, 4525.
- Chen, B., Xu, X.-D., and Zhao, T., 2013. Main moisture sources affecting lower Yangtze River Basin in boreal summers during 2004–2009. *International Journal of Climatology* **33**, 1035-1046.
- Cheng, H., Edwards, R. L., Broecker, W. S., Denton, G. H., Kong, X. G., Wang, Y. J., Zhang, R., and Wang, X. F., 2009a. Ice Age Terminations. *Science* **326**, 248-252.
- Cheng, H., Edwards, R. L., Wan, Y. J., Ko, X. G., Ming, Y. F., Kelly, M. J., Wang, X. F., Gallup, C. D., and Liu, W. G., 2006. A penultimate glacial monsoon record from Hulu Cave and two-phase glacial terminations. *Geology* **34**, 217-220.
- Cheng, H., Fleitmann, D., Edwards, R. L., Wang, X., Cruz, F. W., Auler, A. S., Mangini, A., Wang, Y., Kong, X., Burns, S. J., and Matter, A., 2009b. Timing and structure of the 8.2 kyr B.P. event inferred from $\delta^{18}\text{O}$ records of stalagmites from China, Oman, and Brazil. *Geology* **37**, 1007-1010.

- Christiansen, B., Schmith, T., and Thejll, P., 2009. A surrogate ensemble study of climate reconstruction methods: stochasticity and robustness. *Journal of Climate* **22**, 951-976.
- Ciais, P. and Jouzel, J., 1994. Deuterium and Oxygen-18 in Precipitation - Isotopic Model, Including Mixed Cloud Processes. *Journal of Geophysical Research: Atmospheres* **99**, 16793-16803.
- Clark, I. D. and Fritz, P., 1997. *Environmental Isotopes in Hydrogeology*. CRC Press, Boca Raton, Florida. 328p.
- Clemens, S. C., Prell, W. L., and Sun, Y. B., 2010. Orbital-scale timing and mechanisms driving Late Pleistocene Indo-Asian summer monsoons: Reinterpreting cave speleothem $\delta^{18}\text{O}$. *Paleoceanography* **25**, PA4207.
- Cole, J. E., Rind, D., Webb, R. S., Jouzel, J., and Healy, R., 1999. Climatic controls on interannual variability of precipitation $\delta^{18}\text{O}$: Simulated influence of temperature, precipitation amount, and vapor source region. *Journal of Geophysical Research: Atmospheres* **104**, 14223-14235.
- Collister, C. and Matthey, D., 2008. Controls on water drop volume at speleothem drip sites: An experimental study. *Journal of Hydrology* **358**, 259-267.
- Cosford, J., Qing, H. R., Eglinton, B., Matthey, D., Yuan, D. X., Zhang, M. L., and Cheng, H., 2008. East Asian monsoon variability since the Mid-Holocene recorded in a high-resolution, absolute-dated aragonite speleothem from eastern China. *Earth and Planetary Science Letters* **275**, 296-307.
- Craig, H., 1961. Isotopic variations in meteoric waters. *Science* **133**, 1702-1703.
- Craig, H., 1965. The measurement of oxygen isotope palaeotemperatures. In Tongiorgi, E. (Ed.) *Stable Isotopes in Oceanographic Studies and Palaeotemperatures*. Consiglio Nazionale della Ricerche Laboratorio di Geologia Nucleare, Pisa. pp. 3-24.
- Craig, H. and Gordon, L. I., 1965. Deuterium and oxygen 18 variations in the ocean and the marine atmosphere. In Tongiorgi, E. (Ed.) *Stable Isotopes in Oceanographic Studies and Palaeotemperatures*. Consiglio Nazionale della Ricerche Laboratorio di Geologia Nucleare, Pisa. pp. 9-130.
- Curl, R. L., 1973. Minimum diameter stalagmites. *Bulletin of the National Speleological Society* **35**, 1-9.
- Dansgaard, W., 1964. Stable Isotopes in Precipitation. *Tellus* **16**, 436-468.
- Darling, W. G., 2004. Hydrological factors in the interpretation of stable isotopic proxy data present and past: a European perspective. *Quaternary Science Reviews* **23**, 743-770.
- Darling, W. G., Bath, A. H., Gibson, J. J., and Rozanski, K., 2006. Isotopes in Water. In Leng, M. J. (Ed.) *Isotopes in Palaeoenvironmental Research*. Developments in Palaeoenvironmental Research **10**. Springer, Amsterdam. pp. 1-66.
- Davidson, E. A., Janssens, I. A., and Luo, Y. Q., 2006. On the variability of respiration in terrestrial ecosystems: moving beyond Q_{10} . *Global Change Biology* **12**, 154-164.
- Day, C. C. and Henderson, G. M., 2011. Oxygen isotopes in calcite grown under cave-analogue conditions. *Geochimica et Cosmochimica Acta* **75**, 3956-3972.
- Day, C. C. and Henderson, G. M., 2013. Controls on trace-element partitioning in cave-analogue calcite. *Geochimica et Cosmochimica Acta* **120**, 612-627.
- Dayem, K. E., Molnar, P., Battisti, D. S., and Roe, G. H., 2010. Lessons learned from oxygen isotopes in modern precipitation applied to interpretation of speleothem records of paleoclimate from eastern Asia. *Earth and Planetary Science Letters* **295**, 219-230.

- Dee, D. P., Uppala, S. M., Simmons, A. J., Berrisford, P., Poli, P., Kobayashi, S., Andrae, U., Balmaseda, M. A., Balsamo, G., Bauer, P., Bechtold, P., Beljaars, A. C. M., van de Berg, L., Bidlot, J., Bormann, N., Delsol, C., Dragani, R., Fuentes, M., Geer, A. J., Haimberger, L., Healy, S. B., Hersbach, H., Hólm, E. V., Isaksen, L., Kållberg, P., Köhler, M., Matricardi, M., McNally, A. P., Monge-Sanz, B. M., Morcrette, J. J., Park, B. K., Peubey, C., de Rosnay, P., Tavolato, C., Thépaut, J. N., and Vitart, F., 2011. The ERA-Interim reanalysis: configuration and performance of the data assimilation system. *Quarterly Journal of the Royal Meteorological Society* **137**, 553-597.
- Ding, Y. and Sikka, D. R., 2006. Synoptic systems and weather. In Wang, B. (Ed.) *The Asian Monsoon*. Springer-Praxis Books in Environmental Sciences Praxis Springer, Berlin. pp. 131-201.
- Ding, Y. H. and Chan, J. C. L., 2005. The East Asian summer monsoon: an overview. *Meteorology and Atmospheric Physics* **89**, 117-142.
- Ding, Y. H., Li, C. Y., and Liu, Y. J., 2004. Overview of the South China Sea monsoon experiment. *Advances in Atmospheric Sciences* **21**, 343-360.
- Dong, J. G., Wang, Y. J., Cheng, H., Hardt, B., Edwards, R. L., Kong, X. G., Wu, J. Y., Chen, S. T., Liu, D. B., Jiang, X. Y., and Zhao, K., 2010. A high-resolution stalagmite record of the Holocene East Asian monsoon from Mt Shennongjia, central China. *Holocene* **20**, 257-264.
- Dreybrodt, W., 1980. Deposition of calcite from thin films of natural calcareous solutions and the growth of speleothems. *Chemical Geology* **29**, 89-105.
- Dreybrodt, W., 1981. The kinetics of calcite precipitation from thin films of calcareous solutions and the growth of speleothems: revisited. *Chemical Geology* **32**, 237-245.
- Dreybrodt, W., 1988. *Processes in Karst Systems: Physics, Chemistry, and Geology*. Springer Series in Physical Environment **4**. Springer-Verlag, Berlin. 288p.
- Dreybrodt, W., 1999. Chemical kinetics, speleothem growth and climate. *Boreas* **28**, 347-356.
- Dreybrodt, W., Buhmann, D., Michaelis, J., and Usdowski, E., 1992. Geochemically controlled calcite precipitation by CO₂ outgassing: Field measurements of precipitation rates in comparison to theoretical predictions. *Chemical Geology* **97**, 285-294.
- Drysdale, R. N., Zanchetta, G., Hellstrom, J. C., Fallick, A. E., Zhao, J. X., Isola, I., and Bruschi, G., 2004. Palaeoclimatic implications of the growth history and stable isotope ($\delta^{18}\text{O}$ and $\delta^{13}\text{C}$) geochemistry of a Middle to Late Pleistocene stalagmite from central-western Italy. *Earth and Planetary Science Letters* **227**, 215-229.
- Duan, F., Wang, Y., Shen, C.-C., Wang, Y., Cheng, H., Wu, C.-C., Hu, H.-M., Kong, X., Liu, D., and Zhao, K., 2014. Evidence for solar cycles in a late Holocene speleothem record from Dongge Cave, China. *Nature Scientific Reports* **4**, 5159.
- Duplessy, J. C., Labeyrie, J., Lalou, C., and Nguyen, H. V., 1970. Continental Climatic Variations between 130,000 and 90,000 Years BP. *Nature* **226**, 631-633.
- Duplessy, J. C., Labeyrie, L., Arnold, M., Paterne, M., Duprat, J., and van Weering, T. C. E., 1992. Changes in surface salinity of the North Atlantic Ocean during the last deglaciation. *Nature* **358**, 485-488.
- Dütsch, M. L., 2013. *Stable Water Isotope Fractionation Along Trajectories*. MSc thesis, ETH Zurich. 56 p.
- Dykoski, C. A., Edwards, R. L., Cheng, H., Yuan, D. X., Cai, Y. J., Zhang, M. L., Lin, Y. S., Qing, J. M., An, Z. S., and Revenaugh, J., 2005. A high-resolution, absolute-dated Holocene and deglacial Asian monsoon record from Dongge Cave, China. *Earth and Planetary Science Letters* **233**, 71-86.

- Eames, K. A. T., 2008. *A Lagrangian trajectory and isotopic fractionation (FLEXPART-MCIM) approach to modelling the isotopic composition of rainfall over the British Isles*. PhD thesis, University of East Anglia. 250 p.
- Ek, C. and Gewalt, M., 1985. Carbon dioxide in cave atmospheres - new results in Belgium and comparison with some other countries. *Earth Surface Processes and Landforms* **10**, 173-187.
- Eltahir, E. A. B. and Bras, R. L., 1996. Precipitation recycling. *Reviews of Geophysics* **34**, 367-378.
- Emiliani, C., 1971. Last Interglacial - paleotemperatures and chronology. *Science* **171**, 571-573.
- Esper, J., Cook, E. R., and Schweingruber, F. H., 2002. Low-frequency signals in long tree-ring chronologies for reconstructing past temperature variability. *Science* **295**, 2250-2253.
- Fairchild, I. J. and Baker, A., 2012. *Speleothem Science: From Process to Past Environments*. Blackwell Quaternary Geoscience Series Wiley-Blackwell, Chichester. 432p.
- Fairchild, I. J., Baker, A., Borsato, A., Frisia, S., Hinton, R. W., McDermott, F., and Tooth, A. F., 2001. Annual to sub-annual resolution of multiple trace-element trends in speleothems. *Journal of the Geological Society* **158**, 831-841.
- Fairchild, I. J., Baker, A., Fuller, L., Borsato, A., Miorandi, R., Frisia, S., Matthey, D., McMillan, E., Spötl, C., Andreo, B., Vadillo, I., and Carrasco, F., 2006a. Speleophysiology: a key to understanding high-resolution information in speleothems. In Onac, B., Tamas, T., Constantin, S., and Persolu, A. (Ed.) *Archives of Climate Change in Karst: Proceedings of the Symposium: Climate Change the Karst Record, IV*. Karst Waters Institute Special Publication **10**. pp. 249.
- Fairchild, I. J., Frisia, S., Borsato, A., and Tooth, A. F., 2007. Speleothems. In Nash, D. J. and McLaren, S. J. (Ed.) *Geochemical Sediments and Landscapes*. Blackwells, Oxford. pp. 240-245.
- Fairchild, I. J., Smith, C. L., Baker, A., Fuller, L., Spötl, C., Matthey, D., McDermott, F., and E.I.M.F., 2006b. Modification and preservation of environmental signals in speleothems. *Earth-Science Reviews* **75**, 105-153.
- Fairchild, I. J. and Treble, P. C., 2009. Trace elements in speleothems as recorders of environmental change. *Quaternary Science Reviews* **28**, 449-468.
- Fairchild, I. J., Tuckwell, G. W., Baker, A., and Tooth, A. F., 2006c. Modelling of dripwater hydrology and hydrogeochemistry in a weakly karstified aquifer (Bath, UK): Implications for climate change studies. *Journal of Hydrology* **321**, 213-231.
- Faure, G. and Mensing, T. M., 2005. *Isotopes: Principles and Applications*. 3rd edition. Wiley, 928p.
- Fischer, M. J. and Treble, P. C., 2008. Calibrating climate- $\delta^{18}\text{O}$ regression models for the interpretation of high-resolution speleothem $\delta^{18}\text{O}$ time series. *Journal of Geophysical Research: Atmospheres* **113**, D17103.
- Fleitmann, D., Burns, S. J., Mudelsee, M., Neff, U., Kramers, J., Mangini, A., and Matter, A., 2003. Holocene forcing of the Indian monsoon recorded in a stalagmite from Southern Oman. *Science* **300**, 1737-1739.
- Frappier, A. B., 2008. A stepwise screening system to select storm-sensitive stalagmites: Taking a targeted approach to speleothem sampling methodology. *Quaternary International* **187**, 25-39.
- Fricke, H. C. and O'Neil, J. R., 1999. The correlation between $^{18}\text{O}/^{16}\text{O}$ ratios of meteoric water and surface temperature: its use in investigating terrestrial climate change over geologic time. *Earth and Planetary Science Letters* **170**, 181-196.

- Frisia, S., Borsato, A., Fairchild, I. J., and McDermott, F., 2000. Calcite fabrics, growth mechanisms, and environments of formation in speleothems from the Italian Alps and southwestern Ireland. *Journal of Sedimentary Research* **70**, 1183-1196.
- Frisia, S., Borsato, A., Preto, N., and McDermott, F., 2003. Late Holocene annual growth in three Alpine stalagmites records the influence of solar activity and the North Atlantic Oscillation on winter climate. *Earth and Planetary Science Letters* **216**, 411-424.
- Gabitov, R. I., Sadekov, A., and Leinweber, A., 2014. Crystal growth rate effect on Mg/Ca and Sr/Ca partitioning between calcite and fluid: An in situ approach. *Chemical Geology* **367**, 70-82.
- Gabitov, R. I. and Watson, E. B., 2006. Partitioning of strontium between calcite and fluid. *Geochemistry Geophysics Geosystems* **7**, Q11004.
- Gascoyne, M., 1983. Trace-element partition coefficients in the calcite-water system and their paleoclimatic significance in cave studies. *Journal of Hydrology* **61**, 213-222.
- Gat, J. R., 1996. Oxygen and hydrogen isotopes in the hydrologic cycle. *Annual Review of Earth and Planetary Sciences* **24**, 225-262.
- Genty, D., 2008. Palaeoclimate Research in Villars Cave (Dordogne, SW-France). *International Journal of Speleology* **37**, 173-191.
- Genty, D., Baker, A., and Vokal, B., 2001. Intra- and inter-annual growth rate of modern stalagmites. *Chemical Geology* **176**, 191-212.
- Genty, D. and Deflandre, G., 1998. Drip flow variations under a stalactite of the Pere Noel cave (Belgium). Evidence of seasonal variations and air pressure constraints. *Journal of Hydrology* **211**, 208-232.
- Genty, D. and Quinif, Y., 1996. Annually laminated sequences in the internal structure of some Belgian stalagmites - Importance for paleoclimatology. *Journal of Sedimentary Research* **66**, 275-288.
- Gimeno, L., Drumond, A., Nieto, R., Trigo, R. M., and Stohl, A., 2010. On the origin of continental precipitation. *Geophysical Research Letters* **37**, L13804.
- Gourcy, L. L., Groening, M., and Aggarwal, P. K., 2005. Stable Oxygen and Hydrogen Isotopes in Precipitation. In Aggarwal, P. K., Gat, J. R., and Froehlich, K. F. O. (Ed.) *Isotopes in the Water Cycle: Past, Present and Future of a Developing Science*. Springer, Dordrecht, The Netherlands. pp. 39-51.
- Gregorič, A., Vaupotič, J., and Šebela, S., 2013. The role of cave ventilation in governing cave air temperature and radon levels (Postojna Cave, Slovenia). *International Journal of Climatology* **34**, 1488-1500.
- Griffiths, M. L., Drysdale, R. N., Gagan, M. K., Zhao, J.-x., Ayliffe, L. K., Hellstrom, J. C., Hantoro, W. S., Frisia, S., Feng, Y.-x., Cartwright, I., Pierre, E. S., Fischer, M. J., and Suwargadi, B. W., 2009. Increasing Australian-Indonesian monsoon rainfall linked to early Holocene sea-level rise. *Nature Geoscience* **2**, 636-639.
- Hakl, J., Hunyadi, I., Csige, I., Gécky, G., Lénart, K. L., and Várhegyi, A., 1997. Radon transport phenomena studied in karst caves – international experiences on radon levels and exposures. *Radiation Measurements* **28**, 675-684.
- Hansen, M., Dreybrodt, W., and Scholz, D., 2013. Chemical evolution of dissolved inorganic carbon species flowing in thin water films and its implications for (rapid) degassing of CO₂ during speleothem growth. *Geochimica et Cosmochimica Acta* **107**, 242-251.
- He, Y., Wang, Y., Kong, X., and Cheng, H., 2005. High resolution stalagmite $\delta^{18}\text{O}$ records over the past 1000 years from Dongge Cave in Guizhou. *Chinese Science Bulletin* **50**, 1003-1008.

- Helsen, M. M., Van de Wal, R. S. W., and Van den Broeke, M. R., 2007. The isotopic composition of present-day Antarctic snow in a Lagrangian atmospheric simulation. *Journal of Climate* **20**, 739-756.
- Helsen, M. M., van de Wal, R. S. W., van den Broeke, M. R., Masson-Delmotte, V., Meijer, H. A. J., Scheele, M. P., and Werner, M., 2006. Modeling the isotopic composition of Antarctic snow using backward trajectories: Simulation of snow pit records. *Journal of Geophysical Research: Atmospheres* **111**, D15109.
- Henderson, G. M., 2006. Caving in to new chronologies. *Science* **313**, 620-622.
- Hendy, C. H., 1971. Isotopic Geochemistry of Speleothems 1. Calculation of Effects of Different Modes of Formation on Isotopic Composition of Speleothems and Their Applicability as Palaeoclimatic Indicators. *Geochimica et Cosmochimica Acta* **35**, 801-824.
- Hendy, C. H. and Wilson, A. T., 1968. Palaeoclimatic Data from Speleothems. *Nature* **219**, 48-51.
- Hill, C. and Forti, P., 1997. *Cave Minerals of the World*. (2nd ed.). National Speleological Society, Huntsville, Alabama. 463p.
- Hoffmann, G. and Heimann, M., 1997. Water isotope modeling in the Asian monsoon region. *Quaternary International* **37**, 115-128.
- Hoffmann, G., Werner, M., and Heimann, M., 1998. Water isotope module of the ECHAM atmospheric general circulation model: A study on timescales from days to several years. *Journal of Geophysical Research: Atmospheres* **103**, 16871-16896.
- Hourdin, F., Musat, I., Bony, S., Braconnot, P., Codron, F., Dufresne, J.-L., Fairhead, L., Filiberti, M.-A., Friedlingstein, P., Grandpeix, J.-Y., Krinner, G., LeVan, P., Li, Z.-X., and Lott, F., 2006. The LMDZ4 general circulation model: climate performance and sensitivity to parametrized physics with emphasis on tropical convection. *Climate Dynamics* **27**, 787-813.
- Hu, C. Y., Henderson, G. M., Huang, J. H., Xie, S., Sun, Y., and Johnson, K. R., 2008. Quantification of Holocene Asian monsoon rainfall from spatially separated cave records. *Earth and Planetary Science Letters* **266**, 221-232.
- Huang, H. M., Fairchild, I. J., Borsato, A., Frisia, S., Cassidy, N. J., McDermott, F., and Hawkesworth, C. J., 2001. Seasonal variations in Sr, Mg and P in modern speleothems (Grotta di Ernesto, Italy). *Chemical Geology* **175**, 429-448.
- Huang, Y. M. and Fairchild, I. J., 2001. Partitioning of Sr²⁺ and Mg²⁺ into calcite under karst-analogue experimental conditions. *Geochimica et Cosmochimica Acta* **65**, 47-62.
- IAEA/WMO, 2014. *Global Network of Isotopes in Precipitation*. The GNIP Database.
- IPCC, 2013. *Climate Change 2013: The Physical Science Basis. Contribution of Working Group I to the Fifth Assessment Report of the Intergovernmental Panel on Climate Change*. Cambridge University Press, Cambridge. 2014p.
- James, P., Stohl, A., Spichtinger, N., Eckhardt, S., and Forster, C., 2004. Climatological aspects of the extreme European rainfall of August 2002 and a trajectory method for estimating the associated evaporative source regions. *Natural Hazards and Earth System Sciences* **4**, 733-746.
- Jex, C. N., Baker, A., Fairchild, I. J., Eastwood, W. J., Leng, M. J., Sloane, H. J., Thomas, L., and Bekaroglu, E., 2010. Calibration of speleothem $\delta^{18}\text{O}$ with instrumental climate records from Turkey. *Global and Planetary Change* **71**, 207-217.
- Jex, C. N., Phipps, S. J., Baker, A., and Bradley, C., 2013. Reducing uncertainty in the climatic interpretations of speleothem $\delta^{18}\text{O}$. *Geophysical Research Letters* **40**, 2259-2264.

- Jiang, D. B. and Wang, H. J., 2005. Natural interdecadal weakening of East Asian summer monsoon in the late 20th century. *Chinese Science Bulletin* **50**, 1923-1929.
- Johnson, K. R., 2004. *A multi-proxy speleothem record of Asian Monsoon variability during the Late Pleistocene from Wanxaing Cave, Gansu Province, China*. PhD thesis, University of California at Berkley. 199 p.
- Johnson, K. R., Hu, C. Y., Belshaw, N. S., and Henderson, G. M., 2006. Seasonal trace-element and stable-isotope variations in a Chinese speleothem: The potential for high-resolution paleomonsoon reconstruction. *Earth and Planetary Science Letters* **244**, 394-407.
- Johnson, K. R. and Ingram, B. L., 2004. Spatial and temporal variability in the stable isotope systematics of modern precipitation in China: implications for paleoclimate reconstructions. *Earth and Planetary Science Letters* **220**, 365-377.
- Jones, P. D., Briffa, K. R., Barnett, T. P., and Tett, S. F. B., 1998. High-resolution palaeoclimatic records for the last millennium: interpretation, integration and comparison with General Circulation Model control-run temperatures. *The Holocene* **8**, 455-471.
- Jones, P. D., Briffa, K. R., Osborn, T. J., Lough, J. M., van Ommen, T. D., Vinther, B. M., Luterbacher, J., Wahl, E. R., Zwiers, F. W., Mann, M. E., Schmidt, G. A., Ammann, C. M., Buckley, B. M., Cobb, K. M., Esper, J., Goosse, H., Graham, N., Jansen, E., Kiefer, T., Kull, C., Kuttel, M., Mosley-Thompson, E., Overpeck, J. T., Riedwyl, N., Schulz, M., Tudhope, A. W., Villalba, R., Wanner, H., Wolff, E., and Xoplaki, E., 2009. High-resolution palaeoclimatology of the last millennium: a review of current status and future prospects. *The Holocene* **19**, 3-49.
- Joussaume, S., Sadourny, R., and Jouzel, J., 1984. A general circulation model of water isotope cycles in the atmosphere. *Nature* **311**, 24-29.
- Jouzel, J., Froehlich, K., and Schotterer, U., 1997. Deuterium and oxygen-18 in present-day precipitation: data and modelling. *Journal des Sciences Hydrologiques* **42**, 747-763.
- Jouzel, J., Hoffmann, G., Koster, R. D., and Masson, V., 2000. Water isotopes in precipitation: data/model comparison for present-day and past climates. *Quaternary Science Reviews* **19**, 363-379.
- Jouzel, J. and Koster, R. D., 1996. A reconsideration of the initial conditions used for stable water isotope models. *Journal of Geophysical Research: Atmospheres* **101**, 22933-22938.
- Kaufmann, G., 2003. Stalagmite growth and palaeo-climate: the numerical perspective. *Earth and Planetary Science Letters* **214**, 251-266.
- Kaufmann, G. and Dreybrodt, W., 2004. Stalagmite growth and palaeo-climate: an inverse approach. *Earth and Planetary Science Letters* **224**, 529-545.
- Kelly, M. J., Edwards, R. L., Cheng, H., Yuan, D. X., Cai, Y. J., Zhang, M. L., Lin, Y. S., and An, Z. S., 2006. High resolution characterization of the Asian Monsoon between 146,000 and 99,000 years B.P. from Dongge Cave, China and global correlation of events surrounding Termination II. *Palaeogeography, Palaeoclimatology, Palaeoecology* **236**, 20-38.
- Kennett, D. J., Breitenbach, S. F. M., Aquino, V. V., Asmerom, Y., Awe, J., Baldini, J. U. L., Bartlein, P., Culleton, B. J., Ebert, C., Jazwa, C., Macri, M. J., Marwan, N., Polyak, V., Prufer, K. M., Ridley, H. E., Sodemann, H., Winterhalder, B., and Haug, G. H., 2012. Development and Disintegration of Maya Political Systems in Response to Climate Change. *Science* **338**, 788-791.
- Kim, S.-T. and O'Neil, J. R., 1997. Equilibrium and nonequilibrium oxygen isotope effects in synthetic carbonates. *Geochimica et Cosmochimica Acta* **61**, 3461-3475.

- Kluge, T. and Affek, H. P., 2012. Quantifying kinetic fractionation in Bunker Cave speleothems using $\Delta 47$. *Quaternary Science Reviews* **49**, 82-94.
- Koster, R., Jouzel, J., Suozzo, R., Russell, G., Broecker, W., Rind, D., and Eagleson, P., 1986. Global sources of local precipitation as determined by the NASA/GISS GCM. *Geophysical Research Letters* **13**, 121-124.
- Koster, R. D., Devalpine, D. P., and Jouzel, J., 1993. Continental water recycling and H_2^{18}O concentrations. *Geophysical Research Letters* **20**, 2215-2218.
- Kowalczyk, A. J. and Froelich, P. N., 2010. Cave air ventilation and CO_2 outgassing by ^{222}Rn modeling: How fast do caves breathe? *Earth and Planetary Science Letters* **289**, 209-219.
- Kuhnert, H., Kuhlmann, H., Mohtadi, M., Meggers, H., Baumann, K.-H., and Pätzold, J., 2014. Holocene tropical western Indian Ocean sea surface temperatures in covariation with climatic changes in the Indonesian region. *Paleoceanography* **29**, 423-437.
- Lachniet, M. S., 2009. Climatic and environmental controls on speleothem oxygen-isotope values. *Quaternary Science Reviews* **28**, 412-432.
- Lachniet, M. S., Bernal, J. P., Asmerom, Y., Polyak, V., and Piperno, D., 2012. A 2400 yr Mesoamerican rainfall reconstruction links climate and cultural change. *Geology* **40**, 259-262.
- Laepple, T. and Huybers, P., 2014. Global and regional variability in marine surface temperatures. *Geophysical Research Letters* **41**, 2528-2534.
- Laskar, A. H., Huang, J.-C., Hsu, S.-C., Bhattacharya, S. K., Wang, C.-H., and Liang, M.-C., 2014. Stable isotopic composition of near surface atmospheric water vapor and rain-vapor interaction in Taipei, Taiwan. *Journal of Hydrology* **519**, 2091-2100.
- Lau, K. M. and Kim, K. M., 2006. Observational relationships between aerosol and Asian monsoon rainfall, and circulation. *Geophysical Research Letters* **33**, L21810.
- Lawrence, J. R., Gedzelman, S. D., Zhang, X., and Arnold, R., 1998. Stable isotope ratios of rain and vapor in 1995 hurricanes. *Journal of Geophysical Research: Atmospheres* **103**, 11381-11400.
- Lawrence, R. J. and Gedzelman, D. S., 1996. Low stable isotope ratios of tropical cyclone rains. *Geophysical Research Letters* **23**, 527-530.
- Lee, J.-E. and Fung, I., 2008. "Amount effect" of water isotopes and quantitative analysis of post-condensation processes. *Hydrological Processes* **22**, 1-8.
- Lee, J.-E., Risi, C., Fung, I., Worden, J., Scheepmaker, R. A., Lintner, B., and Frankenberg, C., 2012. Asian monsoon hydrometeorology from TES and SCIAMACHY water vapor isotope measurements and LMDZ simulations: Implications for speleothem climate record interpretation. *Journal of Geophysical Research: Atmospheres* **117**, D15112.
- Legates, D. R. and Willmott, C. J., 1990. Mean seasonal and spatial variability in gauge-corrected, global precipitation. *International Journal of Climatology* **10**, 111-127.
- LeGrande, A. N. and Schmidt, G. A., 2006. Global gridded data set of the oxygen isotopic composition in seawater. *Geophysical Research Letters* **33**, L12604.
- LeGrande, A. N. and Schmidt, G. A., 2009. Sources of Holocene variability of oxygen isotopes in paleoclimate archives. *Climate of the Past* **5**, 441-455.
- Lekshmy, P. R., Midhun, M., Ramesh, R., and Jani, R. A., 2014. ^{18}O depletion in monsoon rain relates to large scale organized convection rather than the amount of rainfall. *Nature Scientific Reports* **4**,
- Lewis, S. C., LeGrande, A. N., Kelley, M., and Schmidt, G. A., 2010. Water vapour source impacts on oxygen isotope variability in tropical precipitation during Heinrich events. *Climate of the Past* **6**, 325-343.

- Li, J. P. and Zheng, Q. C., 2003. A new monsoon index and the geographical distribution of the global monsoons. *Advances in Atmospheric Sciences* **20**, 299-302.
- Li, Y., Wang, N. a., Zhou, X., Zhang, C., and Wang, Y., 2014. Synchronous or asynchronous Holocene Indian and East Asian summer monsoon evolution: A synthesis on Holocene Asian summer monsoon simulations, records and modern monsoon indices. *Global and Planetary Change* **116**, 30-40.
- Liu, J. R., Song, X. F., Fu, G. B., Liu, X., Zhang, Y. H., and Han, D. M., 2011. Precipitation isotope characteristics and climatic controls at a continental and an island site in Northeast Asia. *Climate Research* **49**, 29-44.
- Liu, W. T. and Tang, W., 2004. *Oceanic Influence on the precipitation in India and China as observed by TRMM and QuikSCAT*. Japan Aerospace Exploration Agency.
- Liu, Y. H., Henderson, G. M., Hu, C. Y., Mason, A. J., Charnley, N., Johnson, K. R., and Xie, S. C., 2013. Links between the East Asian monsoon and North Atlantic climate during the 8,200 year event. *Nature Geoscience* **6**, 117-120.
- Liu, Z., Wen, X., Brady, E. C., Otto-Bliesner, B., Yu, G., Lu, H., Cheng, H., Wang, Y., Zheng, W., Ding, Y., Edwards, R. L., Cheng, J., Liu, W., and Yang, H., 2014. Chinese cave records and the East Asia Summer Monsoon. *Quaternary Science Reviews* **83**, 115-128.
- Lohmann, G., Wackerbarth, A., Langebroek, P. M., Werner, M., Fohlmeister, J., Scholz, D., and Mangini, A., 2013. Simulated European stalagmite record and its relation to a quasi-decadal climate mode. *Climate of the Past* **9**, 89-98.
- Lorens, R. B., 1981. Sr, Cd, Mn and Co distribution coefficients in calcite as a function of calcite precipitation rate. *Geochimica et Cosmochimica Acta* **45**, 553-561.
- Lutgens, F. K. and Tarbuck, E. J., 2000. *The Atmosphere: An Introduction to Meteorology*. 8th edition. Prentice Hall, 512p.
- Maher, B. A., 2008. Holocene variability of the East Asian summer monsoon from Chinese cave records: a re-assessment. *The Holocene* **18**, 861-866.
- Maher, B. A. and Thompson, R., 2012. Oxygen isotopes from Chinese caves: records not of monsoon rainfall but of circulation regime. *Journal of Quaternary Science* **27**, 615-624.
- Majoube, M., 1971. Fractionnement en oxygene 18 et deuterium entre l'eau et sa vapeur. *Journal of Chemical Physics* **10**, 1423-1436.
- Managave, S. R., 2014. Model evaluation of the coherence of a common source water oxygen isotopic signal recorded by tree-ring cellulose and speleothem calcite. *Geochemistry, Geophysics, Geosystems* **15**, 905-922.
- Mann, M. E. and Jones, P. D., 2003. Global surface temperatures over the past two millennia. *Geophysical Research Letters* **30**, 1820.
- Mantua, N. and Hare, S., 2002. The Pacific Decadal Oscillation. *Journal of Oceanography* **58**, 35-44.
- Mariethoz, G., Baker, A., Sivakumar, B., Hartland, A., and Graham, P., 2012. Chaos and irregularity in karst percolation. *Geophysical Research Letters* **39**, L23305.
- Martius, O., Sodemann, H., Joos, H., Pfahl, S., Winschall, A., Croci-Maspoli, M., Graf, M., Madonna, E., Mueller, B., Schemm, S., Sedláček, J., Sprenger, M., and Wernli, H., 2013. The role of upper-level dynamics and surface processes for the Pakistan flood of July 2010. *Quarterly Journal of the Royal Meteorological Society* **139**, 1780-1797.
- Mattey, D. P., Fairchild, I. J., Atkinson, T. C., Latin, J.-P., Ainsworth, M., and Durell, R., 2010. Seasonal microclimate control of calcite fabrics, stable isotopes and trace elements in modern speleothem from St Michaels Cave, Gibraltar. In Pedley, H. M. and Rogerson, M. (Ed.) *Tufas and Speleothems: Unravelling the Microbial and*

- Physical Controls*. Geological Society of London Special Publication **336**. pp. 323-344.
- Mattey, D. P., Lowry, D., Duffet, J., Fisher, R., Hodge, E., and Frisia, S., 2008. A 53 year seasonally resolved oxygen and carbon isotope record from a modern Gibraltar speleothem: Reconstructed drip water and relationship to local precipitation. *Earth and Planetary Science Letters* **269**, 80-95.
- McDermott, F., 2004. Palaeo-climate reconstruction from stable isotope variations in speleothems: a review. *Quaternary Science Reviews* **23**, 901-918.
- McDermott, F., Atkinson, T. C., Fairchild, I. J., Baldini, L. M., and Mattey, D. P., 2011. A first evaluation of the spatial gradients in $\delta^{18}\text{O}$ recorded by European Holocene speleothems. *Global and Planetary Change* **79**, 275-287.
- McGarry, S. F. and Baker, A., 2000. Organic acid fluorescence: applications to speleothem palaeoenvironmental reconstruction. *Quaternary Science Reviews* **19**, 1087-1101.
- Miorandi, R., Borsato, A., Frisia, S., Fairchild, I. J., and Richter, D. K., 2010. Epikarst hydrology and implications for stalagmite capture of climate changes at Grotta di Ernesto (NE Italy): results from long-term monitoring. *Hydrological Processes* **24**, 3101-3114.
- Moberg, A., Mohammad, R., and Mauritsen, T., 2008. Analysis of the Moberg *et al.* (2005) hemispheric temperature reconstruction. *Climate Dynamics* **31**, 957-971.
- Moberg, A., Sonechkin, D. M., Holmgren, K., Datsenko, N. M., Karlén, W., and Lauritzen, S.-E., 2005. Highly variable Northern Hemisphere temperatures reconstructed from low- and high-resolution proxy data. *Nature* **433**, 613-617.
- Moerman, J. W., Cobb, K. M., Adkins, J. F., Sodemann, H., Clark, B., and Tuen, A. A., 2013. Diurnal to interannual rainfall $\delta^{18}\text{O}$ variations in northern Borneo driven by regional hydrology. *Earth and Planetary Science Letters* **369-370**, 108-119.
- Moore, M., Kuang, Z., and Blossey, P. N., 2014. A moisture budget perspective of the amount effect. *Geophysical Research Letters* **41**, 1329-1335.
- Muangsong, C., Cai, B., Pumijumong, N., Hu, C., and Cheng, H., 2014. An annually laminated stalagmite record of the changes in Thailand monsoon rainfall over the past 387 years and its relationship to IOD and ENSO. *Quaternary International* **349**, 90-97.
- Murthy, R., Griffin, K. L., Zarnoch, S. J., Dougherty, P. M., Watson, B., Van Haren, J., Patterson, R. L., and Mahato, T., 2003. Carbon dioxide efflux from a 550 m³ soil across a range of soil temperatures. *Forest Ecology and Management* **178**, 311-327.
- Nan, S., Tan, M., and Zhao, P., 2014. Evaluation of the ability of the Chinese stalagmite $\delta^{18}\text{O}$ to record the variation in atmospheric circulation during the second half of the 20th century. *Climate of the Past* **10**, 975-985.
- Neff, U., Burns, S. J., Mangini, A., Mudelsee, M., Fleitmann, D., and Matter, A., 2001. Strong coherence between solar variability and the monsoon in Oman between 9 and 6 kyr ago. *Nature* **411**, 290-293.
- Niyogi, D., Kishtawal, C., Tripathi, S., and Govindaraju, R. S., 2010. Observational evidence that agricultural intensification and land use change may be reducing the Indian summer monsoon rainfall. *Water Resources Research* **46**, W03533.
- Noone, D. and Simmonds, I., 2002. Associations between $\delta^{18}\text{O}$ of water and climate parameters in a simulation of atmospheric circulation for 1979-95. *Journal of Climate* **15**, 3150-3169.
- Numaguti, A., 1999. Origin and recycling processes of precipitating water over the Eurasian continent: Experiments using an atmospheric general circulation model. *Journal of Geophysical Research: Atmospheres* **104**, 1957-1972.

- Patra, K. C., 2001. *Hydrology and Water Resources Engineering*. CRC Press, Boca Raton, Florida. 561p.
- Pausata, F. S. R., Battisti, D. S., Nisancioglu, K. H., and Bitz, C. M., 2011. Chinese stalagmite $\delta^{18}\text{O}$ controlled by changes in the Indian monsoon during a simulated Heinrich event. *Nature Geoscience* **4**, 474-480.
- Pfahl, S. and Sodemann, H., 2014. What controls deuterium excess in global precipitation? *Climate of the Past* **10**, 771-781.
- Pfahl, S. and Wernli, H., 2008. Air parcel trajectory analysis of stable isotopes in water vapor in the eastern Mediterranean. *Journal of Geophysical Research: Atmospheres* **113**, D20104.
- Pfahl, S. and Wernli, H., 2009. Lagrangian simulations of stable isotopes in water vapor: An evaluation of nonequilibrium fractionation in the Craig-Gordon model. *Journal of Geophysical Research: Atmospheres* **114**, D20108.
- Pfahl, S., Wernli, H., and Yoshimura, K., 2012. The isotopic composition of precipitation from a winter storm – a case study with the limited-area model COSMOiso. *Atmospheric Chemistry and Physics* **12**, 1629-1648.
- Plummer, L. N., Wigley, T. M. L., and Parkhurst, D. L., 1978. Kinetics of Calcite Dissolution in CO_2 -Water Systems at 5° to 60°C and 0.0 to 1.0 atm CO_2 . *American Journal of Science* **278**, 179-216.
- Polyak, V. J. and Asmerom, Y., 2001. Late Holocene climate and cultural changes in the southwestern United States. *Science* **294**, 148-151.
- Porter, S. C. and Zhou, W. J., 2006. Synchronism of Holocene East Asian monsoon variations and North Atlantic drift-ice tracers. *Quaternary Research* **65**, 443-449.
- Proctor, C. J., Baker, A., Barnes, W. L., and Gilmour, R. A., 2000. A thousand year speleothem proxy record of North Atlantic climate from Scotland. *Climate Dynamics* **16**, 815-820.
- Qiu, J., 2013. Monsoon Melee. *Science* **340**, 1400-1401.
- Ran, M. and Feng, Z., 2013. Holocene moisture variations across China and driving mechanisms: A synthesis of climatic records. *Quaternary International* **313-314**, 179-193.
- Rehfeld, K., Marwan, N., Breitenbach, S. M., and Kurths, J., 2013. Late Holocene Asian summer monsoon dynamics from small but complex networks of paleoclimate data. *Climate Dynamics* **41**, 3-19.
- Reynolds, R. W., Rayner, N. A., Smith, T. M., Stokes, D. C., and Wang, W., 2002. An improved in situ and satellite SST analysis for climate. *Journal of Climate* **15**, 1609-1625.
- Risi, C., Bony, S., and Vimeux, F., 2008. Influence of convective processes on the isotopic composition ($\delta^{18}\text{O}$ and δD) of precipitation and water vapor in the tropics: 2. Physical interpretation of the amount effect. *Journal of Geophysical Research: Atmospheres* **113**, D19306.
- Risi, C., Bony, S., Vimeux, F., and Jouzel, J., 2010. Water-stable isotopes in the LMDZ4 general circulation model: Model evaluation for present-day and past climates and applications to climatic interpretations of tropical isotopic records. *Journal of Geophysical Research: Atmospheres* **115**, D12118.
- Rodríguez-Vidal, J., Cáceres, L. M., Finlayson, J. C., Gracia, F. J., and Martínez-Aguirre, A., 2004. Neotectonics and shoreline history of the Rock of Gibraltar, southern Iberia. *Quaternary Science Reviews* **23**, 2017-2029.
- Rohling, E. J., Liu, Q. S., Roberts, A. P., Stanford, J. D., Rasmussen, S. O., Langen, P. L., and Siddall, M., 2009. Controls on the East Asian monsoon during the last glacial

- cycle, based on comparison between Hulu Cave and polar ice-core records. *Quaternary Science Reviews* **28**, 3291-3302.
- Rozanski, K., 2005. Isotopes In Atmospheric Moisture. In Aggarwal, P. K., Gat, J. R., and Froehlich, K. F. O. (Ed.) *Isotopes in the Water Cycle: Past, Present and Future of a Developing Science*. Springer, Dordrecht, The Netherlands. pp. 291-302.
- Rozanski, K., Araguás-Araguás, L., and Gonfiantini, R., 1992. Relation Between Long-Term Trends of Oxygen-18 Isotope Composition of Precipitation and Climate. *Science* **258**, 981-985.
- Rozanski, K., Araguás-Araguás, L., and Gonfiantini, R., 1993. Isotopic patterns in modern global precipitation. In Swart, P. K., Lohmann, K. C., McKenzie, J., and Savin, S. (Ed.) *Climate change in continental isotopic records*. Geophysical Monograph **78**. American Geophysical Union, Washington DC. pp. 1-36.
- Rozanski, K. and Sonntag, C., 1982. Vertical distribution of deuterium in atmospheric water vapour. *Tellus* **34**, 135-141.
- Rozanski, K., Sonntag, C., and Munnich, K. O., 1982. Factors controlling stable isotope composition of European precipitation. *Tellus* **34**, 142-150.
- Sampe, T. and Xie, S.-P., 2010. Large-Scale Dynamics of the Meiyu-Baiu Rainband: Environmental Forcing by the Westerly Jet. *Journal of Climate* **23**, 113-134.
- Schär, C., Lüthi, D., Beyerle, U., and Heise, E., 1999. The Soil–Precipitation Feedback: A Process Study with a Regional Climate Model. *Journal of Climate* **12**, 722-741.
- Schneider, C. A., Rasband, W. S., and Eliceiri, K. W., 2012. NIH Image to ImageJ: 25 years of image analysis. *Nature Methods* **9**, 671-675.
- Schneider, U., Becker, A., Finger, P., Meyer-Christoffer, A., Rudolf, B., and Ziese, M., 2011. *Global Precipitation Climatology Center Full Data Reanalysis Version 6.0 at 1.0°: Monthly Land-Surface Precipitation from Rain-Gauges built on GTS-based and Historic Data*. Deutscher Wetterdienst.
- Sharp, Z., 2007. *Principles of Stable Isotope Geochemistry*. Pearson Prentice Hall, Upper Saddle River, New Jersey. 360p.
- Sherwin, C. M. and Baldini, J. U. L., 2011. Cave air and hydrological controls on prior calcite precipitation and stalagmite growth rates: Implications for palaeoclimate reconstructions using speleothems. *Geochimica et Cosmochimica Acta* **75**, 3915-3929.
- Sinha, A., Berkelhammer, M., Stott, L., Mudelsee, M., Cheng, H., and Biswas, J., 2011a. The leading mode of Indian Summer Monsoon precipitation variability during the last millennium. *Geophysical Research Letters* **38**, L15703.
- Sinha, A., Stott, L., Berkelhammer, M., Cheng, H., Edwards, R. L., Buckley, B., Aldenderfer, M., and Mudelsee, M., 2011b. A global context for megadroughts in monsoon Asia during the past millennium. *Quaternary Science Reviews* **30**, 47-62.
- Smith, T. M., Reynolds, R. W., Peterson, T. C., and Lawrimore, J., 2008. Improvements to NOAA's historical merged land-ocean surface temperature analysis (1880-2006). *Journal of Climate* **21**, 2283-2296.
- Sodemann, H., 2006. *Tropospheric transport of water vapour: Lagrangian and Eulerian perspectives*. PhD thesis, Swiss Federal Institute of Technology. 245 p.
- Sodemann, H., Masson-Delmotte, V., Schwierz, C., Vinther, B. M., and Wernli, H., 2008a. Interannual variability of Greenland winter precipitation sources: 2. Effects of North Atlantic Oscillation variability on stable isotopes in precipitation. *Journal of Geophysical Research: Atmospheres* **113**, D12111.
- Sodemann, H., Schwierz, C., and Wernli, H., 2008b. Interannual variability of Greenland winter precipitation sources: Lagrangian moisture diagnostic and North Atlantic

- Oscillation influence. *Journal of Geophysical Research: Atmospheres* **113**, D03107.
- Sodemann, H. and Stohl, A., 2009. Asymmetries in the moisture origin of Antarctic precipitation. *Geophysical Research Letters* **36**, L22803.
- Sodemann, H. and Zubler, E., 2010. Seasonal and inter-annual variability of the moisture sources for Alpine precipitation during 1995–2002. *International Journal of Climatology* **30**, 947-961.
- Spötl, C., Fairchild, I. J., and Tooth, A. F., 2005. Cave air control on dripwater geochemistry, Obir Caves (Austria): Implications for speleothem deposition in dynamically ventilated caves. *Geochimica et Cosmochimica Acta* **69**, 2451-2468.
- Spötl, C. and Mathey, D., 2006. Stable isotope microsampling of speleothems for palaeoenvironmental studies: a comparison of microdrill, micromill and laser ablation techniques. *Chemical Geology* **235**, 48-58.
- Stohl, A., 2006. Characteristics of atmospheric transport into the Arctic troposphere. *Journal of Geophysical Research: Atmospheres* **111**, D11306.
- Stohl, A., Forster, C., Frank, A., Seibert, P., and Wotawa, G., 2005. Technical note: The Lagrangian particle dispersion model FLEXPART version 6.2. *Atmospheric Chemistry and Physics* **5**, 2461-2474.
- Sturm, C., Zhang, Q., and Noone, D., 2010. An introduction to stable water isotopes in climate models: benefits of forward proxy modelling for paleoclimatology. *Climate of the Past* **6**, 115-129.
- Sturm, K., Hoffmann, G., Langmann, B., and Stichler, W., 2005. Simulation of $\delta^{18}\text{O}$ in precipitation by the regional circulation model REMO_{iso}. *Hydrological Processes* **19**, 3425-3444.
- Tan, L., An, Z., Huh, C.-A., Cai, Y., Shen, C.-C., Shiao, L.-J., Yan, L., Cheng, H., and Edwards, R. L., 2014a. Cyclic precipitation variation on the western Loess Plateau of China during the past four centuries. *Nature Scientific Reports* **4**, 6381.
- Tan, L., An, Z., Huh, C.-A., Cai, Y., Shen, C.-C., Shiao, L.-J., Yan, L., Cheng, H., and Edwards, R. L., 2014b. Cyclic precipitation variation on the western Loess Plateau of China during the past four centuries. *Nature Scientific Reports* **4**,
- Tan, L., Cai, Y., Yi, L., An, Z., and Ai, L., 2008. Precipitation variations of Longxi, northeast margin of Tibetan Plateau since AD 960 and their relationship with solar activity. *Climate of the Past* **4**, 19-28.
- Tan, L., Cai, Y. J., An, Z. S., Edwards, R. L., Cheng, H., Shen, C. C., and Zhang, H. W., 2011. Centennial-to decadal-scale monsoon precipitation variability in the semi-humid region, northern China during the last 1860 years: Records from stalagmites in Huangye Cave. *The Holocene* **21**, 287-296.
- Tan, L., Cai, Y. J., Cheng, H., An, Z. S., and Edwards, R. L., 2009a. Summer monsoon precipitation variations in central China over the past 750 years derived from a high-resolution absolute-dated stalagmite. *Palaeogeography, Palaeoclimatology, Palaeoecology* **280**, 432-439.
- Tan, M., Shao, X., Liu, J., and Cai, B., 2009b. Comparative analysis between a proxy-based climate reconstruction and GCM-based simulation of temperatures over the last millennium in China. *Journal of Quaternary Science* **24**, 547-551.
- Tang, J., Köhler, S. J., and Dietzel, M., 2008. $\text{Sr}^{2+}/\text{Ca}^{2+}$ and $^{44}\text{Ca}/^{40}\text{Ca}$ fractionation during inorganic calcite formation: I. Sr incorporation. *Geochimica et Cosmochimica Acta* **72**, 3718-3732.
- Tesoriero, A. J. and Pankow, J. F., 1996. Solid solution partitioning of Sr^{2+} , Ba^{2+} , and Cd^{2+} to calcite. *Geochimica et Cosmochimica Acta* **60**, 1053-1063.

- Thornthwaite, C. W., 1948. An approach toward a rational classification of climate. *Geographical Review* **38**, 55-94.
- Tingley, M. P., Craigmile, P. F., Haran, M., Li, B., Mannshardt, E., and Rajaratnam, B., 2012. Piecing together the past: statistical insights into paleoclimatic reconstructions. *Quaternary Science Reviews* **35**, 1-22.
- Tokay, A., Roche, R. J., and Bashor, P. G., 2013. An Experimental Study of Spatial Variability of Rainfall. *Journal of Hydrometeorology* **15**, 801-812.
- Tooth, A. F. and Fairchild, I. J., 2003. Soil and karst aquifer hydrological controls on the geochemical evolution of speleothem-forming drip waters, Crag Cave, southwest Ireland. *Journal of Hydrology* **273**, 51-68.
- Tratman, E. K., 1971. The formation of the Gibraltar Caves. *Transactions of the Cave Research Group of Great Britain* **13**, 135-143.
- Truebe, S. A., Ault, T. R., and Cole, J. E., 2010. A forward model of cave dripwater $\delta^{18}\text{O}$ and application to speleothem records. *IOP Conference Series: Earth and Environmental Science* **9**, 012022.
- Ueda, H., Iwai, A., Kuwako, K., and Hori, M. E., 2006. Impact of anthropogenic forcing on the Asian summer monsoon as simulated by eight GCMs. *Geophysical Research Letters* **33**, L06703.
- van der Ent, R. J. and Savenije, H. H. G., 2013. Oceanic sources of continental precipitation and the correlation with sea surface temperature. *Water Resources Research* **49**, 3993-4004.
- van Oldenborgh, G. J. and Burgers, G., 2005. Searching for decadal variations in ENSO precipitation teleconnections. *Geophysical Research Letters* **32**, L15701.
- Vimeux, F., Masson, V., Jouzel, J., Stievenard, M., and Petit, J. R., 1999. Glacial-interglacial changes in ocean surface conditions in the Southern Hemisphere. *Nature* **398**, 410-413.
- Vuille, M., Bradley, R. S., Werner, M., Healy, R., and Keimig, F., 2003. Modeling $\delta^{18}\text{O}$ in precipitation over the tropical Americas: 1. Interannual variability and climatic controls. *Journal of Geophysical Research: Atmospheres* **108**, D6, 4174.
- Vuille, M., Werner, M., Bradley, R. S., and Keimig, F., 2005. Stable isotopes in precipitation in the Asian monsoon region. *Journal of Geophysical Research: Atmospheres* **110**, D23108.
- Wackerbarth, A., Langebroek, P. M., Werner, M., Lohmann, G., Riechelmann, S., Borsato, A., and Mangini, A., 2012. Simulated oxygen isotopes in cave drip water and speleothem calcite in European caves. *Climate of the Past* **8**, 1781-1799.
- Wackerbarth, A., Scholz, D., Fohlmeister, J., and Mangini, A., 2010. Modelling the $\delta^{18}\text{O}$ value of cave drip water and speleothem calcite. *Earth and Planetary Science Letters* **299**, 387-397.
- Wang, B. and Ding, Q., 2006. Changes in global monsoon precipitation over the past 56 years. *Geophysical Research Letters* **33**, L06711.
- Wang, B. and Lin, H., 2002. Rainy season of the Asian-Pacific summer monsoon. *Journal of Climate* **15**, 386-398.
- Wang, X. F., Auler, A. S., Edwards, R. L., Cheng, H., Cristalli, P. S., Smart, P. L., Richards, D. A., and Shen, C. C., 2004. Wet periods in northeastern Brazil over the past 210 kyr linked to distant climate anomalies. *Nature* **432**, 740-743.
- Wang, Y., Liu, X., and Herzschuh, U., 2010. Asynchronous evolution of the Indian and East Asian Summer Monsoon indicated by Holocene moisture patterns in monsoonal central Asia. *Earth-Science Reviews* **103**, 135-153.

- Wang, Y. J., Cheng, H., Edwards, R. L., An, Z. S., Wu, J. Y., Shen, C. C., and Dorale, J. A., 2001. A high-resolution absolute-dated Late Pleistocene monsoon record from Hulu Cave, China. *Science* **294**, 2345-2348.
- Wang, Y. J., Cheng, H., Edwards, R. L., He, Y. Q., Kong, X. G., An, Z. S., Wu, J. Y., Kelly, M. J., Dykoski, C. A., and Li, X. D., 2005. The Holocene Asian monsoon: Links to solar changes and North Atlantic climate. *Science* **308**, 854-857.
- Wang, Y. J., Cheng, H., Edwards, R. L., Kong, X. G., Shao, X. H., Chen, S. T., Wu, J. Y., Jiang, X. Y., Wang, X. F., and An, Z. S., 2008. Millennial- and orbital-scale changes in the East Asian monsoon over the past 224,000 years. *Nature* **451**, 1090-1093.
- Webster, P. J., Magana, V. O., Palmer, T. N., Shukla, J., Tomas, R. A., Yanai, M., and Yasunari, T., 1998. Monsoons: Processes, predictability, and the prospects for prediction. *Journal of Geophysical Research: Atmospheres* **103**, 14451-14510.
- Wernli, B. H. and Davies, H. C., 1997. A lagrangian-based analysis of extratropical cyclones. I: The method and some applications. *Quarterly Journal of the Royal Meteorological Society* **123**, 467-489.
- Wheeler, D. A., 2006. The Gibraltar climate record: Part 1 – the history of weather observations. *Weather* **61**, 36-39.
- Wheeler, D. A., 2007. The Gibraltar climate record: Part 2 – precipitation. *Weather* **62**, 99-104.
- Wheeler, D. A., 2011. The Gibraltar climatic record – Part 3. Temperature. *Weather* **66**, 259-265.
- Whitaker, T., Jones, D., Baldini, J. U. L., and Baker, A. J., 2009. A high-resolution spatial survey of cave air carbon dioxide concentrations in Scoska Cave (North Yorkshire, UK): implications for calcite deposition and re-dissolution. *Cave and Karst Science* **36**, 85-92.
- White, W. B., 1988. *Geomorphology and Hydrology of Karst Terrains*. 1st ed. Oxford University Press, New York. 464p.
- White, W. B., 2007. Cave sediments and paleoclimate. *Journal of Cave and Karst Studies* **69**, 76-93.
- Wong, C. I., Banner, J. L., and Musgrove, M., 2011. Seasonal dripwater Mg/Ca and Sr/Ca variations driven by cave ventilation: Implications for and modeling of speleothem paleoclimate records. *Geochimica et Cosmochimica Acta* **75**, 3514-3529.
- Wu, H., Zhang, X., Xiaoyan, L., Li, G., and Huang, Y., 2014. Seasonal variations of deuterium and oxygen-18 isotopes and their response to moisture source for precipitation events in the subtropical monsoon region. *Hydrological Processes* **29**, 90-102.
- Xie, P. and Arkin, P. A., 1997. Global Precipitation: A 17-Year Monthly Analysis Based on Gauge Observations, Satellite Estimates, and Numerical Model Outputs. *Bulletin of the American Meteorological Society* **78**, 2539-2558.
- Xu, X. D., Chen, L. S., Wang, X. R., Miao, Q. J., and Tao, S. Y., 2004. Moisture transport source/sink structure of the Meiyu rain belt along the Yangtze River valley. *Chinese Science Bulletin* **49**, 181-188.
- Yang, X., Yao, T., Yang, W., Yu, W., and Qu, D., 2011. Co-existence of temperature and amount effects on precipitation $\delta^{18}\text{O}$ in the Asian monsoon region. *Geophysical Research Letters* **38**, L21809.
- Yonge, C. J., Ford, D. C., Gray, J., and Schwarcz, H. P., 1985. Stable Isotope Studies of Cave Seepage Water. *Chemical Geology* **58**, 97-105.

- Yoshimura, K., Kanamitsu, M., Noone, D., and Oki, T., 2008. Historical isotope simulation using Reanalysis atmospheric data. *Journal of Geophysical Research: Atmospheres* **113**, D19108.
- Yuan, D. X., Cheng, H., Edwards, R. L., Dykoski, C. A., Kelly, M. J., Zhang, M. L., Qing, J. M., Lin, Y. S., Wang, Y. J., Wu, J. Y., Dorale, J. A., An, Z. S., and Cai, Y. J., 2004. Timing, duration, and transitions of the Last Interglacial Asian Monsoon. *Science* **304**, 575-578.
- Zhang, J., Chen, F., Holmes, J. A., Li, H., Guo, X., Wang, J., Li, S., Lü, Y., Zhao, Y., and Qiang, M., 2011. Holocene monsoon climate documented by oxygen and carbon isotopes from lake sediments and peat bogs in China: a review and synthesis. *Quaternary Science Reviews* **30**, 1973-1987.
- Zhang, P. Z., Cheng, H., Edwards, R. L., Chen, F. H., Wang, Y. J., Yang, X. L., Liu, J., Tan, M., Wang, X. F., Liu, J. H., An, C. L., Dai, Z. B., Zhou, J., Zhang, D. Z., Jia, J. H., Jin, L. Y., and Johnson, K. R., 2008. A Test of Climate, Sun, and Culture Relationships from an 1810-Year Chinese Cave Record. *Science* **322**, 940-942.
- Zheng, J., Hao, Z., and Ge, Q., 2005. Variation of precipitation for the last 300 years over the middle and lower reaches of the Yellow River. *Science in China Series D: Earth Sciences* **48**, 2182-2193.